PRECISION MEASUREMENTS OF PROPERTIES OF W AND Z BOSONS WITH THE ATLAS EXPERIMENT

By

BENJAMIN R. DAVIS-PURCELL, B.Sc., M.Sc.

A thesis submitted to the Faculty of Graduate and Postdoctoral Affairs
in partial fulfillment of the requirements for the degree of

Doctor of Philosophy

in

Physics

Carleton University
Ottawa, Ontario

Abstract

The ATLAS Experiment measures the properties of particles created in the high-energy proton-proton collisions delivered by the Large Hadron Collider at CERN. The Standard Model of particle physics is our best description of the subatomic world – this well-studied theory provides accurate and precise descriptions of the fundamental particle properties and their interactions. Multiple areas of the Standard Model make predictions that are more precise than the corresponding experimental measurements – in some cases, increased experimental precision could suggest significant discrepancies between the Standard Model prediction and experimental measurement, potentially hinting at new physics to elucidate. One such area of tension between prediction and experiment is in the weak sector, whose force is mediated by W and Z bosons. The current best predictions based on the Standard Model do an inadequate job of precisely predicting one important observable of W and Z bosons: their transverse momentum, p_{T}. Precision measurements of properties like the p_{T} of W and Z bosons improve our knowledge of the weak sector, and are vital stepping stones to critical measurements like the mass of the W boson, whose most recent reported measurement is inconsistent with the Standard Model prediction. In this thesis, I explain my work using ATLAS data to make high-precision measurements of the p_{T} of W and Z bosons using the decay channels $W^{\pm} \to l^{\pm}\nu$ and $Z \to l^{+}l^{-}$ ($l = e, \mu$) at centre-of-mass energies 13 and 5 TeV using a special low-pileup dataset. I show that I have helped reduce the systematic uncertainties to percent-level precision and that statistical uncertainties are dominant, which demonstrates that more low-pileup data should be taken in order to further reduce the total uncertainty to eventually help resolve Standard Model weak-sector discrepancies like that of the W boson mass. I also detail my work to improve the way that electrons are identified by the ATLAS detector using a technique called W tag-and-probe. In particular, I validated the use of a new trigger designed specifically for electron identification with the W tag-and-probe technique.

Acknowledgements

It has never made sense to me why this section comes at the beginning of a thesis, mainly for the reason that it always seems to be the last thing that is written. I will try to keep this short! To anyone reading this thesis, if you do choose to read this section, maybe you should save it for the end too!

Since high school, when I accepted the reality of my crushed childhood dreams of never being a professional hockey player (silly me, I was never anywhere close to good enough), I did not know that I wanted to be a physicist, but I knew that I wanted to be able to come to (and work at) CERN. I took a long, windy road to get here, researching multiple different areas of physics and working and volunteering in teaching and science communication/outreach (all things I am proud of), and now I am very happy to be able to say that I made it.

When I decided to pursue a PhD, I knew if I was going to do so, it had to be as part of a particle physics experimental collaboration that would bring me to CERN. I asked my undergraduate thesis supervisor, Dr. Cliff Burgess, who he would recommend as a potential supervisor. He recommended multiple fantastic researchers (thank you Cliff!), and helped me get where I am today. During my PhD interviews at various universities, the person who I really felt like I hit it off with was Dr. Manuella Vincter – she is now my supervisor, and I am super happy to have been her student. Even in her role as Deputy Spokesperson of the ATLAS Collaboration, a top-level management position, she has been continually supportive and has always set me up to succeed in many different ways. Thank you for somehow always responding to my emails incredibly quickly, providing me with multiple opportunities to live and work at CERN, and just being an all-around excellent supervisor. I promise that one day, I will remember that the word "data" is plural.

There are too many other individual thank you's to mention. I'm sorry to everyone who I am forgetting! First of all, thank you to NSERC (the Natural Sciences and Engineering Research Council of Canada), for funding me with a scholarship. After applying seven times to NSERC scholarships over the years, the eighth time was the charm, and I'm very grateful that it was. Thank you to the ATLAS Early Career Scientist Board for running events that made me feel welcome in a huge collaboration early on – I am privileged to have been able to give back by closing out the second

half of my PhD as a member of this board myself.

Thank you Nataliia for being the first person to show me the ATLAS-analysis ropes. Thank you Bri for being the first friend I made here at CERN, quickly helping my circle expand, and for making a great housemate along with Alex – we formed a fun little trio!

Thank you Kari, my MSc supervisor who is now not just my most trusted mentor, but a good friend who has continually been there for me throughout my whole physics career.

The middle years of my PhD were incredibly difficult. The depths of the COVID-19 pandemic really brought me down. Working alone from home without an exciting, productive physics atmosphere is not my thing. Thank you to my girlfriend Sarah for keeping me company during those dark months, and for putting up with me while I worked seemingly endless long nights, somehow staying positive and supportive throughout.

Lastly, I would not be here without my family, who have always supported me, but more than that, have been genuinely curious and have always wanted to know more and learn about the research that I'm doing. To my Bubie and Zaida – thank you for always asking questions. Bubie, one day I will get some of those "Bosons for Bubies" posts published online. To my sisters Rebecca and Leah, we have all gone through some intense years, and I care more about yours than mine. I know you'll always be there for me, and I will always be there for you too. And Mom and Dad, I don't have much to say. You're the best parents anyone could ever ask for. Period. I love you all very much.

That's it! Through all the hardships, I am truly happy that I did this PhD. Despite the ups and downs, the experience was definitely positive. Hopefully I made a positive impact on others around me as well, and I hope to continue to be able to have a positive impact on physics and science as a whole, perhaps through my own research, but definitely by encouraging more evidence-based thinking and showing that science is beneficial to everyone and is something that we can all love and enjoy.

Contents

Abstract ii
Acknowledgements iii

1 Setting the Stage **1**
1.1 A Quick Note on Units 5

2 The Standard Model of Particle Physics **6**
2.1 The Standard Model: An Overview 6
2.1.1 Fermions 9
2.1.2 Vector Bosons 10
2.1.3 Higgs Boson 10
2.2 Quantum Field Theory of the Standard Model 12
2.2.1 Quantum Electrodynamics 12
2.2.2 Quantum Chromodynamics 13
2.2.3 Electroweak Unification 16
2.3 Shortcomings of the Standard Model 22

3 The ATLAS Experiment and the LHC at CERN **24**
3.1 CERN 25
3.2 Accelerator Physics 26
3.3 The Large Hadron Collider 28
3.4 The ATLAS Experiment 32
3.4.1 The ATLAS Collaboration 33
3.4.2 Detector Overview & Geometry 33

3.4.3 Inner Detector 38
3.4.4 Calorimeters 40
3.4.5 Muon Spectrometer 42
3.4.6 Magnet System 42
3.4.7 Trigger and Data Acquisition 46
3.4.8 Luminosity Measurements 46

4 Measuring Electrons with ATLAS 50
4.1 Data and Simulation 51
4.1.1 Data 51
4.1.2 Monte Carlo Simulation 53
4.2 Electron Efficiency Measurements 54
4.2.1 Tag-And-Probe 55
4.2.2 Reconstruction 57
4.2.3 Identification 58
4.2.4 Isolation 59
4.2.5 Trigger Efficiency 61
4.3 W Tag-And-Probe 62
4.3.1 W Boson Measurement Parameters 64
4.3.2 WTP Framework Setup & Event Selection 66
4.3.3 Trigger Results 68
4.3.4 Kinematic Distributions 73
4.3.5 Control Plots 79
4.3.6 Efficiencies & Scale Factors 85
4.3.7 Conclusions & Next Steps 86

5 Measurements of p_{T}^{W} and p_{T}^{Z} in Drell-Yan Processes 91
5.1 p_{T}^{W} as an Input to m_W 92
5.2 p_{T}^{W} Modeling at Low p_{T} 95
5.3 p_{T}^{W} and p_{T}^{Z} at 5 and 13 TeV 97
5.4 p_{T}^{Z} for Calibration 98
5.5 Conclusion 99

6 Unfolding a Dataset **100**
6.1 Cross-Section Road Map 100
6.2 Unfolding 101
6.2.1 What is Unfolding? 103
6.2.2 Why Unfold? 104
6.2.3 The Unfolding Process 105
6.2.4 Unfolding Bias Uncertainty 112
6.3 Summary 112

7 Measurement of the Z Boson Drell-Yan Process Differential Cross Section as a Function of p_{T}^{Z} **114**
7.1 Event Selection and Backgrounds 116
7.1.1 p_{T}^{Z} Multi-jet Background Estimation 121
7.2 Uncertainties 130
7.2.1 Statistical Uncertainties 130
7.2.2 Systematic Uncertainties 133
7.2.3 Unfolding Bias Uncertainty 134
7.2.4 Luminosity Uncertainty 136
7.2.5 Total p_{T}^{Z} Measurement Uncertainties 138
7.3 Unfolded Cross Sections 141
7.4 Compatibility 149
7.5 Summary 155

8 p_{T}^{W} Reweighting and Unfolding Bias Uncertainty **156**
8.1 Reweighting Strategy 159
8.2 Determination of the Unfolding Bias Uncertainties 170
8.2.1 Fit Uncertainty 171
8.2.2 Parameterization Uncertainty 174
8.2.3 Alternative MC Uncertainty 177
8.2.4 Total Unfolding Bias Uncertainty 184
8.3 Conclusion 186

9 There and Back Again **189**

A Glossary of Terms **193**

B Theory Background Material **196**

B.1 Units 196

B.2 Fields in Particle Physics 197

B.3 The Lagrangian Formalism 198

B.4 Feynman Diagrams 200

B.5 de Broglie Wavelength 202

C Additional W Tag-And-Probe Results **203**

D Complete p_{T}^{Z} Results **209**

E Additional p_{T}^{W} Unfolding Bias Uncertainty Channels **223**

F ATLAS Control Room Operations **231**

F.1 ACR Overview 232

F.2 Run Control Desk 233

F.3 Trigger Desk 236

F.4 Conclusion 239

G Analysis Timeline, Contributions and Scholarships **240**

References **247**

List of Tables

2.1 Leptons in the Standard Model 11
2.2 Vector Bosons in the Standard Model 11

3.1 Muon Spectrometer Parameters 42

4.1 WTP Selection Cuts 69

7.1 Analysis Selection Cuts: $Z \to e^+e^-$ at $\sqrt{s} = 13$ TeV 119
7.2 Analysis Selection Cuts: $Z \to \mu^+\mu^-$ at $\sqrt{s} = 13$ TeV 119
7.3 Analysis Selection Cuts: $Z \to e^+e^-$ at $\sqrt{s} = 5$ TeV 120
7.4 Analysis Selection Cuts: $Z \to \mu^+\mu^-$ at $\sqrt{s} = 5$ TeV 120
7.5 $Z \to l^+l^-$ MJ Events 127
7.6 p_{T}^{Z} Systematic Uncertainties 134

8.1 Parameterization Uncertainty Sample χ^2 175
8.2 Alternative MC Sample χ^2 180

List of Figures

2.1 The Standard Model 8
2.2 QED Vertex 13
2.3 QCD Vertices 15
2.4 Internal Proton Structure 16
2.5 Proton-Proton Collision 17
2.6 EW Vertices 19
2.7 Higgs Boson Vertices 20
2.8 Drell-Yan Process 21

3.1 CERN Accelerator Complex 26
3.2 LHC Aerial View 29
3.3 LHC Beam Pipe 31
3.4 LHC Schedule 32
3.5 The ATLAS Collaboration 34
3.6 ATLAS Detector Overview 35
3.7 ATLAS Detector Geometry 36
3.8 Pseudorapidity 37
3.9 ATLAS Inner Detector 39
3.10 ATLAS Calorimeter 41
3.11 ATLAS Muon Spectrometer 43
3.12 ATLAS Magnet System 44
3.13 ATLAS Toroidal Magnets 44

3.14 Particle Paths in the ATLAS Detector 45
3.15 Run-2 Integrated Luminosity 47
3.16 Run-2 Average Pileup 49

4.1 Low-Pileup Data 52
4.2 Pileup Event Displays 53
4.3 Tag-And-Probe 56
4.4 Electron Traversing Detector 59
4.5 Calorimeter Isolation 60
4.6 Sample Trigger Efficiency 61
4.7 Hadronic Recoil 65
4.8 WTP Selection Cuts 69
4.9 $E_{\mathrm{T}}^{\mathrm{miss}}$ Trigger Efficiency 70
4.10 WTP Data Trigger Efficiency 71
4.11 WTP MC Trigger Efficiency 72
4.12 WTP $E_{\mathrm{T}}^{\mathrm{miss}}$ 74
4.13 $W^- \to e^-\bar{\nu}$ $p_{\mathrm{T}}^{\mathrm{miss}}$ Distribution 74
4.14 WTP m_{T}^{W} 75
4.15 $W^- \to e^-\bar{\nu}$ m_{T}^{W} Distribution 75
4.16 WTP MC Isolation 76
4.17 WTP Data $E_{\mathrm{T}}^{\mathrm{miss}}$ Isolation 77
4.18 WTP Data m_{T}^{W} Isolation 77
4.19 WTP $\Delta\phi$ Distribution 78
4.20 WTP p_{T}^{e} Distribution 78
4.21 WTP Control Plot 81
4.22 ZTP Control Plot 82
4.23 Control Plot Trigger Comparison: $E_{\mathrm{T}} = [30, 35]$ GeV, $\eta = [0.1, 0.6]$ . . 84
4.24 MC Efficiency vs. η 87
4.25 MC Efficiency vs. E_{T} 88
4.26 Data *Medium* Efficiency 89
4.27 WTP *Medium* Scale Factors 90

5.1 m_W Measurements 93

5.2 W/Z Cross-Section Predictions 96
5.3 Z boson Cross-Section $\sqrt{s}$ Dependence 97
5.4 High-Pileup p_{T}^{Z} 99

6.1 Road Map of a Cross-Section Measurement 101
6.2 ECAL Detector Material 102
6.3 p_{T}^{Z} $Z \to e^{+}e^{-}$ Reco-Level Data 105
6.4 p_{T}^{Z} $Z \to e^{+}e^{-}$ Full-Phase Space MC 106
6.5 $Z \to e^{+}e^{-}$ MC Cuts 107
6.6 Purity 108
6.7 Migration Matrix 110
6.8 Migration Matrix Construction 110

7.1 p_{T}^{Z} Contributions 115
7.2 ABCD Method 122
7.3 $\sqrt{s} = 13$ TeV $Z \to e^{+}e^{-}$ MJ Isolation Regions 124
7.4 $\sqrt{s} = 5$ TeV $Z \to e^{+}e^{-}$ MJ Isolation Regions 125
7.5 $\sqrt{s} = 13$ TeV $Z \to e^{+}e^{-}$ MJ CR Shape Fits 128
7.6 $\sqrt{s} = 5$ TeV $Z \to e^{+}e^{-}$ MJ CR Shape Fits 129
7.7 $Z \to e^{+}e^{-}$ MJ Distributions 131
7.8 $Z \to e^{+}e^{-}$ $\sqrt{s} = 13$ TeV p_{T}^{ll} Uncertainty Minimization 136
7.9 $Z \to e^{+}e^{-}$ $\sqrt{s} = 13$ TeV u_{T} Uncertainty Minimization 137
7.10 $Z \to e^{+}e^{-}$ p_{T}^{ll} Uncertainty Breakdown at $\sqrt{s} = 13$ TeV 139
7.11 $Z \to e^{+}e^{-}$ u_{T} Uncertainty Breakdown at $\sqrt{s} = 13$ TeV 140
7.12 $Z \to e^{+}e^{-}$ p_{T}^{ll} Uncertainty Breakdown at $\sqrt{s} = 5$ TeV 141
7.13 $Z \to e^{+}e^{-}$ u_{T} Uncertainty Breakdown at $\sqrt{s} = 5$ TeV 142
7.14 $Z \to e^{+}e^{-}$ Unfolded Cross Section at $\sqrt{s} = 13$ TeV 144
7.15 $Z \to e^{+}e^{-}$ Unfolded Cross Section at $\sqrt{s} = 5$ TeV 145
7.16 $Z \to e^{+}e^{-}$ $\sqrt{s} = 13$ TeV Normalized Cross Section 147
7.17 $Z \to e^{+}e^{-}$ $\sqrt{s} = 5$ TeV Normalized Cross Section 148
7.18 p_{T}^{Z} Lepton Compatibility at $\sqrt{s} = 13$ TeV 150
7.19 p_{T}^{Z} Lepton Compatibility at $\sqrt{s} = 5$ TeV 151
7.20 p_{T}^{Z} Observable Compatibility at $\sqrt{s} = 13$ TeV 153

7.21 p_{T}^{Z} Observable Compatibility at $\sqrt{s} = 5$ TeV 154

8.1 p_{T}^{W} Contributions 158
8.2 p_{T}^{W} Unfolding Bias Estimation Procedure 161
8.3 $r_{\mathrm{NNPDF/CT10}}(p_T^W)$ Parameterization Function 164
8.4 $W^+ \to e^+\nu$ Fit at $\sqrt{s} = 13$ TeV 166
8.5 $W^\pm \to l^\pm\nu$ p_{T} Reweighting at $\sqrt{s} = 13$ TeV 167
8.6 $W^\pm \to l^\pm\nu$ p_{T} Reweighting at $\sqrt{s} = 5$ TeV 168
8.7 $W \to e\nu$ Data/MC 169
8.8 $W^+ \to l^+\nu$ Bias Correction Closure 172
8.9 W Bias Fit Uncertainty: $W^+ \to e^+\nu$ 173
8.10 $W^+ \to e^+\nu$ Alternative Function Data/MC 174
8.11 W Bias Alt. Reweighting Factors 176
8.12 $W^+ \to e^+\nu$ Paramaterization Uncertainty 178
8.13 $W^+ \to e^+\nu$ Alternative MC Data/MC 179
8.14 Alt. MC Reweighting Factors 182
8.15 $W^+ \to e^+\nu$ Alt. MC Uncertainty 183
8.16 $W^+ \to e^+\nu$ Total Bias Uncertainty 185
8.17 ATLAS Previous p_{T}^{W} Measurement Uncertainties 188

9.1 Run-3 Event Display 192

B.1 Feynman Diagram 200
B.2 Feynman Diagram Orders 201

C.1 Control Plot Trigger Comparison: $E_{\mathrm{T}} = [25, 30]$ GeV, $\eta = [0.1, 0.6]$ . . 204
C.2 Control Plot Trigger Comparison: $E_{\mathrm{T}} = [35, 40]$ GeV, $\eta = [0.6, 0.8]$ . . 205
C.3 Control Plot Trigger Comparison: $E_{\mathrm{T}} = [40, 45]$ GeV, $\eta = [0.0, 0.1]$ . . 206
C.4 MC Efficiency vs. η for $E_{\mathrm{T}} = [40, 45]$ GeV 207
C.5 MC Efficiency vs. E_{T} for $\eta = [0.8, 1.15]$ 208

D.1 $\sqrt{s} = 13$ TeV $Z \to \mu^+\mu^-$ MJ Isolation Regions 210
D.2 $\sqrt{s} = 5$ TeV $Z \to \mu^+\mu^-$ MJ Isolation Regions 211
D.3 $\sqrt{s} = 13$ TeV $Z \to \mu^+\mu^-$ MJ CR Shape Fits 212
D.4 $\sqrt{s} = 5$ TeV $Z \to \mu^+\mu^-$ MJ CR Shape Fits 213

D.5 $Z \to \mu^+\mu^-$ MJ Distributions 214
D.6 $Z \to \mu^+\mu^-$ p_{T}^{ll} Uncertainty Breakdown at $\sqrt{s} = 13$ TeV 215
D.7 $Z \to \mu^+\mu^-$ u_{T} Uncertainty Breakdown at $\sqrt{s} = 13$ TeV 216
D.8 $Z \to \mu^+\mu^-$ p_{T}^{ll} Uncertainty Breakdown at $\sqrt{s} = 5$ TeV 217
D.9 $Z \to \mu^+\mu^-$ u_{T} Uncertainty Breakdown at $\sqrt{s} = 5$ TeV 218
D.10 $Z \to \mu^+\mu^-$ Unfolded Cross Section at $\sqrt{s} = 13$ TeV 219
D.11 $Z \to \mu^+\mu^-$ Unfolded Cross Section at $\sqrt{s} = 5$ TeV 220
D.12 $Z \to \mu^+\mu^-$ $\sqrt{s} = 13$ TeV Normalized Cross Section 221
D.13 $Z \to \mu^+\mu^-$ $\sqrt{s} = 5$ TeV Normalized Cross Section 222

E.1 $W \to \mu\nu$ Data/MC 224
E.2 $W \to e\nu$ Data/MC 225
E.3 $W \to \mu\nu$ Data/MC 226
E.4 $W^- \to l^-\bar{\nu}$ Bias Correction Closure 227
E.5 $W^+ \to \mu^+\nu$ Total Bias Uncertainty 228
E.6 $W^- \to e^-\bar{\nu}$ Total Bias Uncertainty 229
E.7 $W^- \to \mu^-\bar{\nu}$ Total Bias Uncertainty 230

F.1 ACR Desks 233
F.2 ACR Photo 234
F.3 Run Control State 236

G.1 Analysis Timeline 241
G.2 Ben Tour Guide Photo 246

Chapter 1

Setting the Stage

As scientists, our goal is to add to our understanding of the Universe. This understanding must be improved intellectually and practically, by systematically making predictions, performing tests, confronting tests to predictions, and slowly building upon the database of human knowledge. To me, this boils down to curiosity and wanting answers to the never-ending question: "Why?". Physicists seek answers to these "Why?" questions about matter, energy, and their motion and behaviour through space and time. As we continue to ask why, digging deeper and deeper, eventually we will reach the study of particle physics where we wish to understand the two most fundamental aspects of the Universe: the fundamental particles and the fundamental forces between these particles, which are in fact transmitted by force-carrying particles themselves. At this level of granularity, at least in this era of particle physics, we must rephrase our questions into those that ask "How?" instead of "Why?". For example, why do the fundamental particles and forces that we observe exist, as opposed to other particles or forces, or more/less of them than the number that we observe? This is a why question that we currently cannot answer, but we *can* answer questions such as: how do these fundamental particles interact with each other and which forces govern their interactions? These are questions that we can provide concrete answers for, given the right tools.

Once we have reached this level of fundamental particles and forces, curiosity still drives us to answers, but as particle physicists, at some point we must choose an area to directly contribute to where we can start providing answers. With this

thesis, I present some of the answers that I have been able to provide. Being an experimental particle physicist and providing these answers is very much a team effort, from understanding the background processes that mimic the physics of interest in a measurement, to understanding how to use the machinery of an experiment to make a measurement, to understanding how a measurement fits into the grander scheme of the field and being able to balance all these things and more in order to make a strong contribution as an individual. I am very happy to have had this opportunity to find my way as a tiny key in the massive cog of particle physics and make meaningful contributions, and I am very lucky to do so as a member of the incredible team that is the ATLAS Collaboration.

My main direct contribution to the field of particle physics is the subject of my thesis: the high-precision cross-section measurement of W and Z bosons as a function of their transverse momentum, measured with the ATLAS Experiment. W and Z bosons are two of these previously-alluded to fundamental force-carrying particles that are described by our best, most well-tested prediction of the fundamental world called the Standard Model. These bosons, the name for particles that transmit forces, are transmitters of one of the four fundamental forces of nature: the weak force. This is the force responsible for nuclear decays. The Standard Model will be covered in more detail in Chapter 2. In particle physics terms, a cross section is the probability that an interaction will occur, and is explained in more detail in Chapter 3.

Why continue to study a well-tested model that already does a good job of describing the fundamental particles in the Universe? Well, there are some aspects of the model that have been theoretically predicted and experimentally measured with incredibly high, nearly equivalent levels of precision, that give consistent results – great news for our knowledge of the Universe, but not the best news for an experimental physics PhD student looking to make a contribution. However, there are other areas of the model where increased precision is required experimentally in order to match the precision of the model. When increased experimental precision is obtained, it could lead to a disagreement between the measured data and the prediction. Additionally, high-precision data in one aspect of the model can help to improve the predictions that can be made in other related aspects of the model. These are both important reasons to precisely measure the transverse momentum of W and Z bosons. These

two bosons work well together themselves: the Z boson is an interesting particle that must have its properties measured to high precision, and high-precision measurements of Z boson properties like its transverse momentum can help to improve similar measurements of the related W boson, because Z boson properties can be measured more easily than those of the W boson.

Conveniently at the time of writing this thesis, an interesting experimental measurement was published, reporting an updated result on one of these properties: the mass of the W boson. This measurement showed a significant discrepancy with both the best predictions and best previous measurements. ATLAS is one experiment that has the potential to resolve this discrepancy and the set of measurements presented in this thesis is the first essential step of the programme to work towards this resolution. This leads to the importance of the aforementioned W and Z boson transverse momentum measurements, covered in Chapter 5. The Z boson transverse momentum high-precision measurement itself is explained in detail in Chapter 7 as one of the principle measurements of this thesis.

How can we make measurements of these most fundamental particles in the Universe? We need a measurement device to "see" these particles, and by seeing we mean measuring their properties. Just like a microscope takes in light to measure the optical properties of substances, the ATLAS detector, the "microscope" of the ATLAS Experiment, records snapshots of particles and measures their properties by converting their energy and passage into electrical signals. There is an enormous amount of work that goes into understanding these signals to correctly interpret them as the particles they originated from, which is why the ATLAS Experiment is not just a detector, but a worldwide collaboration of researchers working together to make these measurements possible. The particles themselves are delivered in the form of (mostly) proton-proton collisions by the Large Hadron Collider at CERN – the largest particle accelerator in the world at the largest particle physics laboratory in the world, located on the French/Swiss border near Geneva, Switzerland. The ATLAS detector is positioned coaxially around one section of the Large Hadron Collider at CERN, allowing the collisions to happen in its centre. This aspect is described in much more detail in Chapter 3.

The ATLAS Experiment and CERN must work directly together in order to make

efficient use of the particles created during these proton-proton collisions. This requires immense planning, extensive calibration, and vigilant monitoring in the ATLAS Experiment Control Room during data-taking in order for ATLAS to record all the useful data coming from the particle collisions produced by the Large Hadron Collider. Everyone should want to be where this data-taking action happens; my experience in the ATLAS Control Room is outlined in Appendix F.

In order to use the ATLAS detector to make measurements of particle properties, it is vital that we understand how efficiently our detector measures these properties, especially for the particles that we most commonly measure such as electrons. We know that the ATLAS detector is very good at measuring electrons. However, this is not good enough: we need to have a precise measure of how well we measure electrons, and how certain we are of this. A precise understanding of the efficiency at which we measure electrons is critical to making a precise measurement of the properties of a process involving electrons, such as the decay of a Z boson to two electrons that I measure in Chapter 7. We must invoke many studies to understand these aspects of the detector. ATLAS' measurement of electron efficiencies, including my contribution to this area, is explained in Chapter 4.

As we have been starting to see, experimental particle physicists who make the measurements and theoretical particle physicists to who make the predictions use each other's results, often even working together, to both push our knowledge forward and help each other at the same time. The measurements that experimentalists make help improve the predictions, and better predictions help guide and improve future measurements. However, we must make sure that experimental measurements can be fully understood by theorists who do not have complete knowledge of the detector that made the measurement. That is why we must work to remove specific effects caused by our detector that can be imprinted on our data. This process, described in detail in Chapter 6, is known as unfolding. The process of unfolding is generally straightforward and contributes a small uncertainty to an overall measurement. The method to determine this uncertainty is usually well-defined in ATLAS for measurements that are based on the Standard Model. However, sometimes in the context of high-precision measurements, this well-defined recommended method to determine this uncertainty, called the unfolding bias uncertainty, cannot be em-

ployed and a unique process must be designed and heavily tested. This is the case for the high-precision measurement of the transverse momentum of the W boson, and the determination of this unfolding bias uncertainty was my contribution to the measurement, which is detailed in Chapter 8.

The primary topic of this thesis is the precise measurement of a property of two fundamental particles: the transverse momentum of W and Z bosons. In order for these measurements to be made, as has been outlined and will be detailed throughout this thesis, many stepping stones are involved. This thesis walks through these steps, beginning with the required Standard Model knowledge and a breakdown of CERN and the ATLAS Experiment itself, before getting into precursor measurements in the middle of the thesis that are needed to ensure the accuracy and high-precision of the culminating measurements reported on in the second half of the thesis. An Appendix is also included to provide additional context or plots where necessary. The Appendix concludes with App. G: a short history of the contributions I made during my PhD, which includes many non-research aspects that did not make it into this thesis.

1.1 A Quick Note on Units

Particle physicists deal with objects (or *particles*) that are very small. In order to work with more manageable numbers, energies are quoted in electron volts (eV) instead of the SI unit of Joules (J), where 1 eV $= 1.602 \times 10^{-19}$ J. Typical quantities in particle physics are of the orders of magnitude $\sim$ MeV (10^6 eV), $\sim$ GeV (10^9 eV), or $\sim$ TeV (10^{12} eV). In fact, particle physicists take this one step further, using the system of *natural units*, where $c = \hbar = 1$ (c – speed of light; $\hbar$ – Planck's constant). Therefore, energy (E), mass (m), and momentum (p) are all quoted in electron volts. This discussion is stated more explicitly in Appendix B.1. I will use the particle physics convention of natural units in this thesis, and will clearly state when I am referring to a mass or momentum as opposed to energy.

Chapter 2

The Standard Model of Particle Physics

This chapter provides an overview of the theoretical underpinnings of the experimental work that makes up the bulk of this thesis. The particle content of the Standard Model of particle physics is detailed in Section 2.1, followed by the fundamental interactions of this theory (Section 2.2). The chapter closes with a brief look at some questions that are not answered by the Standard Model (Section 2.3). Appendix sections on the Lagrangian formalism (B.3) and Feynman diagrams (B.4) complement this chapter. Note that "Standard Model of particle physics" will be abbreviated to "SM" at most points throughout this thesis[1].

The summaries in this chapter and the corresponding appendix are based off of the following references: [1–5].

2.1 The Standard Model: An Overview

The Standard Model of particle physics is our best description of how all of the known elementary particles interact via three of the four fundamental forces of Nature. It is a theoretical model that has been rigorously tested by a multitude of experiments across a wide range of energy scales, and its predictions are consistently confirmed by these experiments.

[1] All acronyms and abbreviated terms/variables are listed in Appendix A.

In its simplest graphical form, like the graphic shown in Figure 2.1, the SM groups all of the elementary particles that have been discovered. It is important to note that an elementary (or *fundamental*) particle is exactly that: it cannot be subdivided into any smaller units[2]. For this reason they are sometimes referred to as 'point' particles. These elementary particles can combine in various ways to form larger constituents of elementary particles that we assign names to: for example, a proton is a particle that is composed of quarks and gluons.

Each type of elementary particle has inherent properties associated with it that are true for every particle of that type. Three of these critical properties are:

- mass, m, with units of [eV][3];
- electric charge (commonly just referred to as charge), q, with units of Coulombs [C], but usually stated in units of the electron charge: $e = 1$ (in natural units);
- spin quantum number (commonly just referred to as spin), s, with units of $\hbar$ and therefore dimensionless in natural units.

Spin is an intrinsic form of angular momentum that each particle has, and is truly a quantum mechanical property. Naively, one might think of an object such as Earth rotating on its axis to compare to quantum mechanical spin. Indeed this would be the correct comparison if elementary particles had size, but since they are point particles, the comparison loses meaning. However, spin does lead to macroscopic effects that we can see in everyday life. For example, a photon's spin is the reason for the polarization of light. These three properties are true of every particle of a given type. Every electron in the Universe has the exact same mass, charge, and spin. Every strange quark in the Universe has the exact same mass, charge, and spin. This pattern continues for every fundamental particle in the SM.

All SM particles fall into one of two categories: particles that only feel forces (half-integral spin objects, fermions, often what we would think of as 'matter'), and particles that carry or mediate forces in addition to feeling them (integral-spin objects, bosons)[4]. Fermions fall into three 'generations', where an increase in generation

[2]This has been tested down to a distance scale of $\sim 10^{-18}$ m [6].
[3]Photons and gluons are massless.
[4]More precisely, bosons mediate changes in momentum; boson self-interactions are possible.

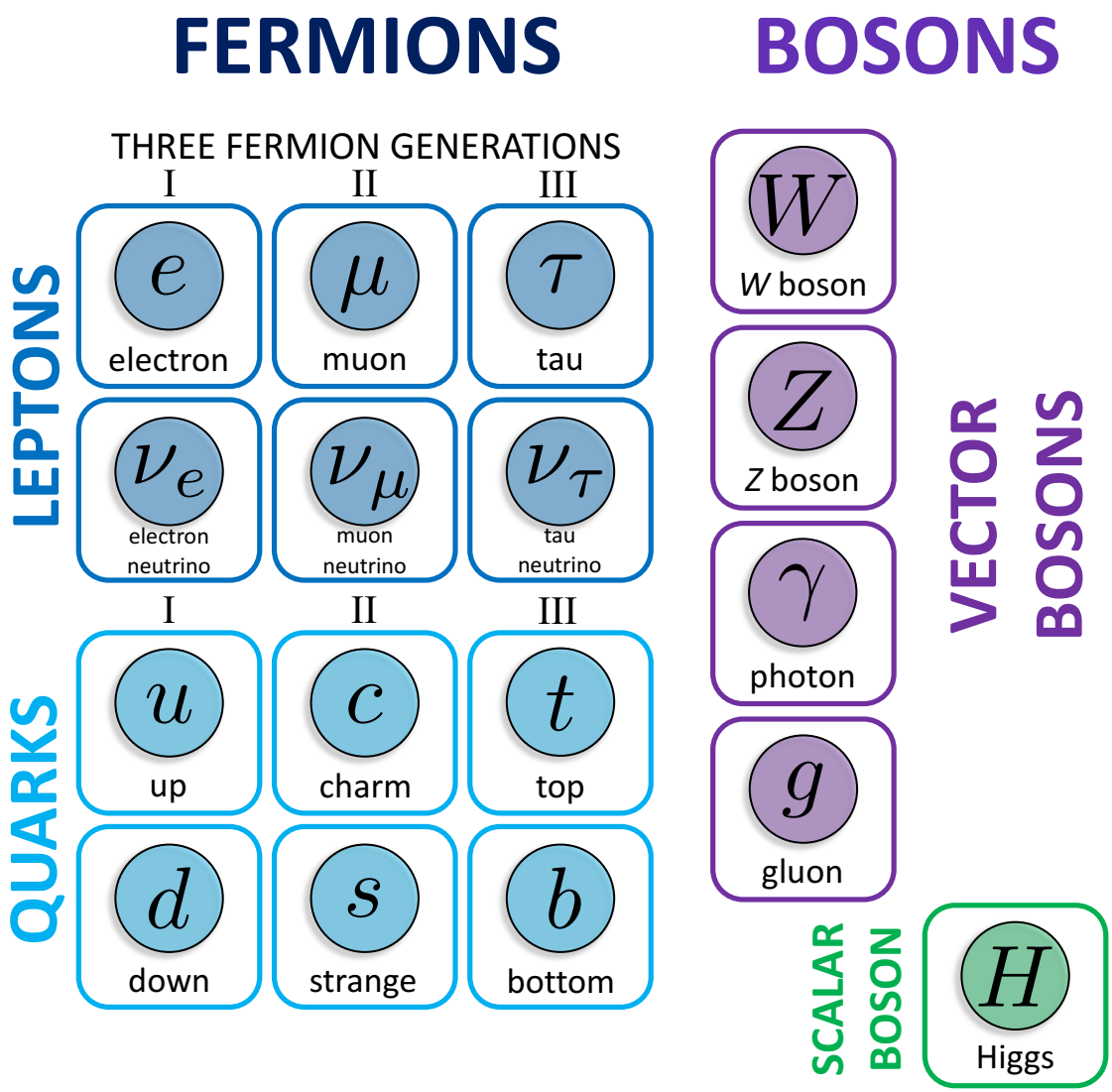

Figure 2.1: The Standard Model of particle physics. Fermions (blue) include leptons (dark blue) and quarks (light blue). Fermions come in three generations; increasing generation (left to right) corresponds to an increase in particle mass. The force-mediating bosons can be vector bosons (purple) or scalar bosons (just the Higgs).

corresponds to an increase in mass. Fermions are also subdivided into two types of particles: leptons and quarks. Bosons are subdivided into two categories as well: vector bosons, which have a spin of 1, and scalar bosons, which have a spin of 0. The Higgs is the only known fundamental scalar boson. Additionally, each SM particle

has a corresponding antiparticle. A particle and its antiparticle are, to our knowledge, identical other than the fact that they have opposite quantum numbers like charge. Antiparticles are usually denoted by placing a bar over top of the particle symbol.

There are four fundamental forces in Nature: electromagnetism, the strong force, the weak force, and gravity. The SM describes the interactions of three of the four forces: gravity does not fit into the framework of the SM. Even though gravity is a force that we feel every day on Earth, and all massive particles interact gravitationally, gravity is incredibly weak at the subatomic particle scale and thus is irrelevant when describing elementary particle interactions. However, the fact that the SM does not describe gravity on subatomic scales remains one of the major shortcomings of the SM. Electromagnetism is the force that is responsible for almost all of our daily interactions. Electromagnetism governs how we see, how we talk on our phones, and is even the (microscopic) reason why our hands do not pass through each other when we clap. The strong force holds quarks together and is the reason why protons and neutrons bind to form atomic nuclei. The weak force is responsible for radioactive decays.

2.1.1 Fermions

There are three generations of lepton pairs: the electron and electron neutrino, muon and muon neutrino, and tau and tau neutrino. Electrons, muons, and taus are all electrically-charged: they each interact with other particles in the same way, only differing by mass. However, muons and taus are unstable and decay into lighter particles. These electrically-charged leptons can interact via the electromagnetic force or the weak force. Due to historical reasons, the antiparticle of the electron is called the positron. Neutrinos are massless in the SM, however they are known to have small but non-zero masses, which is exciting physics beyond the SM (see neutrino oscillations in Section 2.3). Neutrinos only interact via the weak force, which means that they have an extremely low probability of interacting with other particles and therefore can travel for long distances without leaving any trace. In fact, billions of neutrinos are passing through each of us each second! There are also three paired generations of quarks: up and down, charm and strange, and top and bottom.

Quarks have both (fractional) electric charge and 'colour charge'. Colour charge

determines the strength of strong force interactions just like electric charge determines the strength of electromagnetic interactions. Each quark has one of three colour charges: Red (R), Blue (B), or Green (G). Only quarks and gluons have colour charge. One interesting aspect of colour charge is the phenomenon of colour confinement, which causes all composite particles made of quarks to be colour-neutral. There can never be a composite particle with nonzero colour charge. Therefore, the most common composite particles that are made of quarks (all particles that are made of quarks are called hadrons) are three-quark particles (known as baryons) that have combined colour charges of RBG, or two-quark particles (known as mesons) that have a colour-anticolour quark pair such as $R\bar{R}$.

Table 2.1 lists all SM fermions along with their mass and charge. Each particle also has a corresponding antiparticle of equal mass and opposite electric charge[5] that is not listed in the table.

Generally, a fermion must have electric charge in order to interact via the electromagnetic force, colour charge in order to interact via the strong force, and weak charge in order to interact via the weak force (all fermions have weak charge).

2.1.2 Vector Bosons

There are four unique vector bosons in the SM: the photon, the gluon, and the W and Z bosons. Only the W boson, being charged, is not its own antiparticle.

Bosons mediate forces, and thus each boson is associated with the force that it mediates. Table 2.2 lists each vector boson, the associated force that it mediates, along with its charge and mass. Note that the SM predicts exactly $m = 0$ for photons and gluons, but only defines relationships between the masses of the W and Z bosons, not direct masses. These masses must be measured by experiment; the measured values are what is quoted in the table.

2.1.3 Higgs Boson

The Higgs boson is unique in that it is the only spin-0 particle in the SM. It also does not directly correspond to a SM force; instead, the Higgs boson is a manifestation

[5]The electrically-neutral neutrinos are the least well-understood SM particles: ongoing research is trying to determine if $\nu_x = \bar{\nu}_x$, where $x = e/\mu/\tau$.

Generation	Name	Symbol	Charge [e]	Mass [MeV]
Leptons				
1st	electron	e	-1	0.511
	electron neutrino	ν_e	0	$< 1.1 \times 10^{-6}$
2nd	muon	μ	-1	105.658
	muon neutrino	ν_μ	0	$< 1.1 \times 10^{-6}$
3rd	tau	τ	-1	1776.86 ± 0.12
	tau neutrino	ν_τ	0	$< 1.1 \times 10^{-6}$
Quarks				
1st	up	u	$+\frac{2}{3}$	$2.16^{+0.49}_{-0.26}$
	down	d	$-\frac{1}{3}$	$4.67^{+0.48}_{-0.17}$
2nd	charm	c	$+\frac{2}{3}$	1270 ± 20
	strange	s	$-\frac{1}{3}$	93^{+11}_{-5}
3rd	top	t	$+\frac{2}{3}$	172760 ± 300
	bottom	b	$-\frac{1}{3}$	4180^{+30}_{-20}

Table 2.1: Leptons in the SM. The electric charge and mass of each particle are given. Mass values are taken from the *Particle Data Group* [7]. Note that if the mass uncertainty is not stated, then the error is smaller than 0.001 MeV.

Force	Mediator	Symbol	Charge [e]	Mass [GeV]
Electromagnetic	photon	γ	0	0
Strong	gluon	g	0	0
Weak	Z boson	Z	0	91.1876 ± 0.0021
	W boson	$W^{\pm}$	± 1	80.379 ± 0.012

Table 2.2: Each of the three fundamental forces described by the SM has at least one mediating vector boson. For each force, its mediator(s) is (are) stated, along with its electric charge and mass. Mass values are taken from the *Particle Data Group* [7].

of the Higgs field, which is what allows particles to acquire mass. The Higgs boson itself has a mass of $m = 125.25 \pm 0.17$ GeV and has no charge [7].

2.2 Quantum Field Theory of the Standard Model

The Standard Model is a relativistic quantum field theory. Quantum field theories (QFTs) apply the principles of quantum mechanics to dynamic fields as opposed to individual particles. Relativistic QFTs combine the principles of special relativity and QFTs. Fields are everywhere. For example, we know that electric and magnetic fields accelerate particles with electric charge even though we cannot see these fields. Similarly, each force corresponds to a field, and particles are excitations of these fields. The following subsections briefly describe the theoretical underpinnings of the SM as a relativistic quantum field theory. Background material on the need for fields in particles physics (Section B.2), the Lagrangian formalism (Section B.3) and Feynman diagrams (Section B.4) is given in the Appendix.

2.2.1 Quantum Electrodynamics

Quantum electrodynamics (QED) is the QFT that describes the interactions of charged particles via the electromagnetic force, unifying classical electromagnetism and quantum mechanics. Free spin-1/2 particles are described by the Dirac Lagrangian:

$$\mathcal{L}_{\text{Dirac}} = \bar{\psi}(i\gamma^\mu \partial_\mu - m)\psi, \tag{2.1}$$

where ψ is a spin-1/2 charged fermion field, m is that fermion's mass, and γ^μ corresponds to the Dirac matrices which contain the spin information. QED combines free fermions with Maxwell's equations for electricity and magnetism and their interactions. The full QED Lagrangian is

$$\mathcal{L}_{\text{QED}} = \mathcal{L}_{\text{Dirac}} + \mathcal{L}_{\text{Maxwell}} + \mathcal{L}_{\text{int}} \tag{2.2}$$

$$= \bar{\psi}(i\gamma^\mu \partial_\mu - m)\psi - \frac{1}{4}F^{\mu\nu}F_{\mu\nu} - e\bar{\psi}\gamma^\mu\psi A_\mu, \tag{2.3}$$

where $\mathcal{L}_{\text{int}}$ is the Lagrangian describing all of the allowed interactions in the theory, $F_{\mu\nu} = \partial_\mu A_\nu - \partial_\nu A_\mu$ is the electromagnetic field strength tensor which contains all of Maxwell's equations, A_μ is the boson (i.e. photon) field, and e is the electric charge, which defines the strength of the interaction.

Looking at $\mathcal{L}_{\text{int}}$, we see that all QED interactions, or *vertices*, must involve a photon and fermion-antifermion pair. From this, we can draw the fundamental Feynman diagram of QED, as seen in Figure 2.2. All Feynman diagrams in QED must be of this form.

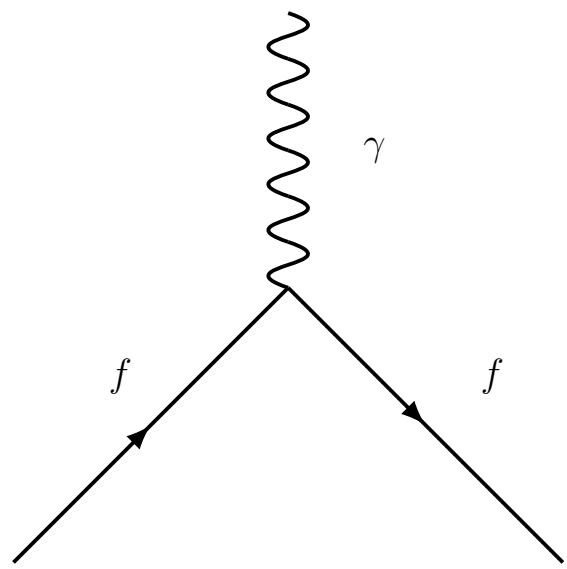

Figure 2.2: The fundamental interaction in QED, corresponding to $\mathcal{L}_{\text{int}}$ in Equation (2.2). From left to right, the diagram represents a charged fermion (for example, an electron), the straight line with an arrow, emitting/absorbing a photon, the squiggly line, and then continuing on in space. Equivalently, one could rotate the diagram by 90 degrees to show a fermion-antifermion pair annihilating into a photon.

2.2.2 Quantum Chromodynamics

Quantum chromodynamics (QCD) is the QFT that describes the interactions of particles via the strong force. As was mentioned before, to interact via the strong force, particles must carry colour charge, limiting strong force interactions to quarks and gluons. Quarks also carry electric charge, so the Lagrangian becomes more complicated than $\mathcal{L}_{\text{QED}}$, because quarks can carry one of three colour charges and can

interact with both photons and gluons. The full QCD Lagrangian is

$$\mathcal{L}_{\text{QCD}} = \bar{\psi}_i \left(i\gamma^\mu (D_\mu)_{ij} - m\delta_{ij} \right) \psi_j - \frac{1}{4} G^a_{\mu\nu} G^{\mu\nu}_a, \tag{2.4}$$

where ψ_j is a quark field with the index j representing one of the three possible colour charges the quark can have, m is the quark mass, and δ_{ij} is a delta function. $(D_\mu)_{ij}$ is a covariant derivative given by

$$(D_\mu)_{ij} = \partial_\mu \delta_{ij} - ig(T_a)_{ij} \mathcal{A}^a_\mu, \tag{2.5}$$

where g is the interaction strength (analogous to e in QED), T_a are Gell-Mann matrices representing the eight gluon colour charge combinations, and $\mathcal{A}^a_\mu$ are the gluon fields. $G^a_{\mu\nu}$ from $\mathcal{L}_{\text{QCD}}$ (2.4) is the gluon field strength, analogous to $F_{\mu\nu}$ in QED, and is given by

$$G^a_{\mu\nu} = \partial_\mu \mathcal{A}^a_\nu - \partial_\nu \mathcal{A}^a_\mu + g f^{abc} \mathcal{A}^b_\mu \mathcal{A}^c_\nu, \tag{2.6}$$

where f^{abc} are the QCD structure constants.

The QCD Lagrangian (2.4) tells us all of the primary vertices of QCD. While QED only has one primary vertex, QCD has three unique vertices, which are shown in Figure 2.3, including the analogous vertex to Figure 2.2 and two gluon self-interaction vertices due to the fact that gluons themselves have colour charge, while photons carry no electric charge. Additionally, since quarks carry electric charge, they also interact via the primary QED vertex (Fig. 2.2). Just like in QED, all of the primary QCD vertex diagrams can be connected as long as the vertices themselves remain intact.

One effect that is important for high-energy hadron collision experiments pertains to our model of a hadron. For example, the proton is the most common hadron that we model, and we usually say it is made of three quarks (u, u, d). However, this is a simplification; these are the *valence quarks* within the proton, but deeper inside the proton (and all hadrons), a much more complicated structure exists. A graphic of this inner structure is shown in Figure 2.4. At lower energies, we must only concern ourselves with the valence quarks within a hadron. However in high-energy collision experiments like those that take place in the Large Hadron Collider, the internal structure of the hadron, the *sea* quarks and gluons, become more important than the valence quarks, and we must change our model of the proton to include this sea

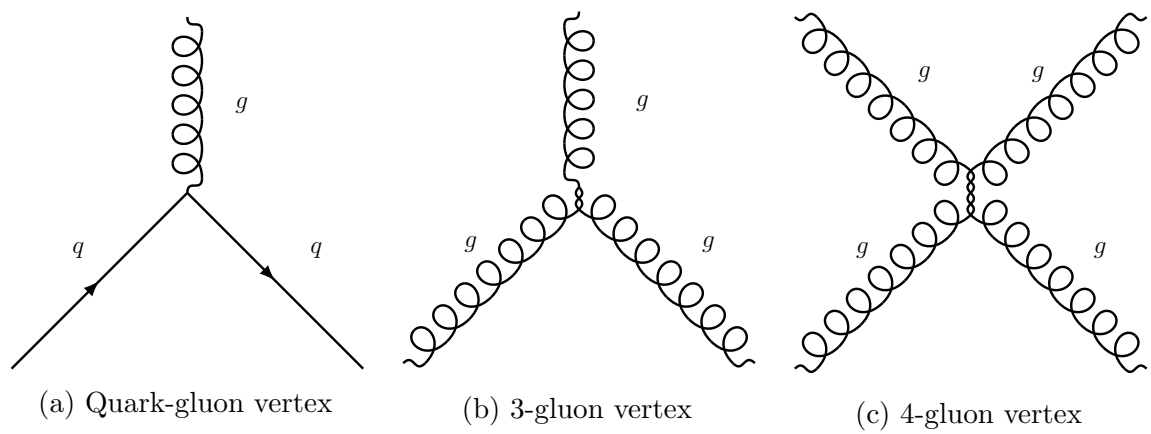

(a) Quark-gluon vertex (b) 3-gluon vertex (c) 4-gluon vertex

Figure 2.3: The three primary vertices of QCD, corresponding to $\mathcal{L}_{\text{QCD}}$ in (2.4). The first diagram is analogous to the QED vertex in Fig. 2.2, except the straight lines can only be quarks and the loopy line represents a gluon. The second and third diagrams are the three-gluon and four-gluon vertices, due to gluons being colour-charged.

of quarks and gluons. A toy Feynman diagram representing a hadron collision at the Large Hadron Collider would look something like what is shown in Figure 2.5, where we must use circles to represent the unknown specific interactions that happen internally within the hadrons. In these high-energy collisions, we cannot know exactly which piece of the hadron substructure was involved in a given collision, and so we model this effect with **parton distribution functions (PDFs)**, where the word *parton* refers to a constituent particle of the hadron (a quark or gluon). PDFs describe the average hadron structure by assigning probability densities to a given parton as a function of momentum fraction x and energy scale. The momentum fraction of all components of a hadron must sum to one to give the total hadron momentum. PDFs must be determined experimentally, but they are universal, meaning that measurements from different experiments can be used.

QCD also has some interesting characteristics that we do not see in QED. At high energies and small distance scales, the interaction strength g between quarks and gluons decreases. This phenomenon is known as *asymptotic freedom*. At low energies, the interaction strength increases, forcing quarks and gluons to remain bound together as hadrons. When making QCD predictions, like in most QFTs, perturbation theory is often used. However, this fact that QCD interaction strength increases at low energies means that perturbation theory cannot be used to make predictions in this

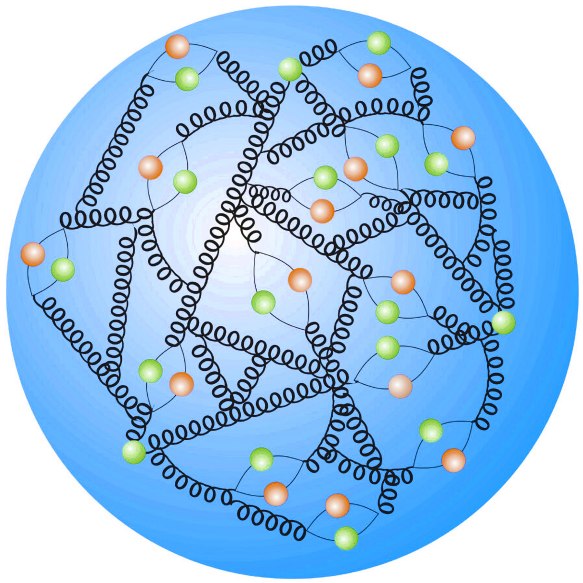

Figure 2.4: Representation of the inner structure of a proton [8].

low-energy region, leading it to often be called the *non-perturbative* region.

Another unique QCD phenomenon is *colour confinement*, which was mentioned in Section 2.1. This property that only colour-neutral particles exist means that as quarks within hadrons try to separate, the interaction energy between them increases until the energy is so great that a quark-antiquark particle pair is created from the energy generated in the quark-gluon field before any separation actually occurs. In high-energy experiments where hadrons are collided, this confinement effect creates streams of collimated hadrons called jets. This process is known as hadronization, which is also nicely represented by Fig. 2.5.

2.2.3 Electroweak Unification

All quarks and leptons can interact via the weak force, mediated by the charged W boson and the neutral Z boson. A classic important weak interaction is beta decay, where a neutron is converted to a proton, creating an electron and a neutrino, or a proton is converted to a neutron, creating a positron and a neutrino. The weak force is called 'weak' because the range of the interaction is very short: the weak interaction is only important at subatomic distance scales. This is because the W and Z bosons have relatively large masses and have short lifetimes, so weak interactions

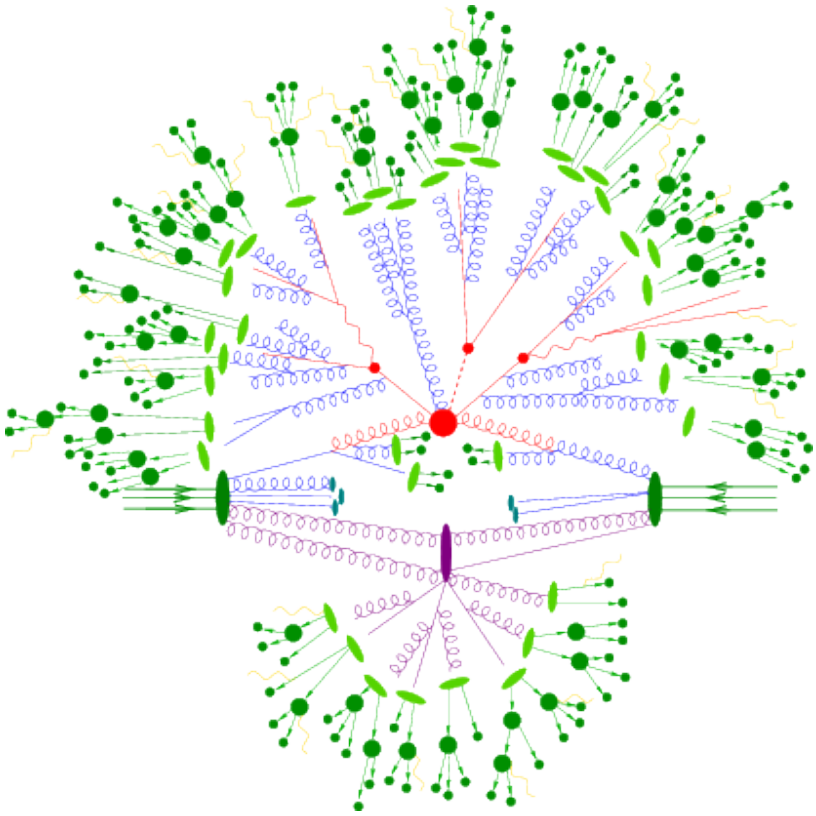

Figure 2.5: Sample toy Feynman diagram of a high-energy proton-proton collision. At high energies, the sea quarks and gluons within the proton become more important than the valence quarks. Interactions with sea quarks and gluons are represented by circles, showing that we cannot exactly predict which individual hadron components were involved in a given interaction. This figure was created by the Sherpa Team [9].

must occur on a timescale that is less than the lifetime of these bosons. At high energies (or equivalently short distances) where weak interactions are important, the weak and electromagnetic forces effectively combine into one unified force known as the electroweak (EW) force. This was first proposed by Glashow [10], Weinberg [11], and Salam [12]. Therefore at these short distance scales, neutral interactions can be mediated by the photon or the Z boson.

The Lagrangian describing electroweak interactions is

$$\mathcal{L}_{\mathrm{EW}} = -\frac{1}{4}W^a_{\mu\nu}W^{\mu\nu}_a - \frac{1}{4}B_{\mu\nu}B^{\mu\nu} + (D_\mu H)^\dagger (D_\mu H) + m^2 H^\dagger H - \lambda \left(H^\dagger H\right)^2, \quad (2.7)$$

where W^a_μ are the weak force vector bosons, B_μ is the hypercharge vector boson

(hypercharge is the symmetry analogous to QED electric charge), H is the Higgs boson complex scalar, m is the mass of the Higgs boson, λ is a normalization constant, and $D_\mu H$ is the covariant derivative:

$$D_\mu H = \partial_\mu H - igW^a_\mu \tau^a H - \frac{1}{2} ig' B_\mu H; \tag{2.8}$$

g and g' are the weak and hypercharge coupling constants, and τ^a are the weak generators. The Higgs potential in Equation (2.7) induces a nonzero vacuum expectation value (the lowest energy state). These terms break the weak gauge symmetry (SM symmetries are derived from group theory), allowing the weak bosons to acquire mass terms themselves. Without the Higgs boson, the SM would predict the W and Z bosons to be massless, making the Higgs integral to electroweak interactions.

The covariant derivative (Equation (2.8)) can be expanded and diagonalized to show that

$$B_\mu = \cos\theta_w A_\mu - \sin\theta_w Z_\mu \tag{2.9}$$

and

$$W^3_\mu = \sin\theta_w A_\mu + \cos\theta_w Z_\mu, \tag{2.10}$$

where A_μ is the usual photon, Z_μ is the Z boson, and θ_w is the weak mixing angle which relates the two coupling constants g and g':

$$\tan\theta_w = \frac{g'}{g}. \tag{2.11}$$

In this formulation, W^1_μ and W^2_μ are linear combinations of the charged W bosons. Inserting Equations (2.9) and (2.10) back into the full Lagrangian of Equation (2.7) and expanding gives all the kinetic and interaction terms for electroweak theory, which we can see will lead to interactions between the vector bosons and fermions, vector boson self-interactions, as well as Higgs boson interactions with fermions, the vector bosons, and itself. The derivation is much more complex, but all the allowed electroweak interactions can still be summarized with a small set of Feynman diagrams. The vector boson diagrams are shown in Figure 2.6, while the diagrams involving the Higgs boson are shown in Figure 2.7.

One important EW process at high-energy hadron-hadron colliders is the Drell-

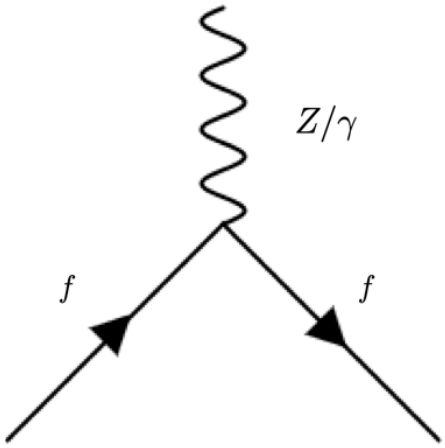

(a) EW neutral-fermion vertex

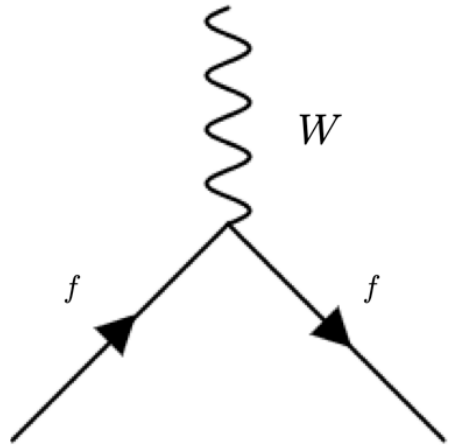

(b) EW charged-fermion vertex

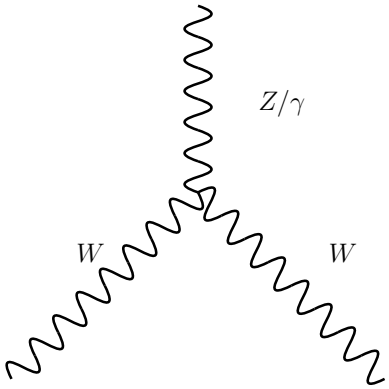

(c) EW 3-boson vertex

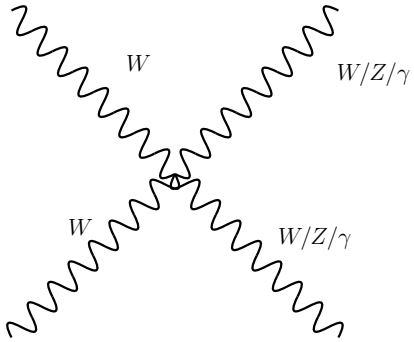

(d) EW 4-boson vertex

Figure 2.6: The four primary vertex diagrams of EW theory. Each of these diagrams represents multiple fundamental vertices, depending on the boson mediating the interaction. The diagram on the top left (2.6a) is the neutral-current vertex, which is similar to the QED primary vertex diagram, except for EW interactions (the solid lines) can be any fermion if the mediator (squiggly line) is a Z boson and any charged fermion if the mediator is a photon. The second diagram (2.6b) is the charged-current vertex, where the solid lines are any charged lepton-neutrino pair or quark-antiquark pair and the mediator is a W boson. These two sets of diagrams lead to many possible single-vertex interactions. The third diagram (2.6c) represents the EW boson self-interaction three-vertex, where two of the lines must be same-sign W bosons and the third line can be either a photon or a Z boson. The diagram on the bottom right (2.6d) represents the EW boson self-interaction four-vertex, where two of the lines must be W bosons, and the other two lines can also be two W bosons, or two Z bosons, two photons, or a Z boson and a photon.

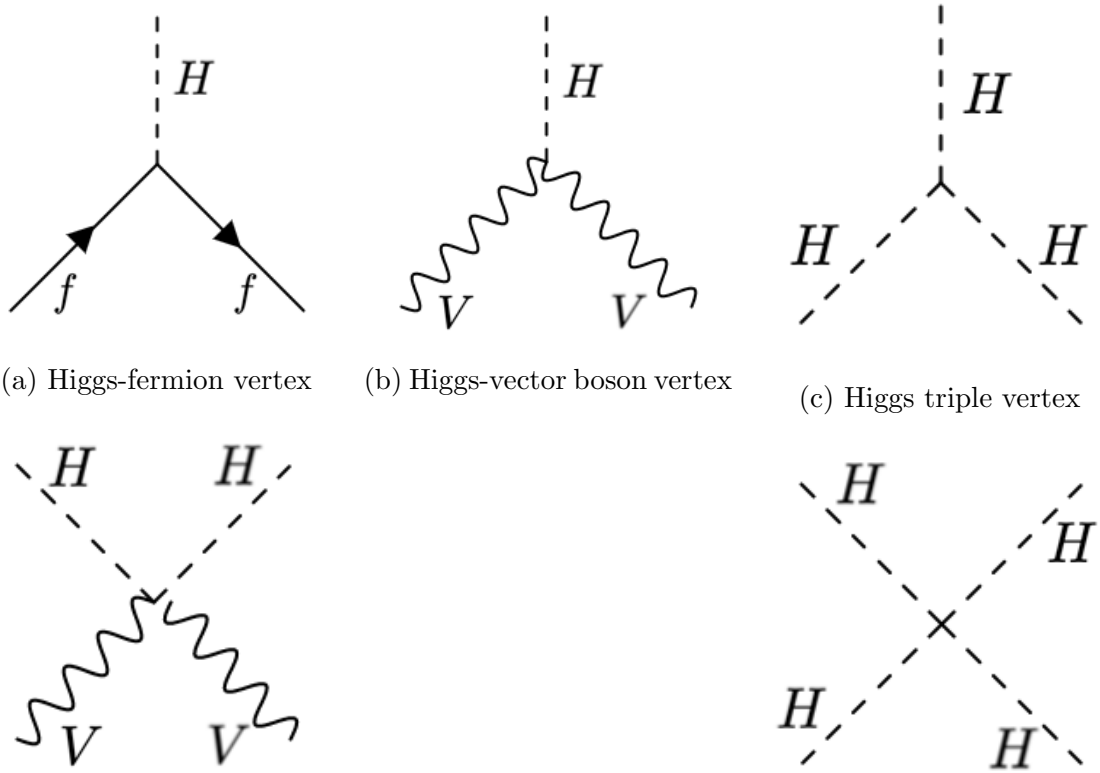

(a) Higgs-fermion vertex

(b) Higgs-vector boson vertex

(c) Higgs triple vertex

(d) di-Higgs-di-vector boson vertex

(e) Higgs quadruple vertex

Figure 2.7: The five primary vertex diagrams of the Higgs boson. Each diagram represents multiple fundamental vertices, depending on the boson mediating the interaction. The solid dashed line represents the Higgs boson (H). Fermion lines (f) and vector boson lines (V) are also labeled.

Yan process [13]. A sample Feynman diagram of one type of this process is shown in Figure 2.8. The Drell-Yan process is the interaction of a quark and an antiquark producing a lepton pair. This interaction creates a *virtual* photon, W, or Z boson, where virtual means that these bosons are only intermediate particles in the process and they must obey the uncertainty principle (Equation (B.3)). The virtual boson quickly decays into the lepton pair, which can be measured experimentally. Since the Drell-Yan process requires collisions between sea quarks of at least one of the hadrons, this process is an important way to experimentally determine the poorly-understood sea quarks. Analyses of the Drell-Yan process, specifically $Z \to l^+l^-$ and $W^\pm \to l^\pm\nu$, are the subject of this thesis.

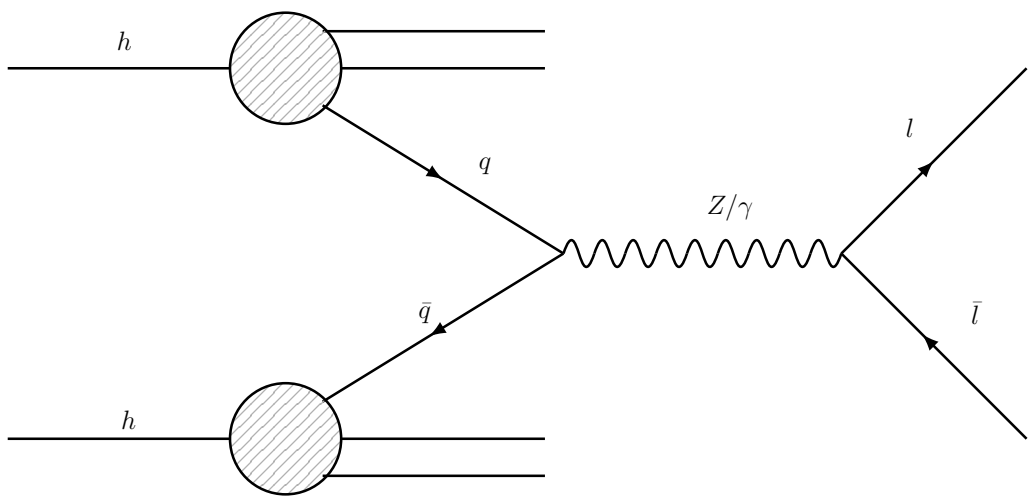

Figure 2.8: Feynman diagram of the neutral Drell-Yan process, resulting in a leptonic final state. The diagram shows two hadrons (h) approaching each other, followed by an inelastic collision between a quark from one hadron and an antiquark from the other. These quarks annihilate into either a Z boson or a photon, which then decays into a lepton-antilepton pair ($l\bar{l}$). This process can also have a charged mediator ($W^{\pm}$), which would then decay into a charged lepton and neutrino lepton-antilepton pair.

2.3 Shortcomings of the Standard Model

The Standard Model is a highly-successful theory, making many theoretical predictions that have been verified experimentally to incredible precision. It has even been able to predict the existence of multiple fundamental particles that were then confirmed experimentally, including the top quark [14, 15], the W [16, 17] and Z [18, 19] bosons, and the Higgs boson [20, 21]. However, we also know that the SM is not a complete theory of the fundamental interactions of the Universe.

We have already discussed how the SM does not include a theory for gravity. While the theoretical boson of the gravitational force called the graviton has been postulated, it has not been confirmed experimentally. Many theories *beyond the Standard Model* (BSM) attempt to unify gravity with the SM, but none have done so successfully thus far. Many physicists have spent large portions of their careers searching for such a *Grand Unified Theory* (GUT), including Einstein, and there are some promising avenues towards a GUT such as string theory or supersymmetry, but so far none successfully achieve this unification.

The Big Bang is the singularity that was the starting point for our Universe, and according to current theories, the Big Bang should have created matter and antimatter particles in exactly equal parts. However, we know that we live in a matter-dominated Universe today. If we had equal parts matter and antimatter, all of the matter and antimatter would annihilate, leaving us with a Universe of only pure energy. We know that this is not the case, so why did our Universe become matter-dominated? The SM currently does not answer this question.

We know that matter accounts for only about five percent of the energy density of the Universe. Roughly 25% of the Universe is made of *dark matter*, a form of matter that is weakly-interacting – to date, we have only been able to observe its interactions via the force of gravity. The remaining approximately 70% of the Universe is made of *dark energy*, our placeholder term to explain the Universe's accelerating expansion. The SM has no answer for dark matter or dark energy.

Neutrinos, the least well-understood particles within the SM, oscillate between their flavours. An electron neutrino emitted from the Sun has some probability of either remaining an electron neutrino, or turning into a muon neutrino or tau neutrino by the time it reaches Earth. This phenomenon known as neutrino oscillations is

not explained by the SM. Many experiments are currently working to improve our understanding of neutrinos.

Finally, why is the SM the SM? We can draw a graphic of all the particles in the SM, as is done in Figure 2.1, but why is this graphic correct? Why are there three generations of fermions instead of four, two, or any other number? Why do the particles have masses that we can only determine experimentally? The SM requires the manual input of many numerical constants that we have measured experimentally, but the values of these constants seem arbitrary. Many physicists believe that these constants should come naturally from our model instead of having to be determined experimentally and then inserted back into the model.

The SM itself still makes many predictions that we have yet to measure experimentally. Making these measurements allows us to further examine its accuracy and consistency. Perhaps making seemingly straightforward measurements will lead to inconsistencies between the measurement and the SM prediction, helping guide the way to the hopefully overarching theory that goes beyond the SM. As experimental physicists, we will continue to make these measurements and welcome the exciting discoveries along the way.

Chapter 3

The ATLAS Experiment and the LHC at CERN

The ATLAS Experiment is located at the CERN particle physics laboratory. ATLAS observes the aftermath of proton-proton collisions generated by the Large Hadron Collider (LHC), recording data that carry information on the properties of particles created during these collisions[1]. The focus of this thesis is using these data to make cross-section measurements of $Z \to l^+l^-$ and $W^\pm \to l^\pm\nu$ ($l = e, \mu$). In particle physics, a cross-section is effectively the probability that an interaction between particles will occur. In order to measure a cross-section, it is important to know the *integrated luminosity*: the amount of data that were recorded. The measurement of final-state particles, electrons and muons, requires multiple ATLAS detector components that each contribute to quantifying these particles' energy and momentum. These include the Inner Detector, Calorimeter, and Muon Spectrometer.

This chapter provides an overview of the necessary prerequisites for understanding accelerator physics experiments at CERN with the LHC (Sections 3.1, 3.2 and 3.3), and also outlines how the ATLAS Experiment and detector work (Section 3.4) in order to record data like that which is used in this thesis.

[1] ATLAS also studies the decay products of heavy ion collisions generated by the LHC.

3.1 CERN

The European Organization for Nuclear Research, now simply known as CERN, is a European research organization and the largest particle physics laboratory in the world. It is located along the Franco-Swiss border, with multiple laboratory sites in French or Swiss towns near the border. The closest large European city to CERN is Geneva, Switzerland.

CERN was founded in 1954 by 12 countries known as Member States. Today there are 23 CERN Member States: all but one of the Member States are European countries (Israel is the outlier) [22]. CERN welcomes thousands of users from universities, laboratories and other institutions around the world. One need not be from a Member State to work at or be associated with CERN.

CERN is primarily focused on providing particle accelerators for high-energy physics research and facilitating an environment to enable this world-class research. The first particle accelerator at CERN was the Synchrocyclotron (SC), which became active in 1957. Soon after in 1959, the next accelerator called the Proton Synchrotron (PS) became active to focus on particle physics experiments, as the SC was slowly phased out to focus on nuclear physics. Today, CERN is most famous for housing the Large Hadron Collider, the huge 27-kilometre circumference circular accelerator. In order for particles that are accelerated within the LHC to reach their high energies, they must have their energies ramped up by a series of smaller accelerators. The PS is still active today as one of these initial ramp-up accelerator components to the LHC. Figure 3.1 shows a diagram of the CERN accelerator facility. The protons accelerated through this accelerator chain begin at rest as a canister of hydrogen gas at a linear accelerator (the new Linac4 as of 2020) where the ramp-up process begins. These hydrogen atoms are stripped of their electrons, and then a little over four minutes later they are traveling at speeds high enough to enter the LHC.

CERN is home to 20 active accelerator-based experiments, and many more completed experiments. Eight of these experiments use the LHC. CERN also has multiple experimental facilities, and is the main site for a few non-accelerator experiments. Of note, CERN is also famous for being the birthplace of the World Wide Web [24].

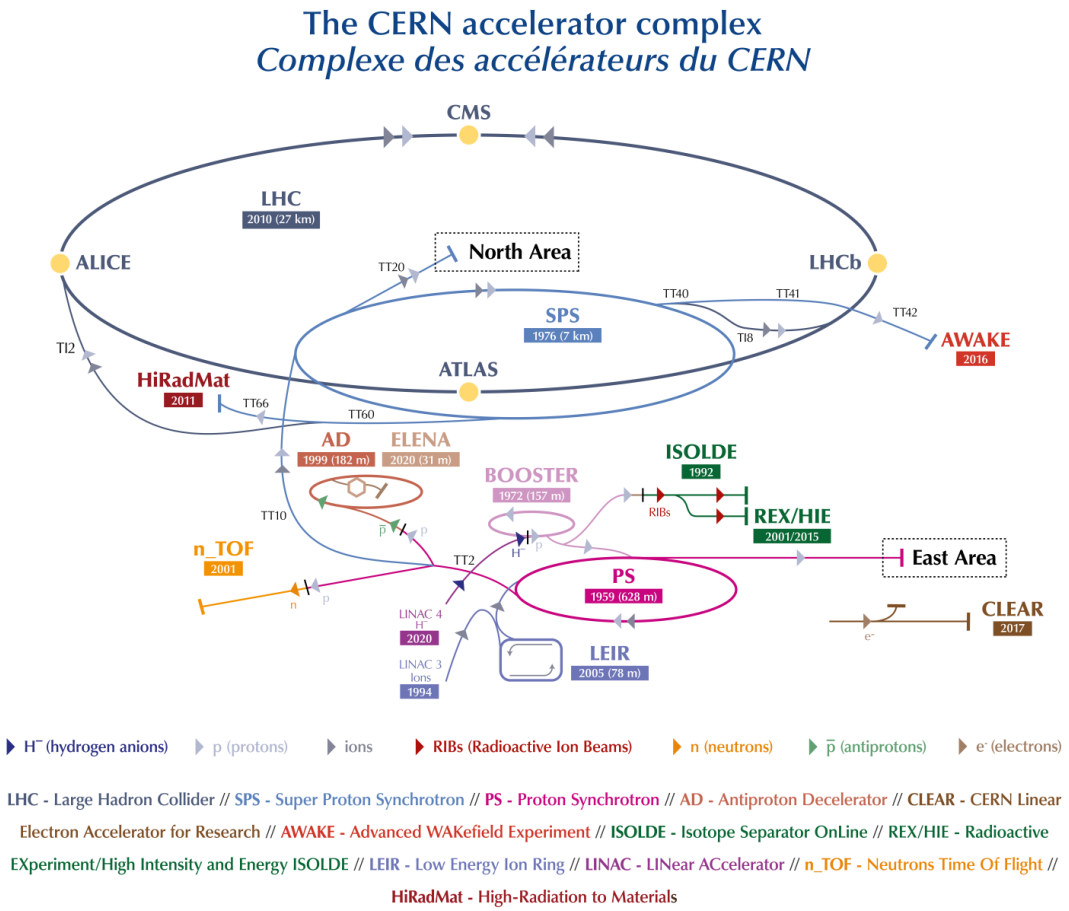

Figure 3.1: The accelerator complex at CERN. Each accelerator component is labeled with its name, date of first operation, and length. Each accelerator experiment is also labeled [23].

3.2 Accelerator Physics

Most of the discussions in this section are based off of the following references: [1, 7, 25, 26].

Particle accelerators have become synonymous with high-energy particle physics. They require substantial monetary investments to build and operate, especially when they are on the scale of the LHC. However, accelerators are the only way (for humans) to reliably produce new particles and new states, especially in large quantities.

We have discussed the production of new particles and states by referencing the

equation $E = mc^2$ (B.1). Accelerators allow us to collide particles at energy scales of MeV up to TeV, allowing for the consistent production of particles or states up to these energy scales as well. Additionally, in order to probe the structure of sub-atomic systems, we need a probe that is smaller than the scale of that system. For example, it would be impossible to accurately estimate the width of a single strand of hair with a ruler. It would also be impossible to examine a proton with a standard optical microscope, because the wavelength of visible light is roughly $300 - 700$ nanometres, more than eight orders of magnitude larger than the size of a proton (roughly 10^{-15} m). This argument is explained further in Appendix Section B.5.

In order to better describe particle interactions, we need quantities that are based on collision dynamics. One of, if not the most important quantity in particle physics is **cross section**, usually assigned the variable σ. To define a cross section, we can create a scenario where we aim a beam of mono-energetic particles at a target and fire. Let us say that we have a detector placed at an angle θ from the beam direction (the z-axis) that measures all particles scattered by this angle into the solid angle $d\Omega$. The number of particles ($\mathcal{N}$) per unit time (t), $\frac{d\mathcal{N}}{dt}$, that are measured by the detector is then given by

$$\frac{d\mathcal{N}}{dt} = F\sigma(\theta)d\Omega, \tag{3.1}$$

where F is the particle flux and $\sigma(\theta)$ is the coefficient of proportionality, or roughly the probability that particles will scatter at angle θ. This is called the *differential cross section*. If we integrate over all solid angles, we find the total number of particles scattered per unit time, leading to the total scattering cross section:

$$\sigma_{\text{tot}} = \int \sigma(\theta)d\Omega. \tag{3.2}$$

Cross section has units of area, and in particle physics we introduce a unit called "barns" to describe cross sections in order to not consistently work with tiny numbers. One barn (b) is defined as

$$1 \text{ b} = 10^{-24} \text{ cm}^2 = 100 \text{ fm}^2. \tag{3.3}$$

We can think of σ_{tot} as the area effective in scattering a particle. Stated another way, cross section is a measure of the probability for an interaction between particles to

occur.

We can also define a related highly-important parameter called **luminosity**, L. Luminosity (sometimes called *instantaneous* luminosity) is the number of events (N) detected per unit time per unit cross section (of the given interaction):

$$L = \frac{1}{\sigma}\frac{dN}{dt}. \tag{3.4}$$

Here the word "event" refers to a collision of interest. For example, if we are only interested in collisions producing a single Z boson, then N is the number of collisions producing individual Z bosons that were recorded by the experiment.

We often use integrated luminosity $\mathcal{L}$ to find the total luminosity during a time period of interest:

$$\mathcal{L} = \int L dt. \tag{3.5}$$

Combining Equations (3.4) and (3.5) and rearranging, the total number of expected events for a given process is:

$$N = \sigma\mathcal{L}. \tag{3.6}$$

$\mathcal{L}$ has units of [b^{-1}]: *inverse barns*. In a simple collider experiment where we have two beams of particles colliding head-on over an area A, with N_1 particles in the first beam and N_2 particles in the second beam, the integrated luminosity would be given by:

$$\mathcal{L} = \frac{N_1 N_2}{A}. \tag{3.7}$$

3.3 The Large Hadron Collider

The Large Hadron Collider, true to its name, is the largest particle accelerator in the world. It mostly accelerates and collides protons, but also collides heavy atom ions such as lead. The LHC was completed in 2008 and recorded its first proton-proton collisions in 2009. Eight experiments at CERN have their detectors located at various positions around the LHC ring, collecting data based on the observation of particles created during the LHC hadron-hadron collisions. The four largest experiments at CERN are ALICE (A Large Ion Collider Experiment) [27], ATLAS (A Toroidal LHC ApparatuS) [28], CMS (Compact Muon Solenoid) [29], and LHCb (Large Hadron

Collider beauty) [30]. ALICE, ATLAS and CMS have their detectors built coaxially around their unique sites along the LHC ring such that the hadron-hadron collisions take place in the center of each experiment's detector. The collision spots are called interaction points (IPs). LHCb detects mainly forward particles, so it has a detector component close to but not surrounding the IP. Figure 3.2 shows an aerial view of the LHC and the location of these experiments with respect to the Franco-Swiss border and surrounding region. The ALICE detector is optimized to study heavy-ion collisions. The LHCb detector is optimized to study heavy quarks, specifically b and c quarks, along with the composite particles that they form. The ATLAS and CMS detectors are designed to be general purpose in that they are not optimized for a specific subset of particles, and can measure properties of hadrons, electrons, muons, and photons.

Figure 3.2: Aerial view of the LHC at CERN. The LHC is marked by the yellow circle where it resides underground. The four major LHC experiments are also labelled. The dashed white line shows the Franco-Swiss border. The Swiss Alps can be seen on the horizon. [Image Credit: CERN].

The LHC is a 27-kilometre ring of superconducting magnets and accelerating ma-

chinery. It is located underground beneath the CERN site, ranging from depths of about 50 metres to 175 metres due to the geography of the region. The LHC is stationed in a valley near Geneva's Lac Léman, in between the French Jura Mountains and the western Swiss Alps. Inside the LHC, two beams of hadrons travel in opposite directions in two separate beam pipes. Each pipe is held at ultrahigh vacuum, with pressures lower than that of the vacuum of outer space. The beams of hadrons are directed around the LHC ring by a strong magnetic field that is maintained by superconducting electromagnets; magnets whose coils conduct electricity with very little resistance or energy loss. In order to maintain their superconducting state, the magnets must be cooled to a temperature of $-271.3\,^{\circ}$C, just 1.9 degrees Kelvin above absolute zero. The magnets are cooled by liquid helium, which is constantly being pumped through the outer LHC beam pipe. Particle accelerators like the LHC generally contain three main electromagnetic acceleration components: dipole magnets for bending particles, quadrupole magnets for focusing particles, and radiofrequency (RF) cavities for accelerating and maintaining near-constant energy by compensating for energy losses. The main LHC dipole magnets generate magnetic fields of 8.3 Tesla, which is more than 100,000 times greater than Earth's magnetic field. Figure 3.3 shows a side and cross-sectional view of the LHC dipole magnets and the beam pipes within. In total, there are more than 9000 magnets in the LHC, with 1232 main dipole magnets and 392 main quadrupoles. There are also 16 RF cavities that work together to increase the energy of the particles by more than 14 times their injection energy into the LHC.

Inside the LHC beam pipe, accelerating protons reach speeds of more than $0.99999c$, where c is the speed of light. This speed is equivalent to an energy of $E = 6.5$ TeV per proton (or proton beam), corresponding to a centre-of-mass energy equal to 13 TeV when two protons collide. (Heavy ions are accelerated to centre-of-mass energies of up to 2.56 TeV per nucleon.) As has been mentioned before, the LHC does not accelerate individual protons, but beams of protons instead, because it would be impossible to align individual protons such that they are forced to collide. In fact, there are approximately $N_b = 1.2 \times 10^{11}$ protons per bunch at the start of each beam cycle, and up to $n = 2808$ bunches of protons per proton beam. Each bunch is separated by about 25 nanoseconds or roughly 7.5 metres, and makes $f = 11245$ turns around

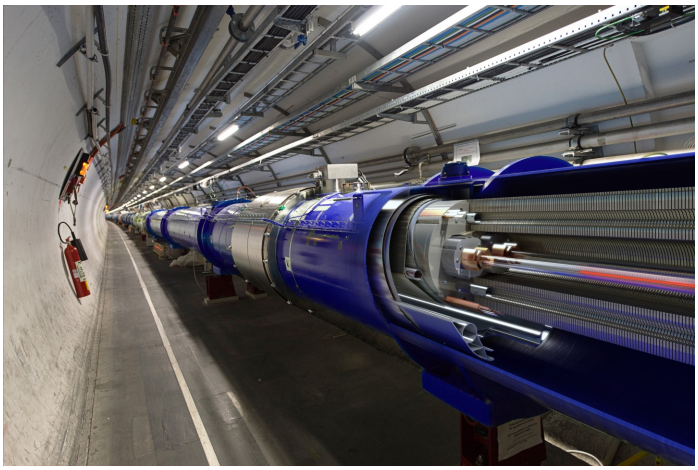

(a) LHC beam pipe side view

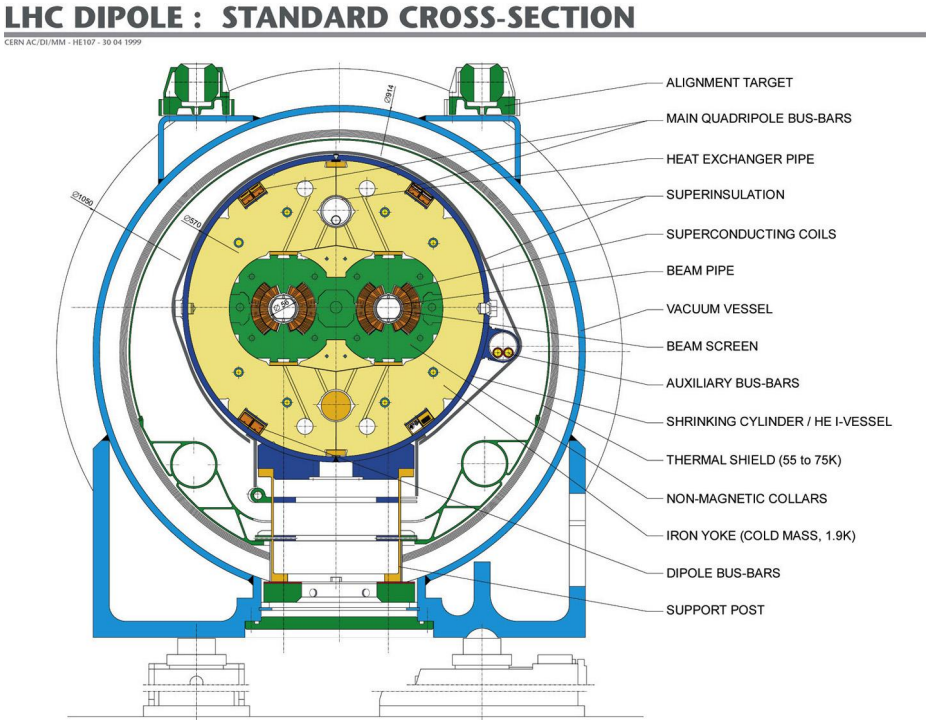

(b) LHC dipole magnet cross section

Figure 3.3: Inside the LHC beam pipe. The top image shows the beam pipe inside its underground tunnel. The two smaller beam pipes containing the hadrons can also be seen. The bottom image is a cross-sectional view of the LHC dipole magnets and the beam pipes within. Different components of the magnet and cooling system are shown. [Image Credit: CERN].

the LHC each second. In total, there are about one billion proton-proton collisions in the LHC each second [31].

The LHC has a roughly 30-year scheduled experimental timeline, but it is not running all the time. The schedule of the LHC is divided into experimental data-taking "Runs", and "Long Shutdown" periods for maintenance and upgrades of both the LHC and the experiment detectors. Figure 3.4 shows the most recent (updated January 2022) timeline of the LHC, beginning in 2021 and extending to the future to include the High-Luminosity LHC.

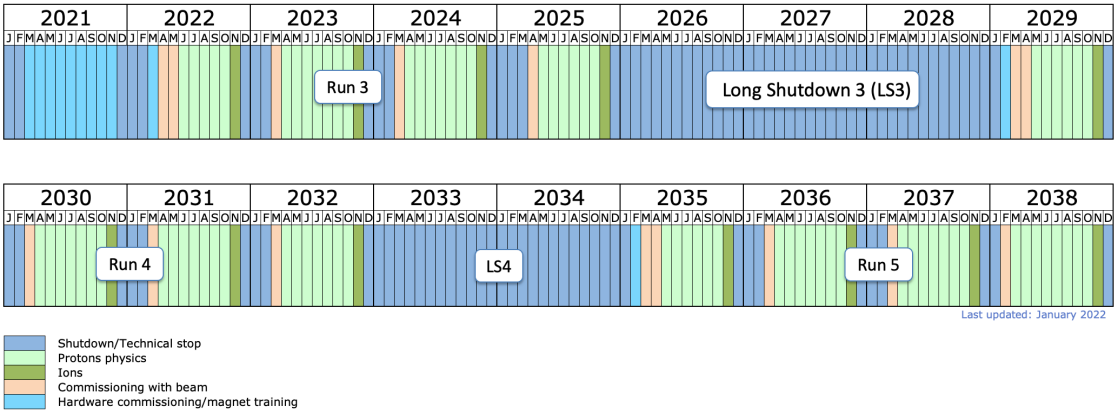

Figure 3.4: Timeline of the LHC from 2021 onwards, divided into experimental data-taking Runs, and Long Shutdown periods [32]. Run 1 took place from 2010 to early 2013 and Run 2 took place from 2015 - 2018.

3.4 The ATLAS Experiment

ATLAS is a general-purpose particle physics experiment at CERN that uses the proton-proton collisions from the LHC to detect both fundamental and composite particles created by these collisions. The ATLAS Experiment comprises of a huge detector – the largest detector ever built for a particle collider – but more importantly, ATLAS is a collaboration of researchers from around the world working together to improve and operate the detector and analyze the recorded collision data.

3.4.1 The ATLAS Collaboration

ATLAS is an international collaboration of researchers, including physicists, engineers, and technicians. In total, ATLAS has almost 6000 members including over 2000 students and about 3000 active scientific authors (many of these 2000 students are active authors). Figure 3.5 shows two maps of the ATLAS Collaboration displaying the countries with institutes who work on the ATLAS Experiment (3.5a) and the nationalities of ATLAS Collaboration members (3.5b). The experiment is based at CERN so naturally it is the main hub for ATLAS with the largest number of localized researchers, but much of the work can be done just as well from anywhere in the world. There are some difficulties that arise from the international nature of the experiment, such as the difficulty to schedule meetings that are convenient for collaborators across many time zones, but the benefits of having a diverse international collaboration far outweigh these minor difficulties. As a huge team, we all learn from each other and benefit from the vast set of viewpoints and both physics and personal backgrounds that each member uniquely brings to the collaboration.

3.4.2 Detector Overview & Geometry

The ATLAS detector is roughly 44 m $\times$ 25 m, weighs 7000 tonnes, and surrounds nearly the entire 4π solid angle around the interaction point. The detector is a complex piece of physics and engineering that contains many smaller sub-detector components that work together to measure properties of electrons, muons, photons, hadrons, and hadronic jets. By measuring properties of these particles that interact with the detector components, one can reconstruct the initial state of interest. For example, the detector cannot directly measure properties of a Z boson like one that is created during Drell-Yan processes, but we can precisely measure the properties of the electron and positron that the Z boson can decay into, allowing us to reconstruct the Z boson itself to infer its mass, momentum, and other properties.

Figure 3.6 shows an overview of the ATLAS detector and its sub-components. The detector is forward-backward symmetric with respect to the IP. The multiple detector subsystems can be divided into 'barrel' components, which are wrapped concentrically outward in layers around the IP, and 'end-cap' components, which are still positioned radially around the IP, but are offset from the IP along the LHC

(a) ATLAS Collaboration countries

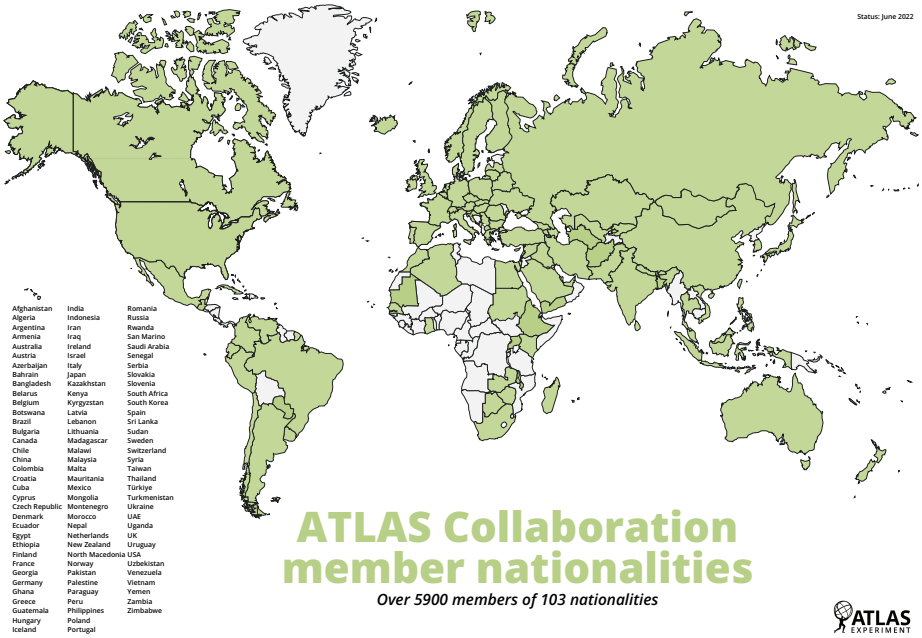

(b) ATLAS Collaboration nationalities

Figure 3.5: Shaded maps of the ATLAS Collaboration around the world. The upper map shows the countries with institutions who have active collaboration members, while the lower map shows the nationalities of all of these members [33].

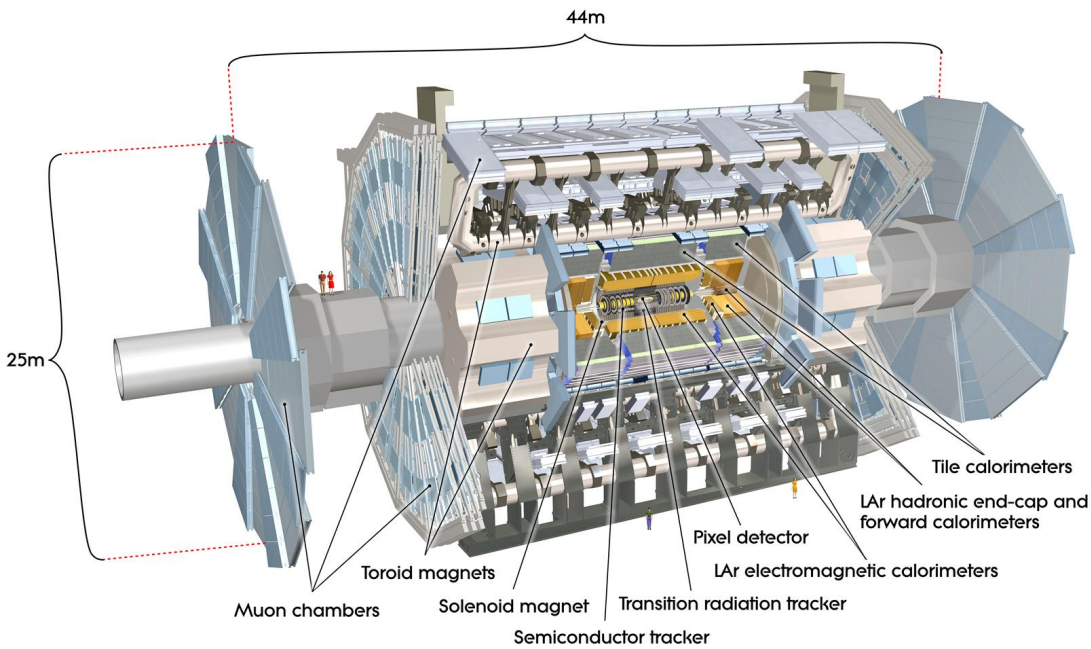

Figure 3.6: Cutaway view of the ATLAS detector and its main sub-detector components. The detector is roughly 44 metres long and 25 metres in height. Two people are shown for scale [28].

beam axis. Starting with the closest sub-detector to the IP, the ATLAS detector can be subdivided into the **inner detector**, the **calorimeters** (electromagnetic and hadronic), and the **muon spectrometer**. There is also a **magnet system** for bending charged particles into various detector components. These sub-components are outlined in following subsections.

Before moving on to discuss the detector components, we must introduce the ATLAS geometry. Figure 3.7 shows the ATLAS detector diagram overlaid with its Cartesian coordinate system (x, y, z) and the momentum vector $(\mathbf{p})$ from a sample outgoing particle created during a hadron-hadron collision.

The transverse momentum of an outgoing particle, p_{T}, is an important particle property to measure for many ATLAS analyses. It is defined as the quadratic sum of the particle's momentum along the x (p_x) and y (p_y) axes:

$$p_{\mathrm{T}} = \sqrt{p_x^2 + p_y^2}. \tag{3.8}$$

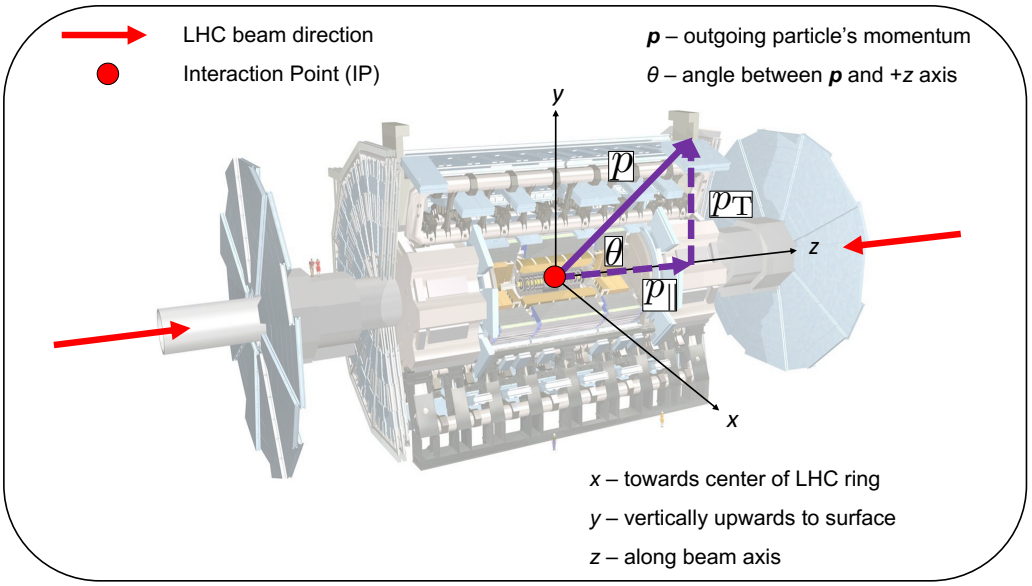

Figure 3.7: Basic orientation and geometry of the ATLAS Experiment. The ATLAS detector is overlaid with the orientation of its Cartesian coordinates (x, y, z). The LHC beam direction and hadron-hadron IP are also labelled. A vector representing the momentum of an outgoing particle from a collision is shown as a solid purple line (p), along with its angle (θ) from the z-axis. The vector p can be decomposed into momentum parallel to the z-axis ($p_{\parallel}$) and perpendicular to the z-axis (p_{T}), both displayed as dashed purple vectors.

It is also useful to use a spherical coordinate system (R, ϕ, θ) due to the geometry of the ATLAS detector: ϕ is the angle between the x-axis and y-axis and spans the angles $[-\pi, \pi]$ and θ is the polar angle between the z-axis and the $x - y$ plane and spans the angles $[0, \pi]$.

While spherical coordinate systems make sense for a coaxial detector, angular separations in θ are not invariant under Lorentz boosts. This means that if we were to do calculations or measurements involving θ in four-dimensional spacetime like is necessary for QFTs, we would get a different answer depending on our reference frame. Calculations in particle physics must be invariant under Lorentz transformations, and so we must introduce new variables that better characterize particle collisions and decay products within the Lorentz frame that are also relative to the beam axis (z). We define *rapidity* (which is given the variable y, not to be confused with the

Cartesian coordinate) as

$$y = \frac{1}{2} \ln \left(\frac{E + p_z}{E - p_z} \right), \tag{3.9}$$

where E is a particle's energy and p_z is its momentum along the beam axis. Rapidity is additive under Lorentz transformations, making it a much more useful variable for examining multiple incoming and outgoing states at once in a given process. In practice for measurements we use *pseudorapidity*, η, a Lorentz-invariant angular variable, allowing us to identify decay particles as a function of angle from the beam axis. Pseudorapidity is defined as

$$\eta = -\ln \left[\tan \left(\frac{\theta}{2} \right) \right], \tag{3.10}$$

where θ is still the angle shown in Figure 3.7. η is a bit of an unintuitive quantity: it spans $[-\infty, +\infty]$, such that $\eta = \pm\infty$ directly along the $\pm z$-axis, and $\eta = 0$ along the y-axis. Figure 3.8 compares some values of η and θ. In the limit of mass going to 0, η converges to rapidity y. η is the variable that is most commonly used to express the angular coverage of an ATLAS detector component. We also define a Lorentz-invariant angular distance (ΔR) across two variables, η and ϕ, as

$$\Delta R = \sqrt{(\Delta\eta)^2 + (\Delta\phi)^2}. \tag{3.11}$$

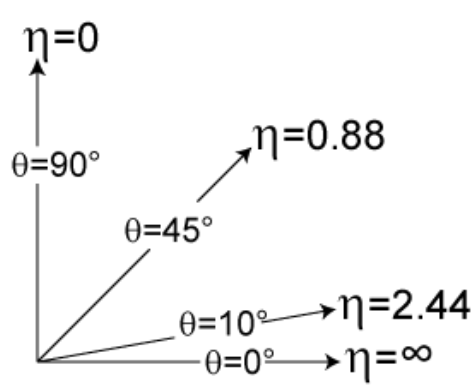

Figure 3.8: Sample values of pseudorapidity (η) and the corresponding θ values. $\eta = \infty$ along the beam axis [34].

3.4.3 Inner Detector

The Inner Detector (ID), shown in Figure 3.9, is the portion of the ATLAS detector that is closest to the IP and therefore the first detector component to see collision decay products. It begins a radial distance of about three centimetres from the IP, and extends out to a radius of 2.1 metres. The main purpose of the ID is particle tracking, i.e. high-precision measurements of momentum and vertex position for particles with $p_{\mathrm{T}} > 0.1$ GeV and $|\eta| < 2.5$. It also can identify electrons with $|\eta| < 2.0$. In order to have this high precision, the ID must be finely grained, but granularity decreases as the radii increases. The ID can be subdivided into four components, ordered by proximity to the IP: the Insertable B-Layer (IBL), silicon pixel detector (Pixels), silicon microstrip tracker (SCT), and Transition Radiation Tracker (TRT). All four components are immersed in a 2 Tesla magnetic field generated by the central solenoid magnet (see Figure 3.12), which bends electromagnetic particles as they pass through the detector. The IBL is a newer ID component, installed after Run 1 in order to improve the robustness and performance of the tracking system [35].

The IBL, pixel detector, and SCT are all silicon semiconductor detectors. When charged particles pass through the sensors of silicon semiconductor detectors, ionizing radiation produces electron-hole pairs, and an applied electric field pushes these charge carriers as a signal to the readout components [26].

The TRT is a transition radiation detector. When a high-energy charged particle moves from a medium with one dielectric constant to another, the electric field around the particle quickly changes, generating transition radiation that is proportional to the particle's momentum [26]. The ATLAS TRT combines classic transition radiation detection with tracking, and is the ID component that can identify electrons [28].

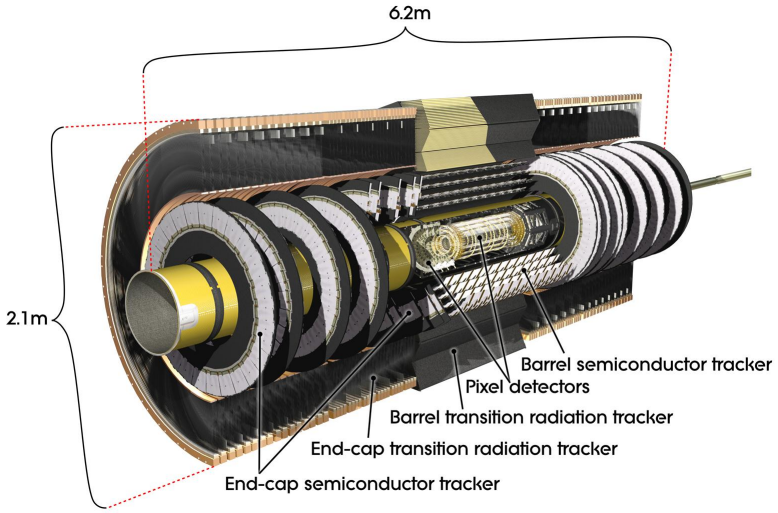

(a) Cutaway side view

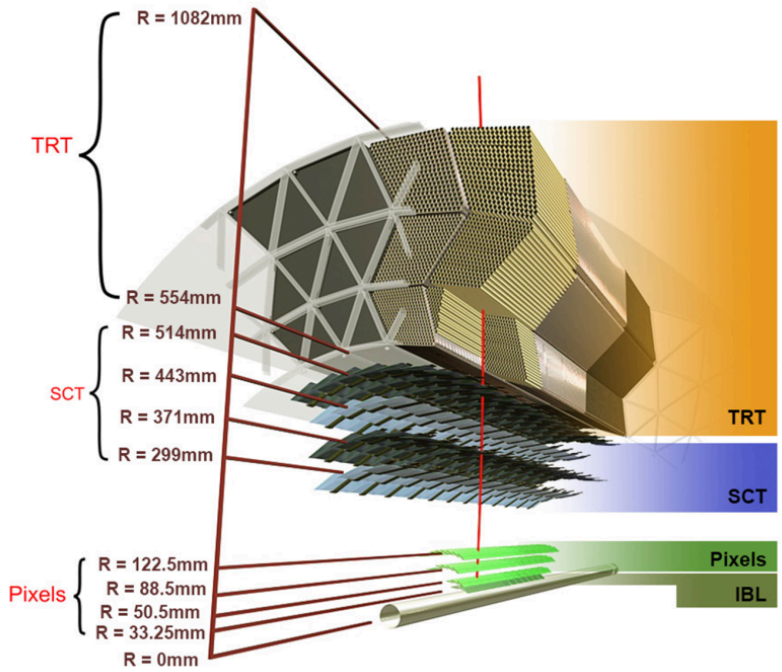

(b) Sub-detector radii

Figure 3.9: The ATLAS Inner Detector. A side view with overall dimensions (top) [28] and front view with the radii of the four sub-detectors (bottom) are shown [36].

3.4.4 Calorimeters

The ATLAS calorimeter is also a system of smaller components. Overall, the calorimeter system makes up the bulk of the barrel portion of the ATLAS detector. Figure 3.10 shows a diagram of the calorimeter system. The calorimeter surrounds the ID in both the barrel and end-cap regions. Calorimeters are generally designed to measure a particle's energy. They can do this by sampling the energy of a particle as it passes through the calorimeter, or by containing all of the particle's energy, including secondary particle showers that are created when a particle interacts with the calorimeter material.

There are two types of particle showers that can be produced when a particle interacts with a material: electromagnetic showers, which are initiated by electrons (or positrons) or photons and contain only these particles, and hadronic showers, which are initiated by hadrons and are much more complex due to their hadronic nature and the fact that the showers can contain both hadronic and electromagnetic secondary showers [26]. This also leads to two main categories of calorimeters: electromagnetic and hadronic. Each type is optimized to measure the energy of their respectively-named particles and the particle showers that they produce. A well-designed calorimetry system should absorb all of the energy from incoming particles aside from neutrinos and muons. ATLAS has both electromagnetic (ECAL) and hadronic calorimeters (HCAL) as part of its calorimetry system. Overall, the ATLAS calorimeter covers the range $|\eta| < 4.9$, which is nearly the entire pseudorapidity phase space other than directly along the beam line.

The ATLAS detector has two main calorimeter components: the Liquid Argon (LAr) Calorimeter and the Tile Calorimeter. The LAr calorimeter has both ECAL and HCAL components, while the Tile calorimeter is entirely hadronic. Both types of calorimeters have coverage in the barrel and end-cap regions.

The LAr ECAL is what is known as a *sampling* calorimeter, where instead of a continuous medium, the calorimeter is made of interleaved layers of absorbing material and detectors. The ATLAS ECAL has alternating layers of lead as the absorbing material, which also creates electromagnetic showers, and liquid argon as the detecting material which becomes ionized by the shower particles producing a current that is the measured signal. The ECAL features a characteristic accordion structure with

a honeycomb pattern to provide complete ϕ coverage and ensure that no particle escapes.

The Tile portion of the HCAL surrounds the ECAL in the barrel region. It is also a sampling calorimeter, with steel as the absorbing material and plastic scintillating tiles as the detecting material. When hadronic particles interact with the steel, hadronic showers are created, which produce photons upon interaction with the plastic tiles that are then directed into photomultiplier tubes as the readout signal. The end-cap portion of the HCAL is similar to the ECAL, except it uses copper plates as the absorption material instead of lead. Each end-cap HCAL component consists of two double-layered independent wheels that are located directly behind the ECAL. The forward portion of the LAr calorimeter (FCAL) contains three modules in each end-cap: one that is optimized as an ECAL and uses copper as its absorption material, and two that are optimized as HCALs and use tungsten [28].

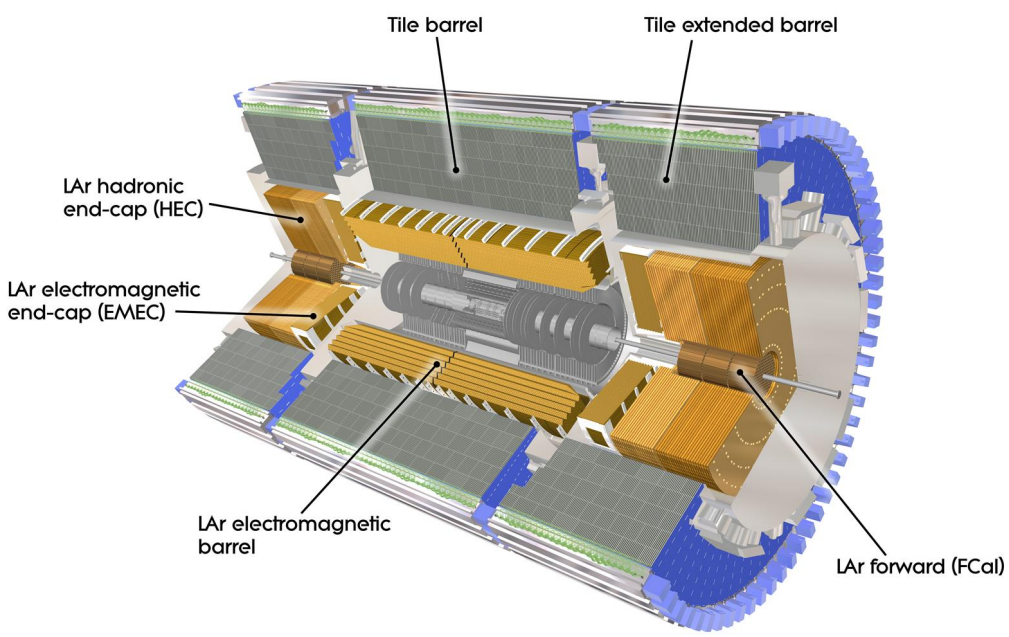

Figure 3.10: Cutaway view of the ATLAS calorimeter [28].

3.4.5 Muon Spectrometer

The Muon Spectrometer (MS) is both the largest detector component and the farthest from the IP. As expected from the name, the purpose of the MS is to identify and measure the momenta of muons. Muons only lightly interact with the more interior components of the detector, so a dedicated muon measurement device is vital for the accurate reconstruction of decay vertices since many interesting processes involve muons. The ATLAS detector is designed such that only muons (and neutrinos, which are unidentifiable) reach the MS. Figure 3.11 shows a cutaway view of the MS and its four main subsections, along with the two major magnet components that bend muons into the MS.

The four subsections of the MS are the resistive plate chambers (RPCs), thin gap chambers (TCGs), cathode strip chambers (CSCs), and monitored drift tubes (MDTs). Overall, the MS has a coverage of $|\eta| < 2.7$. Individual parameters of each subsection are shown in Table 3.1.

Subsection	Function	Coverage
MDTs	Precision tracking	$\|\eta\| < 2.7$
CSCs	Precision tracking	$2.0 < \|\eta\| < 2.7$
TGCs	Triggering	$1.05 < \|\eta\| < 2.7$
RPCs	Triggering	$\|\eta\| < 1.05$

Table 3.1: Main parameters of the muon spectrometer. The innermost layer of the MDTs only covers $|\eta| < 2.0$. The TGCs only have triggering coverage up to $|\eta| = 2.4$ instead of $|\eta| = 2.7$ [28].

3.4.6 Magnet System

The ATLAS magnet system is an important component of the detector. While the magnets themselves do not physically measure the properties of any particles, they bend charged particles through various layers of the detector. Two types of magnets perform the bending: solenoids, which produce linear magnetic fields through the centre of straight coiled wires with an applied current, and toroids, which produce

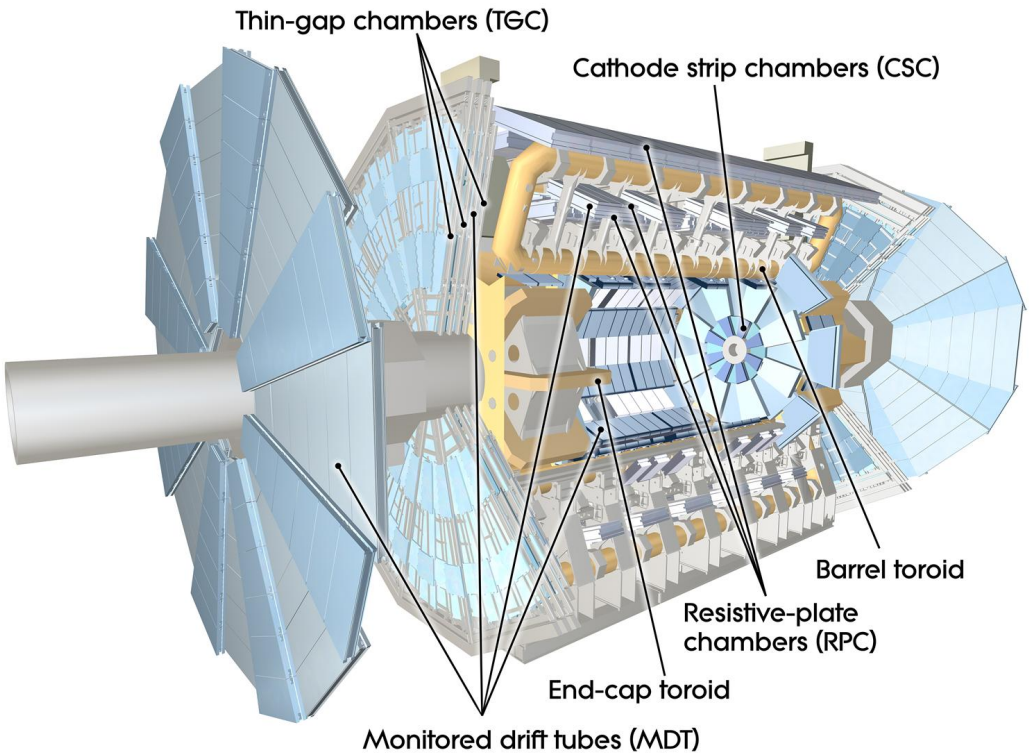

Figure 3.11: Cutaway view of the ATLAS muon spectrometer [28].

circular magnetic fields by running a current through wires that are wrapped around a ring.

Figure 3.12 shows a diagram of the ATLAS magnet system. There are three main sections of the magnet system: the central solenoid magnet, the barrel toroid magnets, and the end-cap toroids. This system must be cooled to 4.5 K to maintain the strong magnetic fields of the magnets.

The central solenoid magnet surrounds the ID, located between the ID and the ECAL. It creates a 2 T magnetic field to bend charged particles for momentum measurements.

The barrel toroid magnet system is made of eight massive toroidal magnets that are positioned between the HCAL and the barrel portion of the muon spectrometer. Each of these magnets is 25.3 m long – the eight combined toroids form the largest toroidal magnet ever constructed, creating a 4 T magnetic field. The end-cap toroids are located in the end-cap regions of the detector just before the end-cap portion of the muon spectrometer to extend the magnetic field. Both toroids are designed to

bend muons in order to allow for their momenta to be measured by the MS. The barrel toroid bends muons in the $|\eta| < 1.4$ range and the end-cap toroids bend muons in the $1.6 < |\eta| < 2.7$ range [28].

Perhaps the most iconic photo of the ATLAS detector shows the huge barrel toroids with a person standing in the center. Figure 3.13 shows this photo.

Figure 3.14 summarizes the paths of particles through the cross section of the ATLAS detector.

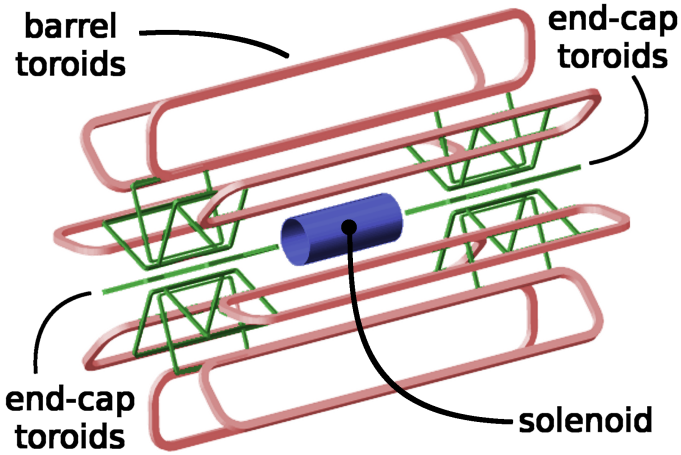

Figure 3.12: The isolated magnets of the ATLAS Magnet System [37].

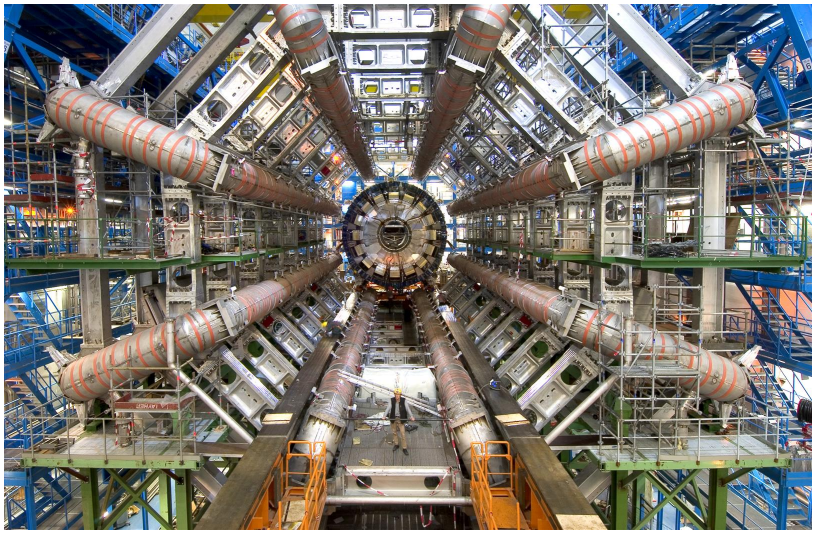

Figure 3.13: Photo of the eight massive toroidal magnets in the barrel region of the ATLAS detector [38].

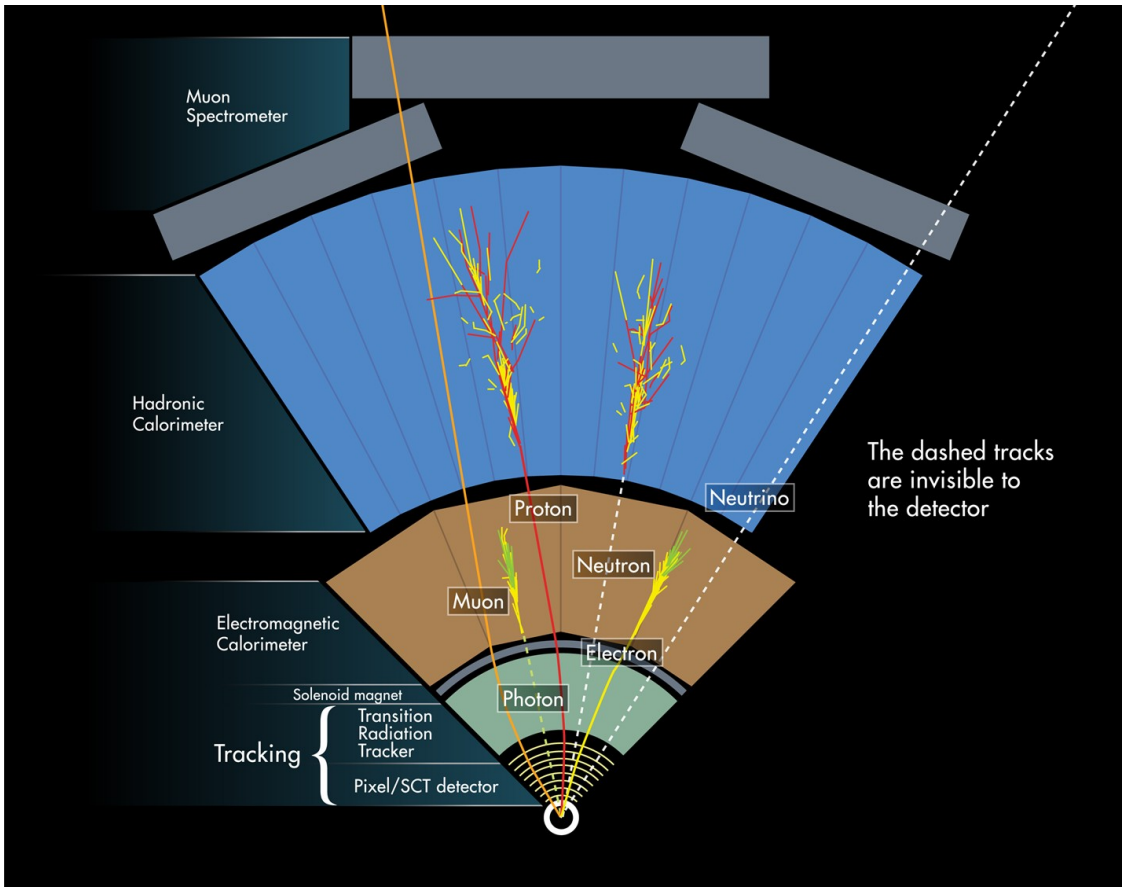

Figure 3.14: Cross-sectional diagram of the paths of particles through the ATLAS detector. Beginning from the IP, charged particles (including electrons, muons, and protons) are tracked by the Inner Detector, losing a portion of their energy and bent by the solenoid magnet. Neutral particles pass through the ID without leaving tracks. Electrons and photons are then stopped entirely by the electromagnetic calorimeter, depositing all of their energy within it. Protons and muons lose a small amount of energy to the ECAL but pass through. Neutrons, largely uninteracting up to this point, reach the hadronic calorimeter which absorbs all of their energy. The same thing happens to protons in the HCAL. Muons again lose a small fraction of their energy but pass through the HCAL to the muon spectrometer. Only muons reach the muon spectrometer and ionize gas as their final measurement method, but for the most part they continue on to eventually lose all of their energy after leaving the detector. Neutrinos do not interact with any part of the detector and escape as missing energy [39].

3.4.7 Trigger and Data Acquisition

ATLAS can observe up to about 1.7 billion p-p collisions per second, which translates to more than 60 million megabytes of data per second – an incredible amount of data! It would be impossible to record and save all of the data at this rate, so this number must be reduced drastically and quickly. Only a portion of these events are interesting from a physics point of view, and the trigger and data acquisition system (often combined to the acronym TDAQ) removes the uninteresting events to perform this data reduction.

There are two levels to the trigger system. The first level (L1) is a hardware trigger made with electronics that are attached to the ATLAS detector. The L1 trigger uses information from the calorimeter and the muon spectrometer to make its decisions. In less than 2.5 μs, the L1 trigger reduces the number of events from about 40 million per second to below 100,000 per second. The second level of the trigger (called the HLT – High Level Trigger) is a software trigger that further reduces the event rate to an average of 1.2 kHz. After the data rate has been reduced by the L1 trigger and the HLT, the data are recorded to disk with a data size of roughly 1 MB per event (storing 1.2 GB/s) [40].

Raw data from the HLT are stored in the form of ROOT files - a framework for data processing originating at CERN [41]. The ROOT files are managed centrally and processed in various reconstruction steps (more on this in Chapter 4). After this reconstruction, the output is stored in Analysis Object Data (AOD) files and grouped in datasets on ATLAS grid-computing sites around the world. These datasets are then processed with the ATLAS derivation framework into Derived Analysis Object Data (DAOD), which are smaller formats tailored to specific analyses or ATLAS groups, containing a subset of events and reduced reconstruction information. DAODs are the datasets that are accessed and processed by individual ATLAS analyzers [42].

3.4.8 Luminosity Measurements

ATLAS has one detector that is dedicated to measuring luminosity. While CERN reports how much luminosity is delivered by the LHC when the beam is on, it is important to know the luminosity at the IP as measured by ATLAS itself. This detector, called LUCID (LUminosity measurement using Cerenkov Integrating Detector), is lo-

cated in the forward region of the experiment along the beam pipe a distance of ±17 m from the IP [28].

Figure 3.15 shows a plot of the total integrated luminosity during Run 2 at a centre-of-mass energy $E_{\mathrm{cm}} = 13$ TeV, comparing what was delivered by the LHC to what ATLAS actually recorded. The plot also shows how much of the recorded data can be used for physics results. Not all data are good for physics. For example, we might find that there was an error in one of the detectors that caused particles to be misidentified for a given time period. We then try to see if this error can be fixed in the software, or if all data recorded during that short time period must be discarded. Things like this account for the difference between what ATLAS records and what is considered "Good for Physics". ATLAS keeps track of this through a Good Run List (GRL). After taking the GRL into account, ATLAS recorded a total integrated luminosity of 139 fb^{-1} during Run 2 that is good for physics results.

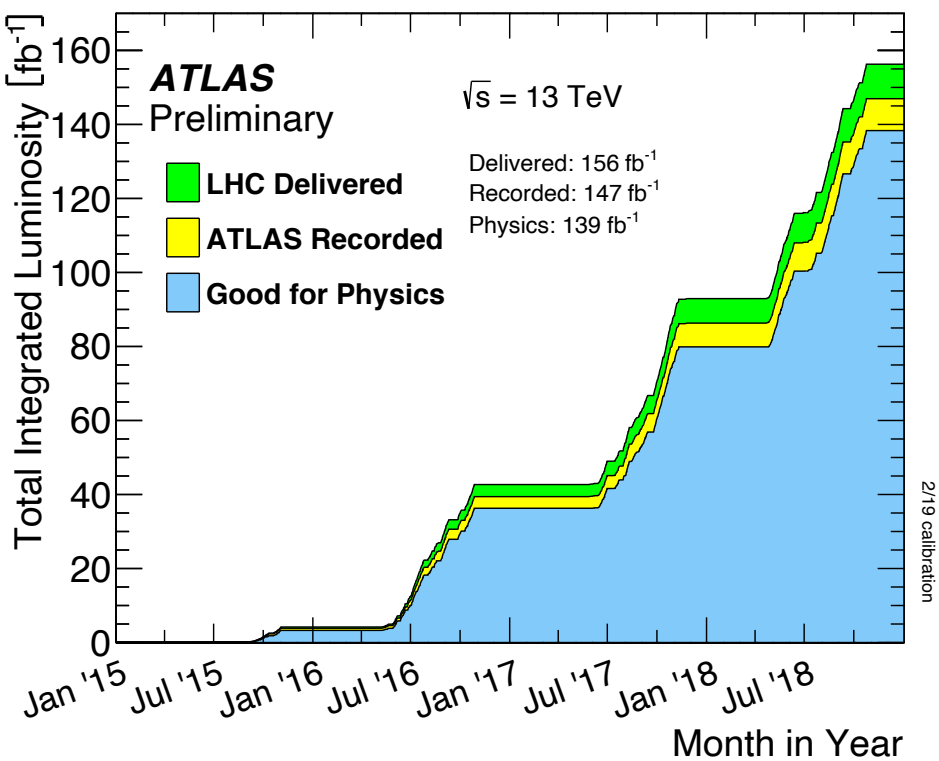

Figure 3.15: Total integrated luminosity delivered by the LHC (green), recorded by ATLAS (yellow), and considered good for physics results (blue) at a center of mass-energy of 13 TeV. $\mathcal{L}$ is shown as a function of half-years in Run 2 [43].

Another aspect of recorded data that must be taken into account is **pileup**. Pileup occurs when multiple *p-p* interactions are measured in the detector at the same time. This can happen for two reasons:

1. The LHC collides bunches of protons in order to ensure that *p-p* collisions actually occur, however only one event per bunch crossing can be studied and the rest must be ignored. All events in excess of one per *p-p* bunch crossing are considered to be *in-time pileup*.

2. A *p-p* bunch crossing occurs roughly every 25 ns. However, it takes more than 25 ns for the particles of interest created during a collision to pass through the detector and for their signals to be read. Therefore, there may be particles from different events being detected at the same time. This is known as *out-of-time pileup* and must also be accounted for.

It is important to understand pileup. ATLAS measures the mean number of interactions per *p-p* bunch crossing, $\langle\mu\rangle$, to get an idea of the average pileup (pileup is given the variable μ, not to be confused with the symbol for a muon). Figure 3.16 shows a plot of the ATLAS-recorded integrated luminosity as a function of $\langle\mu\rangle$ for each year of Run 2.

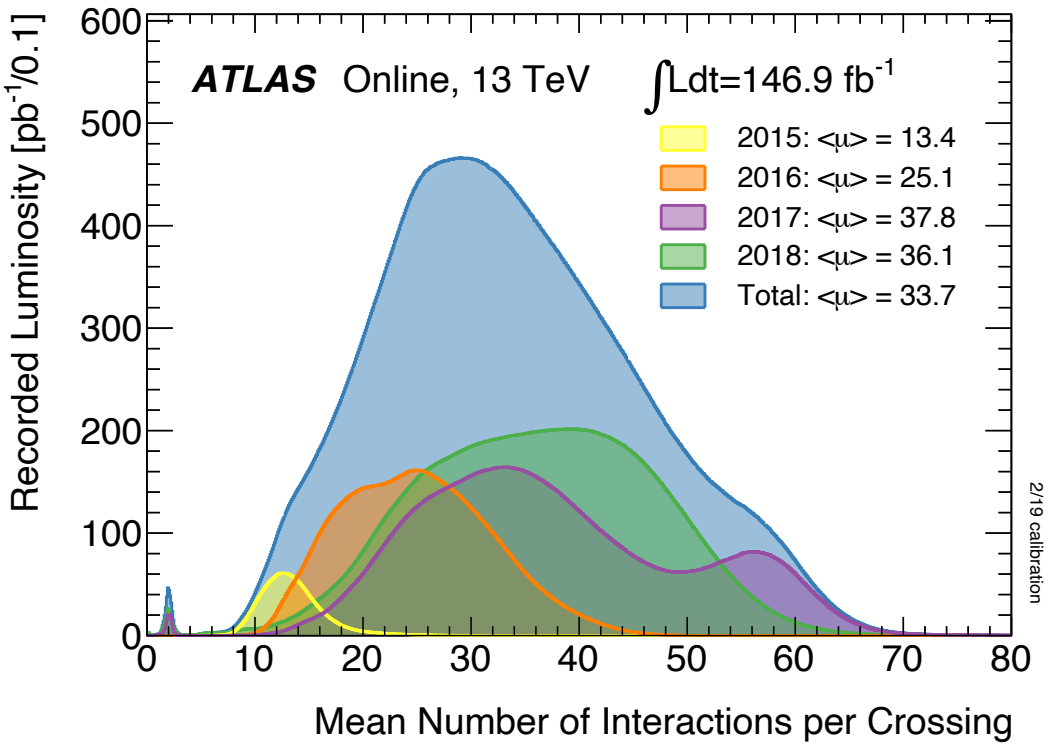

Figure 3.16: Luminosity-weighted distribution of the mean number of p-p interactions per bunch crossing (i.e. average pileup, $\langle\mu\rangle$) for ATLAS data recorded during Run 2 at a centre-of-mass energy of 13 TeV [43].

Chapter 4

Measuring Electrons with ATLAS

Physics analysis results usually garner the most attention in terms of publication visibility, conference presentations, and general prestige. This makes sense – after all, who is not excited about a new particle discovery or a new decay process or increased precision on an important parameter. However, this representation in visibility does not reflect the whole picture. An incredible amount of time and effort goes on behind the scenes to make these analysis results possible. Let us use the example of a new decay process where a particle decays to final-state electrons. As analyzers, we only see the detector signals. How do we know that we are actually seeing electrons in the final state as opposed to different particles like photons that are masquerading as electrons? How can we be sure that we have accurately measured the p_{T} of a final-state electron? How do we make sure that our theoretical predictions are consistent with our experimental data? Considerable work is required to answer questions like these, and the answers become universal aspects of an analysis that are used for all analyses of a given type. We are also constantly working to improve these methods to reduce uncertainties in our analyses. The end product that is a physics analysis result is the conclusion of a long chain of activities and deliverables that are all necessary to its success. This chapter overviews the critical steps that are required to measure electrons in ATLAS and use these measurements in analyses.

It takes a long series of collaborative steps to obtain and use ATLAS data to publish scientific results. It is important to credit these contributions that are made by all ATLAS members, so as a result, all members have equal rights to the data and

all ATLAS publications include our full authorship list in alphabetical order. In order to become an author on all physics publications, ATLAS members must complete a ~ 1 year "Qualification Task" (QT) – a year of service work for the Collaboration that is not part of a physics analysis. This task can be any number of things, including building hardware for the detector or improving the way electrons are measured.

For my qualification task, I worked to improve the way that W boson decays are measured in low-pileup data. I showed that a new, untested but specially-designed trigger is much more effective at identifying W boson Drell-Yan events than the previous best triggers. I also implemented a method called "W tag-and-probe", a new way to gather a clean sample of electrons[1] at low-p_{T}, which can then be used to evaluate the efficiency with which electrons are selected. This method is available to anyone in the Collaboration. I presented my progress and final results at several meetings and wrote internal documentation on the outcome. The totality of these activities allowed me to become a qualified ATLAS author in December 2020. This chapter also overviews the necessary background information for my QT and the reconstruction of events in general, and then details the work that I completed during my QT (Section 4.3).

4.1 Data and Simulation

4.1.1 Data

The complete ATLAS Run-2 dataset corresponds to a total integrated luminosity of 139 fb^{-1}, as was discussed in Section 3.4.8. However, it may not be optimal for each analysis to use this full dataset. The QT discussed in this chapter, along with all analysis work discussed in the remainder of this thesis, uses a special-purpose low-pileup dataset recorded during Run 2 in 2017 and 2018. Figure 4.1 shows this low-pileup dataset in comparison to the rest of the data accumulated in Run 2. Low-pileup data are used when one needs to access objects whose properties need to be measured with high precision. The ATLAS detector is designed to identify and isolate objects like electrons and photons in high-pileup environments. However, some physics objects that must be measured for certain analyses leave more broadly-distributed signals

[1]Note that as was mentioned earlier, "electron" refers to electrons (e^-) or positrons (e^+).

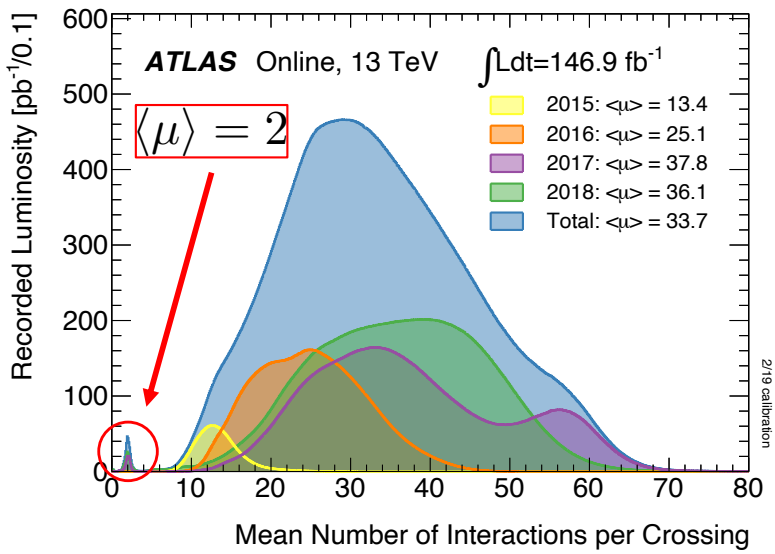

Figure 4.1: The ATLAS Run-2 $\sqrt{s} = 13$ TeV pileup total luminosity plot (Fig. 3.16) with the low-pileup portion highlighted (here low-pileup refers to $\langle\mu\rangle \approx 2$). At this centre-of-mass-energy, ATLAS recorded approximately 190 pb^{-1} of low-pileup data in 2018 (8 days of data-taking) and 150 pb^{-1} in 2017 (6 days of data-taking). ATLAS also recorded approximately 260 pb^{-1} of low-pileup data in 2017 at $\sqrt{s} = 5$ TeV (6 days of data-taking).

that are difficult to isolate within a small portion of the detector, leaving messy energy deposits that can be hard to discern from pileup events. Therefore, low-pileup data must be taken so that these objects can be accurately measured and their performance better evaluated, since little-to-no background due to pileup is left in the detector. Figure 4.2 compares ATLAS detector event displays for the same simulated $Z \to \mu^+\mu^-$ event at low and high pileup, exemplifying the 'cleaner' low-pileup environment. The downside of using low-pileup data is that the dataset is just a small fraction of the total data that are available (as can be seen in Figure 4.1), so the statistics are greatly reduced leading to a larger statistical uncertainty in the measurement. While low-pileup data are critical for a small set of observables, most ATLAS (and other LHC experiment) analyses benefit much more when running at high-pileup, so only a small number of LHC runs in any given year can be reserved for taking low-pileup data[2]. All work done in this thesis uses the low-pileup dataset

[2]Since it was a special-purpose dataset, only three weeks of time was taken away from the main Run-2 data-taking programme to accumulate these low-pileup data.

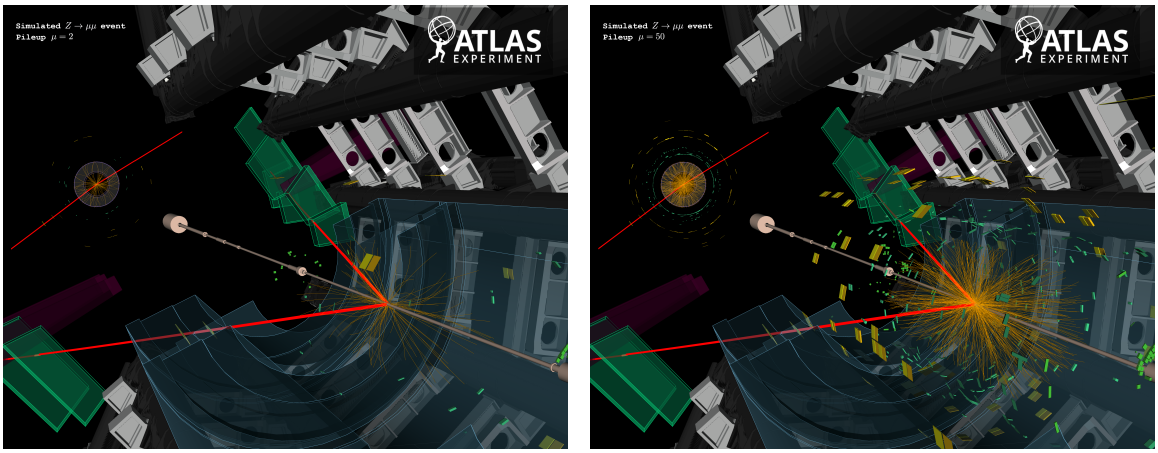

(a) $\langle\mu\rangle = 2$ (b) $\langle\mu\rangle = 50$

Figure 4.2: Event displays of the ATLAS detector showing the same simulated $Z \to \mu^+\mu^-$ event with low pileup (4.2a [44]) and high pileup (4.2b [45]).

because an object known as *hadronic recoil* (discussed in Section 4.3.1), a critical object for measuring high-precision Drell-Yan W boson decays, can only be precisely measured in this clean environment. For the purpose of the remainder of this thesis, *low-pileup data* (low-μ data) will specifically refer to this dataset highlighted in Figure 4.1 where the average number of p-p collisions per bunch crossing is $\langle\mu\rangle \approx 2$.

Pileup is one form of **background** that is present in every dataset. All events that are not the process of interest are considered background and must be separately measured and/or modeled and then subtracted from the dataset before the isolated process of interest can be studied.

4.1.2 Monte Carlo Simulation

Monte Carlo (MC) simulations are used to create simulated datasets based on our best knowledge of the Standard Model process of interest and our understanding of the response of the detector to the particles produced. MC production is limited by computational power, in that it takes time to generate simulated events and reconstruct them in the detector, and this time increases as a function of the number of events and the complexity of the process. For example, it takes more time to generate MC simulations that perform calculations up to next-to-leading order (NLO) compared to just leading order (LO), but the NLO (or NNLO, NNNLO, etc.) MC

will be more accurate than the LO MC (see Appendix B.4 for the discussion on order). However, in the same amount of time, many more events can be generated and reconstructed in a LO-MC compared to one of higher order, so a balance must be maintained based on the needs of the specific analysis. Additionally, a MC must be simulated with a chosen PDF set to model the inner workings of the proton. PDF sets get updated over time as experimental data improve our understanding of a proton's internal structure.

MCs are used to create a simulated dataset of the *signal*, i.e. the process of interest, and also to predict each of the known backgrounds that are expected to be important when studying this process. After a dataset is collected, the relevant background MCs are subtracted from the data to obtain a clean signal. In order to compare experimental results and theoretical predictions for a given process, background-subtracted data are compared to various MCs of this process. The order of the MC, the chosen PDFs, and the accuracy at which the MC models the detector response each contribute experimental uncertainties to the final measurement. In an analysis, it is usually important to state two aspects of a given MC: the generator – the program that performs the simulation at a given order, and the PDF set.

4.2 Electron Efficiency Measurements

Electrons are essential ingredients in the final states of many processes of interest, and so it is imperative that we know how well we are measuring them. There are several things that we must do effectively:

- reconstruct electrons from prompt decays such as $Z \to e^+e^-$;
- identify electrons with high efficiency;
- isolate electrons from misidentified objects i.e. other particles such as hadrons mimicking electron signals in the detector, or electrons from non-prompt processes such as photon conversions.

The electron spectra must be corrected for these (and trigger) selection efficiencies. These efficiencies are commonly calculated using the tag-and-probe method (Section

4.2.1). The total efficiency to select an electron is given by

$$\epsilon_{\text{total}} = \epsilon_{\text{reco}} \times \epsilon_{\text{id}} \times \epsilon_{\text{iso}} \times \epsilon_{\text{trig}} \tag{4.1}$$

$$= \left(\frac{N_{\text{reco}}}{N_{\text{all}}}\right) \times \left(\frac{N_{\text{id}}}{N_{\text{reco}}}\right) \times \left(\frac{N_{\text{iso}}}{N_{\text{id}}}\right) \times \left(\frac{N_{\text{trig}}}{N_{\text{iso}}}\right). \tag{4.2}$$

ϵ_{reco} is the reconstruction efficiency, given by the number of reconstructed electron candidates N_{reco} divided by the total number of produced electrons N_{all} (Section 4.2.2). ϵ_{id} is the identification efficiency[3], given by the number of identified and reconstructed electron candidates N_{id} divided by N_{reco} (Section 4.2.3). ϵ_{iso} is the isolation efficiency, given by the number of identified electron candidates satisfying the isolation, identification, and reconstruction requirements N_{iso} divided by N_{id} (Section 4.2.4). ϵ_{trig} is the trigger efficiency, given by the number of triggered electron candidates N_{trig} divided by N_{iso} (Section 4.2.5). Each efficiency component contributes its own systematic uncertainty to a final measurement [46, 47].

Efficiencies are measured in both data and MC samples. MC samples must be corrected so that they reproduce their corresponding data efficiencies. A multiplicative correction factor must be applied to the MC to ensure that the MC is properly modelling the data, including the effects caused by the detector (i.e. ensuring that the signal in MC matches the signal in data) [48]. This correction is referred to as a *Scale Factor* (SF), and is given by:

$$SF = \frac{\epsilon_{\text{Data}}}{\epsilon_{\text{MC}}}. \tag{4.3}$$

SFs are normally close to one; deviations from unity are usually due to mismodelling in the MC. Scale Factors are provided by ATLAS performance groups to be used in all relevant analyses across ATLAS.

4.2.1 Tag-And-Probe

The tag-and-probe (TP) method is the canonical ATLAS method for determining electron efficiencies. TP aims to use clean, unbiased, easily identifiable decay signatures that produce at least one electron. In practice, this means TP measurements use

[3]This is the portion of the efficiency chain that I contributed to improving.

mostly $Z \to e^+e^-$ samples since the two final-state electrons can be easily measured with the ATLAS detector for $E_\mathrm{T} > 15$ GeV. (E_T is the transverse energy, a quantity similar to p_T; $E_\mathrm{T} = E \sin\theta$). For electron identification efficiency measurements in the range of [4.5, 20] GeV, $J/\psi \to e^+e^-$ decay samples are used [46]. J/ψ is a meson formed by a $c\bar{c}$ bound state with a mass of approximately 3 GeV, which is more ideal for this low-energy range [7].

Strict selection criteria are applied to one of the two decay electrons – this electron is called the "tag". The second electron, known as the "probe", is then used as a source of relatively unbiased electrons for efficiency measurements. Figure 4.3 shows a cartoon image of $Z \to e^+e^-$ TP. Additional event selection criteria are applied such

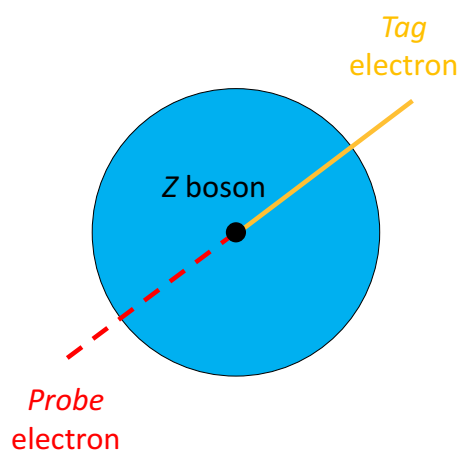

Figure 4.3: Cartoon of $Z \to e^+e^-$ tag-and-probe within the ATLAS detector.

that the tag electron ideally only selects good events. For example, the invariant mass of the two electrons is reconstructed to ensure that they sum to the invariant mass of the initial decay particle, i.e. the Z boson or the J/ψ. The probe electron is then used for efficiency measurements using the formula

$$\epsilon = \frac{N_\mathrm{probes}^\mathrm{passWP}}{N_\mathrm{probes}}, \tag{4.4}$$

where N_probes is the total number of probes and $N_\mathrm{probes}^\mathrm{passWP}$ is the number of probes passing specific selection criteria (WP stands for working point), i.e. stricter criteria pertaining to one of the types of efficiencies such as ϵ_id. The main difficulty in TP

efficiency measurements is background removal – ideally N_{probes} is free of all background events. However, there is always some background contamination in data that must be indirectly estimated. Uncertainties are estimated by varying the efficiency measurement methods and the background models [48].

4.2.2 Reconstruction

The first electron efficiency parameter that one must determine is the reconstruction efficiency ϵ_{reco}. Electrons are defined as objects consisting of a cluster built from energy deposits in the calorimeter (known as superclusters) that are matched to tracks; the number of these objects is N_{reco}. This process begins with an algorithm that selects clusters of energy deposits in topologically-collected ECAL and HCAL cells, called topo-clusters. Topo-clusters are formed by first identifying calorimeter cells for which the cell energy-to-background noise ratio is at least 4. Neighbouring cells are then collected if they have an energy-noise ratio of at least 2. The neighbouring-cell window is then extended one more time to a crown of nearest-neighbour cells, independent of energy. This process is referred to as '4-2-0' topo-cluster reconstruction.

The next step is track reconstruction. Track reconstruction begins with a 'hit' in one of the tracking layers of the inner detector, and then clusters of these hits are assembled. Three-dimensional track seeds are formed in the silicon detector layers, requiring at least seven silicon hits per candidate track. A pattern-recognition algorithm is used to fit track candidates with $p_{\text{T}} > 400$ MeV. Track candidates are then matched to the candidate calorimeter topo-cluster in both η and ϕ. Once topo-clusters have been matched to tracks, superclusters can be reconstructed. First, topo-clusters are tested for use as seed-cluster candidates, by requiring that they have $E_{\text{T}} \geq 1$ GeV and have been matched to a track. When a seed-cluster candidate is found, the algorithm searches for satellite clusters. Satellite clusters must fall within a window of $\Delta\eta \times \Delta\phi = 0.125 \times 0.300$ around the seed cluster barycentre with the same best-matched track as that of the seed cluster. Seed clusters with their associated satellite clusters are called superclusters. This reconstruction process is completed by directly assigning calorimeter cells to a given supercluster.

ϵ_{reco} for $E_{\text{T}} \geq 15$ GeV is greater than 95% for electrons with good track quality (at least one pixel detector hit and at least seven silicon detector hits) [46, 47, 49].

4.2.3 Identification

The third electron efficiency parameter to determine, ϵ_{id}, is also the efficiency parameter that W tag-and-probe can improve for low-μ data (Section 4.3). The electron reconstruction algorithm mentioned previously does not only reconstruct prompt electrons that are most often considered as signal, but also can include background objects such as hadronic jets, secondary electrons from photon conversions, and other unwanted sources. In order to reduce these backgrounds without reducing the number of signal electrons, discriminating variables are introduced to create a menu of selections for background rejection. The discriminating variables include descriptions of the shapes of EM showers in the ECAL, track properties within the ID, and track and energy matching between the ID and ECAL.

A likelihood-based (LH) identification system is used to select electrons in the central region of the detector ($|\eta| < 2.47$). The electron LH is determined separately for both signal, L_S, and background, L_B, using n pdfs (probability distribution functions), P:

$$L_{S(B)}(\mathbf{x}) = \prod_{i=1}^{n} P_{S(B),i}(x_i), \tag{4.5}$$

where $\mathbf{x}$ is a vector of the menu of discriminating variables, $P_{S,i}(x_i)$ is the value of the signal pdf for quantity i at value x_i, and $P_{B,i}(x_i)$ is the corresponding value of the background pdf. The electron LH identification is based on a discriminant d_L, given by:

$$d_L = \frac{L_S}{L_S + L_B}. \tag{4.6}$$

d_L peaks sharply at one for signal and zero for background. The pdfs for Equation (4.5) are determined by simulation in bins of E_{T} and η, but data are needed to correct some imperfect simulation quantities due to detector mismodelling.

Fixed values of the LH discriminant (4.6) are used to define working points (also called operating points) to cover the various required prompt-electron signal efficiencies (and corresponding background rejection factors) that are required by analyses. The most commonly-used working points (WPs) are referred to as *Loose*, *Medium*, and *Tight*, corresponding to increasing thresholds of d_L (i.e. increasing purity of selected electrons at the expense of lower selection efficiency). Each of these three WPs require at least two hits in the pixel detector and seven hits total between the pixel

and silicon-strip detectors. For *Medium* and *Tight*, one of these pixel hits must be in the innermost pixel layer. The fixed efficiency values that define these WPs vary as a function of η and gradually increase as a function of E_{T}; for typical electroweak processes they are, on average, 93%, 88%, and 80% for the *Loose*, *Medium*, and *Tight* WPs, respectively. The WPs act as subsets of each other as the selection criteria becomes more restrictive: an electron candidate satisfying the *Tight* criteria will also have passed the *Medium* and *Loose* criteria, and so on [46–48].

Figure 4.4 shows a schematic of the path of a sample electron through the ATLAS detector to visualize the detector components that help measure ϵ_{reco} and ϵ_{id}.

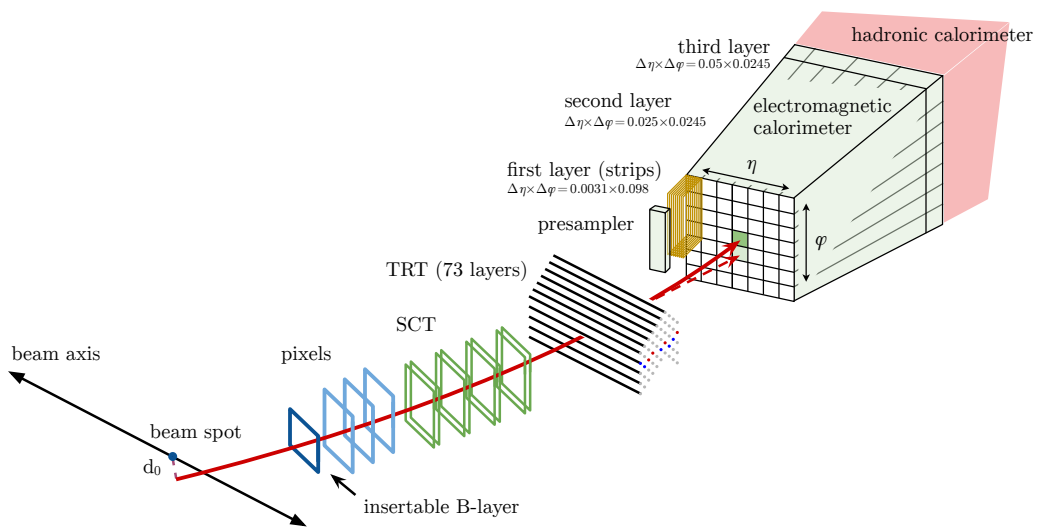

Figure 4.4: Schematic of the path of a hypothetical electron (red) through the ATLAS detector, corresponding to the relevant components for determining ϵ_{reco} and ϵ_{id} [46].

4.2.4 Isolation

The fourth electron efficiency parameter from the total efficiency Equation (4.1) is the isolation efficiency ϵ_{iso}. A characteristic signature of a signal electron is little activity in the detector (both the ECAL and the ID) in an area surrounding the electron candidate (in $\Delta\eta \times \Delta\phi$), i.e. how well this signal is isolated. This isolation is characterized by examining the total transverse energy of topo-clusters within a cone of radius $\Delta R = \sqrt{(\Delta\eta)^2 + (\Delta\phi)^2}$ (Eq. (3.11)) around the electron candidate, excluding the candidate itself.

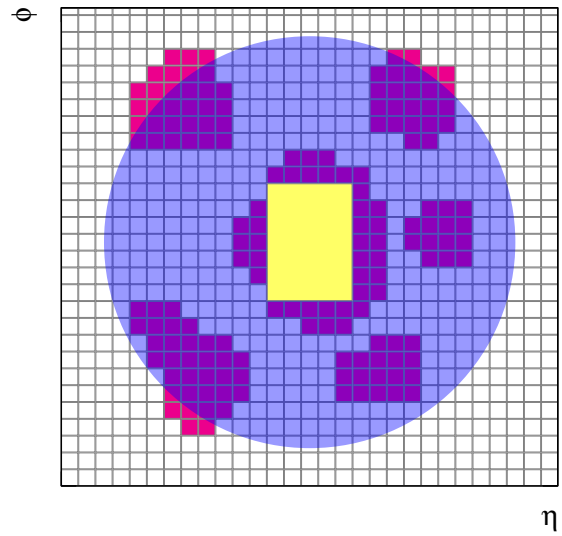

Figure 4.5: Model of the calorimeter isolation method. The grid represents the calorimeter cells in the η and ϕ directions. The isolation cone ΔR is represented by the purple circle, with the electron candidate at the centre. All topo-clusters (red) with barycentres falling within the cone are included in the computation of the isolation variable [46].

The raw calorimeter isolation is determined by summing the transverse energy of topo-clusters in the ECAL whose barycentre falls within a cone centered around the electron cluster barycentre. Included in the raw calorimeter isolation is the EM particle energy, which is subtracted by removing the energy of the EM calorimeter cells contained in a $\Delta\eta \times \Delta\phi = 5 \times 7$ (in cell units) cluster around the barycentre of the EM particle cluster. Figure 4.5 shows a graphic to visualize this calorimeter cell subtraction. Estimates for energy leakage and pileup are determined using MC samples and then are also subtracted to get the fully-corrected calorimeter isolation variable: $E_{\mathrm{T}}^{\mathrm{cone}\Delta R}$.

The track-based isolation variable is determined using the scalar sum of the transverse momentum with $p_{\mathrm{T}} > 1$ GeV within a cone ΔR around the electron candidate: $p_{\mathrm{T}}^{\mathrm{cone}\Delta R}$. The electron candidate track itself is excluded. The tracks considered in the sum must originate from the same primary vertex as the candidate electron and must be of good quality. In messy environments or when studying boosted decay signatures, other objects can be close to the signal electron direction – in these cases, a variable-cone-size track isolation variable can be used: $p_{\mathrm{T,var}}^{\mathrm{cone}\Delta R}$. Here ΔR decreases

as a function of p_{T} of the candidate electron:

$$\Delta R_{\mathrm{var}} = \min\left(\frac{10}{p_{\mathrm{T}}[\mathrm{GeV}]}, \Delta R_{\mathrm{max}}\right), \tag{4.7}$$

where R_{max} is the maximum cone size (typically 0.2), and the 10 GeV value is derived to maximize background rejection [46–48].

4.2.5 Trigger Efficiency

The final electron efficiency parameter to consider in Equation (4.1) is the trigger efficiency ϵ_{trig}. ϵ_{trig} can be measured for electrons at the HLT or for EM clusters at L1. Single-electron triggers are used to select electrons that meet reconstruction, identification, and isolation requirements at trigger-level, and are then compared to the denominator N_{iso} which has no trigger requirement. Trigger efficiencies tend to have a turn-on curve, most commonly around 25 GeV, and tend to reach a maximum of about 95% to 99% efficiency at $E_{\mathrm{T}} \approx 50$ GeV depending on the isolation requirement [50]. Figure 4.6 shows a sample single-electron trigger efficiency plot measured with ATLAS Run-2 $\sqrt{s} = 13$ TeV data. The turn-on curve at about 25 GeV is clearly seen.

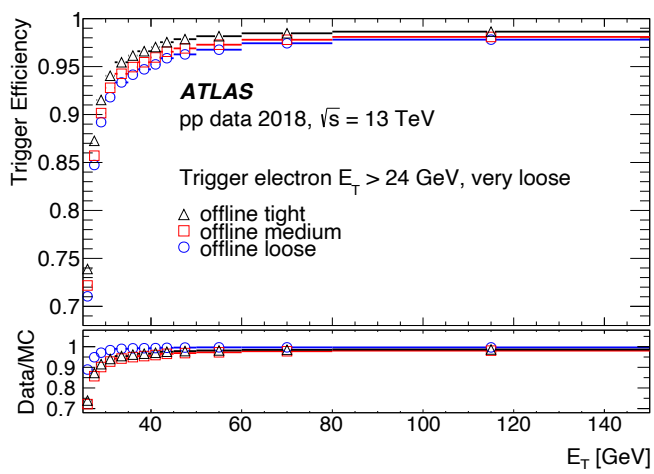

Figure 4.6: Sample trigger efficiency plot as a function of offline E_{T} for a single-electron trigger requiring $E_{\mathrm{T}} > 24$ GeV and *Very Loose* isolation. The trigger efficiencies are measured in data and shown with corresponding statistical and systematic uncertainties. The lower panel shows the data-to-MC ratio [50].

4.3 W Tag-And-Probe

Tag-and-probe measurements should ideally be performed using datasets (both data and MC) that mimic the conditions of the datasets used by the analysis that requires the corresponding TP efficiencies and SFs. However, analyses that use the low-μ dataset outlined in Section 4.1 use efficiencies and apply SFs that were evaluated using high-μ measurements and then extrapolated down to low-μ, either because low-μ efficiency measurements have not been done or the statistics for low-μ $Z \to e^+e^-$ are too low that the systematic uncertainty from the extrapolation is less than the statistical uncertainty from the lower-statistics efficiency measurement. Incorporating W boson decays into TP measurements is beneficial for three reasons:

1. $W \to e\nu$ decays are roughly ten times more common than $Z \to e^+e^-$ decays in ATLAS, so this increase in statistics using W bosons compared to Z bosons would reduce the statistical uncertainty on efficiency measurements, which has increased relevance in the already statistically-limited low-μ dataset;

2. $W \to e\nu$ decays are optimal for efficiency measurements in a different kinematic range: $Z \to e^+e^-$ is optimal for $p_T \sim 45$ GeV and does not populate the low-p_{T} range due to the Z boson mass constraint; $W \to e\nu$ is optimal for $p_T \sim 40$ GeV and does populate the lower-p_{T} range because there is not such a rigid mass constraint given that one of the decay leptons is a neutrino (more on this soon); $J/\psi \to e^+e^-$ is optimal for $p_T \sim 5$ GeV, so $W \to e\nu$ bridges the gap between $Z \to e^+e^-$ TP and $J/\psi \to e^+e^-$ TP;

3. Allows for in-situ efficiency and SF measurements for analyses interested in $W \to e\nu$.

Since the processes $W^+ \to e^+\nu$ and $W^- \to e^-\bar{\nu}$ are equivalent for WTP, they will be referred to together as $W \to e\nu$ for the remainder of this section. Note that 'WTP' and 'ZTP' will be short-form for W boson tag-and-probe and Z boson tag-and-probe, respectively.

The last time ATLAS used WTP for efficiency measurements was in Run 1, a data-taking period with relatively low pileup [51]. Run-2 studies requiring electron efficiencies have used $Z \to e^+e^-$ events, extrapolating where necessary, as these results have been more accurate compared to using $W \to e\nu$ events even after taking

the lower statistics into account. The major downside of WTP is that it is difficult to obtain an accurate background estimate and to reduce the background contamination in probe electrons. This is because in $W \to e\nu$ decays, the neutrino escapes the ATLAS detector without leaving a signal, so its energy and momentum must be estimated by using *missing transverse energy* ($E_{\mathrm{T}}^{\mathrm{miss}}$, or sometimes labelled as 'MET'). In order to deduce the presence of invisible particles like neutrinos, the total momentum of all known particles is summed; the remaining momentum is attributed to the invisible particle(s). In practice, since the fraction of each proton's momentum that participates in a collision is unknown, momentum parallel to the beam line cannot be used, and only the momentum imbalance in the transverse direction is quantified. The magnitude of this momentum is known as $E_{\mathrm{T}}^{\mathrm{miss}}$ [52]. $E_{\mathrm{T}}^{\mathrm{miss}}$ is a common observable in measurements. In $W \to e\nu$ decays, $E_{\mathrm{T}}^{\mathrm{miss}}$ is the best estimate of the neutrino's transverse momentum. This new implementation of WTP uses low-μ data not only so that the efficiencies are optimal for the low-μ dataset, but also to take advantage of the cleaner low-μ environment to reduce the background contamination and better discriminate between signal and background.

In WTP, the electron isolation parameter $E_{\mathrm{T}}^{\mathrm{cone}\Delta R}$ is used as the principal discriminating variable. ZTP can also use the Z boson mass peak for discriminating between signal and background, but this is not possible in $W \to e\nu$ decays due to the neutrino. This newly-created WTP background discrimination method is known as *W boson isolation*. WTP events are tagged using $E_{\mathrm{T}}^{\mathrm{miss}}$ with the electron acting as the probe. This is a major difference from ZTP, because there is only one potential value of $E_{\mathrm{T}}^{\mathrm{miss}}$ per event for $W \to e\nu$, whereas $Z \to e^+e^-$ events have two electrons, with each electron having the possibility of acting as a tag or a probe. Ideally real electrons from W boson decays are isolated: the signal region is defined as $E_{\mathrm{T}}^{\mathrm{cone}\Delta R=0.3}/25\ \mathrm{GeV} < 0.1$. Note that ΔR is set to a value of 0.3 and will no longer be included in the superscript. ΔR values of 0.2 and 0.4 can also be used as variations to establish the systematic uncertainties of the measurement. Background templates are constructed from the control region, which is defined by inverting the isolation requirement, $E_{\mathrm{T}}^{\mathrm{cone}}/25\ \mathrm{GeV} > 0.1$, and by inverting various other electron identification cuts, as will be described in Section 4.3.5.

WTP is initially implemented to measure electron identification efficiencies (Sec-

tion 4.2.3), but can be expanded to other efficiency measurements after optimization. The remainder of this section details the work to re-invent and implement WTP in the common software framework, including tests of a new specialty trigger and initial efficiency results. This was my qualification task project for ATLAS authorship.

4.3.1 W Boson Measurement Parameters

In order to discuss W boson measurements, two important new parameters must be introduced.

We have discussed how one must be able to estimate the transverse momentum of the outgoing neutrino, p_{T}^{ν}, in WTP in order to use this quantity as the tag ($E_{\mathrm{T}}^{\mathrm{miss}}$). The low-$\mu$ environment allows for an improved way to construct $E_{\mathrm{T}}^{\mathrm{miss}}$, which should reduce the background contamination in WTP events – this method involves an observable called *hadronic recoil*, u_{T}. u_{T} is the recoil in the transverse plane of the hadronic matter involved in the p-p collision, so in Drell-Yan processes like $W \to e\nu$, u_{T} is theoretically equal and opposite to the transverse momentum of the boson. Figure 4.7 shows a diagram of the hadronic recoil vector. In Figure 4.7, u_{T} is decomposed into $u_{\perp}$ and $u_{\parallel}$, where perpendicular and parallel are relative to the transverse momentum of the boson: $u_{\perp} = 0$ on average, but it is measured as a distribution to reflect the hadronic recoil resolution which is incorporated into the u_{T} measurement as a source of uncertainty.

u_{T} is reconstructed from the transverse energy of all clusters reconstructed in the calorimeters, excluding energy deposits from decay leptons [54]:

$$\vec{u}_{\mathrm{T}} = \sum_i \vec{E}_{\mathrm{T},i}. \tag{4.8}$$

Since these calorimeter energy deposits come from hadronic showers, the deposits are more spread out and messy, so normal pileup in the detector makes it difficult to precisely measure u_{T}. However, low-μ datasets allow for a higher-precision u_{T} measurement. This also should allow for an improved measurement of p_{T}^{ν}, because in dileptonic Drell-Yan decays,

$$\vec{p}_{\mathrm{T}}^{V} = \vec{p}_{\mathrm{T}}^{l_1} + \vec{p}_{\mathrm{T}}^{l_2}, \tag{4.9}$$

where p_{T}^{V} is the transverse momentum of the W or Z boson, and $p_{\mathrm{T}}^{l_i}$ is the transverse

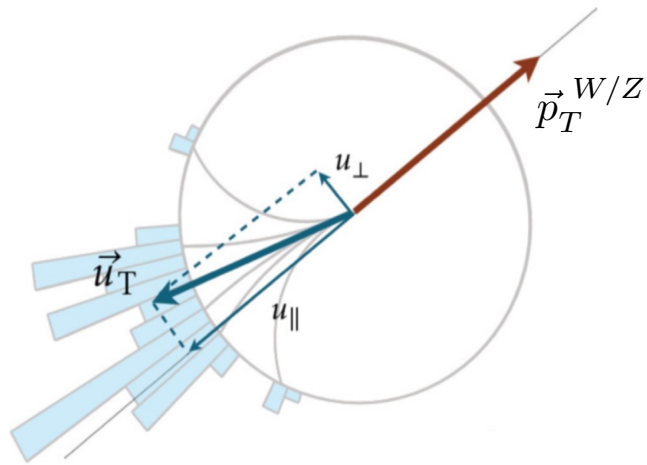

Figure 4.7: Diagram of the p_T of a W or Z boson with the opposing hadronic recoil ($\vec{u}_\mathrm{T}$) vector. The blue rectangles represent the energy deposits of u_T in the calorimeter [53].

momentum of the first or second decay leptons. Given that vectorially,

$$\vec{u}_\mathrm{T} = -\vec{p}_\mathrm{T}^{\,V}, \tag{4.10}$$

we can combine Equations (4.9) and (4.10), and specifying that we are looking at $W \to e\nu$ decays, we see that

$$\vec{p}_\mathrm{T}^{\,\nu} = -\left(\vec{u}_\mathrm{T} + \vec{p}_\mathrm{T}^{\,e}\right). \tag{4.11}$$

Experimentally it can still not be guaranteed that Equation (4.11) accurately reconstructs the neutrino transverse momentum, so it is more correct to use the general equation for missing transverse momentum:

$$\vec{p}_\mathrm{T}^{\,\mathrm{miss}} = -\left(\vec{u}_\mathrm{T} + \vec{p}_\mathrm{T}^{\,l}\right), \tag{4.12}$$

where we now refer to a general charged lepton p_T^{l} instead of specifying that this must be an electron. Equation (4.12) provides an alternate way to measure $E_\mathrm{T}^{\mathrm{miss}}$ and is used extensively in later chapters. In future chapters the vector notation will be

dropped for readability.

A second important variable for W boson measurements is its transverse mass, m_{T}^{W}. Due to the invisible neutrino, the mass of the W boson m_W cannot be directly measured by summing the mass of the outgoing leptons like how m_Z is measured in $Z \to l^+l^-$ decays. Instead, m_W must be determined using fits to p_{T}^{l} and m_{T}^{W}. p_{T}^{l} is an important parameter for both WTP and ZTP, but WTP must also use m_{T}^{W} as its mass constraint since there is no direct access to m_W. The W boson transverse mass gets its name from the fact that it is derived from the transverse missing energy and transverse lepton momentum:

$$m_T^W = \sqrt{2p_T^l p_T^{\mathrm{miss}}\,(1 - \cos\Delta\phi)}, \tag{4.13}$$

where $\Delta\phi$ is the azimuthal angle between p_{T}^{l} and $p_{\mathrm{T}}^{\mathrm{miss}}$ [54]. In WTP, p_{T}^{l} is always p_{T}^{e}.

4.3.2 WTP Framework Setup & Event Selection

Dataset

WTP studies are performed using the 2018 low-μ dataset: the centre-of-mass energy $\sqrt{s} = 13$ TeV, and the total integrated luminosity $\mathcal{L} = 190.2$ pb^{-1}. Signal MCs for $W^+ \to e^+\nu$ and $W^- \to e^-\bar{\nu}$ were also produced specifically for these studies. Various standard TP calibration procedures had to be updated for the low-μ dataset, since TP studies had never been performed with this dataset. These updates included removing pileup reweighting (the ATLAS procedure that takes pileup into account), and incorporating low-μ energy and momentum calibrations into the TP framework.

Triggers

Good WTP events require the presence of one electron and missing energy. Triggers are used to initially select for these good events. The most important triggers for low-μ Drell-Yan studies are:

- Single electron trigger: `HLT_e15_lhloose_nod0_L1EM12`
- $E_{\mathrm{T}}^{\mathrm{miss}}$ triggers: `HLT_xe35` & `HLT_xe35_tc_lcw`

- **WTP trigger:** `HLT_e15_etcut_trkcut_xe30noL1`

Triggers are composed of acronyms and naming conventions to describe what they do. The single electron trigger is a High-Level trigger (`HLT`) that requires the electron to have $p_{\mathrm{T}} > 15$ GeV (`e15`). It also must pass the loose electron identification likelihood (`lhloose`), with no cut on the transverse impact parameter `nod0` (the distance of closest approach of the electron in the transverse plane). This single electron trigger also requires the electron to have $p_{\mathrm{T}} > 12$ GeV at the level-one trigger (`L1EM12`). The missing energy triggers require that $E_{\mathrm{T}}^{\mathrm{miss}} > 35$ GeV (`xe35`), and `tc_lcw` means that $E_{\mathrm{T}}^{\mathrm{miss}}$ is measured from calibrated calorimeter clusters. In addition to what has been stated, the WTP trigger requires that only the E_{T} cut is applied at the HLT (`etcut`) and that there must be the minimum number of silicon tracker hits (`trkcut`). There is also no input seed to the first sequence at level one (`noL1`), another technical requirement. This WTP trigger is a new trigger that was created specifically to improve WTP and was implemented in 2018, but it was not tested or used prior to these studies. The testing of this WTP trigger, including its comparison to the previously-used $E_{\mathrm{T}}^{\mathrm{miss}}$ triggers, is the most important result of my Qualification Task and these studies and is explained beginning in Section 4.3.3.

Event Selection

Events within datasets must be selected such that they align with the requirements of the analysis. In practice, this means ensuring that the data are good to use, and applying selections based on triggers and the event-level requirement that objects pass certain kinematic thresholds. In this way, background events are removed before the dataset is analyzed. This event removal is known as *cutting*, and *cutflow* plots are made to understand the effect of each cut.

It is difficult to select only low-background events with WTP because events are tagged using $E_{\mathrm{T}}^{\mathrm{miss}}$, which only has one value per event. The best solution at the level of event selection is to require that all events pass the aforementioned WTP trigger. This is the only trigger used in event selection; studies shown in Section 4.3.3 present results with other triggers. Other non-kinematic cuts are also made, including the requirement that each event contains at least one electron. The kinematic cuts in WTP event selection are as follows:

- $p_{\mathrm{T}}^{\mathrm{probe}} > 15$ GeV
- $|\eta^{\mathrm{probe}}| < 2.47$
- $E_{\mathrm{T}}^{\mathrm{miss}} > 25$ GeV
- $m_{\mathrm{T}}^{W} > 40$ GeV

Here it is more correct to replace the word electron with probe, because at this point in event selection the event has already been selected as a good WTP event based on $E_{\mathrm{T}}^{\mathrm{miss}}$, so the probe is the electron candidate that must meet these thresholds. In general, an important part of the TP procedure is determining if the selected probe electron candidate is truly the prompt electron from the W or Z boson decay.

Additional cuts are applied based off of the last time WTP was performed in Run 1 [51]. If there is more than one potential probe electron in the event, the highest p_{T} probe is selected since this candidate is more likely to be the real electron. If after the probe electron is selected, there is another electron in the event that passes the *Medium* or *Tight* working points, the event is vetoed to avoid selecting $Z \to e^{+}e^{-}$ events or events containing conversions from photons.

Figure 4.8 shows histograms of the WTP cutflow for data and MC (with corresponding x-axis descriptions in Table 4.1). The largest event reduction comes from the WTP trigger for both data and MC. The $E_{\mathrm{T}}^{\mathrm{miss}}$ kinematic threshold significantly reduces the number of events, especially in data. The final five bins correspond to the electron identification LH requirements ranging from *Very Loose* to *Tight*. Electron identification cuts have a much larger effect on the background-rich data compared to the background-free MC sample.

4.3.3 Trigger Results

The WTP trigger (`HLT_e15_etcut_trkcut_xe30noL1`) was implemented to reduce backgrounds in WTP events while still providing enough events for meaningful efficiency measurement statistics. Before the WTP trigger, the best WTP options required $E_{\mathrm{T}}^{\mathrm{miss}}$ triggers. Figure 4.9 shows the efficiency performance of the complete $E_{\mathrm{T}}^{\mathrm{miss}}$ trigger chain for each year of Run 2, with 2018 data shown in pink triangles. This plot from the $E_{\mathrm{T}}^{\mathrm{miss}}$ trigger performance team shows that the $E_{\mathrm{T}}^{\mathrm{miss}}$ triggers are

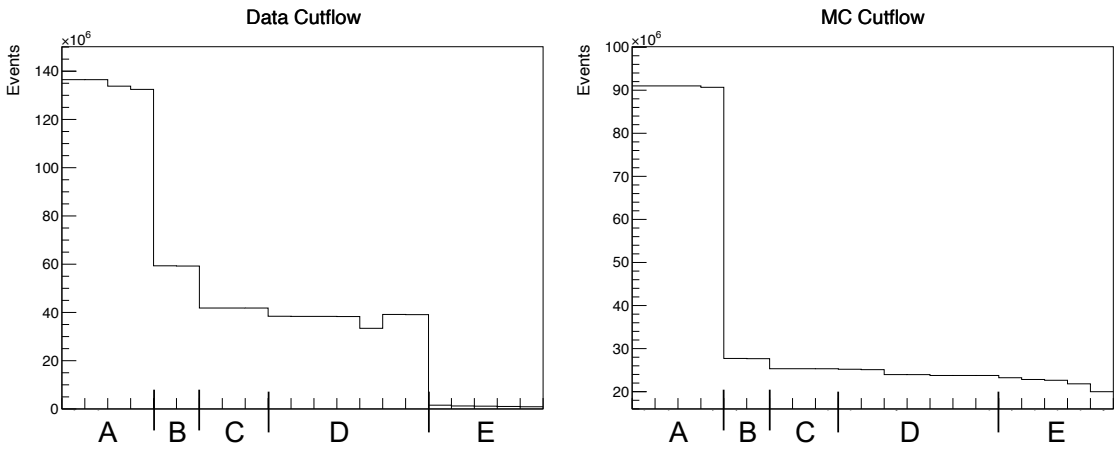

Figure 4.8: WTP $W \to e\nu$ event selection cuts in data (left) and MC (right). The histograms show the total number of events and the reduction in the number of events caused by each step of event selection. The first bin in each histogram is the total number of initial events. For clarity, each x-axis is labeled with the letters A – E. Cuts corresponding to these bin sections are the same for data and MC and are listed in Table 4.1. The most significant event reduction is due to the WTP trigger (bin 5). The other most significant cuts are the $E_{\mathrm{T}}^{\mathrm{miss}}$ requirement (bin 7), the $p_{\mathrm{T}}^{\mathrm{probe}}$ requirement (bin 10, only significant in data), the m_{T}^{W} requirement (bin 14, only significant in data and plotted out of order due to historical reasons), and the electron identification working point cuts (final 5 bins). Overall, large differences between data and MC are seen, especially for the electron identification cuts. This is because the MC is the background-free $W \to e\nu$ signal, while the data contains many background events.

Label	Bins	Cut Description
A	1 – 4	Requirements for good ATLAS data
B	5 – 6	**WTP trigger**; at least 1 electron in event
C	7 – 9	$E_{\mathrm{T}}^{\mathrm{miss}}$ **cut**; fiducial volume cuts
D	10 – 16	$p_{\mathrm{T}}^{\mathrm{probe}}$ **cut**; other probe and track quality cuts; m_{T}^{W} **cut** (bin 14)
E	17 – 21	Electron identification working points: *Very Loose* to *Tight*

Table 4.1: WTP event selection cut descriptions corresponding to the x-axes of Figure 4.8. The most significant cuts are bolded.

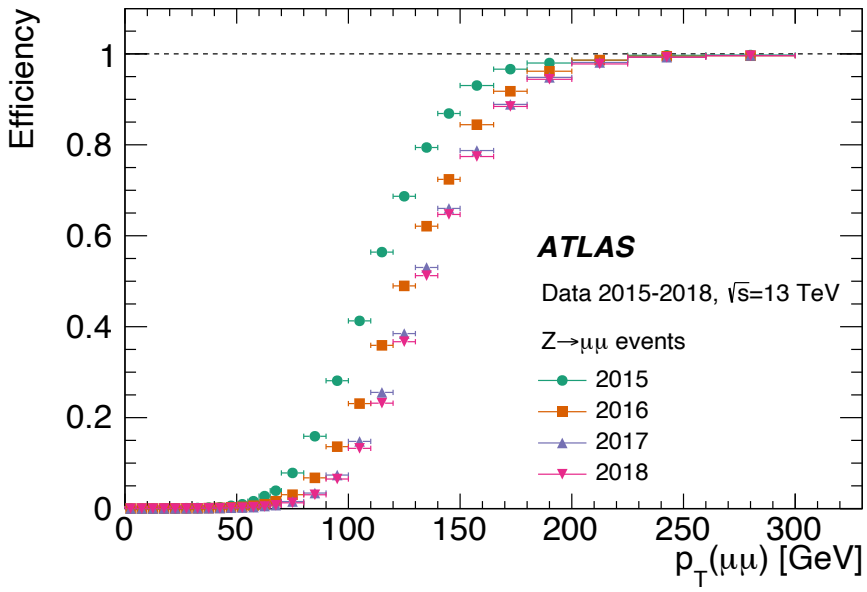

Figure 4.9: Full-chain (L1 and HLT) $E_{\mathrm{T}}^{\mathrm{miss}}$ trigger efficiencies for each year in Run 2 as a function of $p_{\mathrm{T}}^{\mu\mu}$. $E_{\mathrm{T}}^{\mathrm{miss}}$ trigger efficiencies are measured with $Z \to \mu^+\mu^-$ events. Statistical uncertainties are shown [52].

only approximately 10% efficient at a p_{T} of approximately 100 GeV, which is already greater than the p_{T} region of interest for WTP. The results do not directly transfer over to WTP because these trigger efficiencies were measured with $Z \to \mu^+\mu^-$ events, but it is clear that the trigger turn-on curve is at a p_{T} that is too large to work well for WTP and would remove roughly 90% of events, identifying the need for a dedicated WTP trigger.

In order to measure the approximate efficiency of the WTP trigger within the low-μ dataset and TP framework, the number of events passing the trigger was recorded and plotted (similar to a cutflow histogram). The WTP trigger was also compared to each of the relevant low-μ triggers as outlined in Section 4.3.2. The results are shown in Figures 4.10 (data) and 4.11 (MC). The WTP trigger is about 45% efficient in data and about 30% efficient in MC. Importantly, these histograms (Figs. 4.10 and 4.11) clearly show that the WTP trigger significantly increases the number of events selected compared to the two standard $E_{\mathrm{T}}^{\mathrm{miss}}$ triggers, which when used together are only about 15% efficient in data and about 10% efficient in MC (consistent with the prediction based on Figure 4.9). Therefore, all other things being equal, the

WTP trigger increases the number of good WTP events by about a factor of three compared to the $E_{\mathrm{T}}^{\mathrm{miss}}$ triggers. The final trigger included in the plots is the single electron trigger for comparison. This trigger is not used in event selection because the only relevant electron in $W \to e\nu$ is the probe electron; triggering on this electron would bias the WTP studies since this trigger already requires the electron to pass the *Loose* working point.

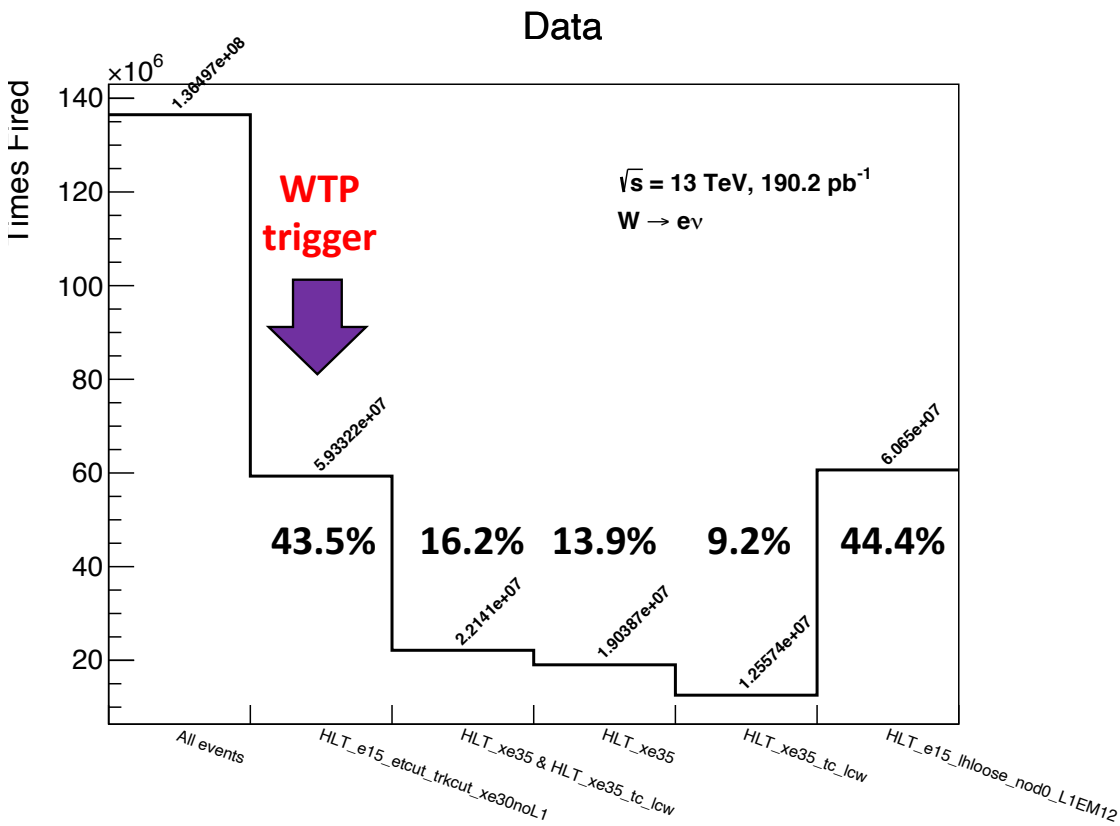

Figure 4.10: Number of events that fired each low-μ trigger in data. The total number of events is shown for each bin, including the total number of initial events in the first bin. Each trigger along the x-axis corresponds to a trigger listed in Section 4.3.2.

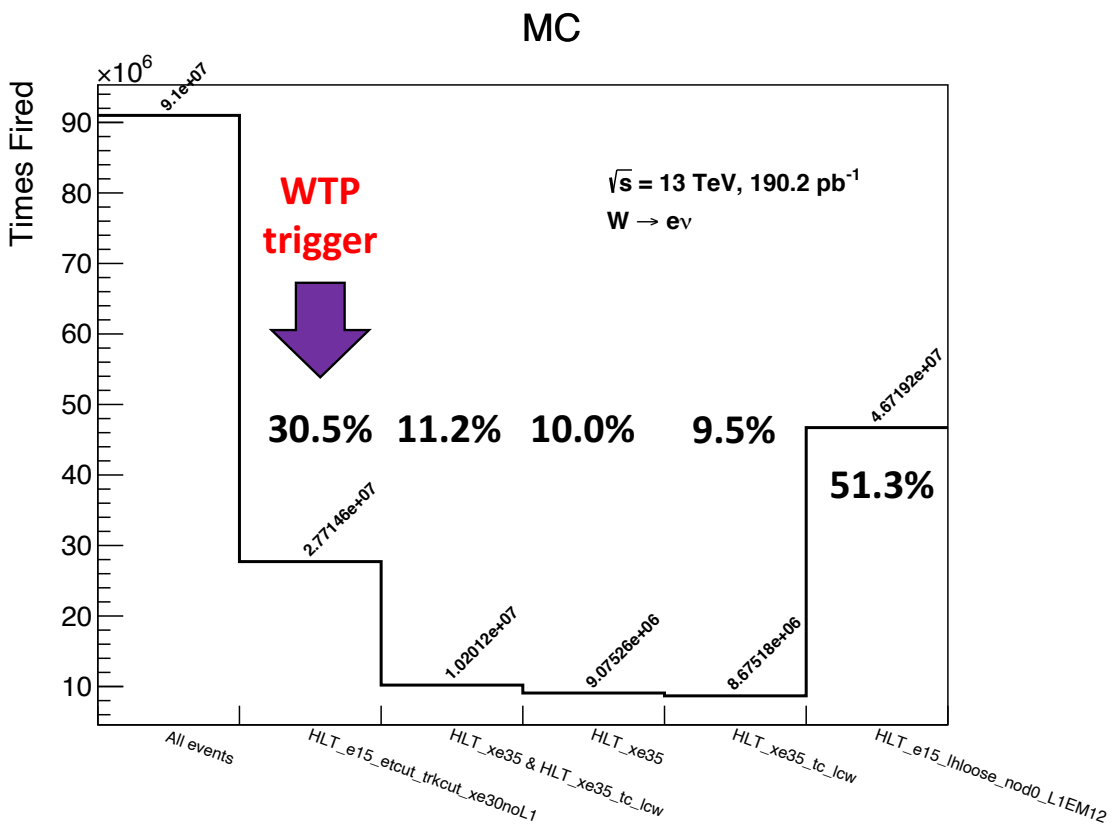

Figure 4.11: Number of events that fired each low-μ trigger in MC. The total number of events is shown for each bin, including the total number of initial events in the first bin. Each trigger along the x-axis corresponds to a trigger listed in Section 4.3.2.

4.3.4 Kinematic Distributions

The most important kinematic distributions to examine for WTP are $E_{\mathrm{T}}^{\mathrm{miss}}$ and m_{T}^{W}. To measure these distributions, the data and MC samples were run through the WTP framework. Histograms of these distributions containing all events passing the event selection (not including the final electron identification working point selection) are plotted. The data and MC distributions of these variables can be compared after event selection to help estimate the amount of remaining background contamination in the data, and to show the improvements coming from the implementation of the WTP trigger. Other interesting and useful distributions for further event selection improvement and background subtraction were also examined and are shown, including $\Delta\phi$, the azimuthal angle between $E_{\mathrm{T}}^{\mathrm{miss}}$ and the probe electron, and p_{T}^{e}, the probe electron transverse momentum distribution.

Figure 4.12 compares the normalized $E_{\mathrm{T}}^{\mathrm{miss}}$ distributions after event selection in data and MC. The MC distribution peaks at $m_W/2$ as expected, while the data distribution's peak is shifted to the left due to background contamination. There is a minor but noticeable change in the data distribution when the WTP trigger is used compared to the $E_{\mathrm{T}}^{\mathrm{miss}}$ trigger, especially in the high $E_{\mathrm{T}}^{\mathrm{miss}}$ tail which appears to be more similar to the corresponding MC distribution after the WTP addition. A sample $p_{\mathrm{T}}^{\mathrm{miss}}$ distribution at $\sqrt{s} = 7$ TeV is shown in Figure 4.13 for comparison to the WTP results.

Figure 4.14 compares the normalized m_{T}^{W} distributions after event selection in data and MC. There is a clear change in the shape of the data distribution when the $E_{\mathrm{T}}^{\mathrm{miss}}$ trigger is replaced by the WTP trigger, suggesting that the WTP trigger removes background events much more efficiently, since this distribution is now closer to the sample m_{T}^{W} distribution at $\sqrt{s} = 7$ TeV shown in Figure 4.15.

Figure 4.16 shows histograms of the two-dimensional normalized MC distributions for $E_{\mathrm{T}}^{\mathrm{miss}}$ and m_{T}^{W} as a function of the discriminating isolation variable $E_{\mathrm{T}}^{\mathrm{cone}}$. As expected, both distributions are well-isolated (most events near $E_{\mathrm{T}}^{\mathrm{cone}} = 0$) because the MCs provide clean $W \to e\nu$ signals that are free of background events. Figures 4.17 and 4.18 show histograms of the two-dimensional normalized data distributions for $E_{\mathrm{T}}^{\mathrm{miss}}$ (Fig. 4.17) and m_{T}^{W} (Fig. 4.18) as a function of the discriminating isolation variable $E_{\mathrm{T}}^{\mathrm{cone}}$. A one-dimensional projection onto the isolation axis is also shown

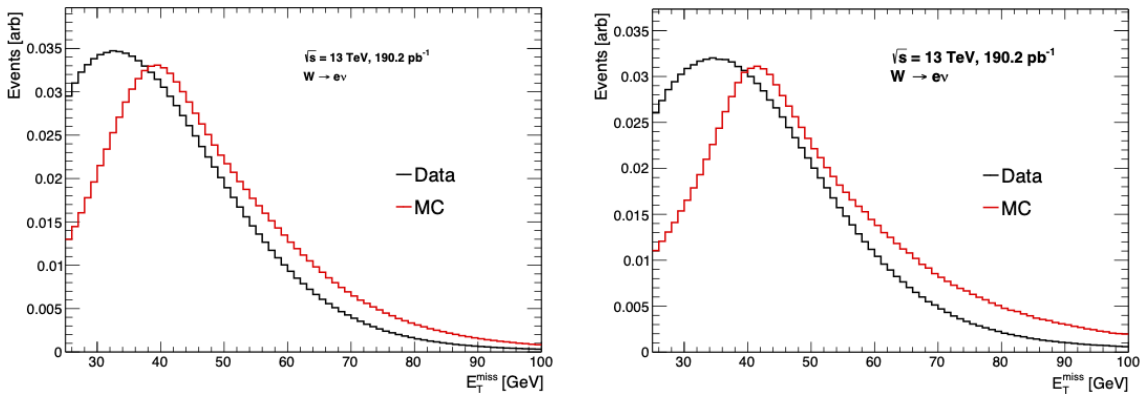

(a) WTP Trigger (b) $E_{\mathrm{T}}^{\mathrm{miss}}$ Triggers

Figure 4.12: Normalized $E_{\mathrm{T}}^{\mathrm{miss}}$ distributions after WTP event selection in data (black) and MC (red). The histogram on the left shows the distributions with the event selection that includes the WTP trigger, while the plot on the right is based on the old $E_{\mathrm{T}}^{\mathrm{miss}}$ triggering. The y-axis is in arbitrary normalized units.

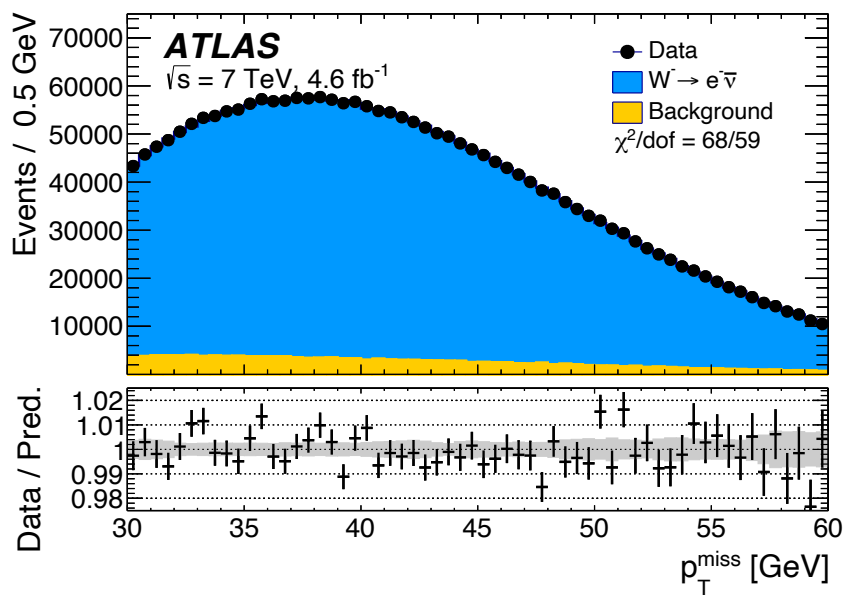

Figure 4.13: Sample $p_{\mathrm{T}}^{\mathrm{miss}}$ (roughly equal to $E_{\mathrm{T}}^{\mathrm{miss}}$) distribution in $W^- \to e^-\bar{\nu}$ events as measured by ATLAS during Run 1. The data (black circles) includes the $W^- \to e^-\bar{\nu}$ signal (blue) and the remaining background (yellow). The lower panel shows the data-to-MC prediction ratio; the error bars show the statistical uncertainty and the grey band shows the systematic uncertainty [54].

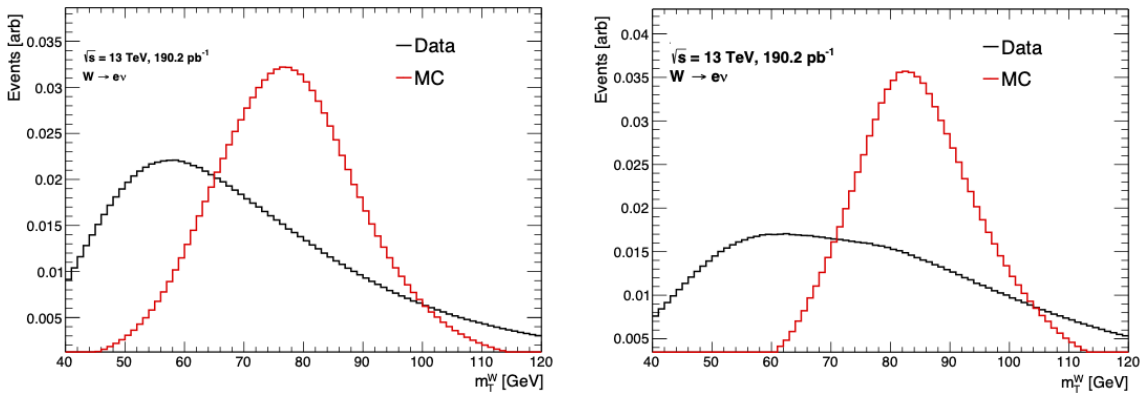

(a) WTP Trigger (b) $E_{\mathrm{T}}^{\mathrm{miss}}$ Triggers

Figure 4.14: Normalized m_{T}^{W} distributions after WTP event selection in data (black) and MC (red). The histogram on the left shows the distributions with the event selection that includes the WTP trigger, while the plot on the right is based on the old $E_{\mathrm{T}}^{\mathrm{miss}}$ triggering. The y-axis is in arbitrary normalized units.

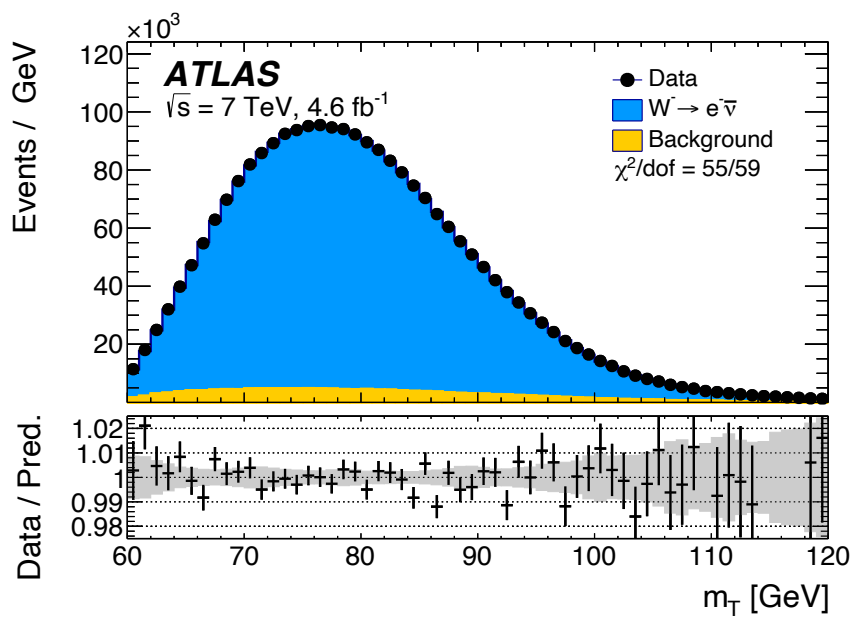

Figure 4.15: Sample m_{T}^{W} distribution in $W^{-} \to e^{-}\bar{\nu}$ events as measured by ATLAS during Run 1. The data (black circles) includes the $W^{-} \to e^{-}\bar{\nu}$ signal (blue) and the remaining background (yellow). The lower panel shows the data-to-MC prediction ratio; the error bars show the statistical uncertainty and the grey band shows the systematic uncertainty [54].

for each. Here, the clear contrast between the background-free MC signal and the background-dominated data can be seen. The data are still dominated by background events even after event selection, but both data figures show that two distinct isolation peaks exist, separated by an approximate boundary of $E_{\mathrm{T}}^{\mathrm{cone}}/25$ GeV $= 0.1$. This $E_{\mathrm{T}}^{\mathrm{cone}}$ distribution allows us to use this isolation value of 0.1 to define the **signal region** (SR) as $E_{\mathrm{T}}^{\mathrm{cone}}/25$ GeV ≤ 0.1 and the **control region** (CR) as $E_{\mathrm{T}}^{\mathrm{cone}}/25$ GeV $>$ 0.1. One major challenge is removing the remaining background events that still contaminate the signal region.

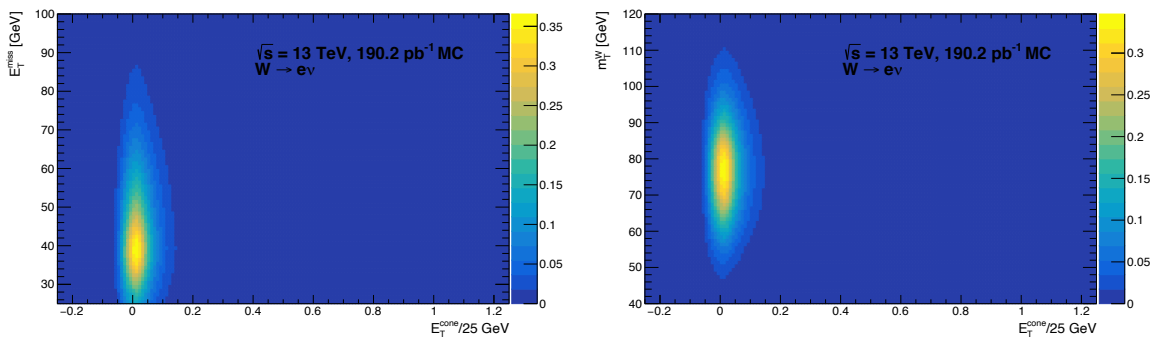

(a) MC $E_{\mathrm{T}}^{\mathrm{miss}}$ isolation (b) MC m_{T}^{W} isolation

Figure 4.16: 2D normalized histograms of MC distributions after event selection. The left plot shows the $E_{\mathrm{T}}^{\mathrm{miss}}$ distribution as a function of the isolation discrimination variable $E_{\mathrm{T}}^{\mathrm{cone}}$, while the right plot shows the m_{T}^{W} distribution as a function of $E_{\mathrm{T}}^{\mathrm{cone}}$. The z-axis shows the normalized magnitude of each bin.

Figure 4.19 shows the normalized $\Delta\phi$ distributions for data (black) and MC (red). The distribution strongly peaks at $\sim \pi$ as expected. This is a two-body decay, so in order for momentum to be conserved, the neutrino and electron from the decaying W boson must be emitted back-to-back in the rest frame of the W boson. This observable is not currently used in event selection but could potentially be useful to help reduce backgrounds.

Figure 4.20 shows the normalized probe electron p_{T}^{e} distributions for data (black) and MC (red). Similar to the $\Delta\phi$ distribution in Figure 4.19, the MC distribution peaks at $m_W/2$ due to momentum conservation. The data still contain many lower p_{T} background events, shifting its p_{T}^{e} distribution to lower values of p_{T}.

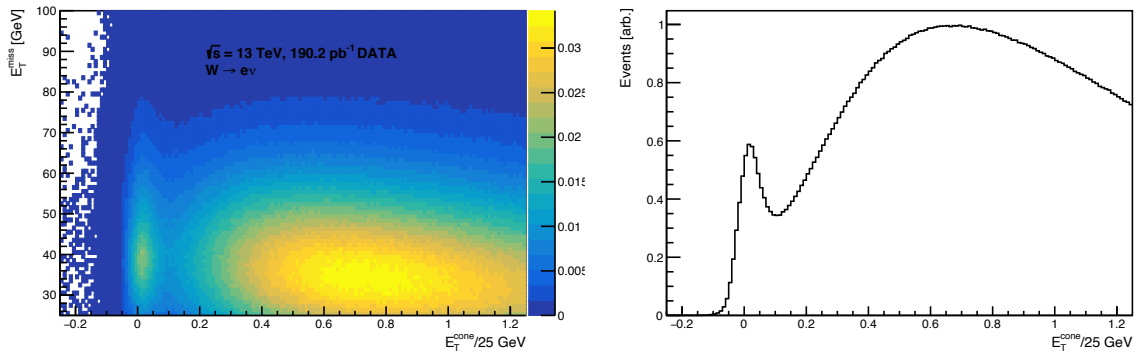

Figure 4.17: Histograms depicting the $E_{\mathrm{T}}^{\mathrm{miss}}$ and isolation distributions in data after event selection. The left plot shows a 2D normalized histogram of $E_{\mathrm{T}}^{\mathrm{miss}}$ as a function of $E_{\mathrm{T}}^{\mathrm{cone}}$, while the right plot shows a 1D histogram of a projection onto the isolation axis.

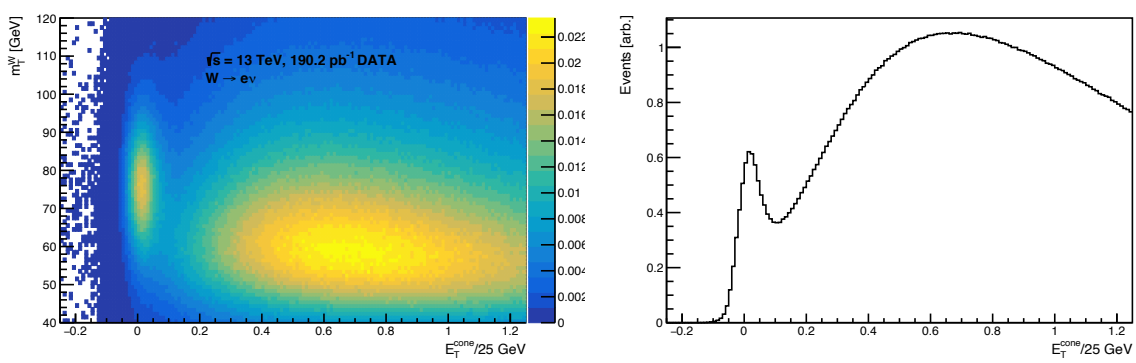

Figure 4.18: Histograms depicting the m_{T}^{W} and isolation distributions in data after event selection. The left plot shows a 2D normalized histogram of m_{T}^{W} as a function of $E_{\mathrm{T}}^{\mathrm{cone}}$, while the right plot shows a 1D histogram of a projection onto the isolation axis.

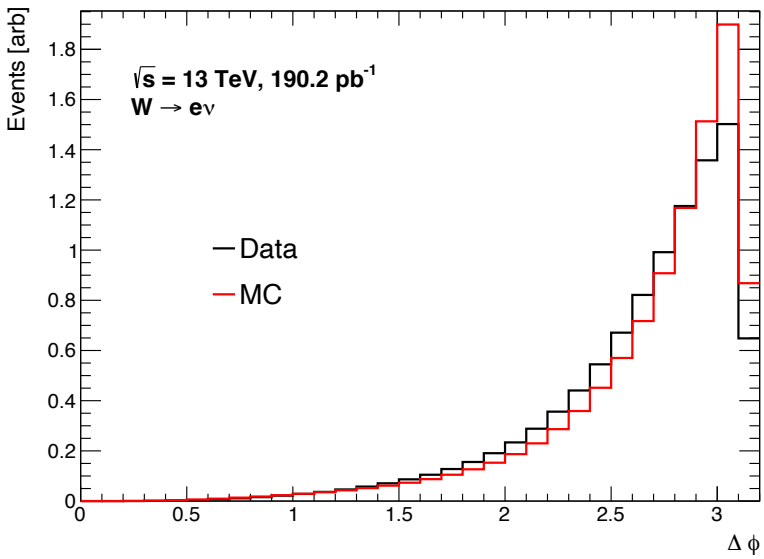

Figure 4.19: Normalized $\Delta\phi$ distribution in data (black) and MC (red). $\Delta\phi$ is the azimuthal angular difference between ϕ^e and ϕ^{miss}.

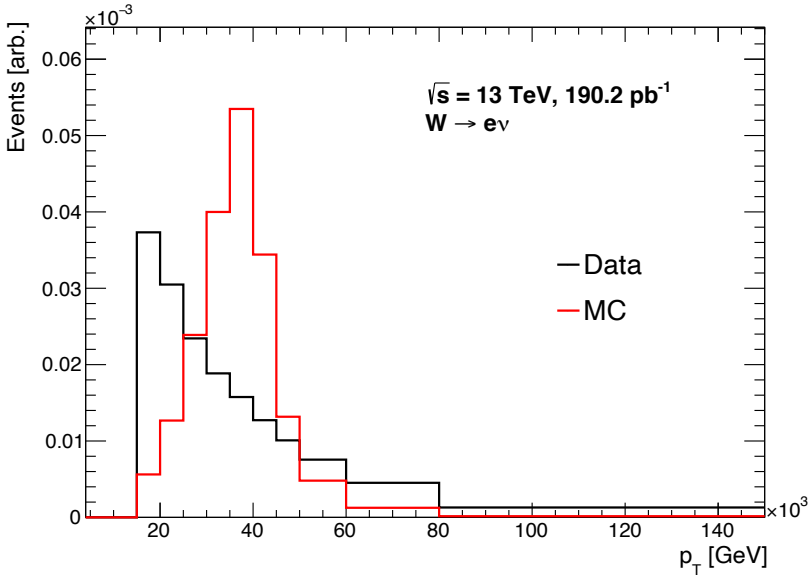

Figure 4.20: Normalized probe electron transverse momentum (p_{T}^e) distribution in data (black) and MC (red).

4.3.5 Control Plots

To ensure accurate and precise TP results, as has been mentioned several times in this section, background modelling is vital. We use *control plots* – plots showing distributions with relaxed or inverted event selection – to better understand background modelling and to compare data to MC. For WTP, we can expand our general efficiency Equation (4.4) by defining the type of probe electrons we are referring to and explaining what is meant by the total number of probes:

$$\epsilon = \frac{N^{\text{pass}}_{\text{sig,SR}}}{N^{\text{pass}}_{\text{sig,SR}} + N^{\text{fail}}_{\text{sig,SR}}}, \tag{4.14}$$

where N still refers to the number of probes, *pass* or *fail* refers to the specific working point (ex. *Tight*), and *sig* refers to signal electrons. In each case, the total number of signal probes N_{sig} is calculated using a background template that is scaled to the CR distribution and then subtracted from the SR as defined by the equation

$$N_{\text{sig}} = N^{\text{iso}\leq 0.1}_{\text{data}} - N^{\text{iso}\leq 0.1}_{\text{bkg}} \frac{N^{\text{iso}>0.1}_{\text{data}}}{N^{\text{iso}>0.1}_{\text{bkg}}}, \tag{4.15}$$

where *iso* refers to $E_{\text{T}}^{\text{cone}}/25$ GeV, so iso ≤ 0.1 is the SR and iso > 0.1 is the CR, and *bkg* refers to the background template that is used. Control plots show a version of the efficiency Equation (4.14), including both the SR and CR requirement:

$$\epsilon = \frac{N^{\text{pass}}_{\text{sig}}}{N^{\text{pass}}_{\text{sig}} + N^{\text{fail}}_{\text{sig}}}, \tag{4.16}$$

where again the word 'probe' is omitted for clarity.

The background template that was chosen for these WTP studies simply requires the electron candidates in an event to fail the *Loose* working point. Future work should include the study of alternate background templates with additional requirements. For example, in ZTP, a similar background template requires that the two electrons in a $Z \to e^+e^-$ decay have the same sign (an impossible decay physically given that the Z boson is neutral, but possible in the detector if the wrong electron is identified) in addition to the 'fail *Loose*' requirement. It is impossible to require this same-sign cut for WTP since there is only one final-state electron.

Control-region plots are presented beginning in Figure 4.21, which show the probes in data (black) compared to the MC signal (pink) and the background as estimated by the background template (blue). The numerator and denominator refer to the numerator and denominator of Equation (4.16). One control plot is generated for each bin of η and E_{T}. The histogram binning for WTP for η and E_{T} is defined as follows:

- $|\eta| = [0.0, 0.1, 0.6, 0.8, 1.15, 1.37, 1.52, 1.81, 2.01, 2.37, 2.47]$
- $E_{\mathrm{T}} = [15, 20, 25, 30, 35, 40, 45, 50, 60, 80, 150]$ GeV.

In order to increase statistics, the sign dependence of η is removed for WTP since positive and negative η regions are expected to give similar results (the detector is forward-backward symmetric). The binning is chosen for historical reasons and is consistent for TP measurements in ATLAS, since consistent recommendations must be given across different analyses as has been discussed. The η binning is chosen to maximize statistics while defining different portions of the detector that correspond to various subdetector coverage regions. For example, the η bin [1.37, 1.52] is the detector 'crack' region between the barrel and end-cap components.

As can be seen in the sample control plot shown in Figure 4.21, by looking at the blue background in the denominator plot, a large number of background events pass through event selection, making the denominator almost entirely background events. This makes it difficult to model how many background events leak into the signal region. Figure 4.22 shows a sample control plot for ZTP, equivalent to the sample WTP control plot shown in 4.21. Comparing the WTP plot to the ZTP plot, we see the difference in background reduction for ZTP compared to WTP, loosely defining the background-reduction goal in order to make a complete efficiency measurement with WTP. The absolute WTP background-reduction method cannot be as precise as the ZTP background-reduction method due to the lack of the lepton-charge requirement in WTP, however it should be possible to obtain an equivalent relative background reduction due to the order-of-magnitude increase in $W \to e\nu$ events relative to $Z \to e^+e^-$ events.

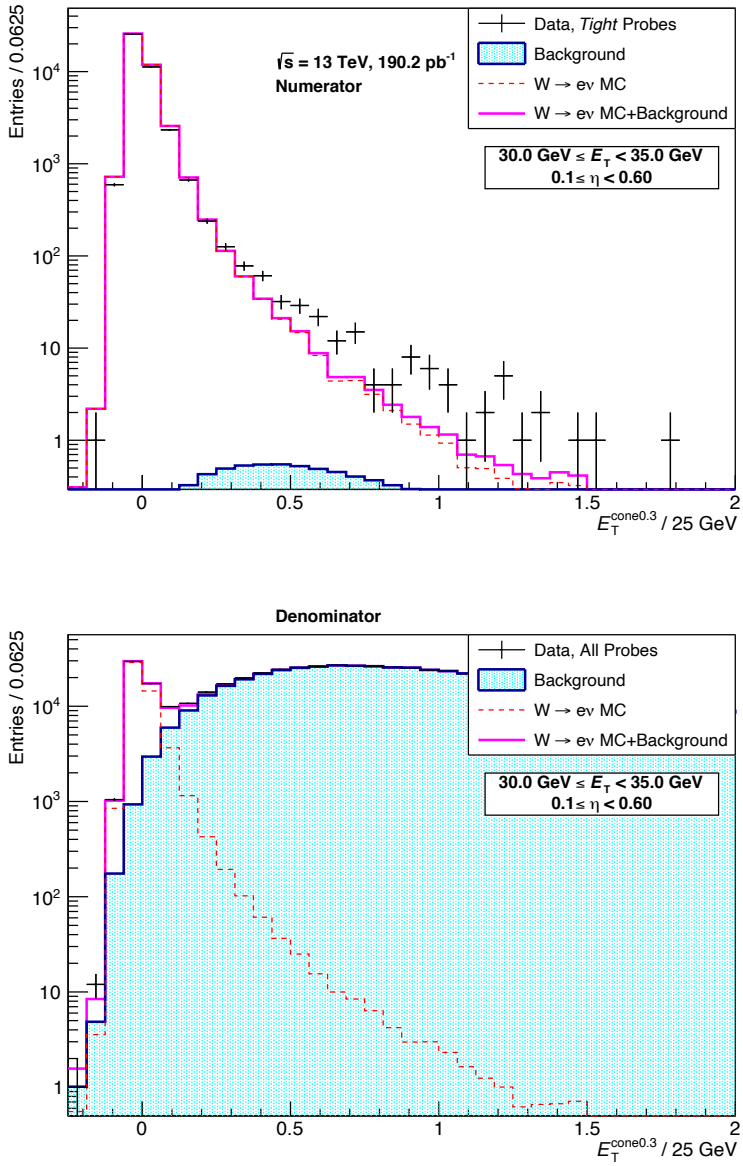

Figure 4.21: WTP control plot showing the total number of probes that pass the *Tight* working point (**Numerator**) compared to the total number of probes (**Denominator**), as defined by the numerator and denominator of Equation (4.16). The data are shown with individual black points and vertical statistical error bars, the total background is shown in blue, the signal MC is shown with a dashed red line, and the background added to the signal MC is shown in pink. The x-axis is the isolation discrimination variable $E_{\mathrm{T}}^{\mathrm{cone}}/25$ GeV, with 0.3 referring to a cone of $\Delta R = 0.3$.

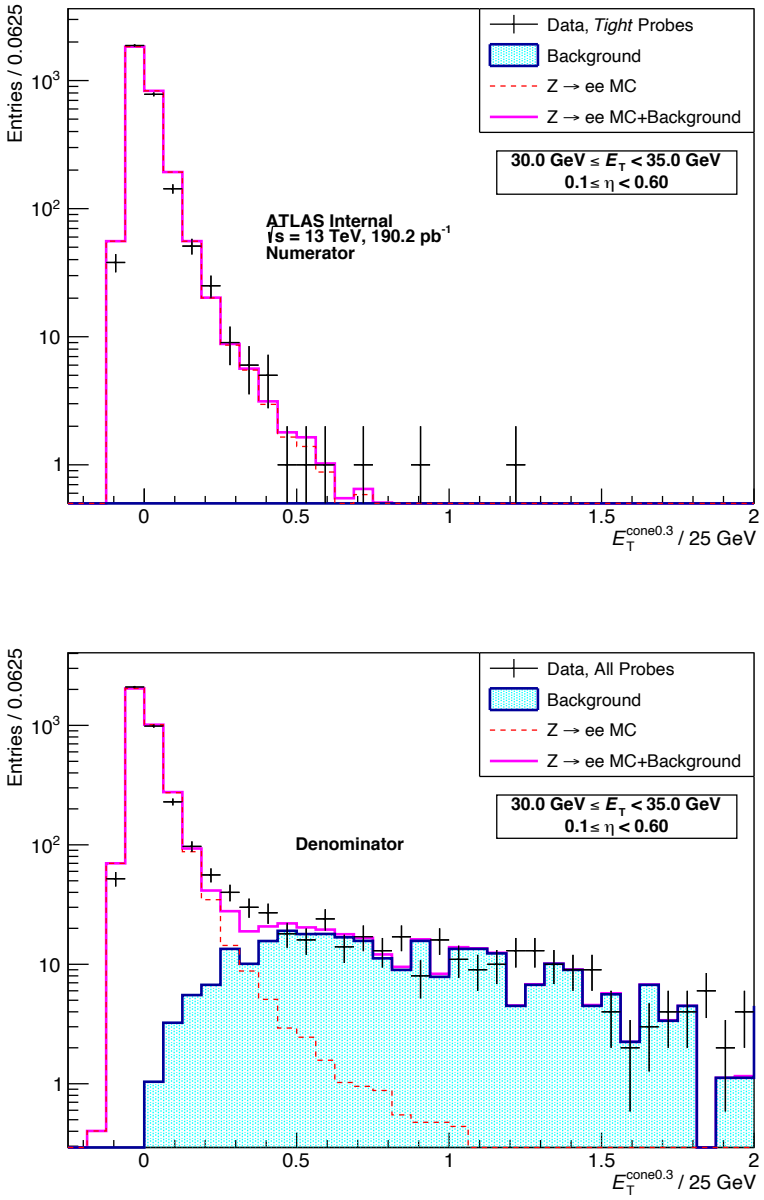

Figure 4.22: ZTP control plot equivalent to the WTP control shown in Figure 4.21.

Despite the fact that the WTP background reduction method itself still needs improvement with a better background template, clear improvement is seen in the data to (MC + background) agreement when using the new WTP trigger compared to the old $E_{\mathrm{T}}^{\mathrm{miss}}$ triggers. Figure 4.23 compares a control plot using the WTP trigger for event selection with a similar control plot where the $E_{\mathrm{T}}^{\mathrm{miss}}$ triggers were used for event selection without changing any other conditions. The data to MC-plus-background ratio is also compared for each control plot numerator. Ideally, the data should be roughly equal to the MC plus background, especially in the high-statistics isolation region of roughly $0.0 < E_{\mathrm{T}}^{\mathrm{cone}}/25\ \mathrm{GeV} < 0.5$, translating to values of approximately unity in the ratio plot. While we do not see values of exactly one, the ratio plot clearly shows once again that the WTP trigger does a better job at removing the background contamination in data relative to the $E_{\mathrm{T}}^{\mathrm{miss}}$ triggers. Note that isolation values below 0.0 can exist, since $E_{\mathrm{T}}^{\mathrm{cone}}$ is based on topo-clusters which can have negative energy clusters.

Figures C.1, C.2 and C.3 in Appendix C show three more examples of the control plot trigger comparison for three different high-statistics E_{T} and η bins. In all cases, the WTP trigger improves the background reduction relative to the $E_{\mathrm{T}}^{\mathrm{miss}}$ triggers.

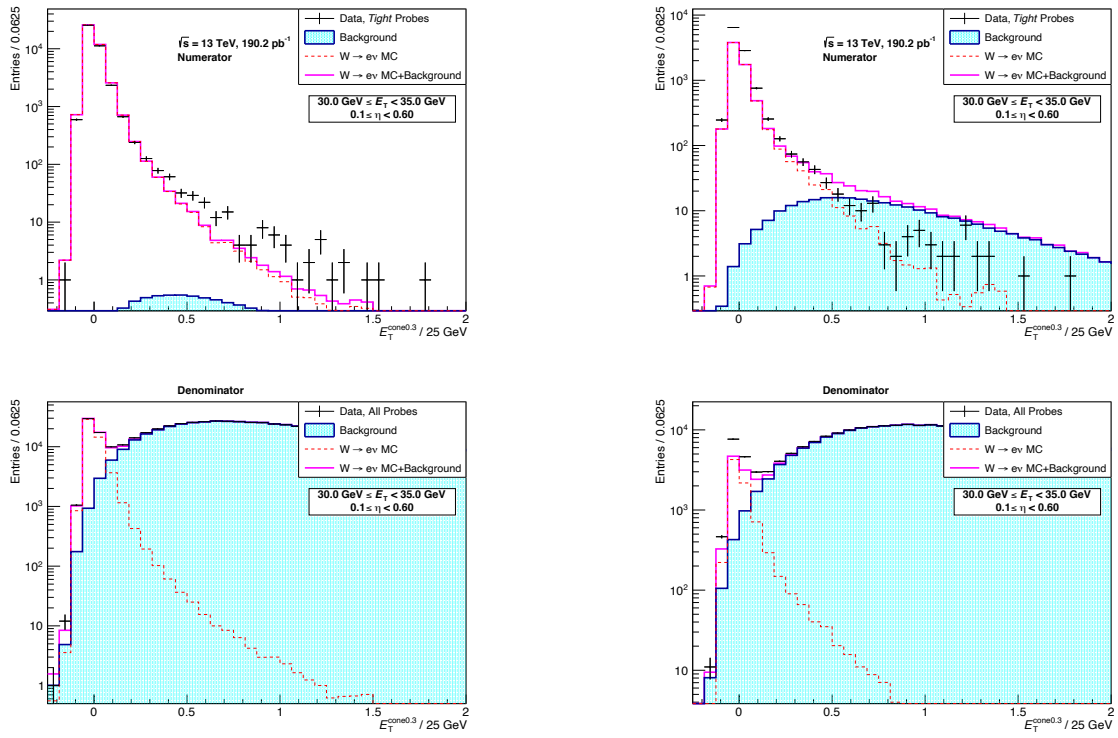

(a) WTP Trigger

(b) $E_{\mathrm{T}}^{\mathrm{miss}}$ Trigger

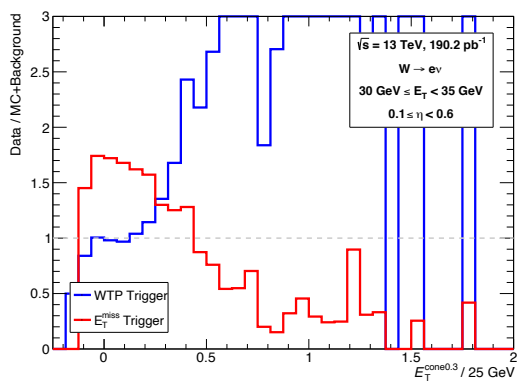

(c) Data/(MC+Background) Ratio

Figure 4.23: Control plot comparison between event selection with the WTP trigger and the $E_{\mathrm{T}}^{\mathrm{miss}}$ triggers for WTP. Each control plot contains all events in the $E_{\mathrm{T}} = [30, 35]$ GeV and $\eta = [0.1, 0.6]$ bin. The top left plot is the same control plot as shown in Fig. 4.21; the top right plot is the same but with the $E_{\mathrm{T}}^{\mathrm{miss}}$ triggers for event selection. The bottom plot shows the Data to (MC + Background) numerator ratio (black data divided by the pink line). A gray line is shown at a value of 1 to guide the eye.

4.3.6 Efficiencies & Scale Factors

The WTP efficiencies and scale factors shown here are still preliminary, because further background reduction in data is required in order to measure accurate efficiencies in data. However, the MC electron ID efficiencies are correct and show that the WTP framework works well, and initial tests of the data efficiencies and therefore corresponding scale factors can also be measured. As a reminder, efficiencies are measured using Equation (4.4). The efficiency that WTP measures is ϵ_{id} from Eq. (4.1) in both data and MC. These efficiencies are then combined into scale factors (Eq. (4.3)) that will eventually become part of the next ATLAS software release recommendations. In the following results histograms, the working point is always *Medium* or *Tight*.

Figure 4.24 shows measured MC efficiencies as a function of η and Figure 4.25 shows measured MC efficiencies as a function of E_{T} for both *Medium* and *Tight* probes. Each histogram compares electron identification efficiencies measured using the following:

- low-μ WTP using the WTP trigger (black);
- low-μ WTP using the $E_{\text{T}}^{\text{miss}}$ triggers (blue);
- Current electron identification recommendations for high-μ as measured using ZTP isolation method, following the process outlined in Ref. [47]. This work was done by a PhD student named Xiaowen Su from Hefei University (red).

Sample efficiencies are compared for the highest-statistics E_{T} and η bins: ($30 \leq E_{\text{T}} < 35$ GeV) and ($0.1 \leq \eta < 0.6$). The current low-μ nominal MC efficiencies (the efficiencies that are used for low-μ analyses) are also included in the histograms in green where possible (only the MC efficiencies for *Medium* probes are available). The errors shown in the histograms are statistical only. An additional high-statistics bin is shown in Appendix C for MC efficiencies as a function of η (Figure C.4) and E_{T} (Figure C.5).

Generally, the largest MC efficiency is measured when using low-μ WTP with the WTP trigger, once again proving its efficacy. Figure 4.26 shows sample data efficiency measurements with WTP. While the measured MC efficiencies for low-μ WTP with the WTP trigger look reasonable and have high efficiency, the data

efficiencies are relatively low because not enough background has been removed. This lack of background removal can clearly be seen in the efficiency versus E_{T} histogram (4.26b), where both WTP results trace out the $E_{\mathrm{T}}^{\mathrm{miss}}$ distribution like what is shown in Figure 4.12 instead of the expected efficiency curve. The scale factors that correspond to this data measurement are shown in Figure 4.27 for completeness, displaying that the WTP framework works well.

4.3.7 Conclusions & Next Steps

W boson tag-and-probe has been implemented and tested with low-μ data. The WTP trigger was tested for the first time, and was shown to have improved results compared to the previous $E_{\mathrm{T}}^{\mathrm{miss}}$ triggers in terms of event selection and background reduction. This trigger will now remain in the ATLAS trigger menu for Run 3 for future WTP and $W \to e\nu$ studies.

Electron efficiencies and scale factors are important components of all analyses that need to measure electrons. Their measurement methods must be continually improved in order to increase precision and keep up to date with the most recent ATLAS software releases. These efficiencies and scale factors can now be measured with WTP, in-situ with low-μ data, and the framework works well. MC efficiencies are measured with high precision. However, background reduction in data must be improved before efficiency and scale factor measurements can be used in analyses. That being said, the initial results are promising. Steps to improve background reduction include implementing hadronic recoil as the $E_{\mathrm{T}}^{\mathrm{miss}}$ object of choice, and creating optimized background templates for WTP.

After the completion of my qualification task, I continued working on the WTP project to follow up with some of these next steps. The software package to calculate hadronic recoil was implemented within the WTP framework, but consistency issues between the old TP software and the new hadronic recoil software meant that the two frameworks were not fully compatible. During my QT, a new TP framework was being built, and it is just becoming operational now. The WTP software is ready to be ported to the new TP framework, which should allow the hadronic recoil package to be run smoothly so that the WTP studies can be completed.

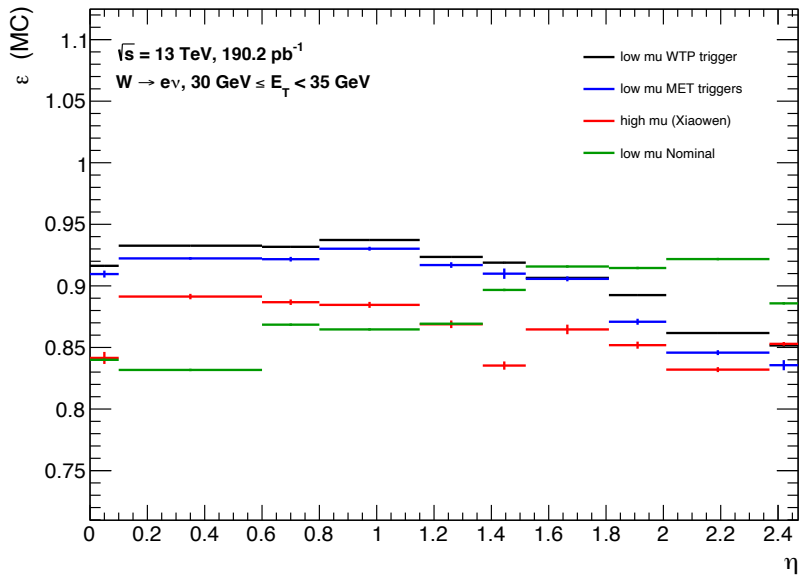

(a) *Medium* Probes

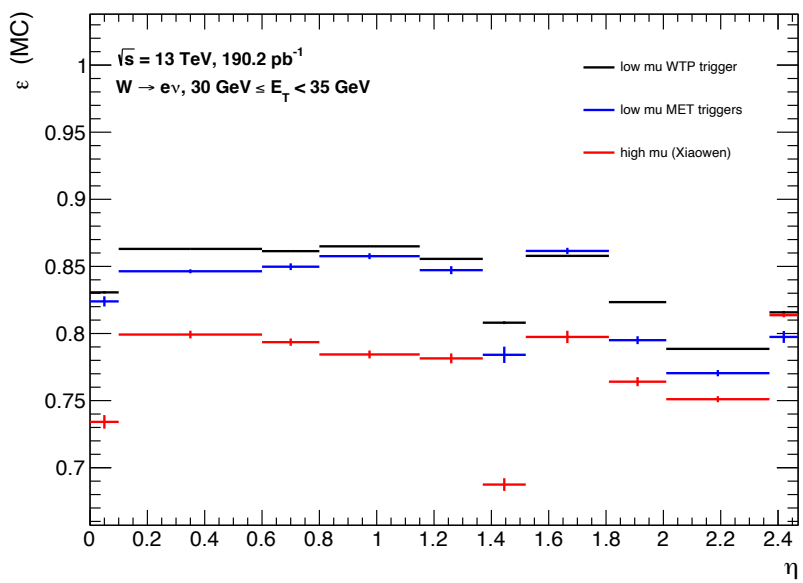

(b) *Tight* Probes

Figure 4.24: MC efficiency as a function of η for *Medium* (top) and *Tight* probes (bottom) for the highest-statistics E_{T} bin ($E_{\mathrm{T}} = [30, 35]$ GeV). For *Medium* probes, four different efficiencies are compared: low-μ WTP results using the WTP trigger (black), low-μ WTP results using the $E_{\mathrm{T}}^{\mathrm{miss}}$ triggers (blue, 'MET' = $E_{\mathrm{T}}^{\mathrm{miss}}$), high-$\mu$ ZTP results (red), and the current nominal low-μ efficiencies that have been extrapolated from high-μ results (green). The nominal low-μ efficiencies are not available for *Tight* probes.

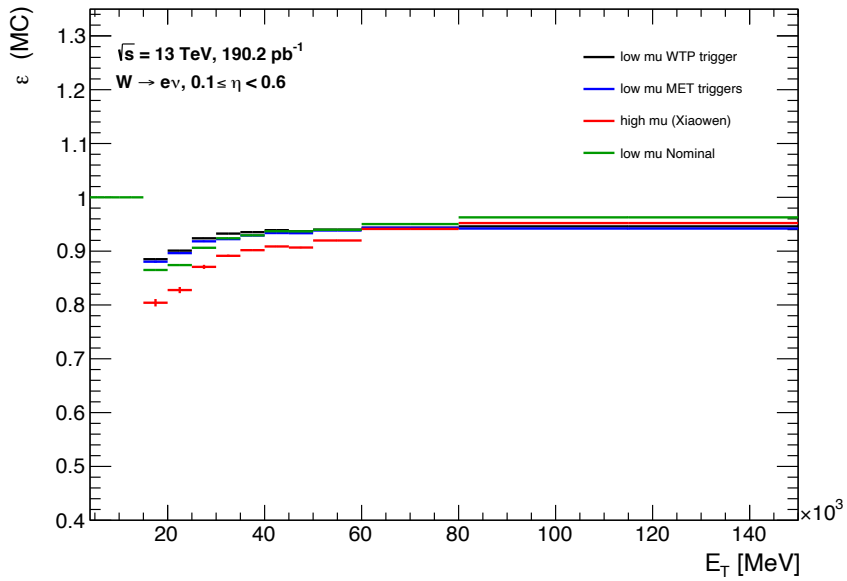

(a) *Medium* Probes

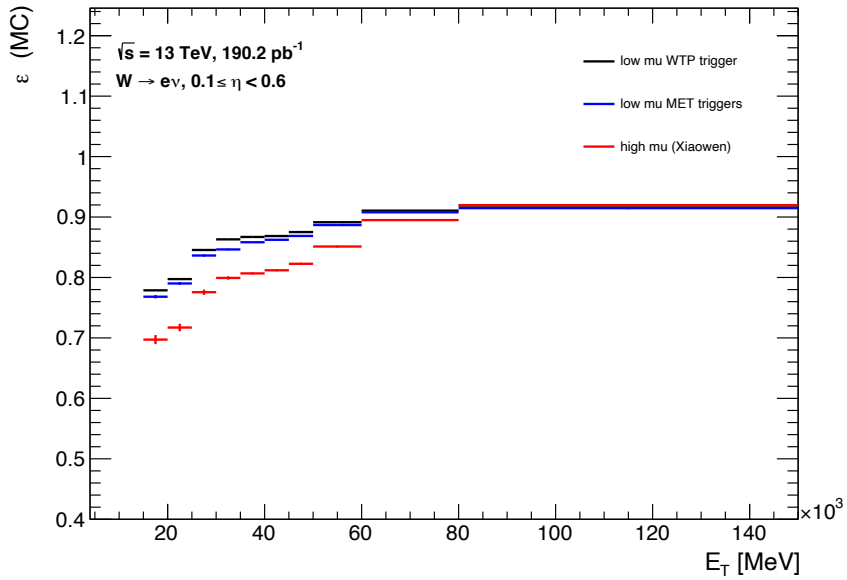

(b) *Tight* Probes

Figure 4.25: MC efficiency as a function of E_{T} for *Medium* (top) and *Tight* probes (bottom) for the highest-statistics η bin ($\eta = [0.1, 0.6]$). For *Medium* probes, four different efficiencies are compared: low-μ WTP results using the WTP trigger (black), low-μ WTP results using the $E_{\mathrm{T}}^{\mathrm{miss}}$ triggers (blue, 'MET' = $E_{\mathrm{T}}^{\mathrm{miss}}$), high-$\mu$ ZTP results (red), and the current nominal low-μ efficiencies that have been extrapolated from high-μ results (green). The nominal low-μ efficiencies are not available for *Tight* probes.

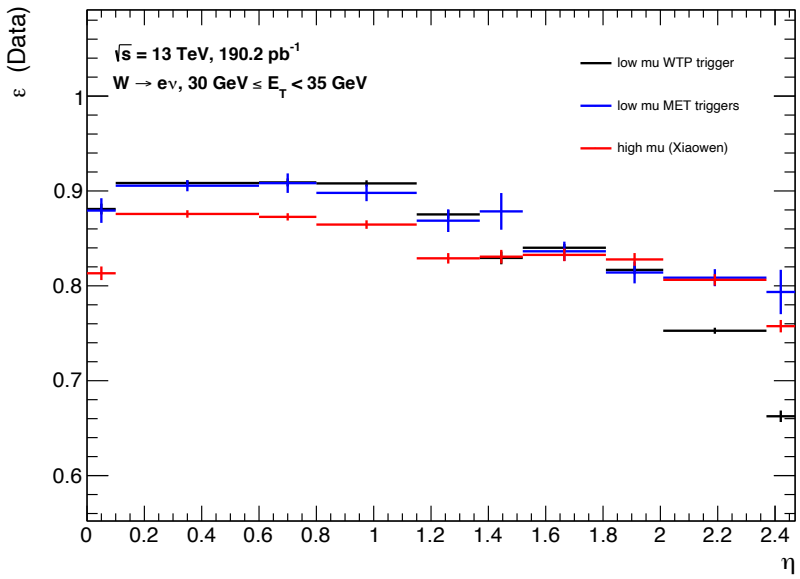

(a) $E_{\mathrm{T}} = [30, 35]$ GeV

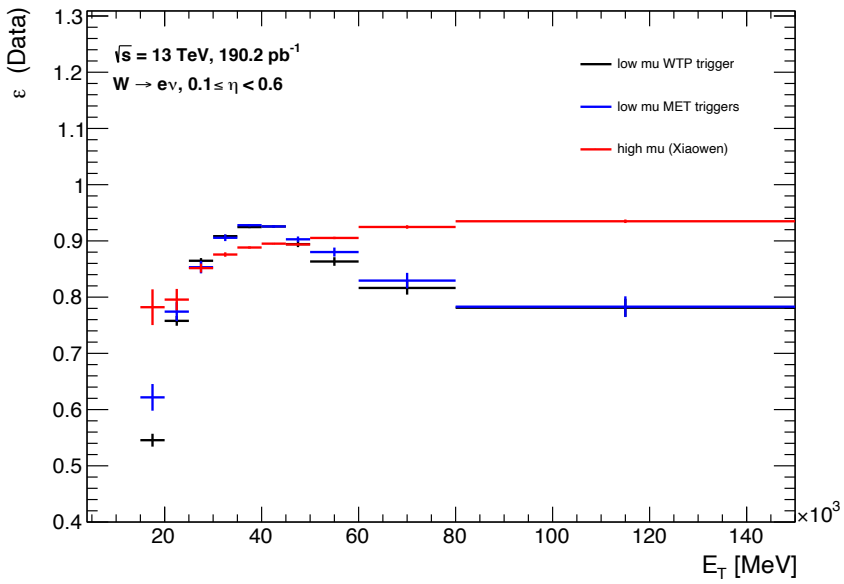

(b) $\eta = [0.1, 0.6]$

Figure 4.26: Sample data efficiency as a function of η (top) and E_{T} (bottom) for *Medium* probes. Three different efficiencies are compared: low-μ WTP results using the WTP trigger (black), low-μ WTP results using the $E_{\mathrm{T}}^{\mathrm{miss}}$ triggers (blue, 'MET' $= E_{\mathrm{T}}^{\mathrm{miss}}$), and high-$\mu$ ZTP results (red).

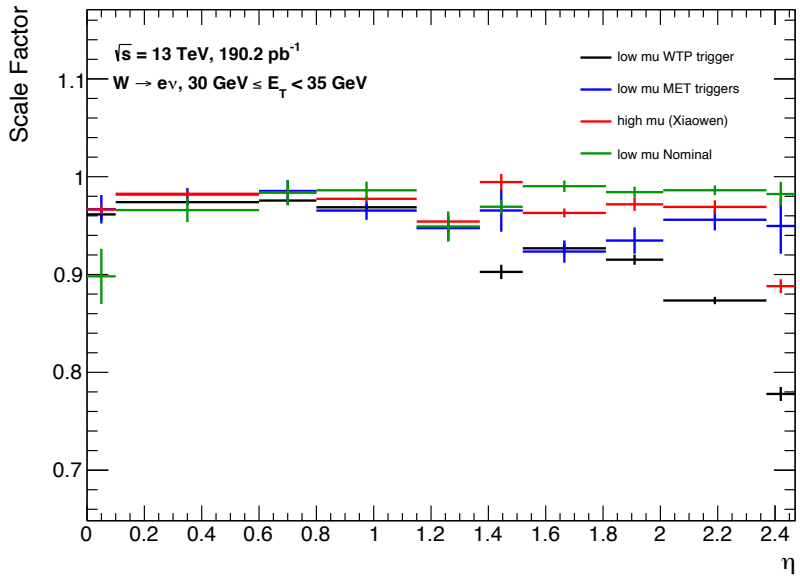

(a) $E_{\mathrm{T}} = [30, 35]$ GeV

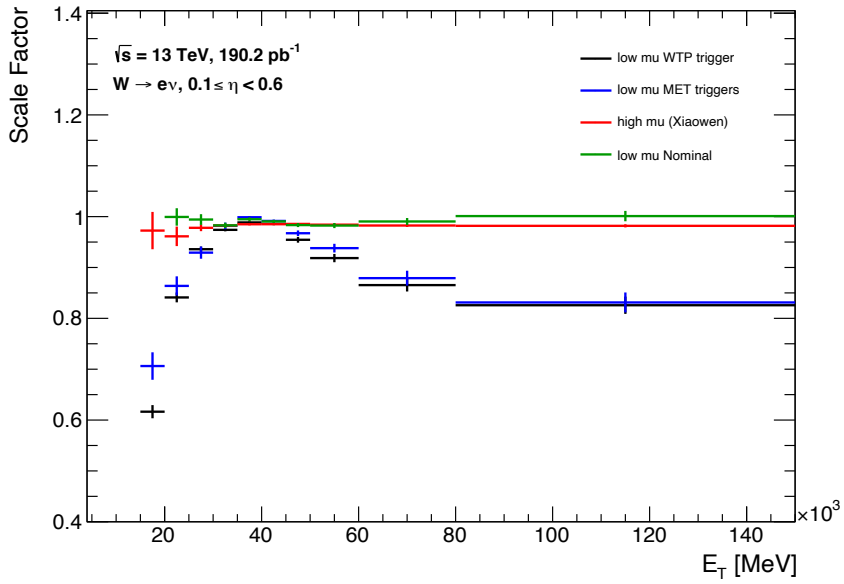

(b) $\eta = [0.1, 0.6]$

Figure 4.27: Sample scale factors as a function of η (top) and E_{T} (bottom) for *Medium* probes. Four different SFs are compared: low-μ WTP results using the WTP trigger (black), low-μ WTP results using the $E_{\mathrm{T}}^{\mathrm{miss}}$ triggers (blue, 'MET' = $E_{\mathrm{T}}^{\mathrm{miss}}$), high-$\mu$ ZTP results (red), and the current nominal low-μ SFs that have been extrapolated from high-μ results (green).

Chapter 5

Measurements of p_{T}^{W} and p_{T}^{Z} in Drell-Yan Processes

Transverse momentum (p_{T}) is a common variable to measure in ATLAS analyses, as was introduced in Chapter 3 with Equation (3.8). p_{T} ranges from being a variable that is only used to select particles in specific kinematic regions, to being the principle observable in an analysis. To leading order in the QCD perturbative expansion, one might expect there to be no net p_{T} in a process such as $pp \to W/Z \to ll$ simply due to momentum conservation. However, we know that there is always at least a small net p_{T} when measuring final-state particles created from LHC p-p collisions. This is true for two reasons:

1. We know that we mostly do not actually collide protons at the LHC, but partons within the proton. The total momentum of the proton is known and is equal to the sum of the momentum of the partons within it. These partons have their own internal momentum that could very well have an intrinsic transverse component, leading to a slightly non-zero initial p_{T} when this parton is involved in a collision that creates a W or Z boson.

2. Higher order (NLO and beyond) processes contribute to these interactions. These processes lead to a p_{T} distribution that can be measured and can have not just small, but high-p_{T} contributions.

Therefore, $p_{\mathrm{T}}^{W,Z}$ measurements are inherently interesting because they provide information about the internal structure of the proton as well as beyond-leading-order

QCD and electroweak processes. The core analysis presented in this thesis is a measurement of the p_{T} spectrum of both W and Z bosons in Drell-Yan processes using low-pileup data at centre-of-mass energies ($\sqrt{s}$) of both 5 and 13 TeV. This chapter motivates the importance of this measurement in more detail, providing the experimental background for the analysis results that are presented in the following chapters.

5.1 p_{T}^{W} as an Input to m_W

The mass of the W boson is a vital parameter in the SM. Described by electroweak theory, to lowest order, m_W can be written as a function of m_Z, the fine-structure constant, α, and the Fermi constant, G_μ. The fine-structure constant is a dimensionless quantity that quantifies the strength of the electromagnetic interaction – effectively a dimensionless version of the electric charge e. It is defined as:

$$\alpha = \frac{e^2}{4\pi\epsilon_0\hbar c}, \tag{5.1}$$

where ϵ_0 is the permittivity of free space, $\hbar$ is the Planck constant, and c is the speed of light. The Fermi constant quantifies the strength of the weak interaction. Using these variables, m_W is written as:

$$m_W^2\left(1 - \frac{m_W^2}{m_Z^2}\right) = \frac{\pi\alpha}{\sqrt{2}G_\mu}(1 + \Delta r), \tag{5.2}$$

where Δr is the placeholder term for higher-order corrections, including the top quark and Higgs boson masses, but also potential corrections from interactions beyond the SM [54, 55]. The precision of m_W is the limiting factor in Equation (5.2) for testing the consistency of the SM. The most recent SM theoretical predictions of m_W are $m_W = 80358 \pm 8$ MeV [56] and $m_W = 80362 \pm 8$ MeV [57], marking 8 MeV as the goal for experimental precision. In comparison, the uncertainty on the Z boson SM prediction is 0.3 MeV [7].

Experimentally, the world average of m_W is $m_W = 80379 \pm 12$ MeV [7], which combines measurements by the ALEPH, DELPHI, L3, and OPAL collaborations at LEP [58–61] and the CDF and D0 detectors at the Tevatron [62–64], along with the

recent ATLAS measurement [54]. These measurement combinations, as well as the SM prediction (the "Electroweak Fit"), are summarized in Figure 5.1.

The SM does not directly predict the masses of the Z boson or W boson; it only relates these parameters through Equation (5.2). Measurements must be inserted into this equation in order to make predictions for its other parameters. This is why it is often stated that the prediction for m_W (and other electroweak parameters) comes from an 'electroweak fit'. The key parameters from Eq. (5.2) that have been measured are m_Z, m_W and the masses of the top quark, m_t, and Higgs boson, m_H (both hidden within the Δr term). The combination of the SM prediction and precisely-measured observables accurately constrained m_t and m_H before they were directly measured. As more of these observables are measured with increased precision, each individual observable can itself be further constrained by the global fit. At the same time, theoretical precision is being increased as calculations that predict higher order terms contained in Δr improve. Fitting packages like Gfitter [56] and HEPfit [57] perform these global fits, which become the SM prediction for these electroweak observables.

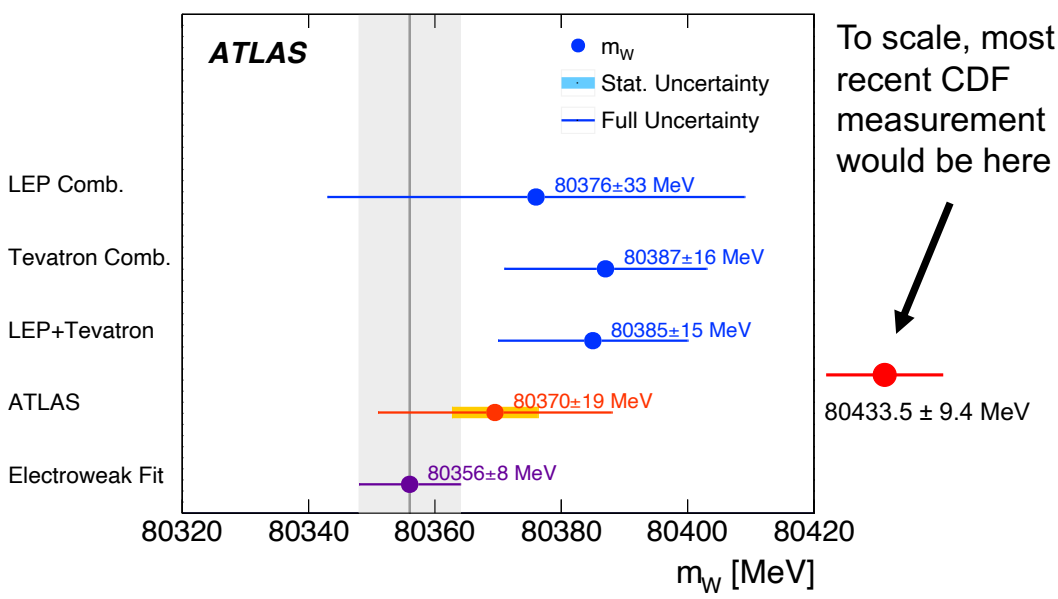

Figure 5.1: Summary of recent m_W measurements at LEP, the Tevatron, and ATLAS, along with the SM prediction (Electroweak Fit). m_W on the x-axis is reported in units of MeV. The vertical grey band shows the theoretical uncertainty [54]. The recent CDF m_W measurement [65] has been added by hand.

Figure 5.1 shows that potential tension exists between the SM prediction and some of the best experimental measurements. The current limiting factor in resolving this tension is the uncertainty on the experimental m_W measurement, particularly the systematic uncertainty, as can be seen by the orange statistical uncertainty bar in the ATLAS measurement compared to the full uncertainty line. Therefore, a higher-precision m_W measurement is needed. Specifically for the ATLAS measurement, the two largest sources of uncertainty on the m_W measurement are both systematic uncertainties: the QCD uncertainty ($\delta m_w = 8.3$ MeV), and the PDF uncertainty ($\delta m_w = 9.2$ MeV).

An even more recent result by the CDF Collaboration reports a new m_W value of $m_W = 80433.5 \pm 9.4$ MeV – the most precise measurement to date [65]. This measurement is in direct tension with both the ATLAS measurement ($m_W = 80370 \pm 19$ MeV [54]) and the SM prediction (stated above), with a discrepancy of 7σ from the SM prediction, proving that more precision measurements are urgently needed to elucidate this discrepancy. This most recent data point has been manually added to Figure 5.1.

m_W is measured from the Drell-Yan decays $W \to e\nu$ and $W \to \mu\nu$ by fitting templates to the charged lepton transverse momentum, p_{T}^{l}, and the W boson transverse mass, m_{T}^{W}, as was mentioned in the previous chapter (4.3.1). As a reminder, m_{T}^{W} depends on the transverse momentum of the escaping neutrino ($p_{\mathrm{T}}^{\mathrm{miss}}$); $m_T^W = \sqrt{2p_T^l p_T^{\mathrm{miss}}(1-\cos\Delta\phi)}$ (Equation (4.13)). $p_{\mathrm{T}}^{\mathrm{miss}}$ is measured indirectly by measuring p_{T}^{W} with hadronic recoil (u_{T}): $\vec{p}_{\mathrm{T}}^{\mathrm{miss}} = -\left(\vec{u}_{\mathrm{T}} + \vec{p}_{\mathrm{T}}^{l}\right)$ (Equation (4.12)). ATLAS had to use extrapolations from p_{T}^{Z} measurements to insert into m_{T}^{W} instead of measuring p_{T}^{W} directly for its m_W measurement, because no precise p_{T}^{W} measurement existed and u_{T} could not be measured with high-enough precision to make an in-situ p_{T}^{W} measurement without a low-μ dataset (this is further discussed in the next section). The extrapolation from p_{T}^{Z} to p_{T}^{W} greatly contributes to both the QCD and PDF uncertainties on m_W mentioned above. Therefore, a higher-precision p_{T}^{W} measurement leads to an improved m_{T}^{W} measurement, leading to a reduced uncertainty on the m_W measurement.

5.2 p_{T}^{W} Modeling at Low p_{T}

p_{T}^{W} and p_{T}^{Z} are especially difficult quantities to predict at low p_{T} ($p_{\mathrm{T}} < 10$ GeV). This stems from one of the effects of QCD mentioned in Chapter 2 called asymptotic freedom. W and Z bosons are created from interactions of the hadronic material inside the colliding protons from the LHC. Due to asymptotic freedom, the name for the effect that increases (reduces) the strength of QCD interactions as energy decreases (increases), it has so far not been possible to accurately predict QCD interactions at low energies.

When trying to predict $p_{\mathrm{T}}^{W,Z}$ at low p_{T}, the same techniques that provide our most accurate QCD predictions at high energies diverge as $p_{\mathrm{T}}^{W,Z}$ tends to zero. These $p_{\mathrm{T}}^{W,Z}$ predictions are critical for modeling the spectra associated with m_W measurements. At high p_{T}, fixed-order perturbative QCD calculations [66, 67] are used to predict the $p_{\mathrm{T}}^{W,Z}$ spectra. High-p_{T} calculations are based on the principle that the QCD interaction strength g (see Section 2.2.2) decreases as a function of order (and energy), so this small parameter can be used in perturbation theory. More specifically, g is what is known as a running coupling constant, meaning its strength depends on energy (or equivalently momentum). g can be redefined as the running QCD coupling constant α_s:

$$\alpha_s(p^2) = \frac{g^2(p^2)}{4\pi} \propto \ln \frac{M^2}{p^2}, \tag{5.3}$$

where M is the mass of an intermediate particle involved in the interaction, and p is that particle's momentum [3, 4]. When calculating a differential cross section where α_s is important, such as in Drell-Yan processes, there are terms in the cross section that are proportional to $\alpha_s^i \ln^j \frac{M^2}{p_{\mathrm{T}}^2}$, where M and p_{T} are the mass and transverse momentum of the W or Z boson, i is the QCD order of the process, j is the number of radiated partons/jets, and $j \leq 2i$. These terms in the differential cross section are what diverge as p_{T} tends to 0. In order to calculate these terms, a method called resummation must be employed [4]. Resummation still involves summing orders of the interaction, but at low p_{T} due to the logarithmic term, each order of α_s is known as leading log (LL), next-to-leading log (NLL), next-to-next-to-leading log (NNLL), etc. (this is the low-p_{T} analogue of LO, NLO, NNLO, etc.). Calculations that include these low-p_{T} terms are performed, but they are much more difficult to do and therefore

less accurate than the high-p_{T} terms [68]. Parton showers can also be used to simulate this low-p_{T} region [69], but neither method is precise, and it is difficult to model $p_{\mathrm{T}}^{W,Z}$ at low p_{T}.

Figure 5.2 shows an example of this $p_{\mathrm{T}}^{W,Z}$ mismodelling by plotting the W/Z cross-section ratio as a function of $p_{\mathrm{T}}^{W,Z}$ using the Pythia 8 AZ [69, 70] MC and three resummation programs. In order to improve this modelling, data-driven approaches

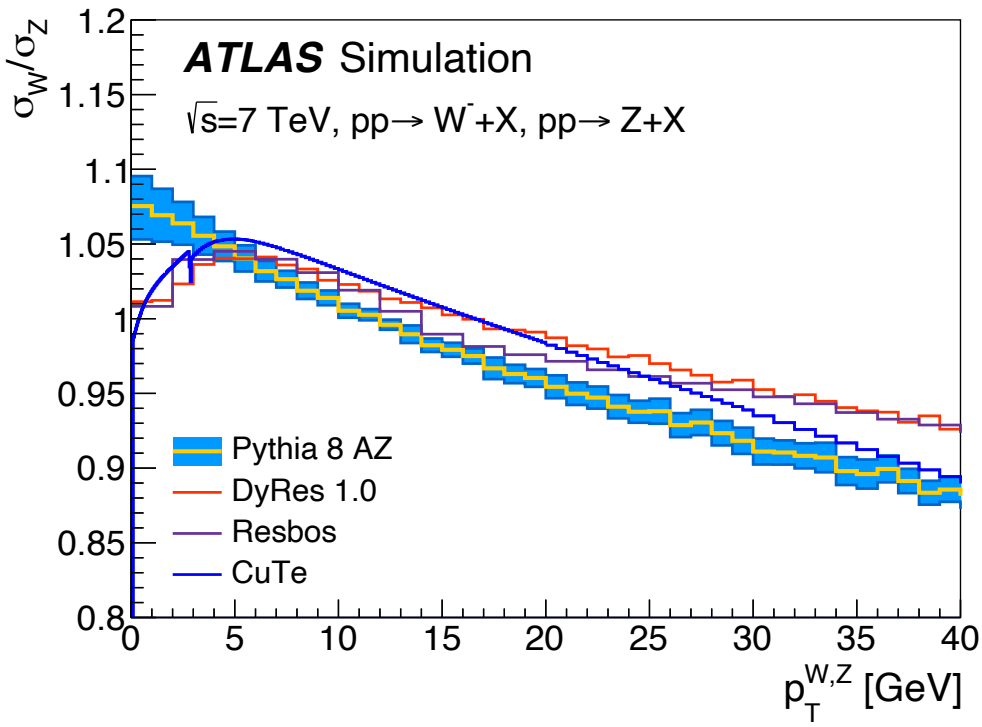

Figure 5.2: Ratio of the normalized W/Z cross sections as a function of p_{T} for W^-, as predicted by the Pythia 8 AZ [69, 70] MC and three resummation programs. The uncertainty band for the Pythia 8 prediction is shown [54].

are used, where high-precision measurements are made at low p_{T} which are then used to tune the inaccurate predictions. This method works well for p_{T}^{Z}. Its shape can be measured across the full p_{T} spectrum to percent-level precision. p_{T}^{W} is much more difficult to measure due to the escaping neutrino, and the necessary percent-level precision at low p_{T} was not obtained for the previous ATLAS m_W measurement [54]. Instead, the p_{T}^{Z} spectrum was used as a proxy to tune the parton shower MC, the aforementioned Pythia 8 AZ, to produce a prediction of the p_{T}^{W} spectrum at a precision of two to three percent. p_{T}^{W} must be directly measured at low p_{T} in order to remove

some of the arbitrary choices required for this tuning and to reduce the uncertainty on the measurement overall. It was shown that a p_{T}^{W} measurement with approximately one percent precision would be needed to discriminate between various physics models at low p_{T} like those shown in Figure 5.2, and to propagate the result to lead to a significantly reduced uncertainty on m_W in a future measurement [54, 71].

5.3 p_{T}^{W} and p_{T}^{Z} at 5 and 13 TeV

The ATLAS low-μ runs were taken at two different centre-of-mass energies: 5 and 13 TeV. This means that two separate high-precision differential measurements can be made for both p_{T}^{W} and p_{T}^{Z} which also helps improve their theoretical predictions, especially by probing their energy dependence.

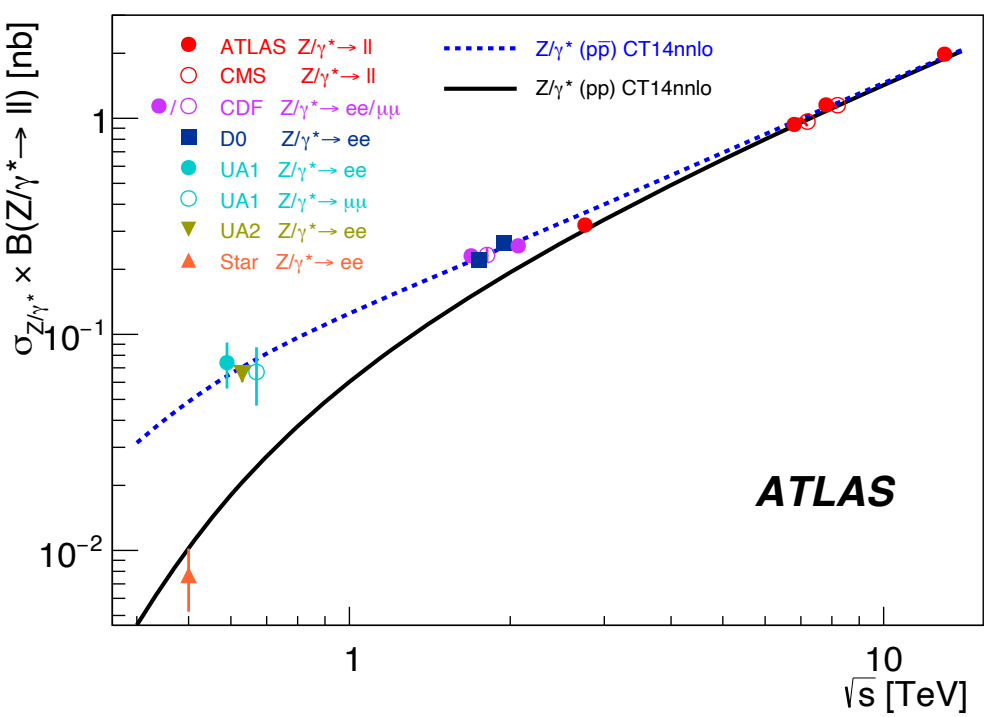

Figure 5.3: Measured $Z/\gamma*$ cross-section times branching ratio ($Z/\gamma* \rightarrow ll$) for p-p and p-$\bar{p}$ collisions as a function of $\sqrt{s}$, compiled for various experiments. All data points are shown together with their total uncertainty. Some data points are slightly staggered for readability. Theoretical predictions are plotted without uncertainties [72].

Additionally, this is the first time that ATLAS has measured p_{T}^{Z} at $\sqrt{s} = 5$ TeV. This low-μ result can then be combined with previous high-μ results at $\sqrt{s} = 2.76$, 7, 8, and 13 TeV to examine the total production cross section as a function of centre-of-mass energy and further improve the tuning of MC predictions. Figure 5.3 shows a sample plot that would be improved by an additional data point at $\sqrt{s} = 5$ TeV.

5.4 p_{T}^{Z} for Calibration

While being an interesting result in its own right, the p_{T}^{Z} measurement is also important for calibration and cross-checking. As part of a separate analysis, ATLAS recently measured p_{T}^{Z} at $\sqrt{s} = 13$ TeV but with high-μ data (see Figure 5.4) [66]. The statistical precision on the p_{T}^{Z} measurement at high-μ is much better than the similar low-μ p_{T}^{Z} result discussed as part of this thesis, but the low-μ p_{T}^{Z} measurement still provides a valuable cross-check.

Measuring p_{T}^{Z} and p_{T}^{W} as part of the same low-μ dataset analysis also allows the Z boson to be used as a proxy to calibrate the W boson p_{T}^{W} measurement. This is because p_{T}^{Z} can be measured with two different observables: the dilepton transverse momentum, p_{T}^{ll}, and the hadronic recoil, u_{T},

$$p_{\mathrm{T}}^{Z} = p_{\mathrm{T}}^{l^+} + p_{\mathrm{T}}^{l^-} = p_{\mathrm{T}}^{ll} = -u_{\mathrm{T}}, \tag{5.4}$$

where l refers to an electron or muon. Since p_{T}^{W} can only be measured with u_{T} due to the escaping neutrino, measuring p_{T}^{Z} with both observables allows for the calibration of u_{T} by showing that the p_{T}^{Z} results obtained with p_{T}^{ll} and u_{T} are consistent. If the p_{T}^{ll} and u_{T} measurements for p_{T}^{Z} are shown to be consistent, it would further support the accuracy of using u_{T} to measure p_{T}^{W}.

p_{T}^{Z} is also an important measurement to make in conjunction with a p_{T}^{W} measurement, because then the ratio of their cross sections can be taken. u_{T} is measured in the same way for both p_{T}^{Z} and p_{T}^{W}, so their respective uncertainties due to hadronic recoil calibration are correlated. When the ratio is taken, these recoil calibration uncertainties therefore cancel, eliminating a dominant uncertainty in the p_{T}^{W} analysis.

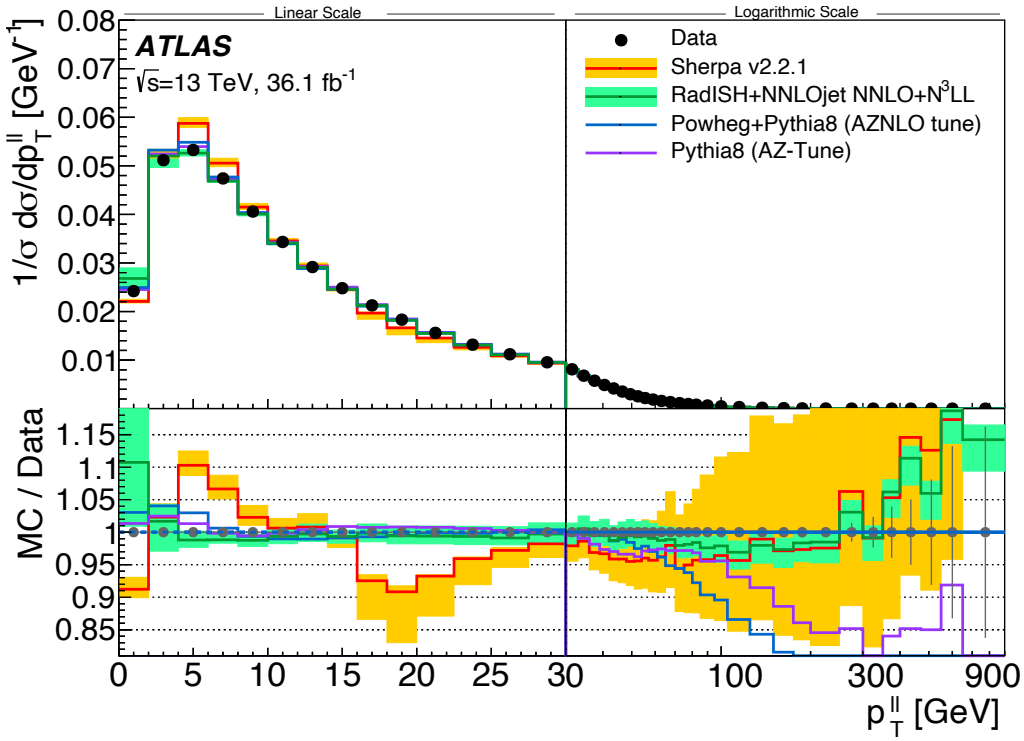

Figure 5.4: Normalized differential cross-section distribution and MC-to-data ratio for $Z \to l^+l^-$ decays as a function of p_{T}^{Z}, measured using the summed dilepton transverse momentum p_{T}^{ll}. The data (black points) are compared to different MC predictions. The data uncertainty is shown as vertical bars, and the MC uncertainties are shown as coloured bands [66].

5.5 Conclusion

Measuring p_{T}^{W} and p_{T}^{Z} to high precision is necessary not only to reduce the uncertainty on a follow-up m_W measurement, but also as important measurements in their own right. p_{T}^{W} must be measured to a precision of order one percent in order to hope to reduce the systematic error bars on a future ATLAS m_W measurement by a factor of two, and p_{T}^{Z} must be measured in conjunction with p_{T}^{W} to achieve this increased precision. p_{T}^{W} and p_{T}^{Z} measurements at low p_{T} are also critical for improving our QCD modelling in this region. In addition to the importance of increasing the precision on these parameters, ATLAS will add a new measurement to its repertoire by measuring p_{T}^{Z} at $\sqrt{s} = 5$ TeV for the first time.

Chapter 6

Unfolding a Dataset

When the ATLAS detector records the raw data from LHC proton-proton collisions, the measurement process has only just begun. Many steps must follow before these data are ready to be presented as a final measurement, which for many ATLAS analyses (including mine) is a cross section. This chapter presents a graphical road map (Section 6.1) for this measurement process, which will also be referred to in Chapters 7 and 8 to highlight my primary analysis contributions. One specific step, **unfolding** the data, is explained in more detail in Section 6.2 since this step was critical to the analysis and was an area where I heavily contributed. In this section, the general unfolding process is explained as it pertains to my analysis and the work that I performed.

6.1 Cross-Section Road Map

Beginning with a dataset and Monte Carlo prediction, many steps are needed before cross-section results can be finalized. Figure 6.1 provides an overview of key steps of this process. All of these steps have been discussed already, or will be discussed in this or upcoming chapters. The steps do not necessarily need to be performed in the exact top-to-bottom order as they are shown, but they tend to roughly follow the order defined by the arrow of time. Most steps require input from both data and MC and are therefore coloured in purple, however some steps are more specific to the data (in blue) or MC (in red).

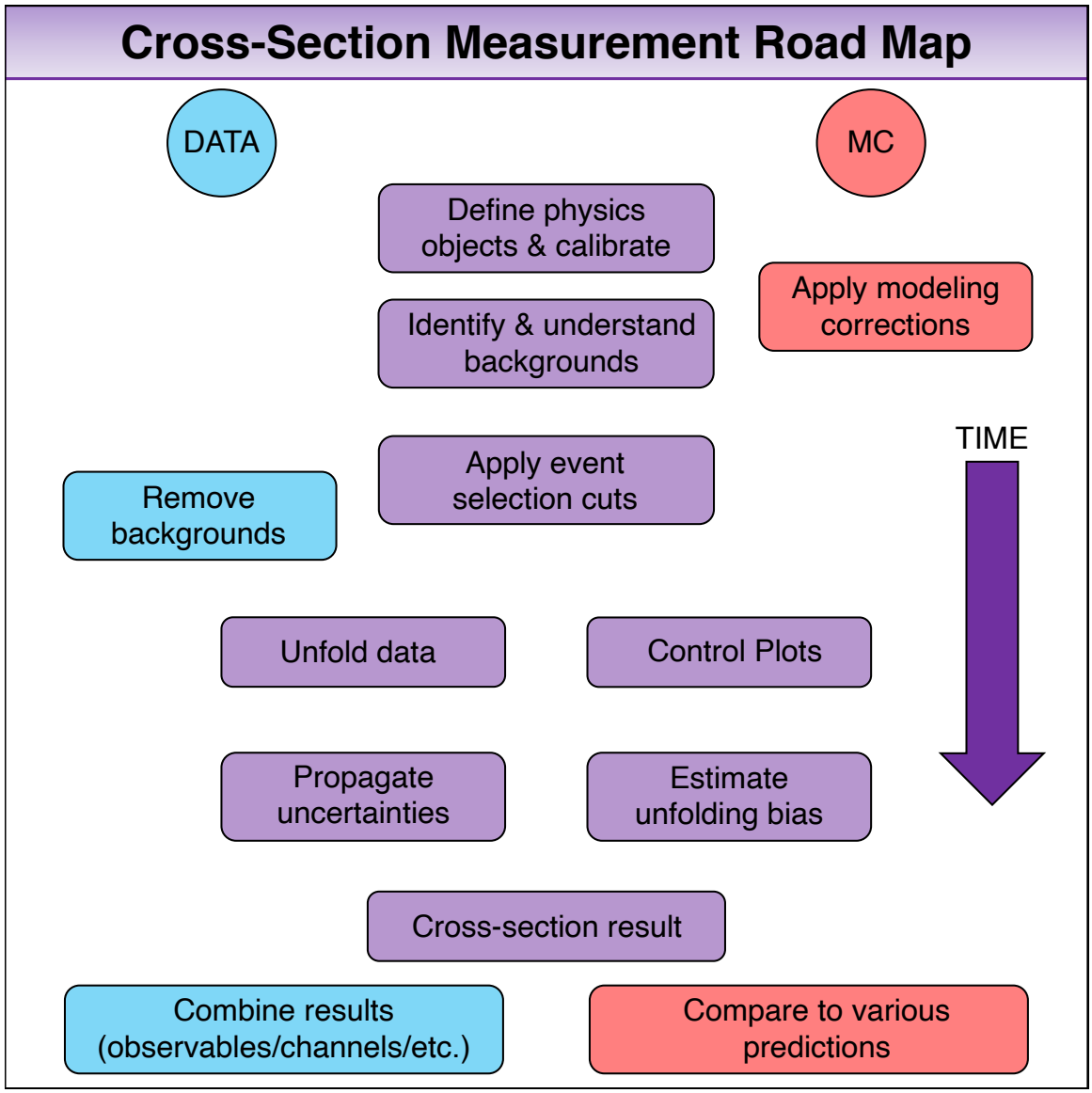

Figure 6.1: General steps of a cross-section measurement, beginning with a dataset and Monte Carlo prediction. Steps are roughly ordered in the direction of time.

6.2 Unfolding

ATLAS (and all particle physics experiments) make measurements of observables that have inherent statistical fluctuations. A quantity must be measured many times in order to produce a distribution: the central value of this distribution becomes the final result, and the spread or standard deviation of the distribution quantifies the statistical uncertainty. However, measurement distributions are distorted due to

experimental limitations, so for experiments like ATLAS, the average value of a measured observable cannot simply be reported as its true value – first these distortions due to experimental limitations must be removed, or *unfolded*. The most common experimental limitation in ATLAS is the sheer amount of material that a particle must cross before it reaches a detection device, causing the particle to lose energy. For example, in the electromagnetic calorimeter, electrons must pass through at least two radiation lengths of material before they are able to be detected. Radiation length, X_0, is the average distance that a high-energy electron can travel in a material before losing all but $1/e$ of its energy, and is a characteristic of the material [26]. Figure 6.2 shows the cumulative amount of material in units of X_0 that an electron must pass through in front of the presampler and accordion sections of the ATLAS electromagnetic calorimeter before it can be detected. X_0 is plotted as a function of $|\eta|$.

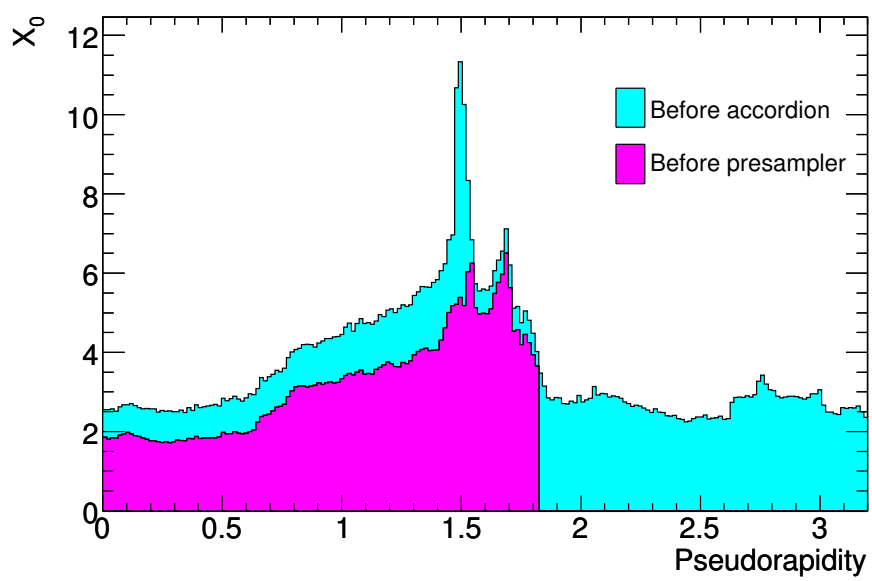

Figure 6.2: Cumulative amount of material in units of X_0 that an electron must pass through in front of the ECAL as a function of $|\eta|$. The ECAL sections are divided into before the presampler (pink) and before the accordion (blue) [28].

Unfolding is the process of estimating the distribution of an observable with a 'perfect' detector and infinite event statistics. A 'perfect' detector must also be defined: when making a measurement, we can refer to the fiducial phase space or the

full phase space. Full phase space means absolute coverage with no restrictions, so no limitations on p_{T} or η. The fiducial phase space is a subset of the full phase space, where detector coverage limits the minimum or maximum measureable p_{T} and the measureable η range. Usually unfolding is performed in two steps: unfolding data to the fiducial phase space of the detector, and then using MC simulations to extrapolate to the full phase space.

6.2.1 What is Unfolding?

To restate the previous definition, unfolding is the process of removing detector effects (and other experimental limitations) from a measurement in order to have a measurement that can be directly compared to a corresponding theoretical prediction that requires no detector information as input, or at least no more information than the fiducial region of the detector (i.e. η, p_{T} range). We can define unfolding mathematically beginning with our measured distribution, $f_{\mathrm{meas}}(x)$. This distribution that we measure (by accumulating a series of events that make up our dataset) is equal to the convolution of the 'true' distribution of the observable of interest, $f_{\mathrm{true}}(y)$, and a response function, $R(x|y)$, that we assume to be known and to depend only on the measuring apparatus i.e. the ATLAS detector. Combining these variables, we get an equation for our measured distribution:

$$f_{\mathrm{meas}}(x) = \int R(x|y) f_{\mathrm{true}}(y) dy. \tag{6.1}$$

Unfolding is the process of solving Eq. (6.1) for $f_{\mathrm{true}}(y)$ by inverting the response function, which amounts to inverting a matrix [73]. In reality, we deal with finite, binned distributions in the form of histograms as opposed to infinite continuous distributions, so the response function R becomes a conditional probability:

$$R_{ij} = P\left(O_i | T_j\right), \tag{6.2}$$

where O_i is the observation in bin i, and T_j is the true value in bin j.

6.2.2 Why Unfold?

Unfolding allows for data to be compared to pure, or *true* theoretical predictions, as opposed to predictions that have been smeared to mimic experimental limitations. In many cases one can include detector information in a theoretical prediction and then use this to create a data-to-MC ratio, which is generally easier to do compared to unfolding. However, if one wants to easily compare a measured distribution to measurements of the same observable made by other experiments and/or other theoretical predictions, it is necessary to unfold. Therefore unfolding also preserves the measurement so that it can be compared to not-yet-completed experiments or predictions that would require different smearing matrices. Additionally, if one wants to tune a MC prediction by fitting parameters to data, the data must be unfolded [74].

Another important aspect is simply that in many cases, only ATLAS researchers know their data well enough to properly unfold it. If the data as recorded were provided to the world, it would not be of much use to anyone (theorists, for example) outside of the ATLAS Collaboration. Unfolding makes the data universally available to the outside world.

When making a measurement, fiducial detector effects must be well-understood in advance and be included as part of an analysis. These effects get treated as event selection cuts so that, for example, unobservable portions of the detector get removed from the analysis phase space. In the event selection, this set of cuts is called *truth-level* (also called fiducial cuts), which are based on detector and data acquisition limitations. Truth-level cuts also provide more specific insight into why unfolding is necessary. For example, as was outlined in Chapter 3, there is a section of the ATLAS calorimeter where two large components come together. The intermediary region between these two components, the barrel and the end-cap, is difficult to use for accurate particle detection because there is less active detecting material and more structural material. The truth-level cuts from the p_{T}^{Z} analysis (discussed in Chapter 7) are shown below.

Truth-Level:

- Event must have fired trigger
- p_{T} above minimum threshold (designed to match the minimum trigger thresh-

old)

- No forward electrons: $|\eta| < 2.47$ (no tracking is available beyond $|\eta| = 2.5$)
- No electrons in barrel/endcap calorimeter crack: $1.37 < |\eta| < 1.52$ (as mentioned above, and can be seen for example in Figure 6.2, showing that there is much more material in this region)

6.2.3 The Unfolding Process

We will now walk through the unfolding process using a sample dataset and MC from the $\sqrt{s} = 13$ TeV $Z \to e^+e^-$ channel of the p_{T}^Z differential cross-section measurement. This dataset will be described in more detail in Chapter 7. We begin with the data that were recorded, shown in Figure 6.3 as number of $Z \to e^+e^-$ events per p_{T}^Z bin. The events in this dataset were required to pass various event selection cuts that were specifically chosen to isolate the $Z \to e^+e^-$ process. In general, cuts like these are called *reconstructed-level* (often abbreviated to reco-level). At this stage, these events measured by the detector have already been calibrated. The reco-level cuts for this channel are shown below.

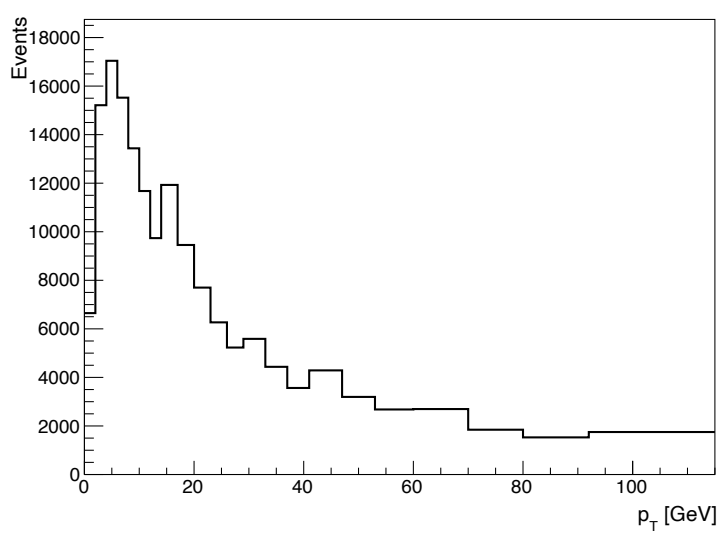

Figure 6.3: Sample reconstructed-level $Z \to e^+e^-$ data. The total number of $Z \to e^+e^-$ events are shown as a function of p_{T}^Z.

Reco-Level:

- Electron-positron pair in final state
- Electron-positron pair matched to corresponding trigger information
- Electrons are isolated from other nearby activity in the detector
- $p_{\mathrm{T}}^{e} > 25$ GeV, to match minimum threshold of the trigger
- $66 < m_{ee} < 116$ GeV, the invariant mass of the two decay leptons, so as to match the mass of a Z boson ($m_Z \approx 91$ GeV)

To summarize these commonly-used terms, when referring to data, one must specify if it is reco-level or unfolded. Similarly, when referring to a MC, it is important to specify if it is reco-level, truth-level or has no cuts yet i.e. full phase space.

In parallel to the data acquisition, a $Z \to e^+e^-$ MC is generated based on theoretical predictions, without applying any initial cuts. Figure 6.4 shows this full-phase space MC prediction. There are many more events in the full-phase space MC distribution compared to the reco-level data distribution, because no cuts have been applied to the MC yet.

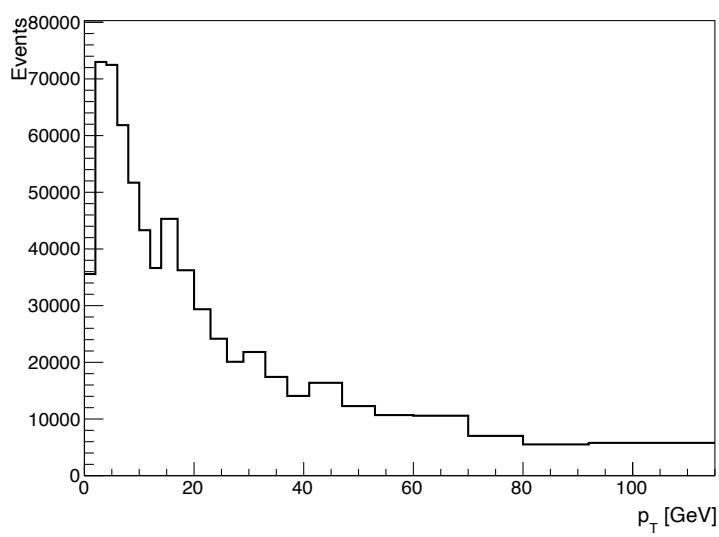

Figure 6.4: Initial full-phase space $Z \to e^+e^-$ MC. The total number of $Z \to e^+e^-$ events are shown as a function of p_{T}^{Z}.

From this initial MC, the truth-level cuts and reco-level cuts are separately applied. The MCs after truth-level cuts and reco-level cuts are shown in Figures 6.5a and 6.5b, respectively. The same reco-level cuts are applied to data and MC. Exam-

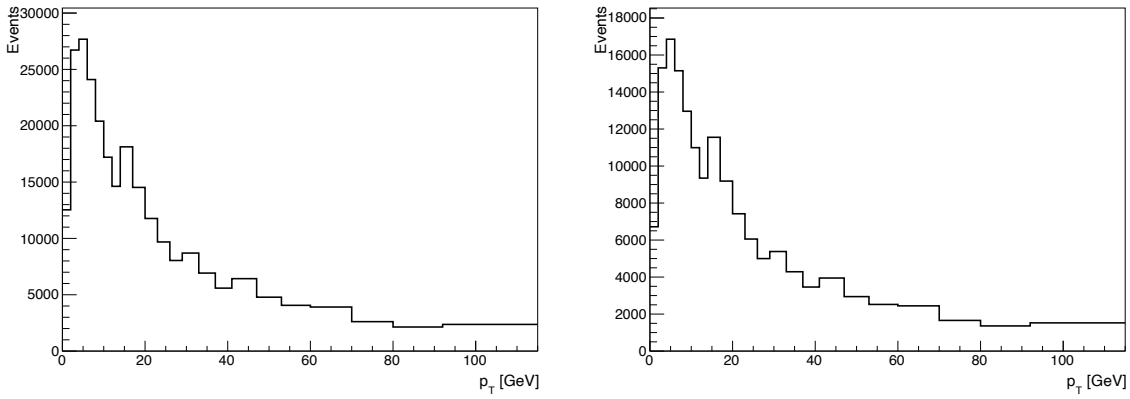

(a) Truth-Level cuts (b) Reco-Level cuts

Figure 6.5: $Z \to e^+e^-$ events in the MC as a function of p_{T}^Z after truth-level cuts (left) and reco-level cuts (right) are applied. The cuts are made separately beginning with the full-phase space MC (shown in Fig. 6.4).

ining Figure 6.5, we notice that the shapes of each plot are now more similar to the reco-level data, but the total number of events are still different[1].

From here, we are ready to unfold. Two unfolding methods are generally considered by ATLAS analyses: bin-by-bin unfolding, and iterative (Bayesian) unfolding [75].

Bin-by-Bin Unfolding

Bin-by-bin unfolding is the simplest unfolding method. Beginning with truth-level and reco-level MC distributions (i.e. Figures 6.5a and 6.5b), we define T_i as the number of events in bin i of the truth-level distribution and R_i as the number of events in bin i of the reco-level distribution. We must also assume that our original MC simulation has been generated to an order that accurately represents the process of interest, which is a reasonable assumption when measuring a well-known process like $Z \to e^+e^-$. (This would not be a reasonable assumption when trying to model

[1]The number of events in the MC are initially reweighted to match the luminosity collected with the data.

new physics, for example.) We then define a correction factor C_i:

$$C_i = \frac{T_i}{R_i}. \tag{6.3}$$

We can then unfold our data, bin by bin, using the equation

$$U_i = C_i \times D_i, \tag{6.4}$$

where D_i is the measured event spectrum (the reco-level data i.e. Figure 6.3) and U_i is the unfolded data. We are now done, and T_i should estimate U_i. Clearly this process is simple, needing only Equations (6.3) and (6.4). However, bin-by-bin unfolding is only accurate if *purity* is high. Purity (p) is the fraction of events at reco-level that are in the same bin at truth-level. For a given bin i, this can be written as:

$$p_i = \frac{N_i^{T,R}}{N_i^R}, \tag{6.5}$$

where $N_i^{T,R}$ is the number of events passing both truth and reco-level cuts, while N_i^R is the number of events passing only reco-level cuts. Figure 6.6 shows sample purity plots for the $Z \to e^+e^-$ p_{T}^Z distribution for the dilepton transverse momentum (p_{T}^{ll}, left) and hadronic recoil (u_{T}, right) observables. Observables with 'high purity'

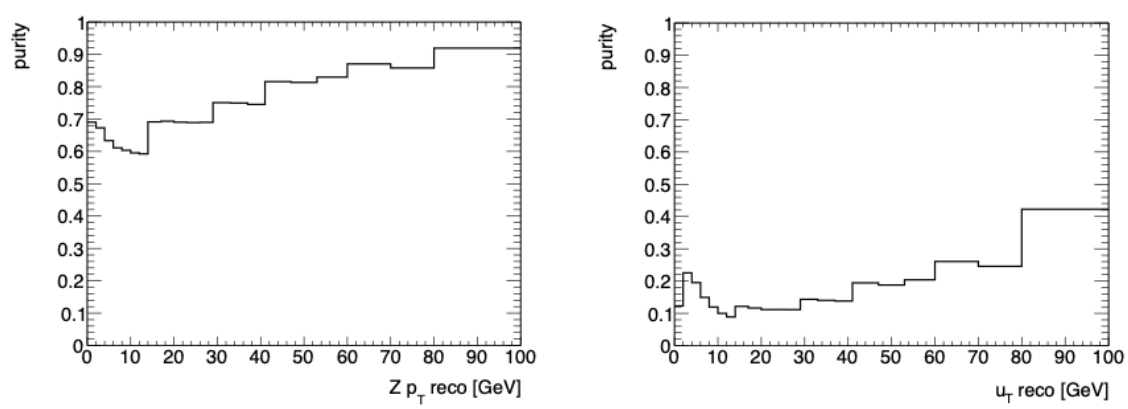

(a) p_{T}^{ll} Purity (b) u_{T} Purity

Figure 6.6: Sample purity plots for the $Z \to e^+e^-$ differential cross section as a function of p_{T}^Z, measured using p_{T}^{ll} (left) and u_{T} (right). The y-axis is the fraction of events at reco-level that are in the same bin at truth-level.

(approximately 0.7 or greater) can be unfolded using bin-by-bin unfolding. However, low-purity observables like u_{T} have large bin-to-bin event migration, which bin-by-bin unfolding cannot take into account, so a different unfolding method must be employed. Since u_{T} is a critical observable for the p_{T}^{Z} (and p_{T}^{W}) analysis, the second ATLAS unfolding method must be used.

Iterative Bayesian Unfolding

Iterative unfolding takes bin-to-bin migrations into account in addition to the differences between reco-level and truth-level binned event distributions. ATLAS analyses generally use the iterative Bayesian unfolding method as described by D'Agostini [76]. The first step of this process involves constructing a *migration matrix*, which accounts for these bin-to-bin event migrations. Migration matrices are constructed by analysis tools that take the truth-level and reco-level MC distributions and match their events to form a two-dimensional matrix of truth-level versus reco-level events that are normalized to 1 in each truth-level bin. The value of the migration matrix in bin i, j is defined as

$$M_{ij} = \frac{N_{ij}}{\sum_k N_{kj}}, \tag{6.6}$$

where N_{ij} is the number of events in reco-level bin i and truth-level bin j. Figure 6.7 shows sample migration matrices for p_{T}^{ll} (left) and u_{T} (right). This is another example of the 'less clean' u_{T} observable compared to p_{T}^{ll}, as the event smearing is much more visible in the u_{T} migration matrix. Figure 6.8 summarizes the process of constructing the migration matrix, starting from the full-phase space MC.

Once the migration matrix is created, it must be inverted, acting as the response function $R(x|y)$ from Eq. (6.1). Rewriting this equation to now represent our recorded, binned data D_i, we have

$$D_i = \sum_j M_{ij} T_j + B_i, \tag{6.7}$$

where M is the migration matrix (Eq. (6.6)), T is the truth-level distribution, and B is the sum of all background events. Both D and B are at reco-level.

Iterative Bayesian unfolding inverts the migration matrix to unfold the data by weighting the reco-level data based on the initial truth-level MC. This process is re-

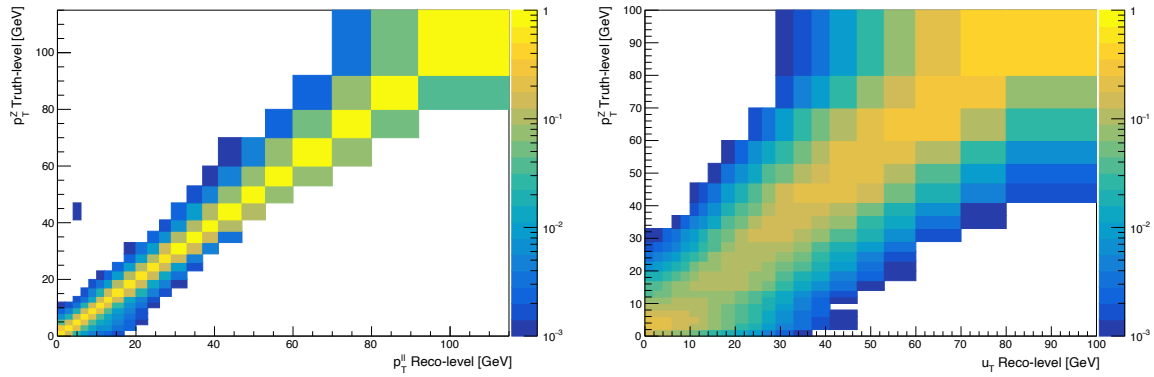

(a) p_{T}^{ll} Migration Matrix (b) u_{T} Migration Matrix

Figure 6.7: Sample migration matrices for p_{T}^{Z} measured using p_{T}^{ll} (left) and u_{T} (right). The truth-level distributions are on the y-axis and the reco-level distributions are on the x-axis. The z-axis is normalized.

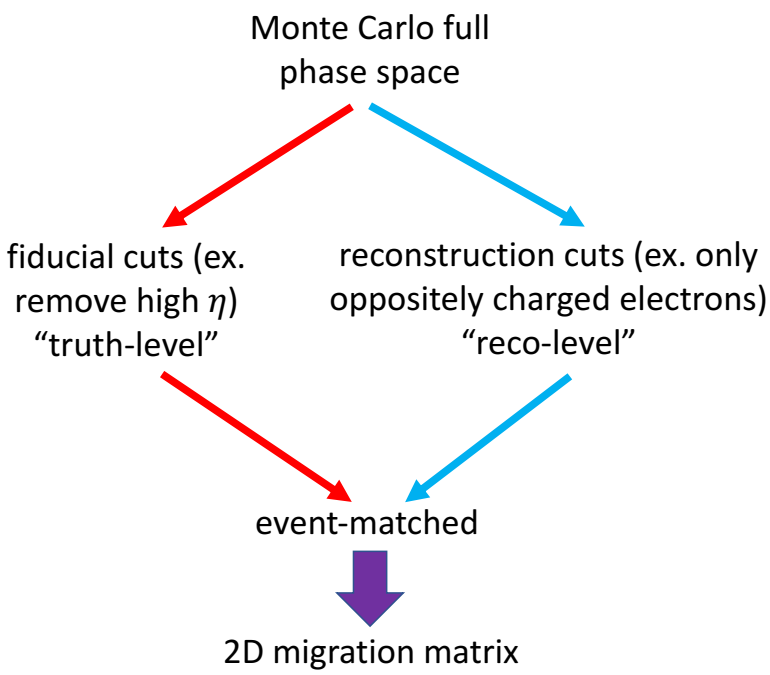

Figure 6.8: Summary of the migration matrix construction process, beginning with the full phase space MC.

peated for N iterations, where for each iteration, the Nth unfolded spectrum becomes the prior spectrum for the $(N+1)$ iteration. After one unfolding iteration, the binned unfolded data distribution (per bin j) is given by

$$\tilde{U}_j = \sum_i U_{ij}(D_i - B_i) \times p_i, \tag{6.8}$$

where $\tilde{U}$ is the unfolded data distribution, and U represents the unfolding transformation determined by the iterative Bayesian unfolding algorithm [76], which in the simplest case is just the inverse of the migration matrix M. The background-subtracted data distribution $D - B$ is multiplied by the purity p to account for the reco-level events that are not matched to a truth-level event.

As N increases, bin-by-bin fluctuations in the unfolded spectrum increase, increasing the statistical error of the unfolded data. However, more iterations means that the unfolded data distribution is less influenced, or *biased* by the initial truth-level distribution. The goal of iterative Bayesian unfolding is to unfold the data with a minimal unfolding bias error coming from the number of unfolding iterations (N), while ensuring that the resultant unfolded data distribution is not improperly biased towards the initial truth-level MC distribution. The optimal number of unfolding iterations is selected by tracking the unfolding bias uncertainty and the statistical uncertainty as a function of N and selecting a minimum value (shown in more detail in Section 7.2.3). Iterative Bayesian unfolding is performed using an analysis package called RooUnfold [77].

Iterative Bayesian unfolding is the unfolding method that is used for both the Z and W boson Drell-Yan differential cross-section measurements as a function of p_{T}^{Z} and p_{T}^{W}. While the purity is shown to be good for the p_{T}^{ll} observable of the Z boson cross-section measurement, meaning that bin-by-bin unfolding would be acceptable, iterative unfolding is required for u_{T} (for both p_{T}^{Z} and p_{T}^{W}) due to its low purity. Therefore for consistency, iterative Bayesian unfolding is used for all processes in the analysis, and is the method "unfolding" refers to when discussed in Chapters 7 and 8.

6.2.4 Unfolding Bias Uncertainty

Iterative Bayesian unfolding biases the data towards the truth-level MC used in the migration matrix. This unfolding bias must be estimated and included as an analysis uncertainty. Assuming that the truth-level MC provides a reasonable prediction for the process of interest, a **Data-driven Closure Test** is usually used to estimate this unfolding uncertainty. There are four steps to the Data-driven Closure Test:

1. Fit a smooth function to the ratio of the background-subtracted reco-level data distribution and the reco-level MC, i.e. (Data - Bkg.)/(Reco-level MC).

2. Use this fit function to reweight the truth-level MC.

3. Unfold this reweighted truth-level MC as pseudo-data[2] using the migration matrix.

4. Take the relative difference between this unfolded, reweighted MC and the reweighted truth-level MC. The relative difference is the unfolding bias uncertainty.

In some cases, no truth-level distribution exists that well-represents the data. Under these circumstances, more complicated unfolding bias uncertainty estimation procedures must be developed. Chapter 8 focuses on explaining the custom unfolding bias estimation process that was developed for the p_{T}^{W} analysis.

6.3 Summary

The road to a final cross-section result is long and technical, even when disregarding the massive undertaking that is building and understanding the detector. Many steps are involved, with each step containing many checkpoints and cross-checks in order to ensure the final result is reported with proper statistical and systematic rigor. Once a measurement is finalized, it is important for the result to last far into the future so that it can be used for more than just a number in a publication, but future experiments and predictions as well. Unfolding the data is the best way

[2]The term "pseudo-data" refers to simulated datasets that are given the same treatment as recorded ATLAS data.

to ensure that a measurement can be used for future (and past) experiments and predictions. Unfolding procedures, while often time-consuming, are usually well-defined. Occasionally circumstances arise that require substantial modifications to the unfolding procedure as we will see in Chapter 8.

Chapter 7

Measurement of the Z Boson Drell-Yan Process Differential Cross Section as a Function of p_{T}^{Z}

In November of 2017, ATLAS collected 256.83 pb^{-1} of low-pileup data at centre-of-mass energy $\sqrt{s}$ = 5 TeV and 144.93 pb^{-1} at $\sqrt{s}$ = 13 TeV across six days of data-taking for each. An additional 190.25 pb^{-1} of low-pileup data was collected at $\sqrt{s}$ = 13 TeV during 2018 across eight more days of data-taking. For the remainder of this thesis, the total $\sqrt{s}$ = 5 TeV dataset will be referred to as "5 TeV data" and the total $\sqrt{s}$ = 13 TeV dataset of 335.18 pb^{-1} will be referred to as "13 TeV data". These low-pileup datasets, with an average number of p-p collisions per bunch crossing ($\langle\mu\rangle$) of two, were taken primarily to precisely measure properties of Z and W bosons, with an initial target being the precision measurement of the differential cross sections ($\frac{d\sigma}{dp_{\mathrm{T}}}$) of $Z \to l^+l^-$ and $W^\pm \to l^\pm\nu$ ($l = e, \mu$) as a function of p_{T}^{Z} and p_{T}^{W}, respectively, at both centre-of-mass energies. In order to avoid using the full description each time, these measurements will be generally referred to as the "p_{T}^{Z} measurement" and the "p_{T}^{W} measurement" for the remainder of this thesis. The motivation for these measurements has already been discussed in Chapter 5. A dedicated MC campaign was also produced to match the special conditions of this low-μ data. ATLAS formed an analysis team of approximately 20 collaborators to make these precision p_{T}^{Z} and p_{T}^{W} measurements in 2018 – I joined this team in the fall of 2019. This chapter presents

the results of the p_{T}^{Z} measurement in $Z \to l^{+}l^{-}$ Drell-Yan decays, for which I was the primary analyzer for many components of the analysis chain, as is highlighted in the cross-section road map shown in Figure 7.1.

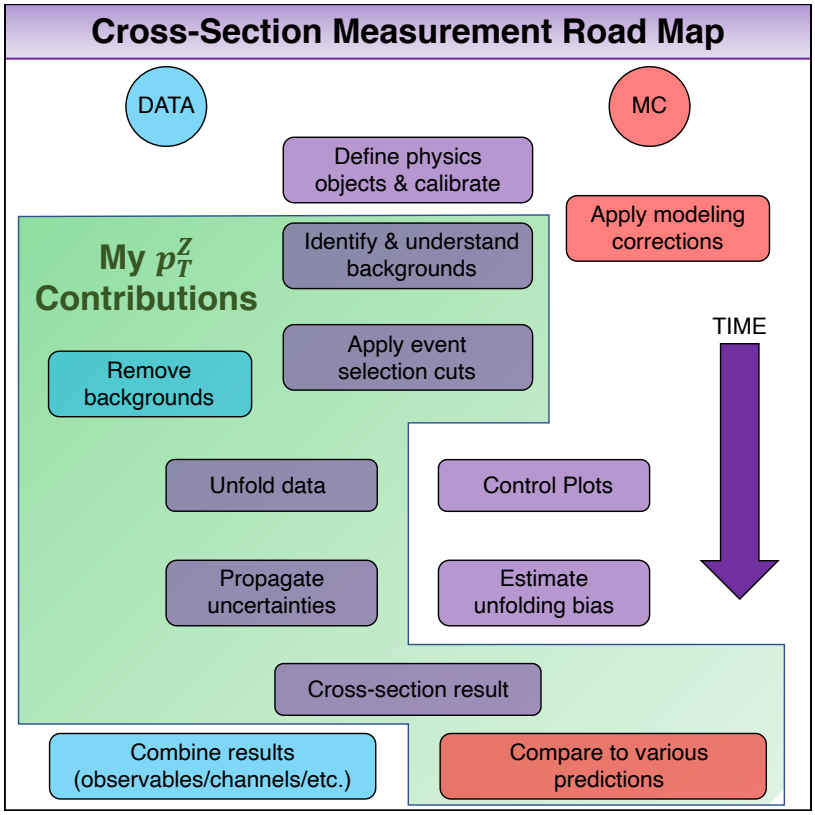

Figure 7.1: My contributions to the p_{T}^{Z} cross-section analysis (encapsulated in the light-green box) as a subset of the cross-section road map (Fig. 6.1).

Details on the documentation of the work that I did and where the work was presented are provided in Appendix G. Due to the nature of large-scale collaboration work with ATLAS, especially with an analysis team of this size, it can take a long time for the results to be finalized within the collaboration and be ready for publication. This is especially true when making a precision measurement. A series of internal steps must be passed before the first draft of the paper can be circulated within ATLAS. One critical step is the review of the analysis by an Editorial Board: ATLAS experts who are not involved in the analysis, but who read the long internal notes and hold discussions with the analysis team in order to critically review the analysis before recommending that it moves forward for collaboration approval. I presented the p_{T}^{Z}

results to our Editorial Board in 2020. While this marked the completion of the major work for the p_{T}^{Z} measurement, the full analysis could not be approved at that time due to difficulties with the p_{T}^{W} measurement. As part of the final result, the p_{T}^{Z} and p_{T}^{W} measurements are presented together and the finalized unfolding bias uncertainty estimation method for p_{T}^{W} (see Chapter 8) must be applied to p_{T}^{Z} to synchronize the channels. Additionally, the ultimate goal is to take the W/Z ratio, so even though the major p_{T}^{Z} results were finalized in 2020, it was only half of the analysis so it could not yet be approved. Currently the analysis as a whole is being finalized, and the paper should be circulated to the collaboration by Fall, 2022.

Given that there are two decay channels ($Z \to e^+e^-$ and $Z \to \mu^+\mu^-$), two p_{T}^{Z} observables for each decay channel (p_{T}^{ll} and u_{T}), and two datasets ($\sqrt{s}$ = 5 TeV and 13 TeV), many measurements have been made for this work, but the process is often similar. Only subsets of these measurements will be shown in this chapter in order to aid the explanations – additional channels or observables will be shown when comparisons are important. All final results plots are included in Appendix D.

This chapter is divided into five sections. Section 7.1 discusses the background processes with a focus on the estimation of the multi-jet uncertainty, along with the event selection. Section 7.2 reviews the unfolding process and the uncertainty propagation. Section 7.3 presents the cross-section results, and Section 7.4 shows the compatibility between the decay channels and observables. A summary is provided in Section 7.5.

7.1 Event Selection and Backgrounds

Candidate $Z \to l^+l^-$ events are recorded in data and simulated with MCs. Signal and background MCs are created for each channel and $\sqrt{s}$. The nominal signal MCs for each channel are generated using the Powheg event generator [78–81] using the CT10 [82] PDF interfaced to Pythia 8 [69] with the AZNLO tune [70] for low-p_{T} parton showering (see Section 5.2). This set of nominal MCs is often referred to as "Powheg+Pythia8" in this thesis. The data and MCs are each passed through the event selection chain separately – only at the end of the chain are the background MCs subtracted from the data to eventually be compared to signal MC. The end of

this chain provides the total number of reconstructed-level events.

$Z \to e^+e^-$ ($Z \to \mu^+\mu^-$) events are required to contain exactly two electrons (muons), with one of the electrons (muons) being matched to a single electron (muon) trigger. Both electrons and muons must satisfy the *Medium* LH identification criteria (see Section 4.2.3) and must be isolated. Isolation is defined using the variable-cone-size track isolation variable (see Section 4.2.4) as $p_{\mathrm{T,cone}}^{\Delta R=0.2}/\mathrm{min}(p_{\mathrm{T}},50\ \mathrm{GeV}) < 0.1$. The leptons are required to be of opposite charge. Both leptons in each respective decay channel must satisfy the minimum p_{T} cut of $p_{\mathrm{T}}^{l} > 25$ GeV and must be within the invariant mass range $66 < m_{ll} < 116$ GeV, consistent with the mass of the Z boson $m_Z \approx 91$ GeV.

There are many processes that have two final-state leptons, or contain final-state objects that could mimic two final-state leptons in the ATLAS detector and be able to pass through event selection. These processes must be considered as backgrounds when studying $Z \to l^+l^-$ events. Each of these processes is simulated by MC[1]. The backgrounds are grouped into five categories:

1. $Z \to \tau^+\tau^-$;
2. $W^\pm \to l^\pm\nu$;
3. Top: processes containing at least one top quark such as $t\bar{t}$ decays ($t\bar{t} \to l^+l^-X$), where X are other particles such as quarks or neutrinos;
4. Diboson: processes containing two bosons, including WW, ZZ, or WZ, that then decay to states that have two leptons. For example, $ZZ \to q\bar{q}l^+l^-$;
5. Multi-jet: fake leptons from jets (see Section 7.1.1).

The reco-level cuts and background processes are combined into tables showing the number of events left after applying each selection criterion. These are often referred to as "cutflow tables" in analyses (as a reminder, the cutflow for the WTP analysis was shown in Section 4.3.2). The cutflow tables are shown in Tables 7.1, 7.2, 7.3 and 7.4 for $Z \to e^+e^-$ and $Z \to \mu^+\mu^-$ at $\sqrt{s} = 13$ TeV and $Z \to e^+e^-$ and $Z \to \mu^+\mu^-$ at $\sqrt{s} = 5$ TeV, respectively. Overall, the backgrounds are relatively small, contributing

[1]Multi-jet backgrounds cannot be well-understood by simulations and must be estimated using a data-driven method.

at a level of about 0.5% for both channels and energies. The dominant backgrounds are those coming from Top and Diboson processes. In total after event selection, about 379×10^3 $Z \to l^+l^-$ candidate events are selected at $\sqrt{s} = 13$ TeV and about 122×10^3 at 5 TeV.

Cut	Data	Signal	$Z \to \tau\tau$	$W^{\pm} \to l^{\pm}\nu$	Top	Diboson	Multi-jet
No cut	56038636	641080 ± 180	86920 ± 280	7012290 ± 930	108430 ± 150	14530 ± 130	-
Two electrons	237221	196941 ± 97	838 ± 25	479.6 ± 8.6	2304 ± 20	599 ± 23	-
Electron trig matched	236820	196625 ± 97	832 ± 24	425.5 ± 7.8	2300 ± 20	599 ± 23	-
Isolation	224967	194586 ± 96	809 ± 24	263.7 ± 6.1	2048 ± 19	585 ± 22	-
Opposite charge	222256	192148 ± 96	798 ± 24	194.9 ± 5.4	1974 ± 19	552 ± 22	-
Both $p_T^e > 25$ GeV	172651	162036 ± 88	169 ± 11	37.7 ± 2.0	1402 ± 16	420 ± 19	-
$66 < m_{ee} < 116$ GeV	165027	158000 ± 87	79.7 ± 7.5	16.5 ± 1.4	501.4 ± 9.9	324 ± 15	110 ± 68

Table 7.1: Analysis cutflow for $Z \to e^+e^-$ 13 TeV signal selection. The displayed uncertainties on the MC backgrounds are MC statistics only.

Cut	Data	Signal	$Z \to \tau\tau$	$W^{\pm} \to l^{\pm}\nu$	Top	Diboson	Multi-jet
No cut	56038636	645950 ± 180	86920 ± 280	6964690 ± 930	108430 ± 150	14530 ± 130	-
Two muons	365843	267040 ± 110	802 ± 24	887 ± 12	3978 ± 26	790 ± 27	-
Muon trig matched	362610	262180 ± 110	783 ± 24	867 ± 12	3891 ± 25	770 ± 26	-
Isolation	292967	257410 ± 110	756 ± 23	101.0 ± 3.6	2417 ± 20	730 ± 26	-
Opposite charge	292692	257410 ± 110	754 ± 23	89.7 ± 3.4	2370 ± 20	713 ± 26	-
Both $p_T^\mu > 25$ GeV	223806	213230 ± 100	160 ± 11	22.4 ± 1.9	1630 ± 16	525 ± 22	-
$66 < m_{\mu\mu} < 116$ GeV	214035	207860 ± 100	79.7 ± 7.6	11.9 ± 1.4	553.9 ± 9.2	414 ± 17	177 ± 44

Table 7.2: Analysis cutflow for $Z \to \mu^+\mu^-$ 13 TeV signal selection. The displayed uncertainties on the MC backgrounds are MC statistics only.

Cut	Data	Signal	$Z \to \tau\tau$	$W^{\pm} \to l^{\pm}\nu$	Top	Diboson	Multi-jet
No cut	11372289	176338 ± 72	26630 ± 140	1975840 ± 600	7638.7 ± 7.3	3622.1 ± 8.8	-
Two electrons	72037	63254 ± 42	282 ± 13	116.9 ± 4.8	165.93 ± 0.88	203.4 ± 3.9	-
Electron trig matched	71412	63108 ± 42	280 ± 13	100.0 ± 4.5	165.32 ± 0.88	202.7 ± 3.9	-
Isolation	69068	62643 ± 41	275 ± 13	61.8 ± 3.2	143.51 ± 0.81	195.6 ± 3.7	-
Opposite charge	68229	61828 ± 41	273 ± 13	45.9 ± 2.9	137.65 ± 0.78	185.7 ± 3.7	-
Both $p_T^e > 25$ GeV	53684	52566 ± 38	43.0 ± 5.0	7.83 ± 0.94	94.26 ± 0.65	133.9 ± 2.2	-
$66 < m_{ee} < 116$ GeV	51772	51310 ± 37	23.1 ± 3.7	3.98 ± 0.63	35.47 ± 0.40	109.1 ± 2.0	0^{+87}_{-0}

Table 7.3: Analysis cutflow for $Z \to e^+e^-$ 5 TeV signal selection. The displayed uncertainties on the MC backgrounds are MC statistics only.

Cut	Data	Signal	$Z \to \tau\tau$	$W^{\pm} \to l^{\pm}\nu$	Top	Diboson	Multi-jet
No cut	11372289	170822 ± 95	26630 ± 140	1936610 ± 590	7638.7 ± 7.3	3622.1 ± 8.8	-
Two muons	111874	88644 ± 68	367 ± 15	178.0 ± 7.1	341.7 ± 1.3	293.6 ± 3.1	-
Muon trig matched	111000	86936 ± 67	360 ± 15	172.2 ± 7.0	333.7 ± 1.3	287.3 ± 3.0	-
Isolation	94735	85728 ± 67	354 ± 15	25.9 ± 2.1	178.34 ± 0.89	257.1 ± 2.8	-
Opposite charge	94651	85723 ± 67	354 ± 15	23.2 ± 2.0	172.50 ± 0.87	245.0 ± 2.8	-
Both $p_T^\mu > 25$ GeV	73105	71541 ± 61	76.4 ± 6.7	6.2 ± 1.4	114.79 ± 0.71	175.2 ± 2.3	-
$66 < m_{\mu\mu} < 116$ GeV	70447	69819 ± 60	38.6 ± 4.8	3.7 ± 1.3	43.97 ± 0.44	144.9 ± 2.1	15.9 ± 7.9

Table 7.4: Analysis cutflow for $Z \to \mu^+\mu^-$ 5 TeV signal selection. The displayed uncertainties on the MC backgrounds are MC statistics only.

7.1.1 p_{T}^{Z} Multi-jet Background Estimation

Multi-jet (MJ) processes are the group of background events originating from jets that mimic the signature of prompt electrons in the detector. This includes electrons from photon conversions in the detector material, non-prompt leptons from the decay of hadrons containing heavy flavours, and jets that are misidentified as electrons in the detector. This "fake" lepton component (MJ) is obtained using data-driven techniques. Note the specific use of electron or lepton in this description: the MJ background component for decays involving exclusively muons (like $Z \to \mu^+\mu^-$) only contains non-prompt muons from the decay of hadrons containing heavy flavours, because a jet cannot "fake" a muon signal in the muon spectrometer.

The MJ background for Z boson events is expected to be small because of the clean environment of the low-μ dataset. Moreover, the Z boson event selection requires two opposite-sign, well-identified and isolated leptons, which suppresses the MJ background. Due to the difference between background processes for electrons and muons, generally the number of MJ events arising from muons is expected to be smaller compared to that of electrons.

General Procedure

The data-driven estimation of the MJ background is based on the so-called ABCD method [83,84] – a sketch of this method is shown in Figure 7.2. In the ABCD method three control regions (CR) are defined (B, C, and D) by inverting or sequentially relaxing data event selection requirements. Region A, the signal region (SR), has the usual analysis event selection cuts. The control regions are defined to be rich in events produced from background processes with fake leptons i.e. MJ events. The ABCD method is set up such that the three CRs can be eventually combined to estimate the number of MJ events in the SR, the goal of this process. The premise of the ABCD method is that the ratio of events in regions A and B is equal to the ratio of events in regions C and D i.e. $A/B = C/D$.

The key discriminating variable used to define the CRs is the isolation variable $p_{\mathrm{T,cone}}^{\Delta R=0.2}/p_{\mathrm{T}}^{l}$ of the sub-leading lepton (sub-leading lepton means the lepton from the $Z \to l^+l^-$ decay with the smaller p_{T}). A lepton is defined to be isolated if $p_{\mathrm{T,cone}}^{\Delta R=0.2}/p_{\mathrm{T}}^{l} < 0.1$ and anti-isolated if $p_{\mathrm{T,cone}}^{\Delta R=0.2}/p_{\mathrm{T}}^{l} > 0.1$.

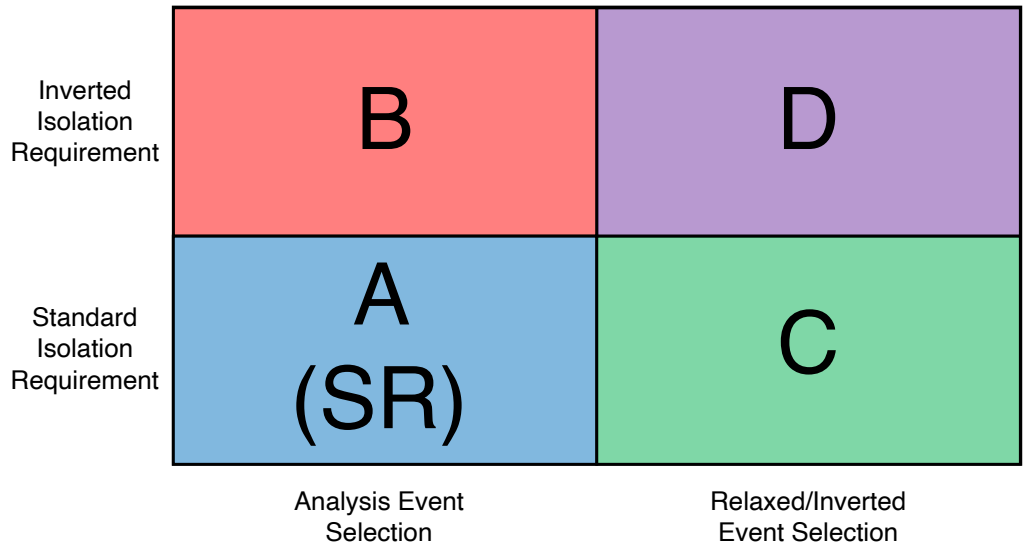

Figure 7.2: Sketch of the ABCD method. The signal region (SR), region A, has the usual analysis event selection cuts. There are three control regions: B, C, and D. Region B has the usual analysis event selection, but with the isolation requirement inverted. Region C has relaxed or inverted selection requirements but the normal isolation requirement, and region D inverts the isolation requirement as well.

The estimation process begins with the SR, A, which has the usual $Z \to l^+l^-$ 'good lepton' selection requirements as stated in the cutflow definition. Each CR, B through D, is given increasingly-relaxed selection requirements. Region B is filled with events that pass the same selections as region A, but are anti-isolated. Region C is filled with events that are isolated, but have other selection requirements relaxed. In both channels, the p_{T} cut of both leptons is relaxed to $p_{\mathrm{T}}^{l} > 20$ GeV. In the $Z \to \mu^+\mu^-$ channel, the muons are also required to be of the same sign (i.e. not possible for a true Z boson dileptonic decay). In the $Z \to e^+e^-$ channel, enforcing this same-sign requirement left region C with too few events, so instead all sign requirements were removed, and multiple background-enrichment attempts were made. It was found that to have a reasonable background-rich region with an isolated sub-leading lepton, the electron identification (ID) requirement for the sub-leading lepton had to be relaxed to *Loose* with *Medium* electrons rejected, and isolation requirements were removed for the leading lepton. Region D is then filled with events that satisfy the respective channel's region C relaxed requirements, but are required to be anti-isolated.

To summarize the $Z \to e^+e^-$ channel, the four regions are defined as the following:

- A (SR): opposite-sign electrons; both electrons isolated; sub-leading electron passes *Medium* ID, both $p_{\mathrm{T}}^{e} > 25$ GeV.
- B: same as A but the sub-leading electron is anti-isolated.
- C: no sign requirement; leading electron isolation requirement removed; sub-leading electron satisfies the *Loose* but not *Medium* ID; sub-leading electron is isolated; both electrons' p_{T} requirement is relaxed to $p_T^e > 20$ GeV.
- D: same as C but the sub-leading electron is anti-isolated.

To summarize the $Z \to \mu^+\mu^-$ channel, the four regions are defined as the following:

- A (SR): opposite-sign muons; both muons isolated; both $p_{\mathrm{T}}^{\mu} > 25$ GeV.
- B: same as A but the sub-leading muon is anti-isolated.
- C: same-sign muons; both muons isolated; both muons' p_{T} requirement is relaxed to $p_{\mathrm{T}}^{\mu} > 20$ GeV.
- D: same as C but the sub-leading muon is anti-isolated.

In the $Z \to e^+e^-$ channel, it was found that the CRs, defined as above, were still too signal-dominated to extract a MJ estimate. Therefore to further reduce this signal contamination, the peak of the Z boson invariant mass was excluded for the extraction: only events with a di-electron invariant mass in the range between [66, 81] GeV and [101, 116] GeV were considered for the MJ extraction in all four regions A - D. The [81,101] GeV mass peak was also excluded for region A in order for this SR to still be statistically comparable to the CRs.

Once the selections for the four regions are defined, the requirements for each region are applied to the dataset. The data are then plotted as a function of sub-leading lepton isolation. The MC signal along with all the known backgrounds are included on the same plot. The difference between data and MC signal plus background is the numerical MJ estimation in the CR. Figure 7.3 shows this sub-leading lepton isolation distribution in each of the four regions in the $Z \to e^+e^-$ channel at $\sqrt{s} = 13$ TeV.

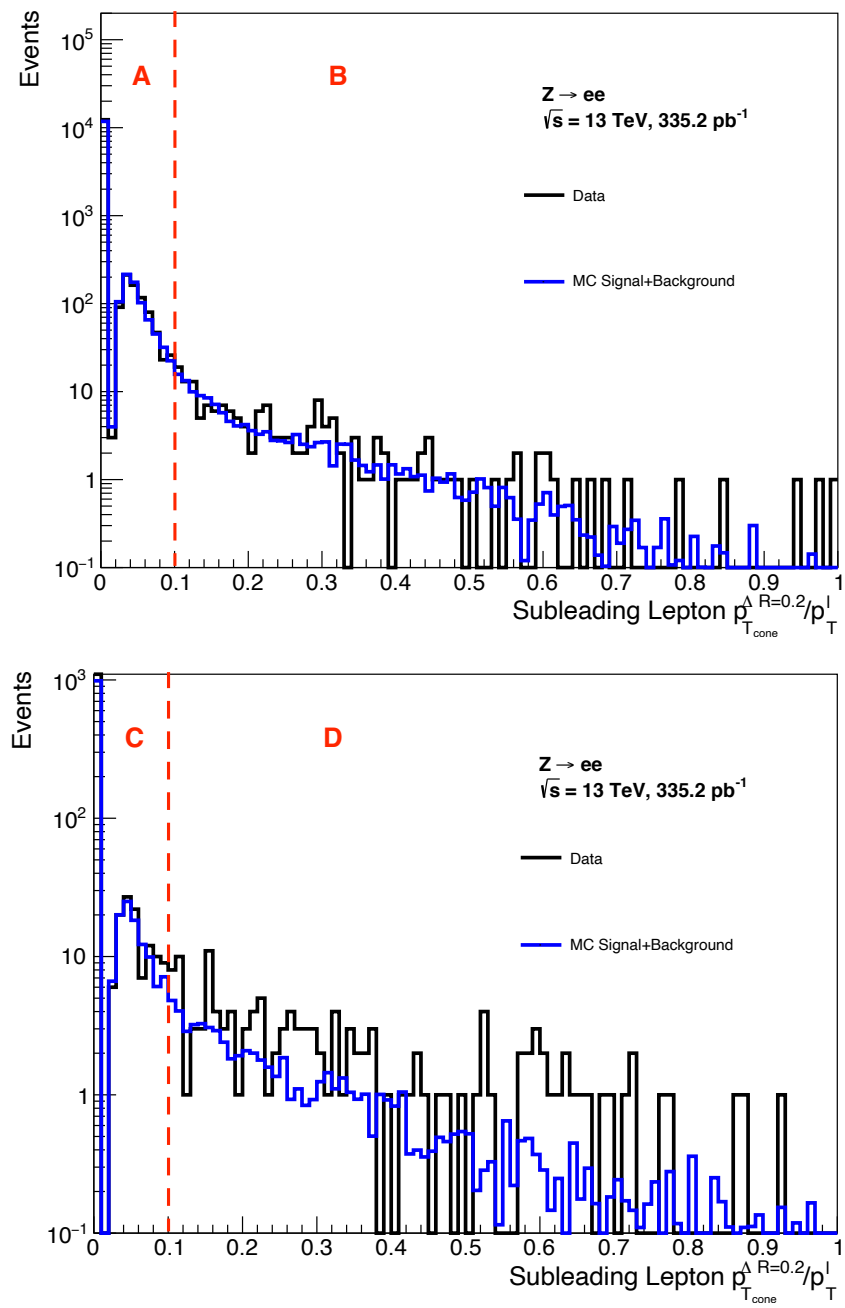

Figure 7.3: $\sqrt{s} = 13$ TeV $Z \to e^+e^-$ sub-leading lepton isolation event distribution for the four regions of the ABCD method as part of the MJ estimation. Data (black) and the addition of the signal and background MCs (blue) are shown. Events on the left side of the red line are considered to be isolated, and events on the right of the red line are anti-isolated.

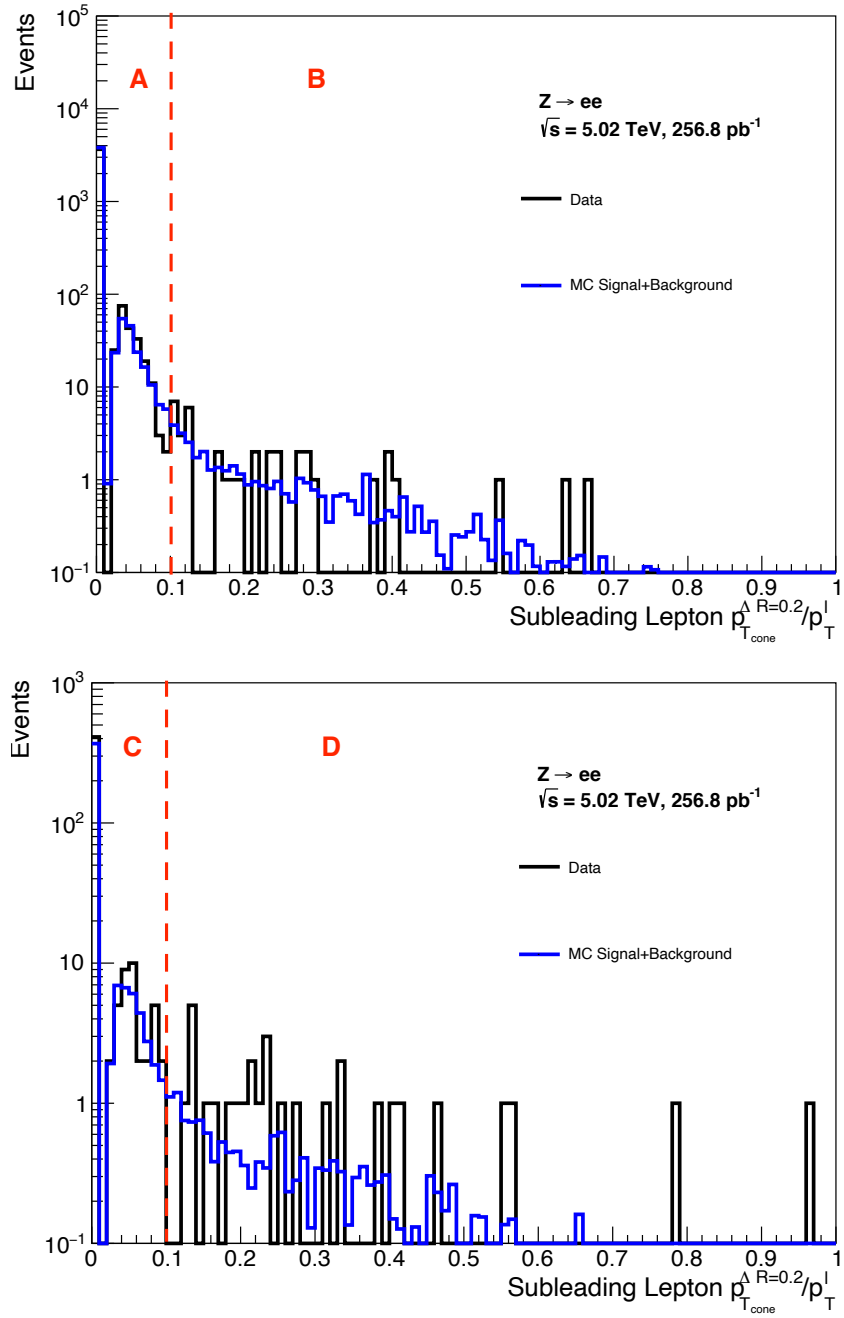

Figure 7.4: $\sqrt{s} = 5$ TeV $Z \to e^+e^-$ sub-leading lepton isolation event distribution for the four regions of the ABCD method as part of the MJ estimation. Data (black) and the addition of the signal and background MCs (blue) are shown. Events on the left side of the red line are considered to be isolated, and events on the right of the red line are anti-isolated.

Similar plots but for the $\sqrt{s} = 5$ TeV $Z \to e^+e^-$ channel are shown in Figure 7.4. The corresponding plots for the $Z \to \mu^+\mu^-$ are shown in Appendix D.

MJ events in the B, C and D regions (N^B_{MJ}, N^C_{MJ} and N^D_{MJ}) are estimated by subtracting the MC signal plus backgrounds from the data (separately for each region) and then integrating. The total MJ event yield is then linearly extrapolated to the signal region (region A) using the formula:

$$N^{\mathrm{SR}}_{\mathrm{MJ}} = N^B_{\mathrm{MJ}} \times \frac{N^C_{\mathrm{MJ}}}{N^D_{\mathrm{MJ}}}. \tag{7.1}$$

This process is performed once per channel as a normalization over all p_{T} bins. In both $Z \to e^+e^-$ channels where the Z boson mass peak was excluded, the MJ event yield $N^{\mathrm{SR}}_{\mathrm{MJ}}$ is multiplied by 50/30 to linearly interpolate the MJ yield to the full m_{ee} range: [66, 116] GeV[2].

MJ Background Yield Estimate

Due to the limited statistics of the low-μ dataset and the robust $Z \to l^+l^-$ event selection, the extrapolated number of expected MJ events is small, but measurable. Table 7.5 shows the number of MJ events in each signal region calculated using Equation (7.1) as well as the number of (data - MC) events in each of the B, C and D control regions. The uncertainty is taken to be the square root of the number of events in each bin, and then the final uncertainty for the MJ estimate in the SR is calculated via standard error propagation.

In the $Z \to e^+e^-$ channel at $\sqrt{s} = 5$ TeV the final MJ event estimate in the SR was found to be consistent with 0, originating from N^B_{MJ} that is consistent with 0. To obtain an upper limit on the MJ yield in this channel, the full size of the statistical uncertainty on the yield in region B was taken as the central value ($\delta N^B_{\mathrm{MJ}} = 23$) in order to propagate the uncertainty.

In all channels, the MJ event estimate is $\lesssim O(10^{-3})$ with respect to the data. The SR values reported in the second column of Table 7.5 are the same numbers that are listed in the Multi-jet column of the cutflow tables beginning with Table 7.1.

[2]The 50/30 multiplicative factor comes from the fact that p_{T} is divided into 1 GeV bins, the mass range in the signal region is 50 bins wide, and the middle 20 of these bins make up the mass peak that is removed.

Channel	SR	B	C	D
$Z \to e^+e^-$ at $\sqrt{s} = 13$ TeV	$\mathbf{110 \pm 68}$	40 ± 23	321 ± 62	117 ± 20
$Z \to \mu^+\mu^-$ at $\sqrt{s} = 13$ TeV	$\mathbf{177 \pm 44}$	725 ± 60	53 ± 11	217 ± 25
$Z \to e^+e^-$ at $\sqrt{s} = 5$ TeV	$\mathbf{0.0^{+87}}$	0.0^{+23}	80 ± 35	21.2 ± 9.2
$Z \to \mu^+\mu^-$ at $\sqrt{s} = 5$ TeV	$\mathbf{15.9 \pm 7.9}$	97 ± 28	12.6 ± 4.7	77 ± 11

Table 7.5: Number of MJ events as estimated using the ABCD method for each $Z \to l^+l^-$ channel and energy. The number of (data – MC) events in each control region is shown. The SR is calculated using Equation (7.1). The uncertainty is calculated as $\sqrt{N}$ where N is the number of events in each region.

MJ p_{T} Distributions

Once the integrated number of MJ events is found for each channel, they must be distributed as a function of p_{T}^{Z} instead of isolation (which uses p_{T}^{l}). This is the final step of the ABCD method, and must be performed separately for each of the p_{T}^{ll} and u_{T} observables since their shapes differ.

All events in control regions C and D were used to extract a shape to distribute the number of expected MJ events throughout the p_{T}^{ll} and u_{T} distributions. In each p_{T} bin, the events in these two regions were summed (i.e. the full isolation distribution per p_{T}), and then plotted as a function of p_{T}. To suppress statistical fluctuations and smooth the distributions, the p_{T}^{ll} and u_{T} spectra were fit to Landau functions, which peak at $p_{\mathrm{T}} \approx 10$ GeV. The approximately 10 GeV-peak Landau functions were chosen to empirically match the MJ distributions. Figure 7.5 shows the MJ p_{T}^{ll} and u_{T} C and D control region distributions and corresponding Landau fits for the $Z \to e^+e^-$ channel at $\sqrt{s} = 13$ TeV. Figure 7.6 shows the same distribution but at $\sqrt{s} = 5$ TeV. The $Z \to \mu^+\mu^-$ channels are shown in Appendix D.

The resulting fitted distributions were then normalized to the total number of MJ events for each channel (as listed in Table 7.5). The uncertainty on the number of MJ events has the same shape as the nominal values, but the fitted distribution was normalized to the MJ uncertainty for each channel instead of its nominal value. For the $Z \to e^+e^-$ channel at $\sqrt{s} = 5$ TeV where there are no nominal MJ events, the shape-fitting method was still used to obtain a distribution for the MJ uncertainty. The integrated MJ event numbers are the same in each channel for p_{T}^{ll} and u_{T} because they are both measurements of p_{T}^{Z} i.e. measurements of the same MJ events.

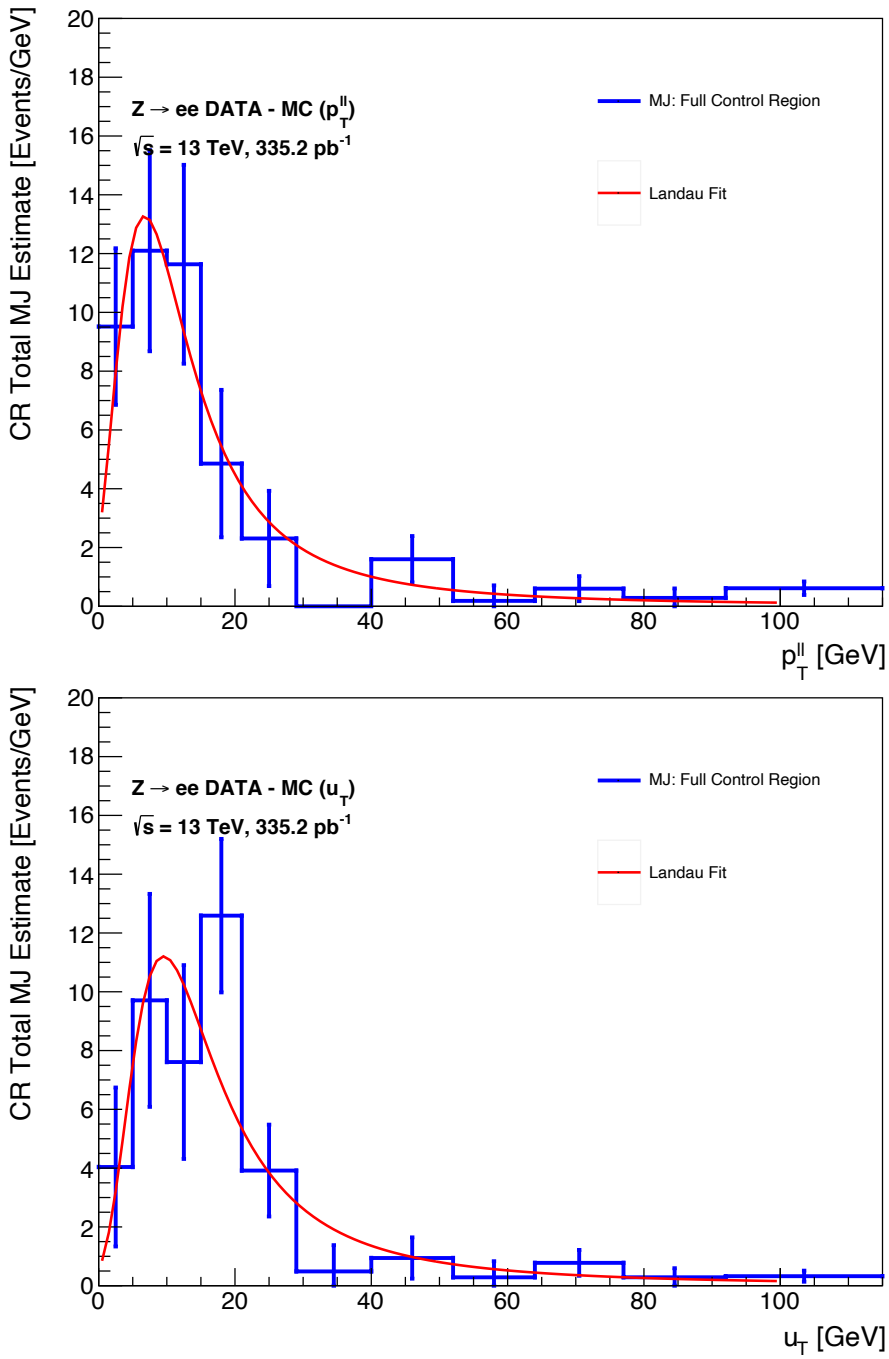

Figure 7.5: Landau fit (red) to the shape of the MJ $C + D$ control regions (black) as a function of the p_{T}^{ll} (top) and u_{T} (bottom) observables for the $Z \to e^+e^-$ channel at $\sqrt{s} = 13$ TeV.

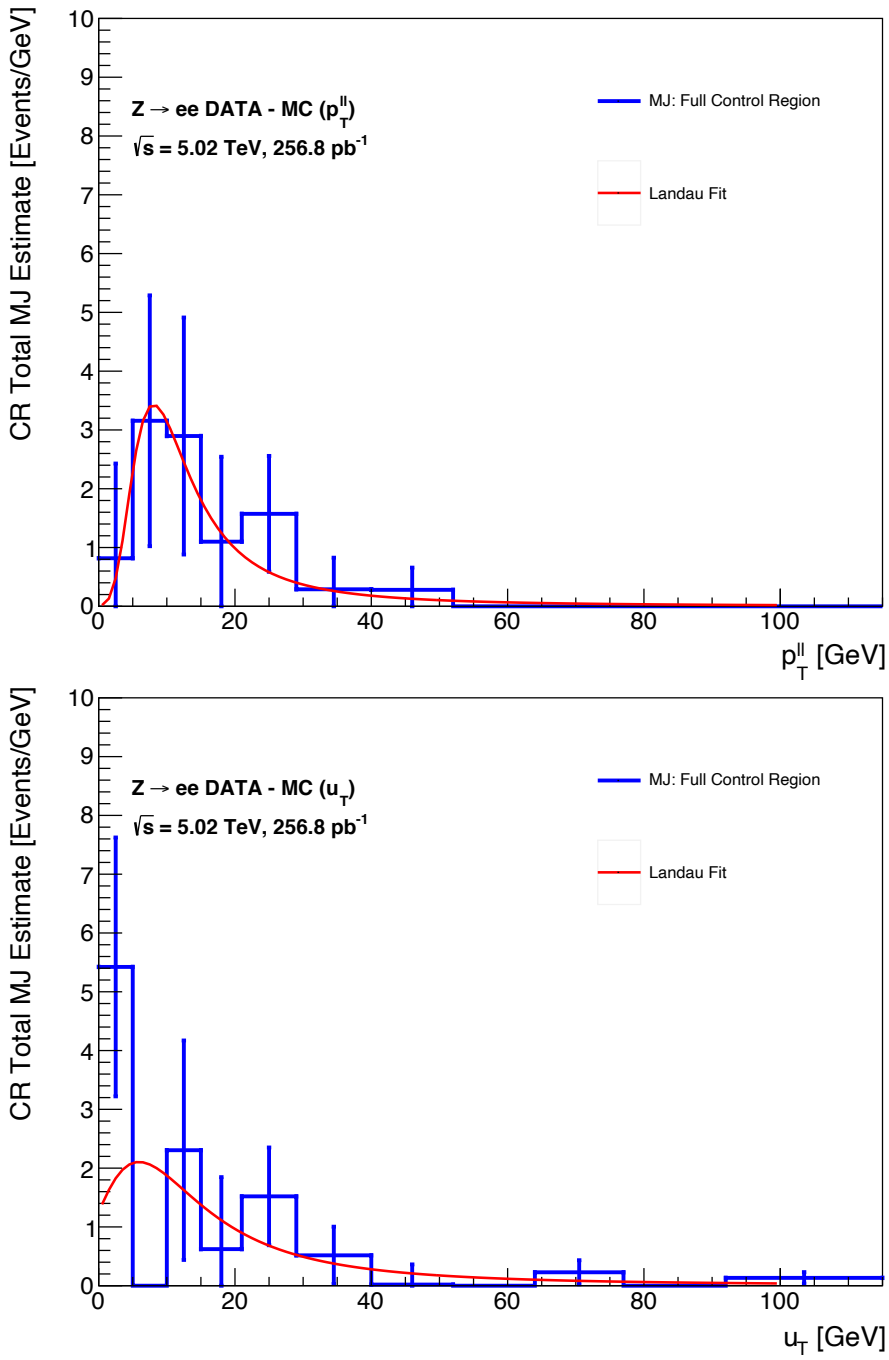

Figure 7.6: Landau fit (red) to the shape of the MJ $C + D$ control regions (black) as a function of the p_{T}^{ll} (top) and u_{T} (bottom) observables for the $Z \to e^+e^-$ channel at $\sqrt{s} = 5$ TeV.

Figure 7.7 shows the $Z \to e^+e^-$ MJ distribution for both observables at $\sqrt{s} = 13$ TeV and 5 TeV. The $\sqrt{s} = 5$ TeV distribution is the upper limit since the nominal estimate is zero events. The corresponding $Z \to \mu^+\mu^-$ plots are shown in Figure D.5 of the Appendix.

The distributions shown in Figures 7.7 and D.5 are included as one of the background uncertainties that are passed through the uncertainty propagation chain, just like each of the other uncertainties. It is important to note that there is no systematic error as part of this MJ analysis. This is because once all of the simulated background processes for the p_{T}^{Z} measurement were understood, it was seen that the p_{T}^{Z} MJ background would be very small. It was therefore decided that a complete statistical and systematic uncertainty analysis of the MJ background was not needed for this measurement, because it would be even more difficult to evaluate what would still end up being a negligible number. This is the reason why the uncertainty on the MJ estimate is given a generous estimate itself. The estimate of the MJ background for the p_{T}^{W} measurement (not part of this thesis) was a much more arduous process, because the MJ background is non-negligible for p_{T}^{W}. The p_{T}^{W} MJ estimate took approximately three years to complete.

Uncertainty propagation is explained in the next section (Section 7.2).

7.2 Uncertainties

Uncertainties in an analysis come from many different sources and each must be identified and understood. In high-precision analyses like this one, this is often the most important and time-consuming step. In analyses where the final result is unfolded, each uncertainty must be unfolded as well, which adds to the computational length of the unfolding process. This section outlines the subsets of the uncertainties that must be estimated for the p_{T}^{Z} analysis and presents the overall total unfolded measurement uncertainties.

7.2.1 Statistical Uncertainties

All distributions in both data and simulation are produced with a finite number of events, and thus are subject to random fluctuations. The impact of these random fluc-

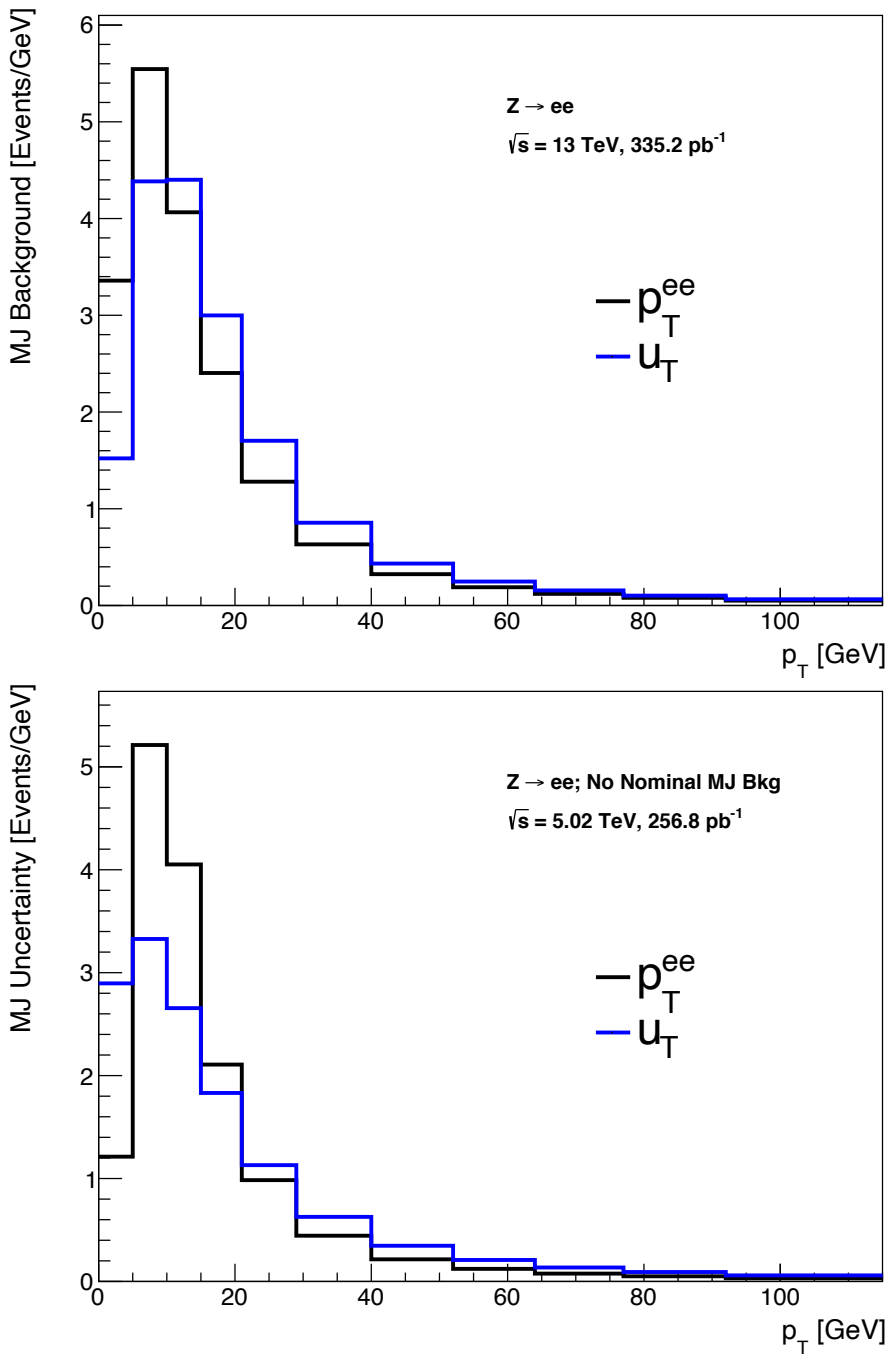

Figure 7.7: MJ distributions for the p_{T}^{ll} and u_{T} observables at $\sqrt{s} = 13$ TeV (top) and 5 (bottom) TeV in the $Z \to e^+e^-$ channel determined using the ABCD method. The nominal MJ background at $\sqrt{s} = 5$ TeV is consistent with 0, so the uncertainty is plotted instead.

tuations must be understood and propagated as a statistical uncertainty. A technique known as the bootstrap method [85, 86] is used to evaluate statistical uncertainties for large datasets. The bootstrap method propagates statistical fluctuations through a resampling of the distributions in the analysis and measures their impact.

The impact of statistical fluctuations is evaluated with the bootstrap method by creating ensembles of pseudo-datasets for both data and MC. The number of events with given characteristics is fluctuated around the number of events that were actually observed (or simulated) within the expected statistical uncertainty. When working with histograms (like in this and most ATLAS analyses), the histogram bin contents are randomly fluctuated around their nominal values within the statistical uncertainty. The bootstrap method naturally accounts for the correlations of statistical fluctuations between the observables and distributions of relevance for the analysis. The method is repeated many times to generate an ensemble of datasets in order to mimic the expected fluctuations with sufficient precision. In practice, ~ 100 pseudo-datasets are often enough to properly evaluate the statistical uncertainties. The more pseudo-datasets, the better, but this can become too computationally time-consuming. However in this analysis since the low-μ dataset is smaller, 400 pseudo-datasets are used for each set of bootstrapping in order to have a stronger handle on the statistical uncertainties.

Once the pseudo-datasets have been generated using the bootstrap method, the statistical uncertainty can be calculated. Unfolding must be incorporated into the calculation process. Data statistical uncertainties result from fluctuations in the observed spectrum D. For each pseudo-dataset α and for a given reco-level bin i (j refers to a truth-level bin), the unfolded spectrum is

$$\tilde{U}_j^\alpha = \sum_i U_{ij}(D_i^\alpha - B_i), \tag{7.2}$$

where B is the sum of all backgrounds, and U_{ij} is the migration matrix. Assuming N_s pseudo-datasets, the corresponding covariance is estimated as

$$C_{kl}^{\text{stat,Data}} = \frac{1}{N_s - 1} \sum_{\alpha=1}^{N_s} (\tilde{U}^{\alpha_k} - \langle \tilde{U} \rangle_k)\,(\tilde{U}^{\alpha_l} - \langle \tilde{U} \rangle_l), \tag{7.3}$$

where $\langle U \rangle_{k,l}$ denotes the average over the bootstrap datasets. The total statistical uncertainty on the unfolded data, per bin, is then the square root of each diagonal component of the covariance matrix:

$$\delta \tilde{U}_k = \sqrt{C_{kk}^{\text{stat,Data}}}. \tag{7.4}$$

MC statistical uncertainties are calculated in a similar fashion to data, except that instead of having 400 reco-level pseudo-datasets D^α, 400 pseudo-migration matrices are generated with the bootstrap method, denoted by U^α. Therefore, Equation (7.2) becomes

$$\tilde{U}_j^\alpha = \sum_i U_{ij}^\alpha (D_i - B_i), \tag{7.5}$$

and then Equations (7.3) and (7.4) follow in the same way as for the data statistical uncertainty measurement.

7.2.2 Systematic Uncertainties

There are numerous systematic uncertainties in the p_{T}^Z measurement that can generally be decomposed into a large set of uncorrelated sources of uncertainty. These sources include uncertainties stemming from lepton and recoil calibration corrections, lepton efficiency corrections and background subtraction. Table 7.6 lists the sources of p_{T}^Z measurement uncertainties along with brief descriptions of each. Each of the uncertainties arising from scale factors come directly from the methods outlined in Section 4.2. The TTVA uncertainty is determined using the tag-and-probe method as well but with $Z \to \mu^+\mu^-$ events, and is provided by the muon performance group [87]. The recoil uncertainty is determined based on the method of the ATLAS m_W measurement [54], but is updated and redone with the low-μ dataset. The energy calibration uncertainty determination follows the standard ATLAS high-μ process [47]. The background processes were discussed at the beginning of Section 7.1. Each background process is also bootstrapped just like the data to create varied background datasets.

The unfolded uncertainty associated with each of the (non-background) reco-level

Source	Uncertainty Description
Reconstruction	reconstruction scale factor (SF) (Sec. 4.2.2)
Isolation	isolation SF (Sec. 4.2.4)
Trigger	trigger SF (Sec. 4.2.5)
Electron ID	electron identification SF (only for $Z \to e^+e^-$) (Sec. 4.2.3)
TTVA	muon track-to-vertex association process (only for $Z \to \mu^+\mu^-$)
Recoil	construction and calibration of hadronic recoil
Calibration	energy calibration of electrons and muons
Background	simulated (and data-driven) background processes

Table 7.6: Sources of systematic uncertainty for the p_{T}^{Z} measurement.

uncertainties listed in Table 7.6 is given by

$$\tilde{U}_j^a = \sum_i U_{ij}^a (D_i - B_i), \tag{7.6}$$

where a refers to the specific correction involved. The unfolded background uncertainty is calculated using the equation

$$\tilde{U}_j^a = \sum_i U_{ij} (D_i - B_i^a), \tag{7.7}$$

where B^a is a varied estimate of each individual background.

7.2.3 Unfolding Bias Uncertainty

The uncertainty from the unfolding process, the unfolding bias, outlined in Section 6.2.4, acts as its own uncertainty category since it must be estimated using the unfolding process while taking the sum of the statistical and systematic uncertainties into account. The unfolding bias uncertainty for p_{T}^{Z} is estimated using a similar method to that of the p_{T}^{W} measurement. This is the focus of Chapter 8, so the explanation is left for that chapter.

The number of unfolding iterations (N_{iter}) must be chosen by minimizing the

total uncertainty, since the unfolding bias decreases with number of iterations while the statistical (and to a lesser extent, systematic) uncertainties increase with the number of iterations. The process to select N_{iter} is somewhat ad-hoc, since it is impossible to optimize the total uncertainty in every p_{T} bin. Generally, high-purity observables like p_{T}^{ll} require a low number of iterations, while low-purity observables like u_{T} will need more iterations. There are a few different plots one can look at when trying to select N_{iter}. One such plot is shown in Figure 7.8, which shows the total uncertainty (statistical plus systematic plus bias) as a function of p_{T} in the $\sqrt{s} = 13$ TeV $Z \to e^+e^-$ channel for the p_{T}^{ll} observable for increasing numbers of iterations. After one iteration, the N_{iter} curves converge and there is minimal difference in the total uncertainty between the number of iterations, but the 1 iteration curve is significantly larger in the first bin. Therefore the next N_{iter} can be chosen to reach the convergence without unfolding an unnecessary number of times. Using this plot, and knowing that the purity of p_{T}^{ll} is high, we select 2 iterations. A similar process led to selecting 2 iterations for the other p_{T}^{ll} channels as well.

The minimization process can be a bit more complicated for the u_{T} observable because of its low purity, so we need to look at more than just the total uncertainty. Figure 7.9 shows the same total uncertainty plot in the upper panel for the u_{T} observable (still using the $\sqrt{s} = 13$ TeV $Z \to e^+e^-$ channel as an example), while the lower plot still shows the uncertainty percentage as a function of p_{T}, but with the statistical uncertainty and unfolding bias uncertainty shown separately. In the upper plot, the N_{iter} curves do not converge like they do in Figure 7.8, so it is not clear what N_{iter} to choose just by looking at this total uncertainty. In the lower plot, we see that in each individual bin, as N_{iter} increases, the bias uncertainty decreases but the statistical uncertainty increases. We want to choose the N_{iter} curve that gives the greatest decrease in bias uncertainty while increasing the statistical uncertainty the least, focusing on the highest statistics bins. The N_{iter} curves that optimize this are the 9 and 11 iteration curves. Additional plots (not shown) were made for this optimization process to show uncertainty as a function of N_{iter} for each of the first four p_{T} bins in order to really isolate the highest-statistics bins. After combining this information, 10 iterations were chosen for u_{T} at $\sqrt{s} = 13$ TeV and 5 iterations were chosen for $\sqrt{s} = 5$ TeV.

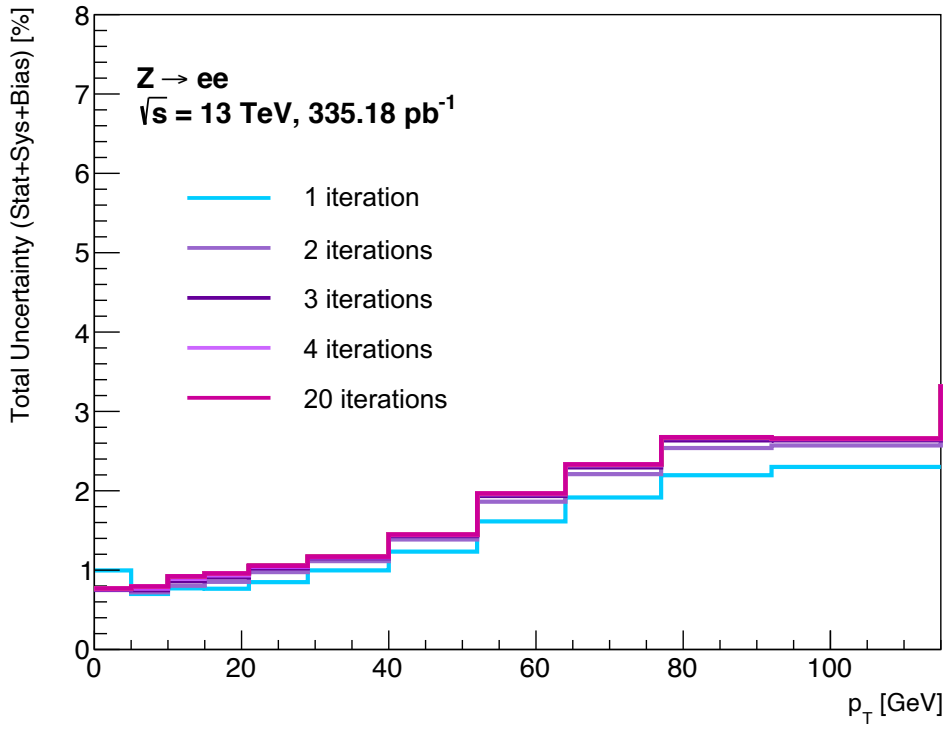

Figure 7.8: Total uncertainty percentage as a function of p_{T} for the p_{T}^{ll} observable in the $Z \to e^+e^-$ channel at $\sqrt{s} = 13$ TeV, for an increasing number of unfolding iterations.

The optimal histogram p_{T} binning was also chosen by considering the total uncertainty but the optimization is not part of this thesis. When bin widths are smaller, the resolution of the measurement increases, but so does the uncertainty per bin. Optimizing the bin width is a balance between a well-resolved measurement and its high precision. The p_{T}^{ll} observable allows for smaller bin widths at low-p_{T} because it is measured with higher precision than u_{T}. Histograms are presented with the optimal bin width for each observable.

7.2.4 Luminosity Uncertainty

The final uncertainty that must be considered is the luminosity uncertainty. This is determined by ATLAS primarily using the LUCID detector for each year of running. Separate measurements are made for special runs including the low-μ run. The uncer-

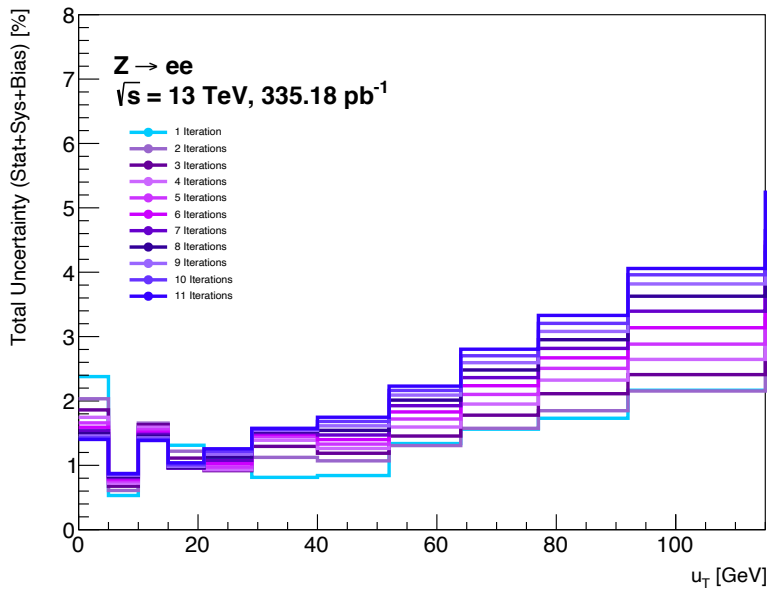

(a) Total Unc.

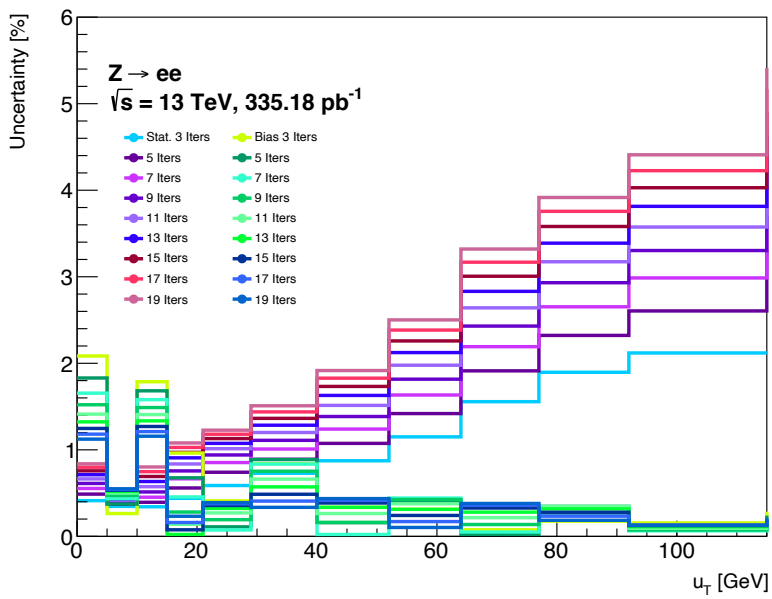

(b) Stat. & Bias Unc.

Figure 7.9: Uncertainty percentage as a function of p_{T} for the u_{T} observable in the $Z \to e^+e^-$ channel at $\sqrt{s} = 13$ TeV, for an increasing number of unfolding iterations. The top plot shows the total uncertainty similar to Fig. 7.8, while the bottom plot shows uncertainty percentage divided between the unfolding bias uncertainty and the statistical uncertainty.

tainty for the 2017 and 2018 low-μ runs was found to be 1.5% for both $\sqrt{s} = 13$ TeV and 5 TeV [88,89]. This uncertainty is constant, irrespective of observable. While this is a large overall uncertainty for this high-precision measurement, when an ATLAS cross-section measurement is normalized to the total cross section, the luminosity uncertainty cancels out. However, the luminosity uncertainty is still important to include in total uncertainty and cross-section results.

7.2.5 Total p_{T}^{Z} Measurement Uncertainties

All of the uncertainties discussed in this section are combined into total percent uncertainty plots as a function of p_{T} for each channel, observable, and energy. Figures 7.10 and 7.11 show the final uncertainty for each individual source in the $Z \to e^+e^-$ channel at $\sqrt{s} = 13$ TeV for the p_{T}^{ll} and u_{T} observables, respectively. Similar plots for $\sqrt{s} = 5$ TeV are shown in Figures 7.12 and 7.13. Corresponding figures for the $Z \to \mu^+\mu^-$ channels can be found beginning with Figure D.6 of Appendix D.

One of the goals of the analysis was to show that all of the sources of systematic uncertainty could be well-understood and measured, summing to a total uncertainty of order approximately 1%. The uncertainty breakdown plots show that we have reached this goal. The largest contributing uncertainty is the luminosity uncertainty (orange curve). This uncertainty is irreducible, and is present and constant for all ATLAS analyses. As we will see, this uncertainty disappears when looking at the normalized cross-section plots in Section 7.3. The next largest uncertainty is the statistical uncertainty coming from the data (pink curve). This is a great sign, because this is an uncertainty that can be reduced simply by taking more data! Increased statistics may also enable finer binning as a function of p_{T}, or the measurement of the double-differential cross section (as a function of p_{T} and rapidity for example) which would provide much more information. As has been discussed, the low-μ dataset is incredibly small relative to the high-μ dataset. These results can be presented to ATLAS to argue for additional low-μ datasets during Run 3, given that the measurement is limited only by luminosity and statistics. If we can double the dataset with an additional two weeks of running with a low number of average p-p collisions per bunch crossing, our statistical uncertainty should decrease by roughly half so that it becomes comparable to the systematic uncertainties. The systematic uncertainties

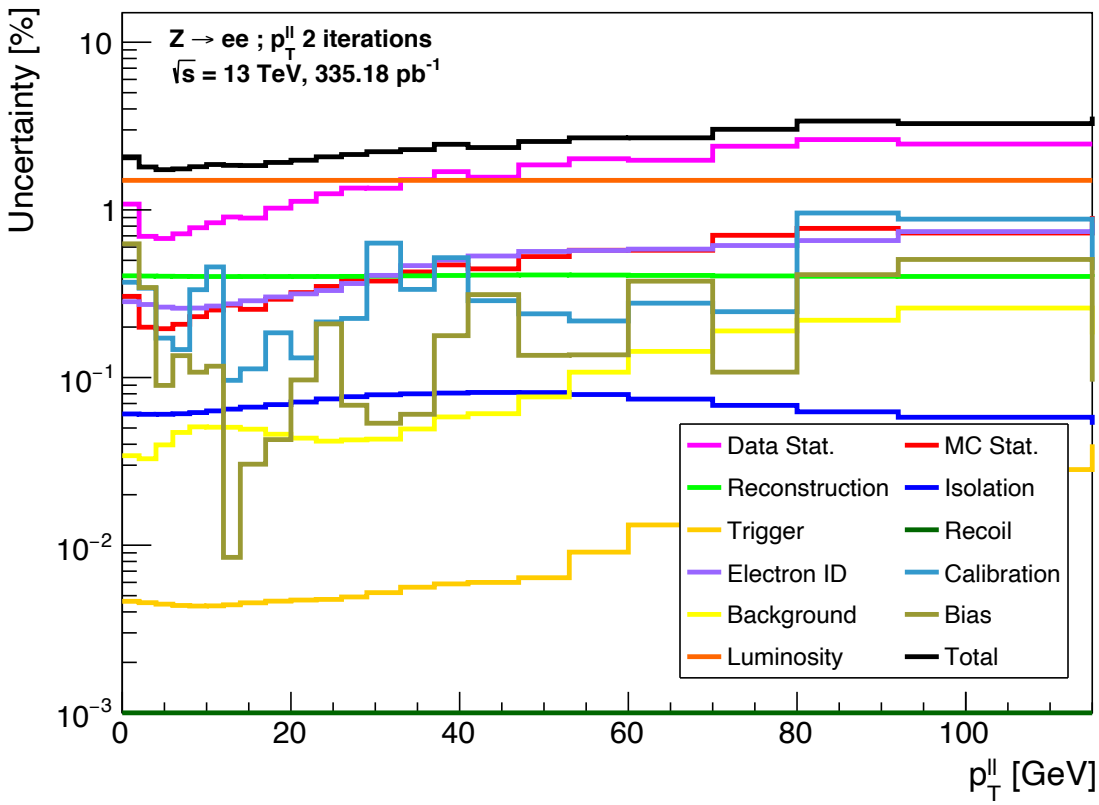

Figure 7.10: Total percent uncertainty as a function of p_{T} for all the sources of uncertainty that contribute to the final p_{T}^{Z} measurement in the $Z \to e^{+}e^{-}$ channel at $\sqrt{s} = 13$ TeV for the p_{T}^{ll} observable. Each contributing source is unfolded with 2 unfolding iterations (aside from luminosity which is not affected by unfolding). The total uncertainty (black) is the sum in quadrature of each individual source.

are more difficult to reduce and do not simply depend on taking more data, so if the systematic uncertainties were dominant, we would not be able to make this argument for more data.

Due to the low purity of the u_{T} observable, the unfolding bias uncertainty for u_{T} remains a relatively large uncertainty in the low-p_{T} bins. Estimating and minimizing this uncertainty source was one of the most difficult portions of the analysis (as we will see in Chapter 8). However, its current value is still roughly a factor of three lower than what it was at the beginning of 2020. Additional data should reduce the bias uncertainty in the future, because then a larger number of unfolding iterations can be selected since the statistical uncertainty will be less dominant. The contribution

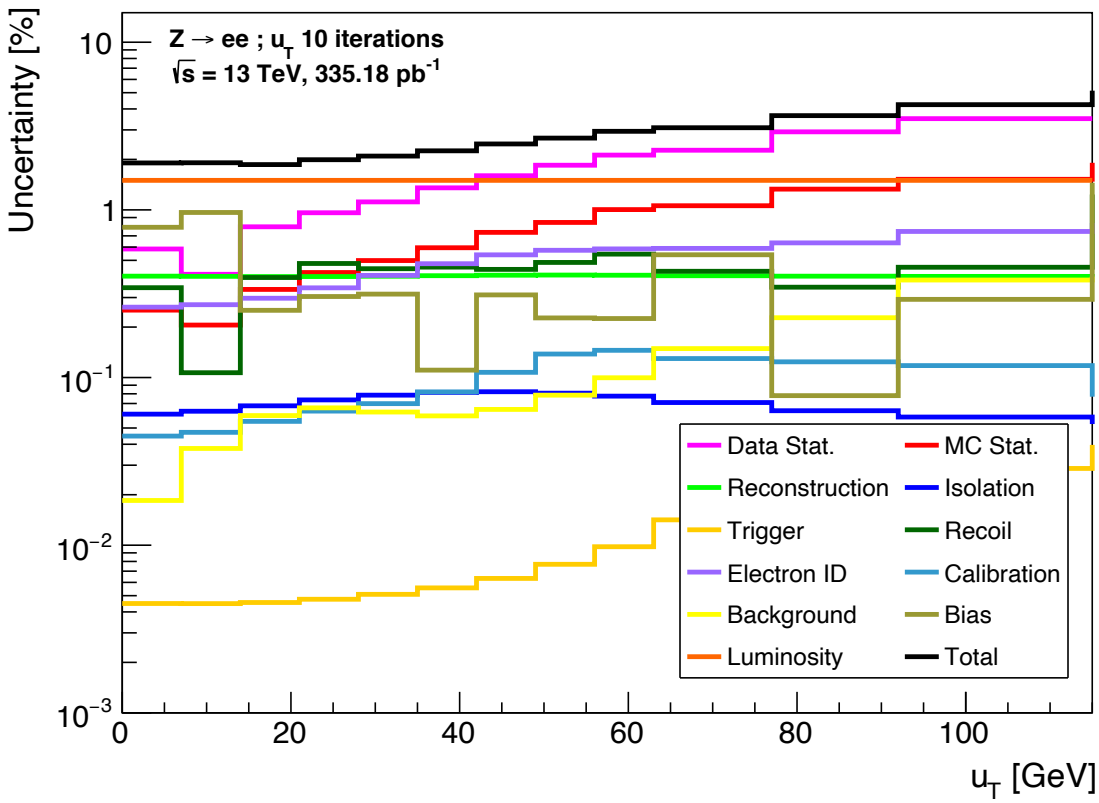

Figure 7.11: Total percent uncertainty as a function of u_{T} for all the sources of uncertainty that contribute to the final p_{T}^{Z} measurement in the $Z \to e^{+}e^{-}$ channel at $\sqrt{s} = 13$ TeV for the u_{T} observable. Each contributing source is unfolded with 10 unfolding iterations (aside from luminosity which is not affected by unfolding). The total uncertainty (black) is the sum in quadrature of each individual source.

from the bias uncertainty will also be less significant when the combination of the $Z \to e^{+}e^{-}$ and $Z \to \mu^{+}\mu^{-}$ channels is taken. The unfolding bias uncertainty is correlated between these channels, so the combination will reduce the effect that it has on the final measurement. Other than the luminosity, statistical, and unfolding bias uncertainties, each systematic uncertainty contributes to the total uncertainty at a level of about 0.5% or less.

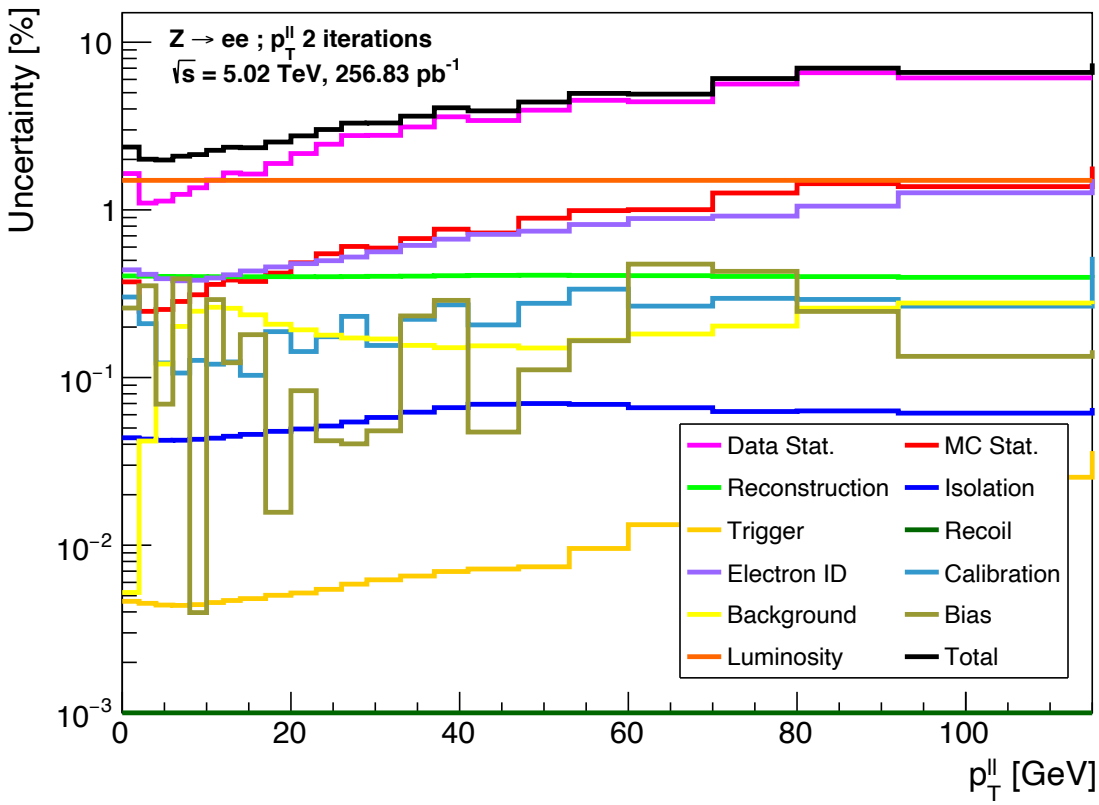

Figure 7.12: Total percent uncertainty as a function of p_{T} for all the sources of uncertainty that contribute to the final p_{T}^{Z} measurement in the $Z \to e^+e^-$ channel at $\sqrt{s} = 5$ TeV for the p_{T}^{ll} observable. Each contributing source is unfolded with 2 unfolding iterations (aside from luminosity which is not affected by unfolding). The total uncertainty (black) is the sum in quadrature of each individual source.

7.3 Unfolded Cross Sections

As has been mentioned, the data and each uncertainty were unfolded using an iterative Bayesian unfolding algorithm. The unfolded cross-section results are presented here. Continuing with $Z \to e^+e^-$ as the sample channel, Figure 7.14 shows the differential cross section as a function of p_{T} for both the p_{T}^{ll} ($\frac{d\sigma}{dp_{\mathrm{T}}^{ee}}$) (top) and u_{T} ($\frac{d\sigma}{du_{\mathrm{T}}}$) (bottom) observables at $\sqrt{s} = 13$ TeV, compared to the nominal MC prediction: Powheg+Pythia8. The data are shown with their full uncertainty, although the total uncertainty is still smaller than the size of the data points. The lower ratio panel shows the data/MC ratio, with the uncertainty bands on the data split between sta-

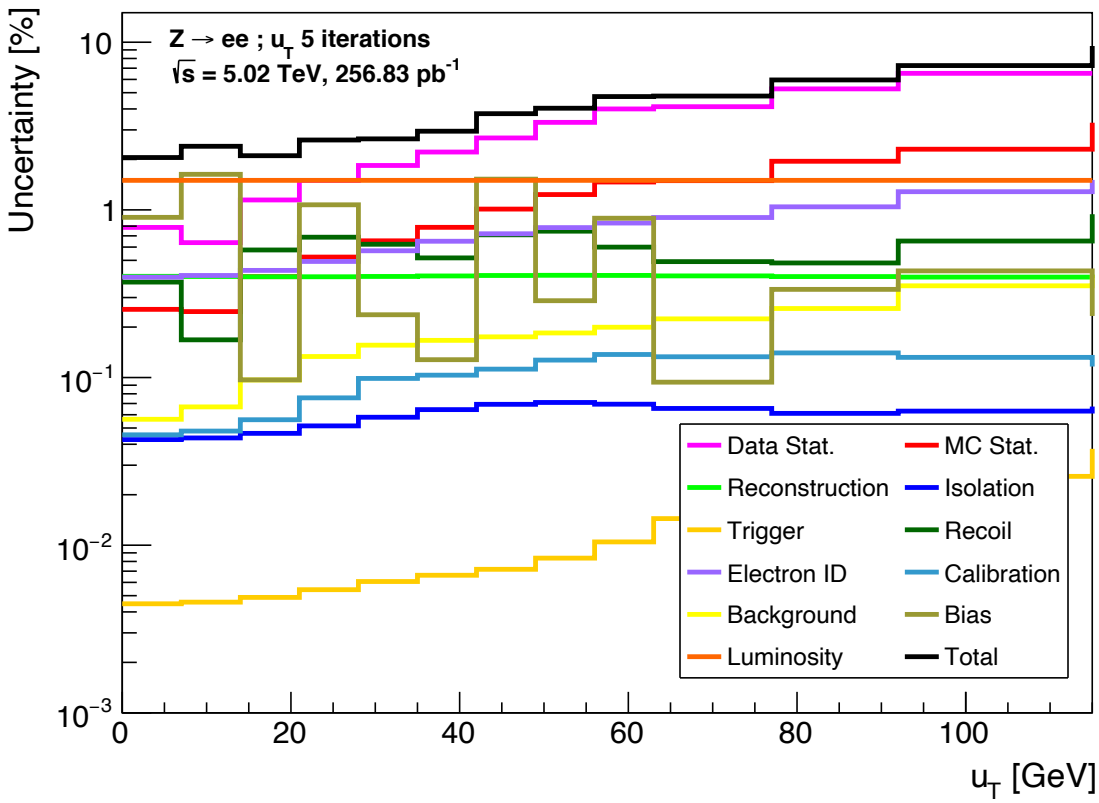

Figure 7.13: Total percent uncertainty as a function of u_{T} for all the sources of uncertainty that contribute to the final p_{T}^{Z} measurement in the $Z \to e^{+}e^{-}$ channel at $\sqrt{s} = 5$ TeV for the u_{T} observable. Each contributing source is unfolded with 5 unfolding iterations (aside from luminosity which is not affected by unfolding). The total uncertainty (black) is the sum in quadrature of each individual source.

tistical, systematic, and luminosity. The MC uncertainty band is also shown but it is negligible relative to the data statistical and luminosity uncertainties. Even still, the total uncertainty is quite small and can barely be seen beyond the data points themselves.

There are a few things to note when discussing this result. The least important aspect of the measurement is the magnitude of the curve. The absolute values are not so important for us, unless we are comparing to total cross sections of other processes, which is not the purpose of this analysis. However, we can still compare the $Z \to e^{+}e^{-}$ total differential cross section at $\sqrt{s} = 13$ TeV to that of $\sqrt{s} = 5$ TeV (comparing Figure 7.14 to Figure 7.15) to see that there is a higher probability of

observing this process at a higher centre-of-mass energy. What is more important is the shape of the curve because this shows the distribution of events as a function of p_{T}, which is especially important at low-p_{T}. This low-p_{T} peak is the sum of all physical processes that produce transverse momentum when a Z boson decays to two leptons. As expected, the curve peaks at a non-zero value, since we always must have some transverse momentum (as was explained at the beginning of Chapter 5). The curve quickly decays as p_{T} increases, since it is much less common to have large transverse momentum contributions from dileptonic decays, especially once the Z boson mass ($m_Z \approx 91$ GeV) is reached.

Comparing the data to the nominal prediction, the prediction slightly undershoots the data in the $Z \to e^+e^-$ channel at $\sqrt{s} = 13$ TeV. This is less-so the case in the $Z \to \mu^+\mu^-$ channel (Figure D.10 of Appendix D). However, the data were also shown to be consistent with the high-μ p_{T}^Z result (that specific comparison result is not part of this thesis), so the difference between data and MC can be attributed to the fact that we still need to improve our understanding of the processes involved, or at least improve the prediction that we are using. The agreement between data and prediction is improved at $\sqrt{s} = 5$ TeV (Figure 7.15 for the $Z \to e^+e^-$ channel and Appendix Figure D.11 for the $Z \to \mu^+\mu^-$ channel). This is the first time that ATLAS has measured p_{T}^Z at $\sqrt{s} = 5$ TeV.

Another interesting point can be made when comparing the p_{T}^{ll} observable to the u_{T} observable. The dilepton transverse momentum plots (top plot in the figures) show more statistical fluctuations (more easily seen in the ratio panel) compared to the hadronic recoil plots, where the curve appears to be more smooth bin-to-bin. This is because of the high purity of the p_{T}^{ll} observable and the low purity of the u_{T} observable. Consecutive bins are more correlated for u_{T} so the curve appears to be smoother. The observables are directly compared in the next section (Sec. 7.4).

While it is important to show the total differential cross section, the normalized differential cross section, $\frac{1}{\sigma}\frac{d\sigma}{dp_{\mathrm{T}}^Z}$, (normalized to the total cross section) is more effective at comparing the shapes of different predictions to the data, especially at low-p_{T} where the predictions need improvement. Additionally, the normalized cross section eliminates the luminosity uncertainty. The normalized differential cross section for $Z \to e^+e^-$ at $\sqrt{s} = 13$ TeV is shown in Figure 7.16, with the p_{T}^{ll} observable on the top

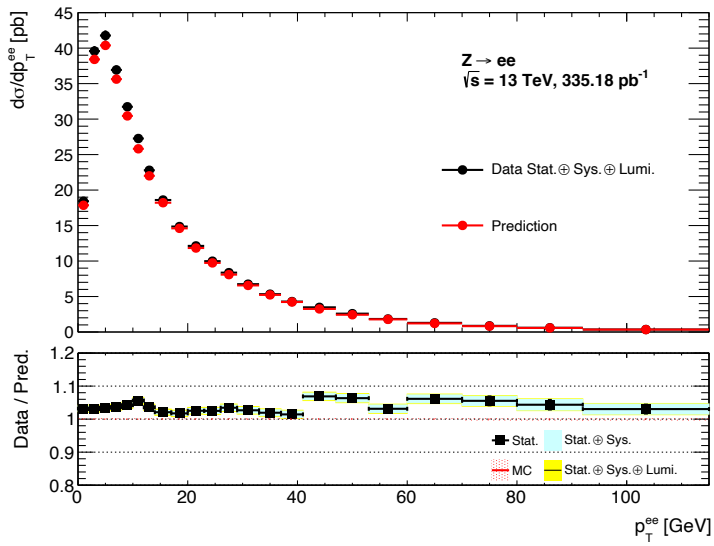

(a) p_{T}^{ll}

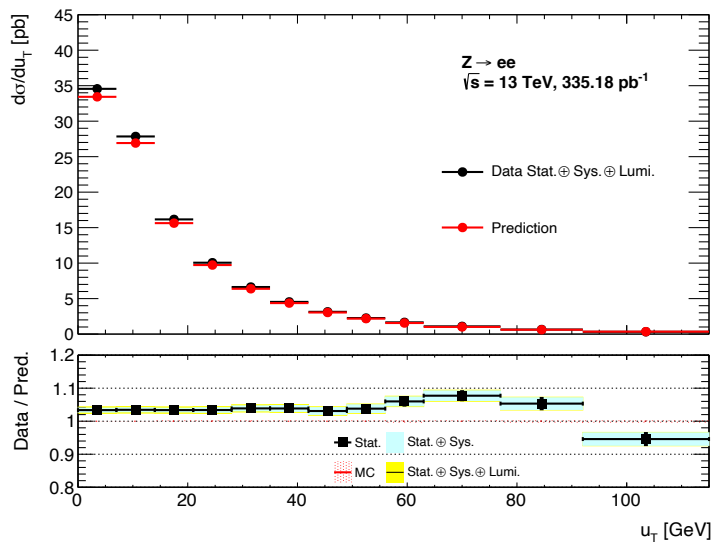

(b) u_{T}

Figure 7.14: Differential cross section as a function of p_{T} in the $Z \to e^+e^-$ channel at $\sqrt{s} = 13$ TeV. The p_{T}^{Z} differential cross section is measured using both the p_{T}^{ll} observable (top) and the u_{T} observable (bottom). The data are shown with their total uncertainty and plotted alongside the nominal MC prediction. The lower ratio panel shows the data-to-prediction ratio. The uncertainty on the data points are shown as increasingly large bands, incorporating the statistical (black vertical bars), systematic (blue band), and luminosity (yellow band) uncertainties. The MC statistical uncertainty (red dotted band) is also shown along the x-axis but it is negligible on this plot.

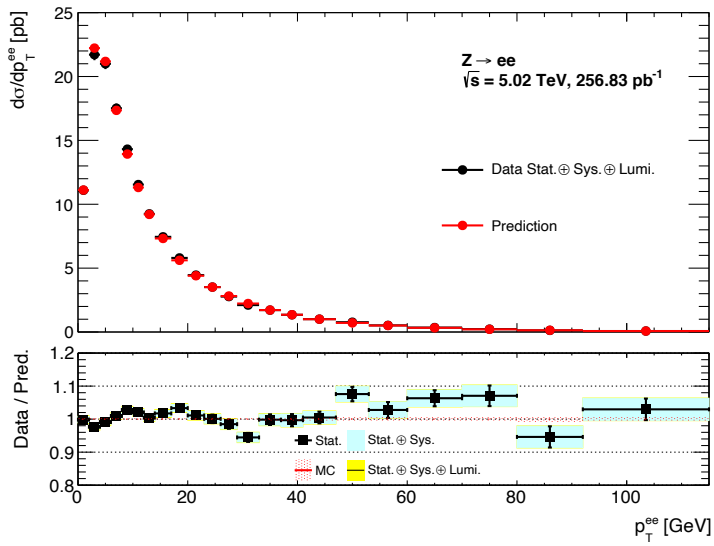

(a) p_{T}^{ll}

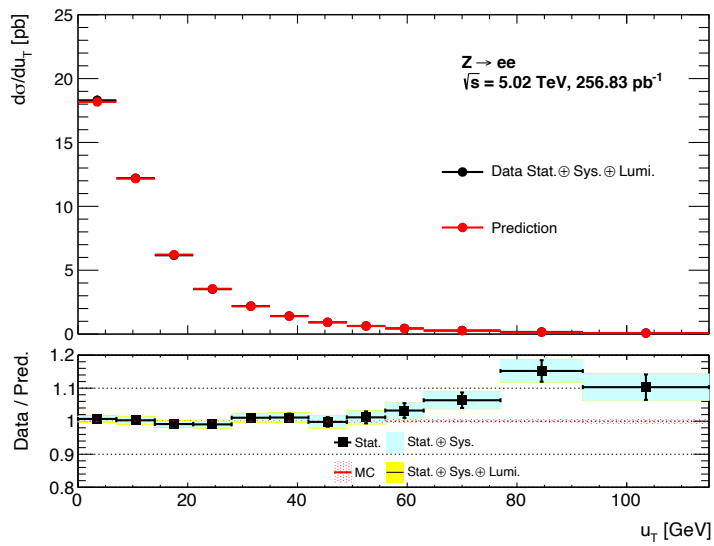

(b) u_{T}

Figure 7.15: Differential cross section as a function of p_{T} in the $Z \to e^+e^-$ channel at $\sqrt{s} = 5$ TeV. The p_{T}^{Z} differential cross section is measured using both the p_{T}^{ll} observable (top) and the u_{T} observable (bottom). The data are shown with their total uncertainty and plotted alongside the nominal MC prediction. The lower ratio panel shows the data-to-prediction ratio. The uncertainty on the data points are shown as increasingly large bands, incorporating the statistical (black vertical bars), systematic (blue band), and luminosity (yellow band) uncertainties. The MC statistical uncertainty (red dotted band) is also shown along the x-axis.

and the u_{T} observable on the bottom. The corresponding $\sqrt{s} = 5$ TeV plots are shown in Figure 7.17. The $Z \to \mu^+\mu^-$ channel plots are shown in Appendix D, Figures D.12 and D.13. In addition to the nominal Powheg+Pythia8 MC, the other predictions that are shown are Sherpa 2.2.1 [90], a different NLO event generator, DYTurbo NNLO+NNLL [91], a numerical program specifically made for the calculation of the QCD p_{T} resummation of Drell-Yan cross sections up to NNLL low-p_{T} and NNLO high-p_{T} accuracy, and the Pythia8 AZ tune mentioned in Section 5.2 that was used for the ATLAS m_W measurement [54].

The normalized plots clearly show the differences between predictions as compared to the data. At $\sqrt{s} = 13$ TeV, no prediction accurately represents the data at low-p_{T}, especially given the high precision of the measurement. As a function of p_{T}, the predictions show large variations relative to each other, depending on the model or tuning that each prediction uses, as well as the order to which each is accurate (see Chapter 5 for a reminder of these details). The nominal prediction still provides the best representation of the data overall. At $\sqrt{s} = 5$ TeV, both Pythia predictions do a reasonable job at representing the data, partially due to the larger error bands. However, Sherpa and DYTurbo still show large fluctuations compared to the data.

This high-precision p_{T}^{Z} measurement will be able to feed into the predictions to improve their accuracy, such that future predictions that they make better represent these dileptonic decays.

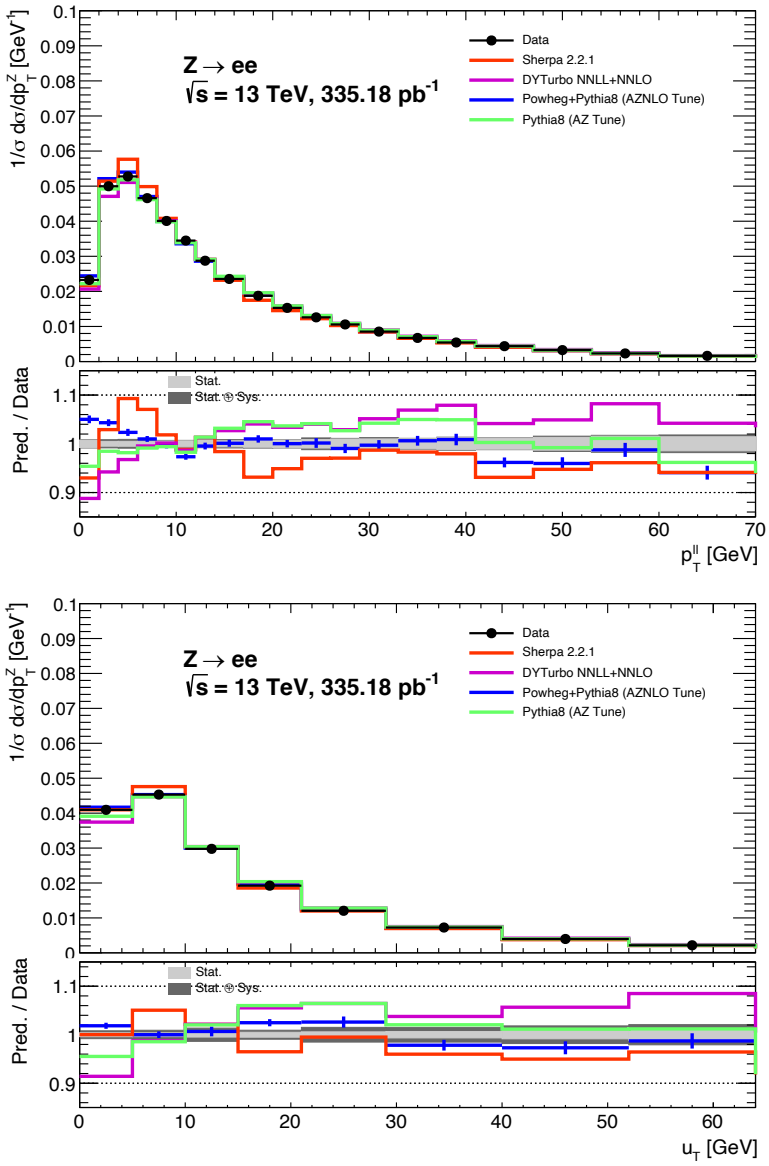

Figure 7.16: $Z \to e^+e^-$ normalized differential cross section as a function of p_{T} for the p_{T}^{ll} (top) and u_{T} (bottom) observables at $\sqrt{s} = 13$ TeV. The differential cross section is normalized to the total cross section. In each plot, the data are compared to four different predictions: the nominal Powheg+Pythia8 MC shown with its statistical error bars (blue curve), Sherpa (red curve), DYTurbo (purple curve), Pythia8 AZ (green curve). The ratio plot in the lower panel shows each prediction divided by the data. The data, with its central value of 1 along the lower panel x-axis, are shown with its statistical uncertainty band (light grey) and the statistical plus systematics uncertainty band (dark grey).

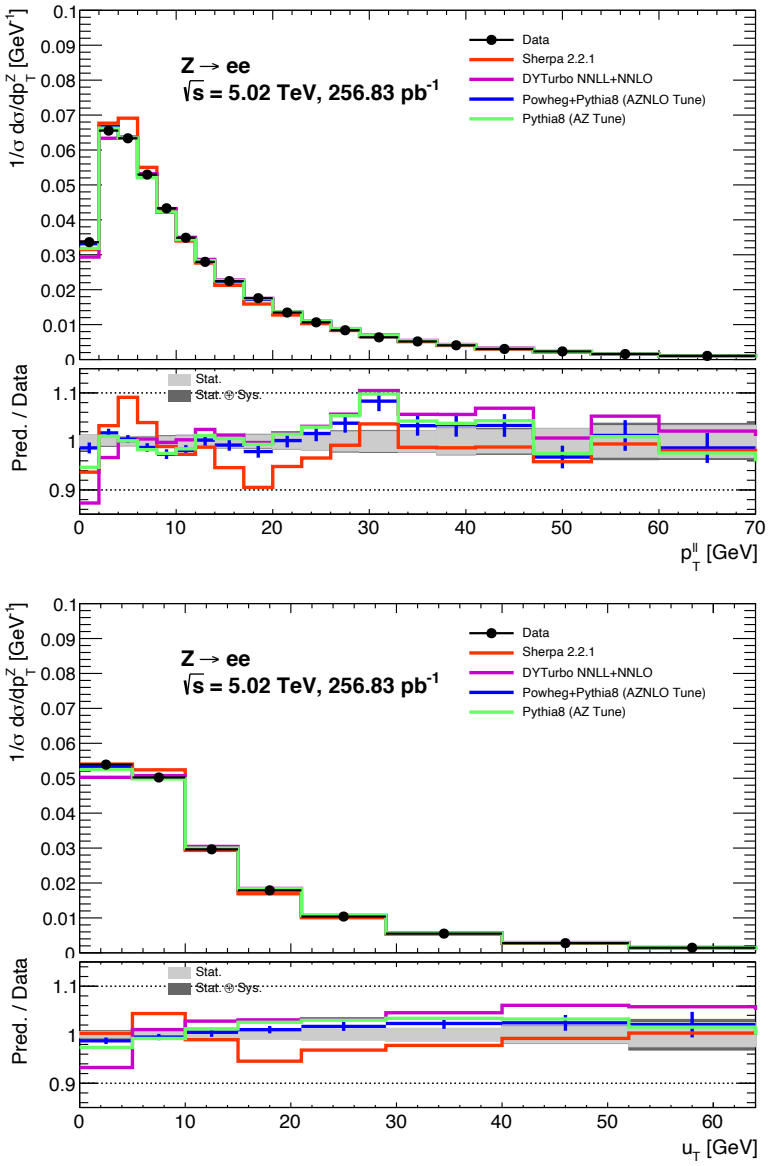

Figure 7.17: $Z \to e^+e^-$ normalized differential cross section as a function of p_{T} for the p_{T}^{ll} (top) and u_{T} (bottom) observables at $\sqrt{s} = 5$ TeV. The differential cross section is normalized to the total cross section. In each plot, the data are compared to four different predictions: the nominal Powheg+Pythia8 MC shown with its statistical error bars (blue curve), Sherpa (red curve), DYTurbo (purple curve), Pythia8 AZ (green curve). The ratio plot in the lower panel shows each prediction divided by the data. The data, with its central value of 1 along the lower panel x-axis, are shown with its statistical uncertainty band (light grey) and the statistical plus systematics uncertainty band (dark grey).

7.4 Compatibility

The p_{T}^{Z} differential cross-section measurement is made in two leptonic decay channels, $Z \to e^+e^-$ and $Z \to \mu^+\mu^-$, and with two equivalent observables, p_{T}^{ll} and u_{T}. At a given centre-of-mass energy, all four of these results should be equivalent, since electroweak theory treats $Z \to e^+e^-$ and $Z \to \mu^+\mu^-$ decays identically, and p_{T}^{ll} and u_{T} are both measures of p_{T}^{Z}. The compatibility between the channels and observables can be tested by taking simple ratio plots.

First, the $Z \to e^+e^-$ and $Z \to \mu^+\mu^-$ compatibility must be confirmed. Figure 7.18 shows the total p_{T}^{Z} differential cross-section measurements at $\sqrt{s} = 13$ TeV with both lepton decay channels shown on the same plot (p_{T}^{ll} on the top and u_{T} on the bottom). The corresponding plots at $\sqrt{s} = 5$ TeV are shown in Figure 7.19. Completely correlated uncertainties like luminosity and recoil calibration are removed for this test, but the rest of the uncertainties for each channel are included in the uncertainty band. As expected, the channels show good consistency. There are deviations from unity at $p_{\mathrm{T}} \approx 20$ GeV and $p_{\mathrm{T}} \approx 40$ GeV where the channels appear to be inconsistent. These deviations were examined in detail and it was determined that they were statistical fluctuations. In the final analysis result, the $Z \to e^+e^-$ and $Z \to \mu^+\mu^-$ channels are combined into a single $Z \to l^+l^-$ differential cross section measurement for both $\sqrt{s} = 13$ TeV and 5 TeV. In these combinations, the correlations between uncertainties are treated more rigorously using covariance matrices for each source of uncertainty instead of simply removing correlated uncertainties and treating the others as completely correlated as is done here. These final lepton-channel combinations are not part of this thesis.

The more interesting compatibility result is the comparison between the observables, p_{T}^{ll} and u_{T}. Measuring p_{T}^{W} is challenging due to the missing neutrino: we only have access to u_{T} as a measure of the transverse momentum of the W boson. With the Z boson, this challenge is absent: we can measure p_{T}^{Z} with both p_{T}^{ll} and u_{T}. These two observables should be completely equivalent, but we need to show this to ensure the efficacy of the p_{T}^{W} measurement, where the transverse momentum of the W boson is measured exclusively using the u_{T} observable.

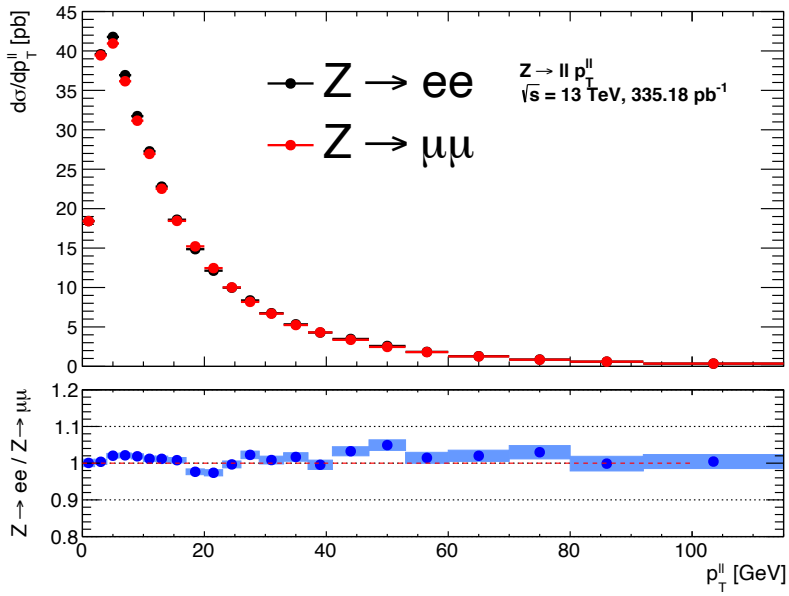

(a) p_{T}^{ll}

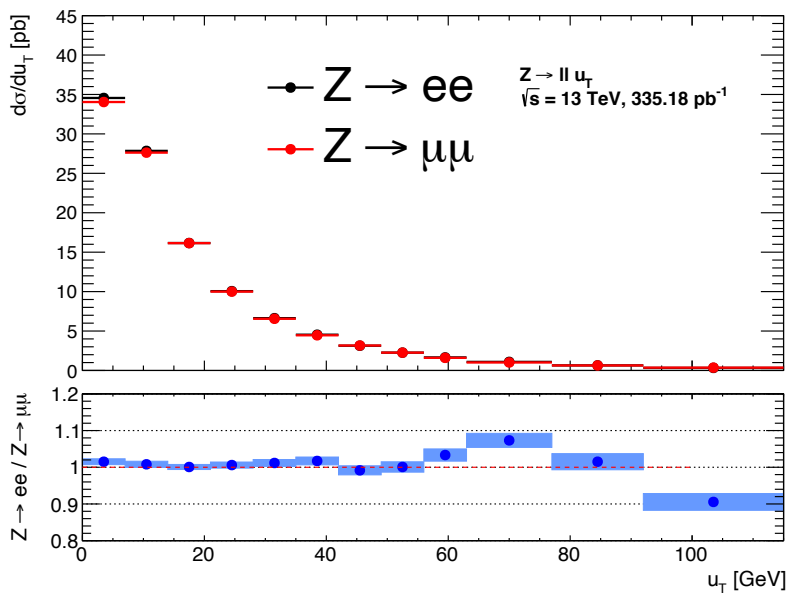

(b) u_{T}

Figure 7.18: Differential cross section as a function of p_{T} for both the $Z \to e^+e^-$ and $Z \to \mu^+\mu^-$ channels at $\sqrt{s} = 13$ TeV. The p_{T}^{Z} differential cross section is measured using both the p_{T}^{ll} observable (top) and the u_{T} observable (bottom). The lower ratio panel shows the $Z \to e^+e^-$ to $Z \to \mu^+\mu^-$ ratio.

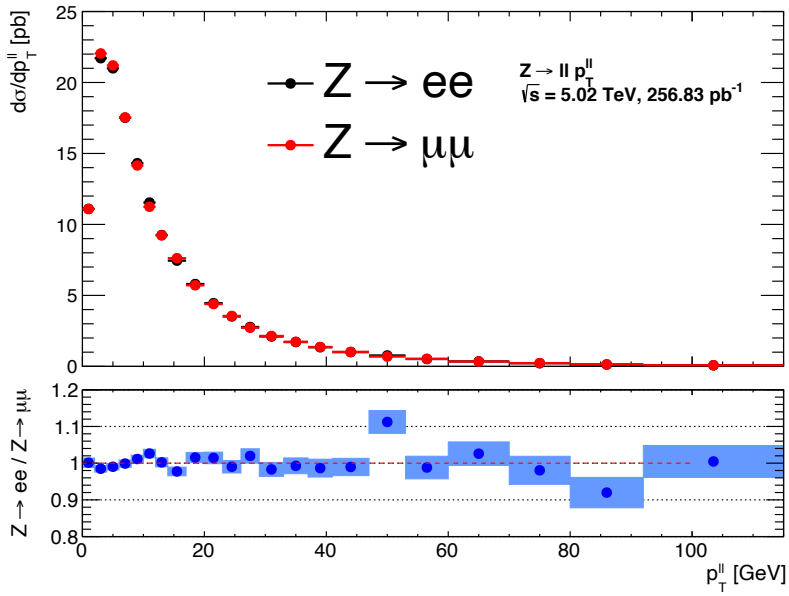

(a) p_{T}^{ll}

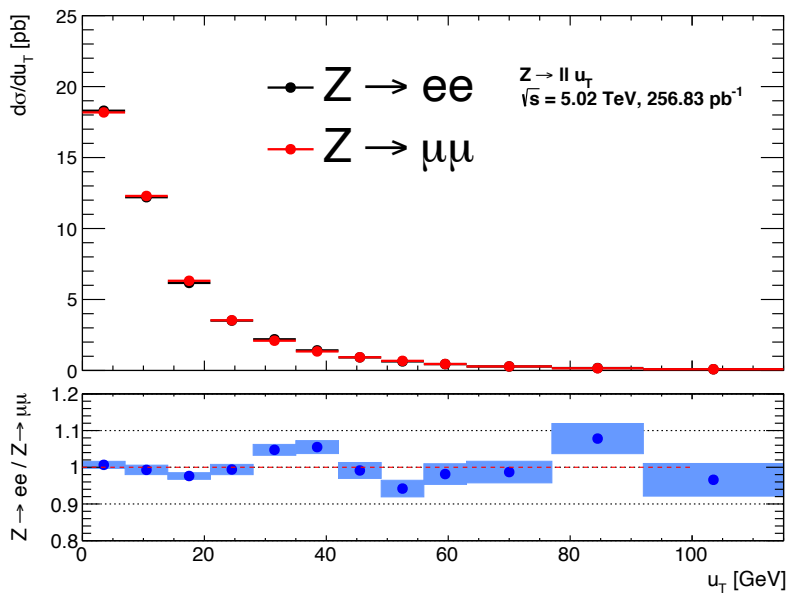

(b) u_{T}

Figure 7.19: Differential cross section as a function of p_{T} for both the $Z \to e^+e^-$ and $Z \to \mu^+\mu^-$ channels at $\sqrt{s} = 5$ TeV. The p_{T}^Z differential cross section is measured using both the p_{T}^{ll} observable (top) and the u_{T} observable (bottom). The lower ratio panel shows the $Z \to e^+e^-$ to $Z \to \mu^+\mu^-$ ratio.

Figure 7.20 shows the p_{T}^{Z} differential cross-section measurement in the $Z \to e^{+}e^{-}$ (top) and $Z \to \mu^{+}\mu^{-}$ (bottom) channels at $\sqrt{s} = 13$ TeV, with both the p_{T}^{ll} and u_{T} observables shown on the same plot. Completely correlated uncertainties like luminosity have been removed, while the remaining uncertainties are included in the uncertainty band. The corresponding comparison plots at $\sqrt{s} = 5$ TeV are shown in Figure 7.21.

For both centre-of-mass energies, it is clear that the two different observables, two completely different ways of measuring p_{T}^{Z}, result in compatible p_{T}^{Z} measurements. This is seen at both $\sqrt{s} = 13$ TeV and 5 TeV, although statistical fluctuations at $\sqrt{s} = 5$ TeV are more prominent. This confirms the efficacy of the hadronic recoil measurement, showing that it accurately reconstructs the transverse momentum of the boson without needing to directly measure the momentum of each of the two individual decay leptons. Hadronic recoil can be used for a high-precision p_{T}^{W} measurement.

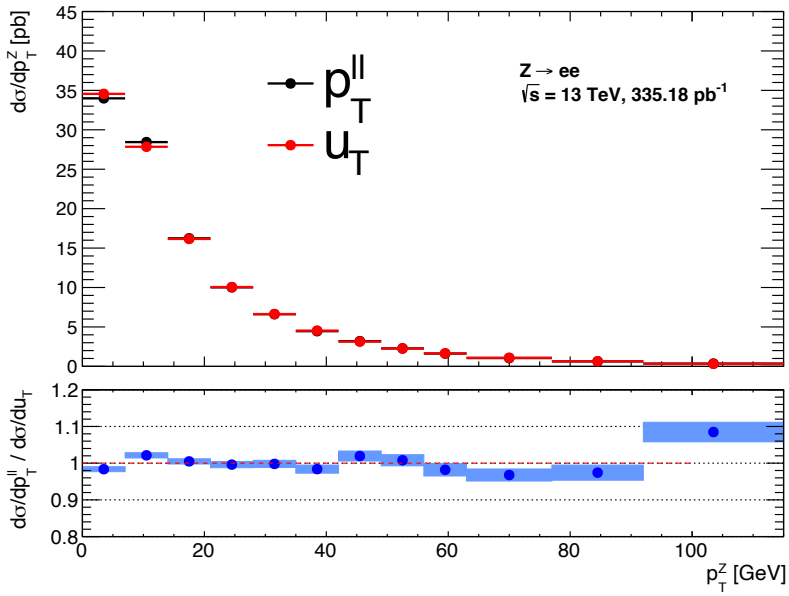

(a) p_{T}^{ll}

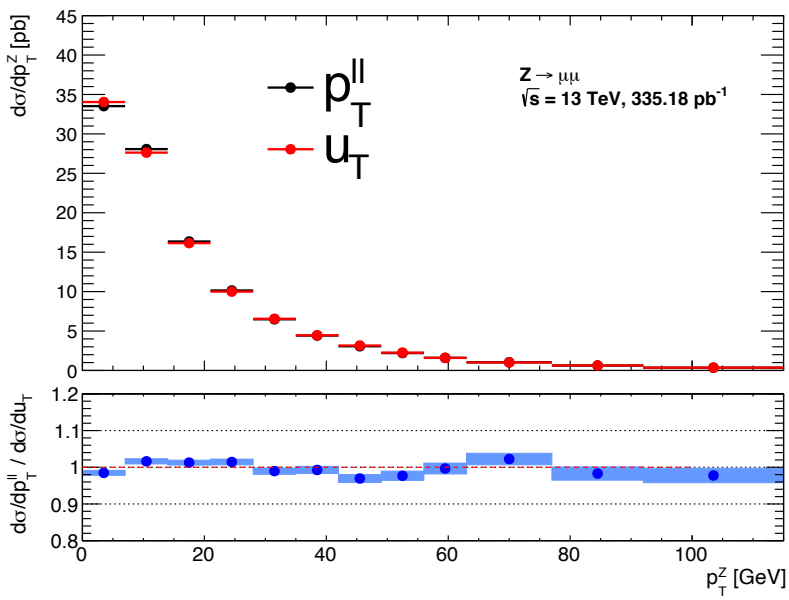

(b) u_{T}

Figure 7.20: Differential cross section as a function of p_{T} for both the p_{T}^{ll} and u_{T} observables at $\sqrt{s} = 13$ TeV. The p_{T}^{Z} differential cross section is measured in both the $Z \to e^+e^-$ (top) and $Z \to \mu^+\mu^-$ (bottom) channels. The lower ratio panel shows the p_{T}^{ll} to u_{T} ratio.

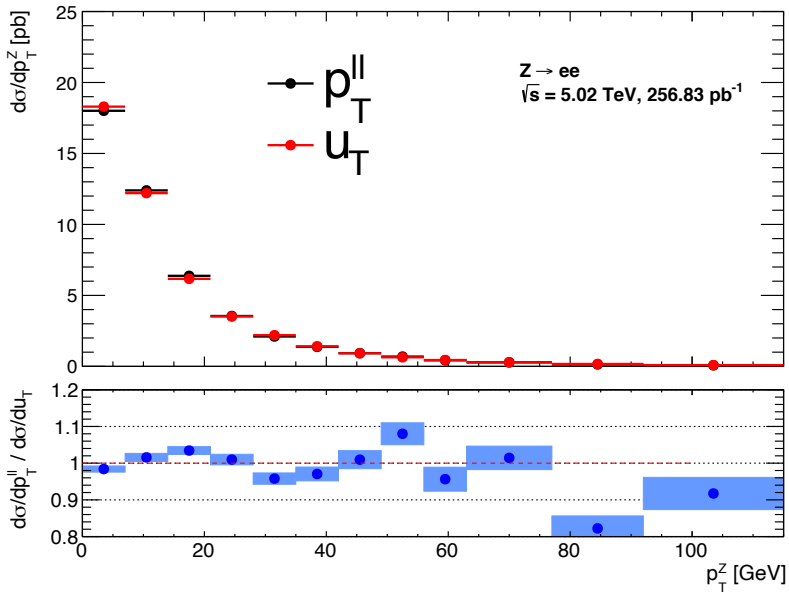

(a) p_{T}^{ll}

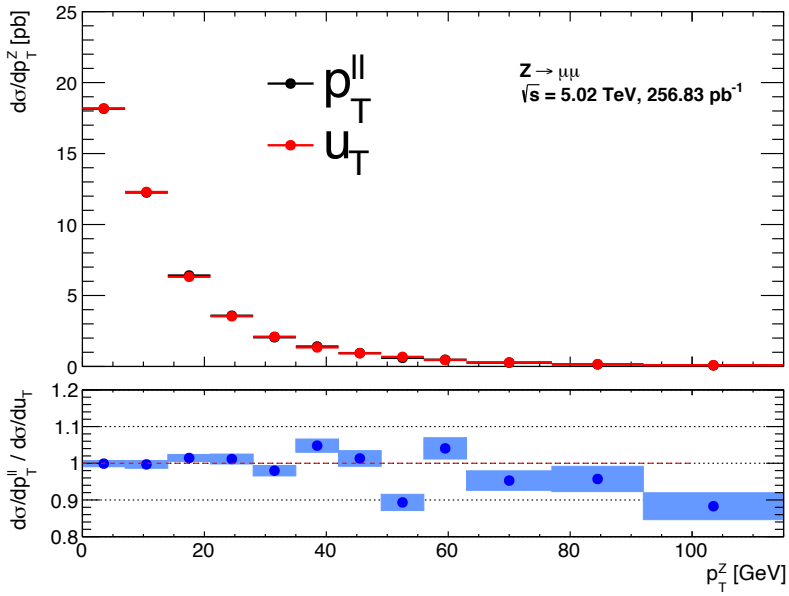

(b) u_{T}

Figure 7.21: Differential cross section as a function of p_{T} for both the p_{T}^{ll} and u_{T} observables at $\sqrt{s} = 5$ TeV. The p_{T}^{Z} differential cross section is measured in both the $Z \to e^+e^-$ (top) and $Z \to \mu^+\mu^-$ (bottom) channels. The lower ratio panel shows the p_{T}^{ll} to u_{T} ratio.

7.5 Summary

After collecting a dataset and producing MC simulations to predict the data, a long chain of steps is required before a final cross-section measurement can be finalized. Initial physics objects must be defined and calibrated, and the backgrounds must be well-understood using both simulation and data-driven techniques. The data and simulation must then pass event selection cuts to isolate the process of interest, and background processes must be removed. The data and simulation must be understood at both reconstructed and unfolded level, as do the uncertainties, which must be carefully measured. Once all the steps can be combined in a cross-section measurement, the multiple channels or observables of the measurement must be compared in order to extract useful information about the result, and the results must be compared to predictions.

Many steps in this process can require multiple team members working together on various smaller components. There are also always roadblocks that must be overcome, often arising from seemingly simple or consistently reproduced analysis steps. Two examples of this in the p_{T}^{Z} analysis were the multi-jet estimation, which proved very difficult to extract from the limited-statistics dataset, and the unfolding bias uncertainty, which had to be continually updated to match the method employed for the p_{T}^{W} measurement (the subject of Chapter 8).

In the end, the p_{T}^{Z} cross-section measurement was successful. A high-precision measurement was achieved that is only limited by luminosity and statistics. The precision of the low-p_{T} region will help to elucidate processes that are difficult to predict, leading to improved future predictions. The measurement is consistent between lepton channels and p_{T}^{Z} observables, the latter showing that hadronic recoil can be trusted as the only measure of p_{T}^{W} for its differential cross-section measurement. Additionally, ATLAS has now made its first-ever p_{T}^{Z} measurement at $\sqrt{s} = 5$ TeV.

Chapter 8

p_{T}^{W} Reweighting and Unfolding Bias Uncertainty

Many components of the p_{T}^{W} and p_{T}^{Z} cross-section measurements can be split between Z boson and W boson processes in order to optimize the workflow. My first analysis was the p_{T}^{Z} measurement, discussed in the previous chapter. For my second analysis, I joined the p_{T}^{W} portion of the measurement: the high-precision measurement of the differential cross section of W boson Drell-Yan processes with respect to p_{T}^{W} with low-pileup data. The same dataset and nominal MC are used for p_{T}^{W} and p_{T}^{Z}, as described in Section 4.1. The p_{T}^{W} cross-section measurement has two decay channels for each of the W^{+} and W^{-} particles at each centre-of-mass energy: $W^{\pm} \to l^{\pm}\nu$ $(l = e, \mu)$. Approximately an order of magnitude more W bosons were selected in the low-μ data compared to Z bosons, due to the larger interaction cross section of these W boson processes: at $\sqrt{s} = 13$ TeV, approximately 2.5 million events were selected in the W^{+} channels and 1.9 million events were selected in the W^{-} channels; at $\sqrt{s} = 5$ TeV, these numbers were approximately 0.9 million and 0.6 million, respectively. There are more events in the W^{+} channels because protons are positively-charged particles, so it is more likely for the net charge of colliding partons within the proton to sum to $+1$ compared to -1. For example, the proton has two positively-charged valence quarks and only one negatively-charged valence quark, so it is more likely to have a positively-charged valence quark involved in a collision (see Table 2.1).

The p_{T}^{W} measurement is more difficult to make with high-precision due to the

final-state neutrino: as described in Section 5.4, only one observable, the hadronic recoil u_{T}, can be used to measure p_{T}^{W} compared to the two equivalent observables for p_{T}^{Z}. As such, it is even more important to understand and estimate potential large sources of uncertainty like the unfolding bias, which as we have seen, can have a large contribution when using u_{T} to measure p_{T}^{Z}.

Both p_{T}^{Z} and p_{T}^{W} are difficult kinematic variables to predict, but since p_{T}^{W} can only be measured with u_{T}, this creates a potential issue when trying to understand the unfolding bias uncertainty: if the initial MC used for unfolding (i.e. used to create the migration matrix) does not provide a good representation of the data to begin with and the purity of the only observable is poor (see Eq.(6.5) and Fig. 6.6b), then the uncertainty from the unfolding process is guaranteed to be large.

The process of estimating the unfolding bias was a major task that took approximately three years to complete, because the usual ATLAS recommended method, detailed in the next section, gave an unacceptably large uncertainty and so a novel method had to be designed. I joined the p_{T}^{W} side of the analysis as the major p_{T}^{Z} tasks were nearing completion – around April 2021. There was turnover within the analysis team, and the p_{T}^{W} unfolding bias uncertainty was still too large (at the 3 – 5 % level) to make it a useful measurement for the subsequent determination of m_W, so I took over the project to redesign the uncertainty estimation method to attempt to reduce this uncertainty source to the 1 - 2 % level in order for it to be comparable to or less than the statistical uncertainty.

Figure 8.1 refers back to the cross-section road map, but now highlights my contributions to the p_{T}^{W} measurement. My work on the p_{T}^{W} measurement was entirely focused on estimating the unfolding bias, which also required applying modeling corrections to the nominal MC prediction. To finalize my results, I wrote up my work on the bias measurement in our analysis Internal Note. Additionally, I presented the bias estimation strategy and initial results to our Editorial board in July 2021, and then again in June 2022 to finalize the bias estimation process and results.

This chapter explains why the novel unfolding bias estimation method was needed, and details the process that I developed and implemented. There are many intermediate steps associated with this unfolding bias estimation process, and each has a full set of plots for each W boson decay channel and $\sqrt{s}$. The method is the same for

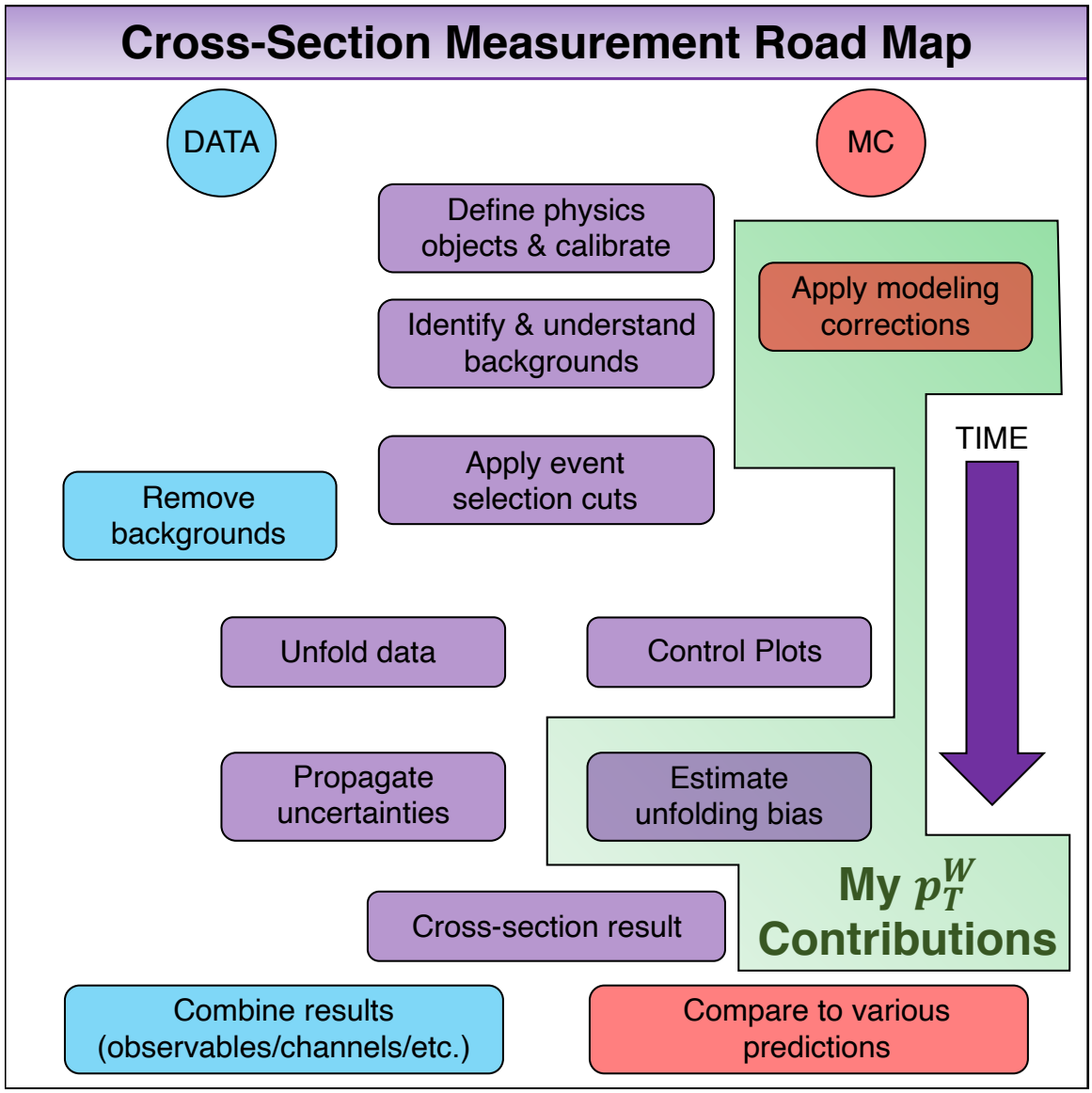

Figure 8.1: My contributions to the p_{T}^{W} cross-section analysis (highlighted in green) as a subset of the cross-section road map (Fig. 6.1).

each channel and $\sqrt{s}$, but the results can differ slightly. Here the method is detailed using a single sample channel at $\sqrt{s} = 13$ TeV: the $W^+ \to e^+\nu$ channel. When it is important to show other channels or results at $\sqrt{s} = 5$ TeV for comparison, they are included. Some additional intermediate results plots are shown in Appendix E. The final unfolding bias uncertainty is presented at the end of the chapter for the $W^+ \to e^+\nu$ channel, and at the end of Appendix E for each other channel.

8.1 Reweighting Strategy

To begin, we will start by rephrasing and expanding on our unfolding bias uncertainty discussion from Section 6.2.4. The uncertainty on the unfolded result of a given variable introduced by the iterative Bayesian unfolding method, known as the unfolding uncertainty or unfolding bias, is usually estimated (in ATLAS) using a procedure recommended by the ATLAS Standard Model group called the data-driven closure test. The general principle is the following:

1. Reweight the MC events at truth-level (for events passing truth-level and reco-level selections) to get the best agreement between the corresponding shapes of the data and MC distributions at reco-level for the physics observable of interest (which in this case is u_{T}).

2. Unfold the corresponding reco-level MC distribution (for events passing truth and reco-level selections) as pseudo-data using the migration matrix from the non-reweighted MC.

3. Compare this unfolded result to the reweighted truth distribution. This is the estimate of the unfolding bias.

Generally in ATLAS, this uncertainty is addressed by reweighting the truth-level distribution with the data-to-MC ratio at reco-level. However in the case of low-purity analyses like this one (see Fig. 6.6b), discrepancies at truth-level might be smeared out at reco-level by resolution effects. The u_{T} distribution is also a less-than-ideal initial guess for a truth-level reweighting: u_{T} on average underestimates the truth-level p_{T}^{W} distribution because signals can be more easily lost in the noise of the calorimeters. The proportionality factor between u_{T} and p_{T}^{W} known as the recoil response is always less than one and depends on p_{T}^{W}. In order to adjust for the recoil response, various alternative functions were tested to reweight p_{T}^{W}, but reasonable data-to-MC agreement was never obtained using this simple reweighting procedure. Instead, a new reweighting method was developed where the MC was reweighted with a parameterized function of p_{T}^{W}, whose parameters are determined by a fit to obtain the best agreement between data and MC at reco-level (the u_{T} distribution is the data).

Figure 8.2 shows a graphic that summarizes the procedure that is the basis of this chapter: the MC reweighting to obtain the bias-corrected MC, and subsequent reweightings to estimate the sources of uncertainty coming from the procedure. This graphic (or road map) will be referred to throughout this chapter. The analysis begins with the background-subtracted data and nominal MC (Powheg+Pythia8, as described in Sec. 7.1) – Step 1 of this "Uncertainties from the unfolding process" road map. The nominal reweighting, Steps 2 – 7, is explained in this section, and the sources of uncertainty, Steps 8 – 10 of the road map, are explained in the next section.

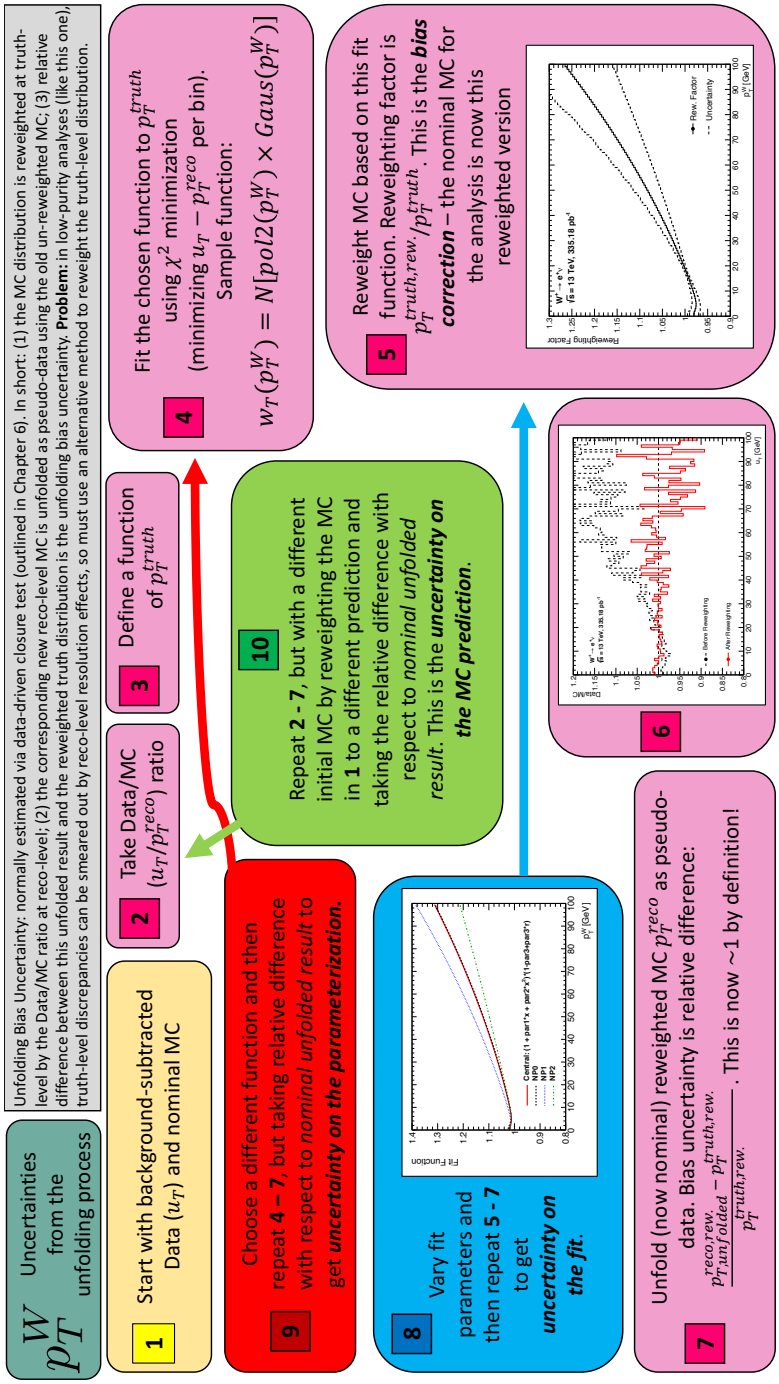

Figure 8.2: Summary of the bias correction and unfolding uncertainty estimation procedure for the p_{T}^{W} cross-section measurement.

The agreement between data and MC is optimized at reco-level by minimizing the following χ^2:

$$\chi^2 = \sum_{ij} \Delta_i^T C_{ij}^{-1} \Delta_j \,; \tag{8.1}$$

$$\Delta_i = (D_i - B_i) - \sum_{ij} R_{ij} \times \left(w_T(p_{\mathrm{T}}^W)\right)_j \,, \tag{8.2}$$

where C_{ij}^{-1} is the total covariance matrix, including statistical and systematic uncertainties on the observed and simulated u_{T} distributions, Δ is the difference between the background-subtracted data distribution $(D-B)$ and the corresponding reco-level MC distribution, which is obtained by taking the product of the response matrix (R) and a truth-level weighting function $w_T(p_{\mathrm{T}}^W)$. (The response function was introduced in Equation (6.1)). The weighting function, $w_T(p_{\mathrm{T}}^W)$, modifies the p_{T}^W distribution in the response matrix for both reco-level and truth-level. The fit parameters of the weighting function are the degrees of freedom in the minimization procedure, ranging from two to six degrees of freedom depending on the weighting function. This minimization is performed for each channel and at each energy. The following weighting functions were tested:

$$\textit{2nd-Order Pol.}\colon\ w_T(x) = 1 + a\,x + b\,x^2; \tag{8.3}$$

$$\textit{Gaus.} \times \textit{Pol.}\colon\ w_T(x) = \left(1 + a\,x + b\,x^2\right)\left(1 - c + c\,G(x;\mu,\sigma)\right); \tag{8.4}$$

$$\textit{Expo.} \times \textit{Pol.}\colon\ w_T(x) = \left(1 + a\,x + b\,x^2\right)\left(1 - c + \frac{c}{\tau}\,e^{-x*\tau}\right); \tag{8.5}$$

$$\textit{2 Gaus.} + \textit{Pol.}\colon\ w_T(x) = 1 + a\,x + b\,x^2 + c\,G(x;\mu,d) + e\,G(x;\mu,f); \tag{8.6}$$

$$\textit{Gaus.} + \textit{Pol.}\colon\ w_T(x) = 1 + a\,x + b\,x^2 + c\,G(x;\mu,d); \tag{8.7}$$

$$\textit{NNPDF/CT10}\colon\ w_T(x) = \left(1 + a\,x + b\,x^2\right)\left(1 - c + c\,r_{\mathrm{NNPDF/CT10}}(x)\right), \tag{8.8}$$

where $x = p_{\mathrm{T}}^W$. All of the above functions contain second-order polynomials to modify the high-p_{T} behaviour of the truth-level p_{T}^W distribution, with additional terms providing more flexibility in the low-p_{T} region. Initially just the simple second-order polynomial was tested, and then modifications were added when it became clear that this simple polynomial could not properly fit the data (in most cases). Various modifications were added by multiplying or adding Gaussian and exponential functions

to the second-order polynomial in order to see which functions could provide the best fit for the low-p_{T} region. The modifications were chosen by looking at local fits that matched the shape of the low-p_{T} region. The functions encapsulate the spread of reasonable fits, such that uncertainties cover other potential functions that were not included. $G(p_{\mathrm{T}};\mu,\sigma)$ is a Gaussian term with mean μ and width σ; $e^{-p_{\mathrm{T}}/\tau}$ is an exponential function with decay parameter τ; a, b, c, d, e, and f are fit parameters; and $r_{\mathrm{NNPDF/CT10}}(p_T^W)$ is a function that represents the ratio of two DYTurbo p_{T}^W predictions [91] obtained using different PDF sets: NNPDF3.0 [92] and CT10NLO. CT10NLO is very similar to the PDF used in the nominal Powheg+Pythia8 MC, and NNPDF3.0 is more modern (2015 compared to 2010). These $r_{\mathrm{NNPDF/CT10}}(p_T^W)$ functions are shown in Figure 8.3 for W^+ and W^- at $\sqrt{s} = 13$ TeV (top) and $\sqrt{s} = 5$ TeV (bottom). This parameterization was chosen to have a function that was expected to directly model the low-p_{T} portion of the data.

Each function is assigned a name for labeling purposes, seen to the left of each equation. All functions are also multiplied by a normalization factor to ensure that the integral of $R \times (w_T\left(p_{\mathrm{T}}^W\right))$ stays equal to the integral of $D - B$ (referring to Equation (8.1)). We have now outlined Steps 2 – 3 of the road map in Figure 8.2.

In Step 4, the fit parameters of these truth-level weighting functions are determined by minimizing the χ^2 defined in Equation (8.1), separately for each electron and muon channel. Once good agreement is found, the χ^2-minimized weighting functions for each electron and muon channel are averaged to create a reweighting function (Step 5). This reweighting function is used to correct the signal MC. The best-fitting reweighting function was chosen to reweight the nominal MC to obtain the new nominal *reweighted* MC. At both $\sqrt{s} = 13$ TeV and $\sqrt{s} = 5$ TeV, this reweighting function is based on the weighting function in Equation (8.8), the so-called *NNPDF/CT10* function, which will be referred to as the Nominal function. The other reweighting functions are used to stress-test this procedure as part of the process to determine the uncertainty contribution from this reweighting procedure. This is discussed in Section 8.2.

The fitted weighting function based on Eq. (8.8) is shown in the upper plot of Figure 8.4 and the corresponding reweighting factor is shown in the lower plot, using the $W^+ \to e^+\nu$ channel as an example (at $\sqrt{s} = 13$ TeV). The central value of the

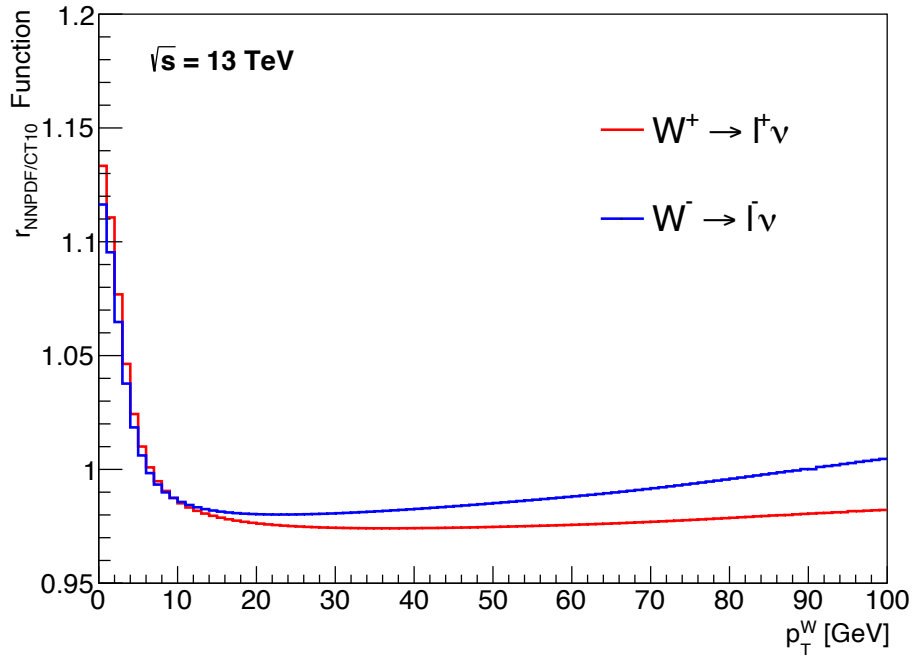

(a) $\sqrt{s} = 13$ TeV

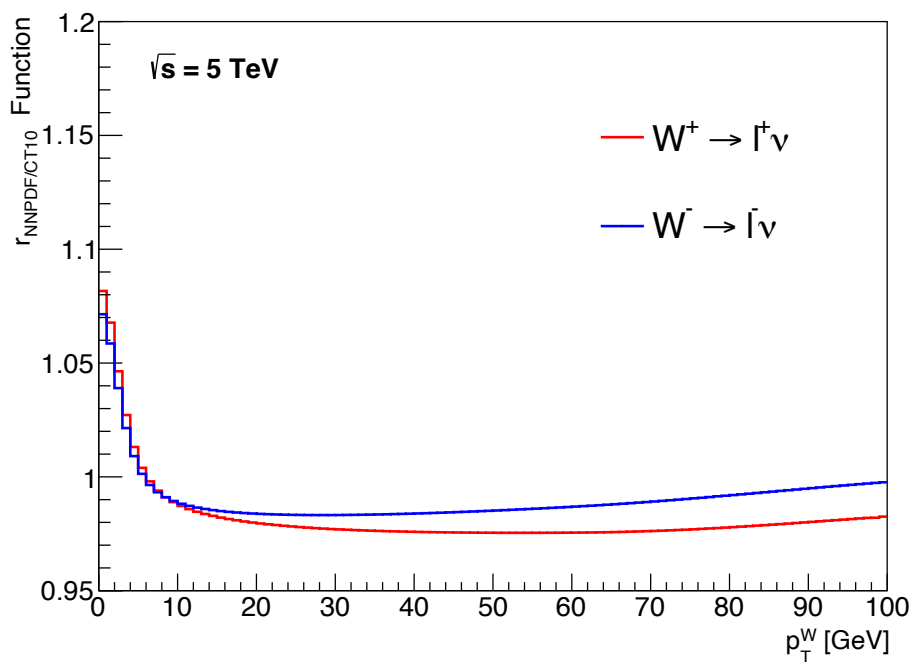

(b) $\sqrt{s} = 5$ TeV

Figure 8.3: Functional form of the $r_{\mathrm{NNPDF/CT10}}(p_T^W)$ term in weighting function Equation (8.8), shown for the W^+ (red) and W^- (blue) decay channels at $\sqrt{s} = 13$ TeV (top) and $\sqrt{s} = 5$ TeV (bottom).

fit is shown in red. Each of the three fit parameters have associated uncertainties after their best fit values are found. Each parameter is, one at a time, maximally varied within its uncertainty. This variation for the first fit parameter is then used to recreate the fit function, and then again for both the second and third fit parameters, thereby obtaining three varied fit functions for each of the three varied fit parameters. These variation fit functions, labeled "NP0", "NP1" and "NP2" ("NP" is short for nuisance parameter), are summed in quadrature to become the uncertainty on the reweighting factor – this is the dashed uncertainty band shown on the lower plot of Figure 8.4.

Each of the reweighting functions for this data-driven procedure to reweight the nominal MC are shown in Figure 8.5 for $\sqrt{s} = 13$ TeV and in Figure 8.6 for $\sqrt{s} = 5$ TeV. Each figure shows two plots, each with the reweighting factors calculated by fitting Equation (8.8) to the non-reweighted MC truth-level p_{T}^{W} distribution. Each plot shows the reweighting factor calculated individually for the $W \to e\nu$ and $W \to \mu\nu$ channels, with the top plot showing $W^{+} \to l^{+}\nu$ and the bottom plot showing $W^{-} \to l^{-}\bar{\nu}$. The uncertainty on each reweighting factor is given by the dashed-line band. For all of these reweighting factors, the electron and muon channels are consistent as expected, and so an average of the electron and muon channel reweighting factor is taken and used to reweight the nominal MC at reco-level for each channel and $\sqrt{s}$. After this process, the nominal reco-level MC is now this reweighted version.

After the reweighting, the data-to-MC agreement at reco-level should be improved, as this was the point of the reweighting procedure. Showing that this is true is Step 6 of the unfolding uncertainties road map (Fig. 8.2). Figure 8.7 shows the data-to-MC ratio at reco-level in the $W^{+} \to e^{+}\nu$ (top) and $W^{-} \to e^{-}\bar{\nu}$ (bottom) channels at $\sqrt{s} = 13$ TeV. Before reweighting, the agreement between data and MC was poor – this is corrected by the reweighting procedure.

After reweighting, the agreement between data and MC is greatly improved. The deviation from unity at high p_{T} is due to the reweighting function being an average of the electron and muon channels – this deviation averages to one when the channels are combined. Similar plots for the $W \to \mu\nu$ channels at $\sqrt{s} = 13$ TeV and all channels at $\sqrt{s} = 5$ TeV are shown at the beginning of Appendix E.

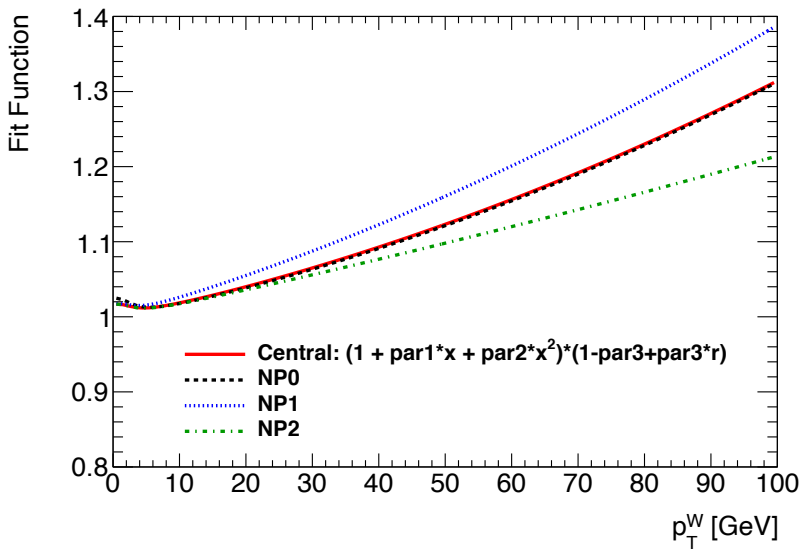

(a) Fit

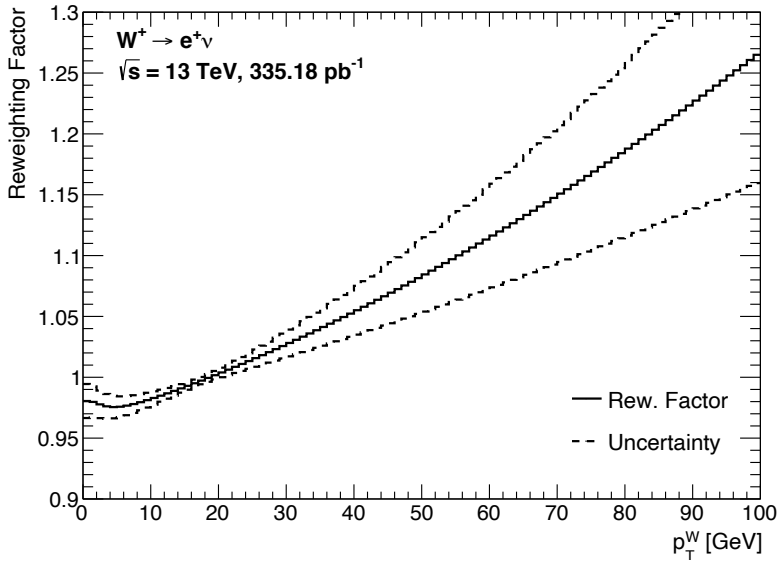

(b) Reweighting Factor

Figure 8.4: Fit function (top) and reweighting factor (bottom) for the $W^+ \to e^+\nu$ channel at $\sqrt{s} = 13$ TeV as a function of p_{T}^W. The fit function is based on the weighting function Eq. (8.8) and has three fit parameters. Individual variations of each fit parameter correspond to the varied fit functions NP0, NP1 and NP2. The sum of these variations form the uncertainty on the reweighting factor. The uncertainty is the dashed uncertainty band shown in the lower plot.

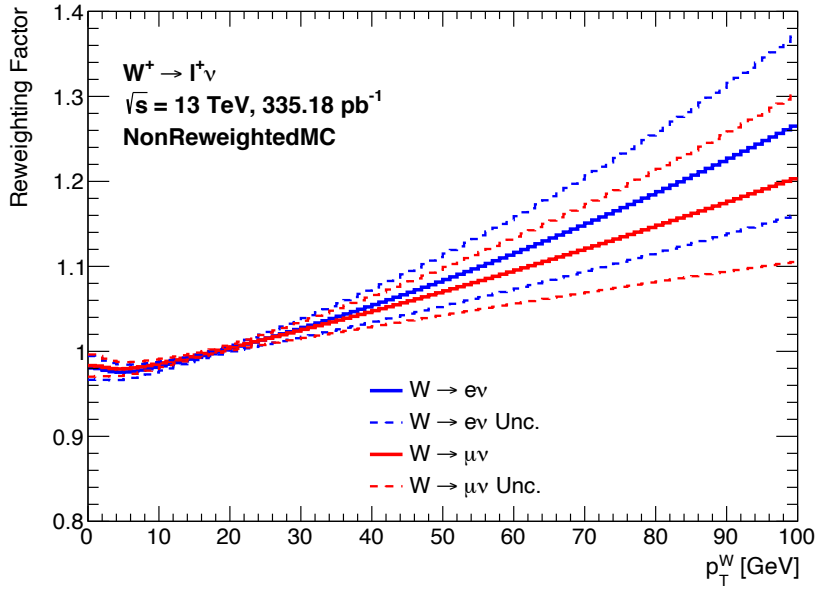

(a) $W^+ \to l^+\nu$

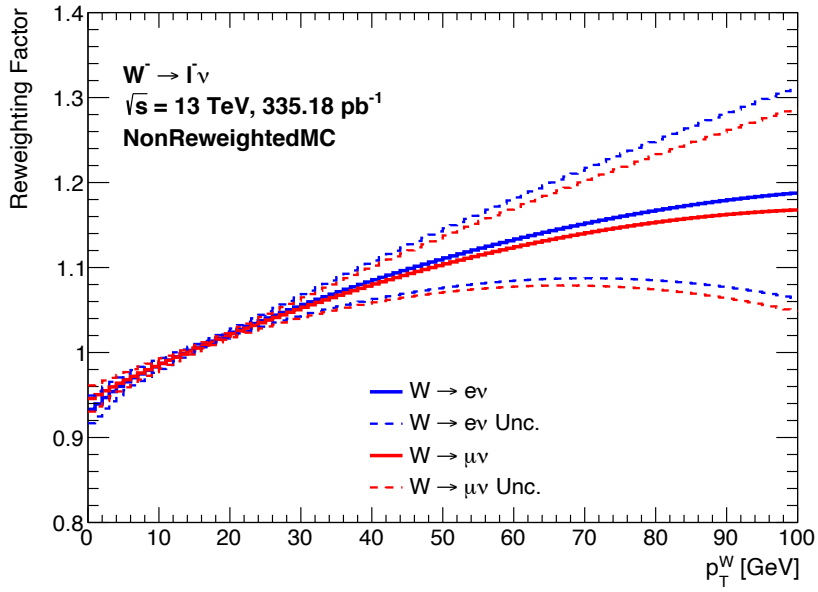

(b) $W^- \to l^-\bar{\nu}$

Figure 8.5: Reweighting factors for the $W \to e\nu$ (blue) and $W \to \mu\nu$ (red) channels at $\sqrt{s} = 13$ TeV. The W^+ channels are shown on the top and the W^- channels on the bottom. The electron-muon average of these functions reweight the nominal (non-reweighted) MC. The reweighting factor is based on the weighting function given by Eq. (8.8). The dashed lines determine the range of the uncertainty on the reweighting functions.

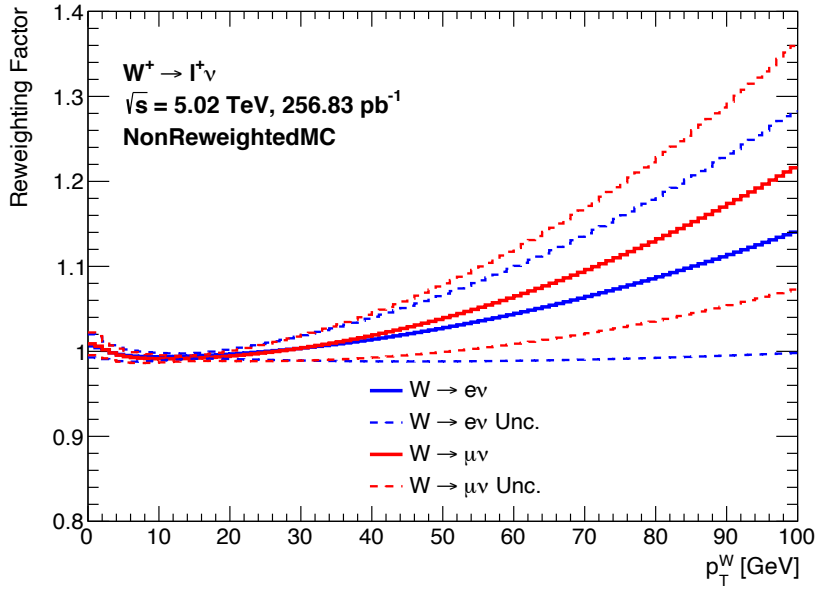

(a) $W^+ \to l^+\nu$

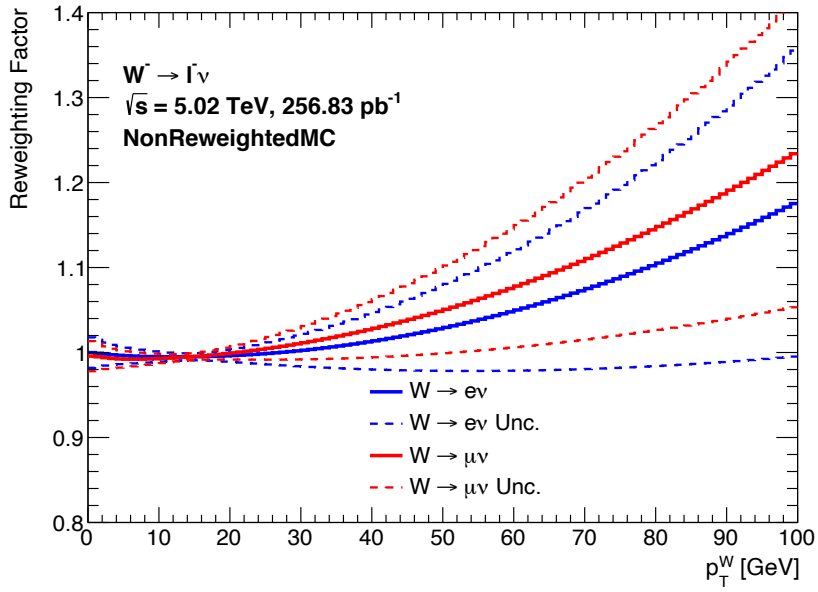

(b) $W^- \to l^-\bar{\nu}$

Figure 8.6: Reweighting factors for the $W \to e\nu$ (blue) and $W \to \mu\nu$ (red) channels at $\sqrt{s} = 5$ TeV. The W^+ channels are shown on the top and the W^- channels on the bottom. The electron-muon average of these functions reweight the nominal (non-reweighted) MC. The reweighting factor is based on the weighting function given by Eq. (8.8). The dashed lines determine the range of the uncertainty on the reweighting functions.

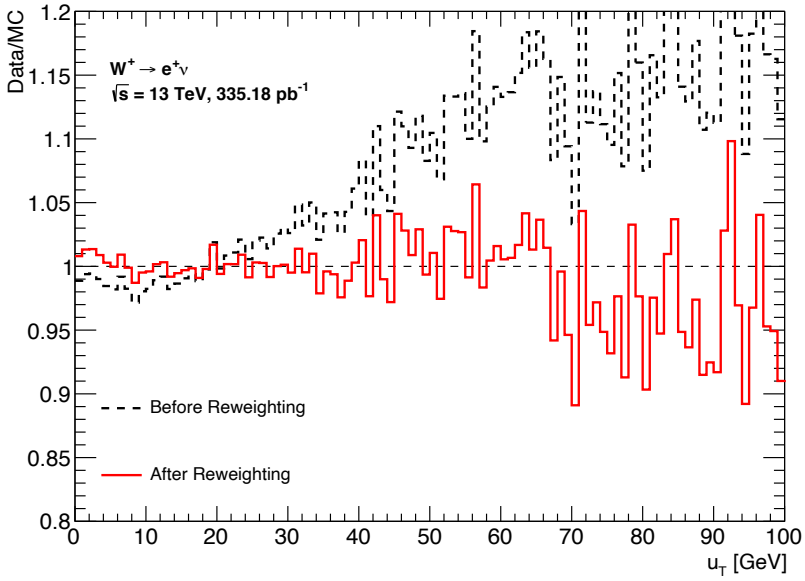

(a) $W^+ \to e^+\nu$

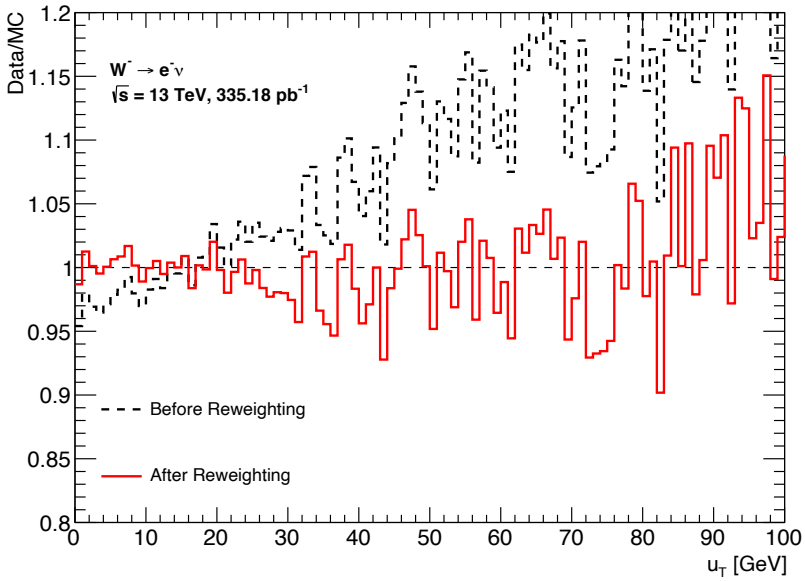

(b) $W^- \to e^-\bar{\nu}$

Figure 8.7: Data-to-MC ratio at reconstructed-level in the $W^+ \to e^+\nu$ (top) and $W^- \to e^-\bar{\nu}$ (bottom) channels at $\sqrt{s} = 13$ TeV before and after the nominal MC has been reweighted.

8.2 Determination of the Unfolding Bias Uncertainties

The reweighting process described in the previous section is a data-driven method to correct the initial MC because the non-reweighted version is incompatible with the data. This is known as the **bias correction**: a new nominal MC for each channel and $\sqrt{s}$ has now been defined. After the correction, this process must be stress-tested by defining several sources of uncertainty associated with the correction that then sum to the total unfolding bias uncertainty. Each source of uncertainty is estimated using reweighting procedures similar to that of the nominal correction. These uncertainties are defined to be physical (i.e. without large jumps in single bins in the varied truth spectra), and to be representative of the largest possible variations allowed by the data at reconstructed level (u_{T}).

The following three types of variations are considered:

1. The fit function parameter variations (**fit uncertainty**, Section 8.2.1, and Step 8 of the Fig. 8.2 road map). These come directly from the fit parameter uncertainties, as was mentioned when discussing Figure 8.4a.

2. The choice of the parameterization function for w_T (**parameterization uncertainty**, Section 8.2.2, and Step 9 of the Fig. 8.2 road map). Alternative w_T weighting functions were tested, in the limit where they resulted in a decent data-to-MC agreement once the MC was reweighted, along with smooth, converging reweighting-function fits. For both $\sqrt{s} = 13$ TeV and $\sqrt{s} = 5$ TeV, the nominal weighting function is given by Equation (8.8) (denoted as *Nominal* or *NNPDF/CT10*). At 13 TeV, the alternative weighting functions are Equations (8.4) (*Gaus.* $\times$ *Pol.*) and (8.5) (*Expo.* $\times$ *Pol.*). At 5 TeV, the alternative weighting functions are Equations (8.3) (*2nd-order Pol.*) and (8.7) (*Gaus.* + *Pol.*).

3. The choice of the baseline truth-level p_{T}^{W} distribution from where the analysis begins (**alternative MC uncertainty**, Section 8.2.3, and Step 10 of the Fig. 8.2 road map). Four alternative predictions are considered to vary this assumption. The alternative predictions are *DYTurboNNPDF30*, *DYTurboCT10*,

Herwig7, and *Pythia* (outlined in more detail in Section 8.2.3).

Each uncertainty component is explained in detail in the subsections below. The plots with unfolded relative differences and unfolding bias uncertainties are the final results, and have therefore all been unfolded with the optimized number of unfolding iterations: 25 iterations for $\sqrt{s}$ = 13 TeV and 9 iterations for $\sqrt{s}$ = 5 TeV. This is based on an optimization procedure similar to that which was described in Section 7.2.3, but is not part of this thesis.

8.2.1 Fit Uncertainty

The fit uncertainty, Step 8 of Figure 8.2, is determined by repeating the same original reweighting procedure but beginning with the reweighted MC. This produces a new reweighting factor that is compatible with 1, by definition. This new set of reweighting factors, denoted the **bias correction closure** reweighting factors, can be seen in Figure 8.8 for the $W^+ \to l^+\nu$ channels at $\sqrt{s} = 13$ TeV and $\sqrt{s}$ = 5 TeV. (The corresponding $W^- \to l^-\bar{\nu}$ plots are shown in Figure E.4 of the Appendix.) The uncertainty band that is shown is obtained by individually fluctuating each fit parameter within its uncertainty in the same way that was explained in the previous section: obtaining three nuisance parameter (NP) reweighting factors, with their quadratic sum forming the error bands.

After this second reweighting step, the newly-reweighted reconstructed-level p_{T} spectrum is unfolded as pseudo-data using the original non-reweighted migration matrix. The relative difference between this unfolded pseudo-data and the original truth-level p_{T}^{W} is the **bias closure**, which is also approximately 1 by construction, with deviations from 1 coming from the small differences between electron and muon channels. The uncertainty comes from three NPs, which are obtained by following the same procedure (obtaining this relative difference), but the reweighting is performed with each of the three NP reweighting factors instead of the central reweighting factor. Each NP is treated individually as a component of the total unfolding bias uncertainty. The relative difference plots showing bias correction closure and the three NPs can be seen in Figure 8.9 for the $W^+ \to e^+\nu$ channel at $\sqrt{s} = 13$ TeV (top) and $\sqrt{s} = 5$ TeV (bottom). Even when each of the three NPs are summed, this source of unfolding bias uncertainty is relatively small.

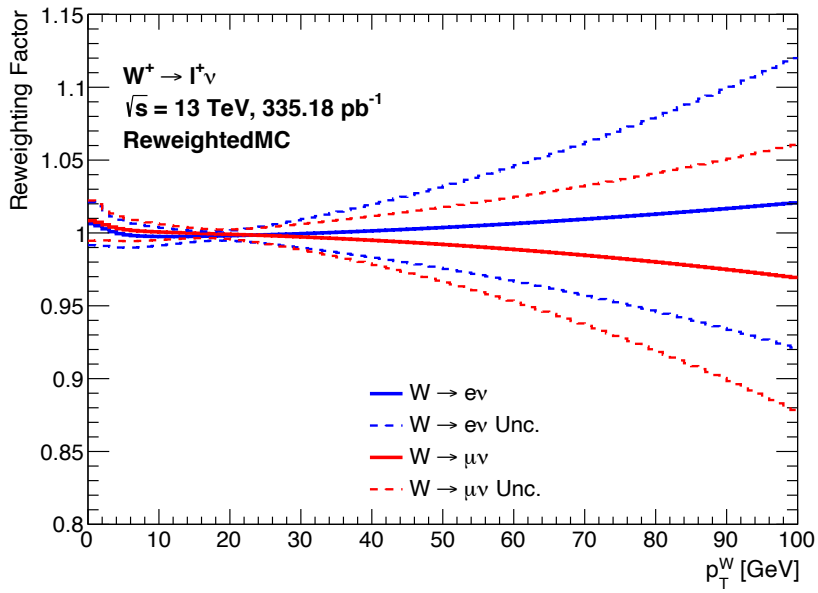

(a) $\sqrt{s} = 13$ TeV

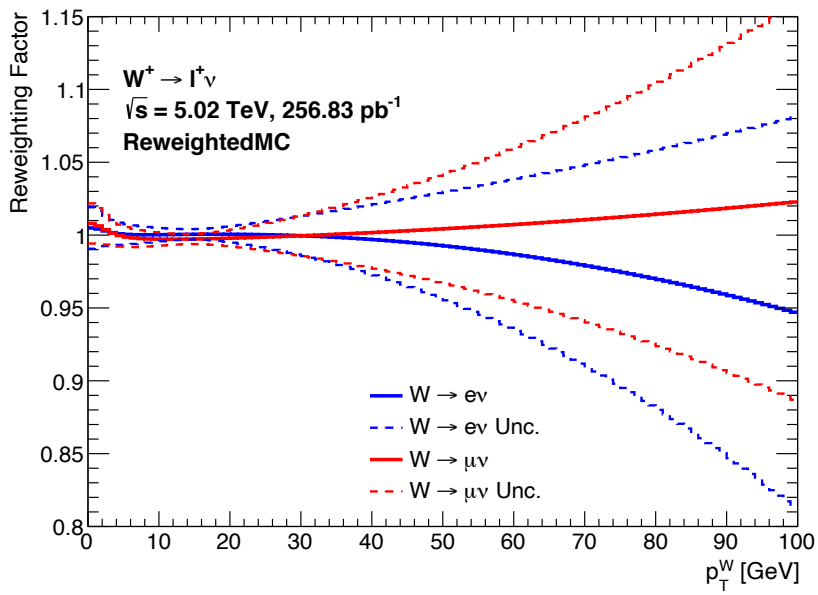

(b) $\sqrt{s} = 5$ TeV

Figure 8.8: Bias correction closure reweighting factors for the $W^+ \to l^+\nu$ channels at $\sqrt{s} = 13$ TeV (top) and $\sqrt{s} = 5$ TeV (bottom). The $W \to e\nu$ channels and their corresponding uncertainty bands are shown in blue, with the $W \to \mu\nu$ channels in red.

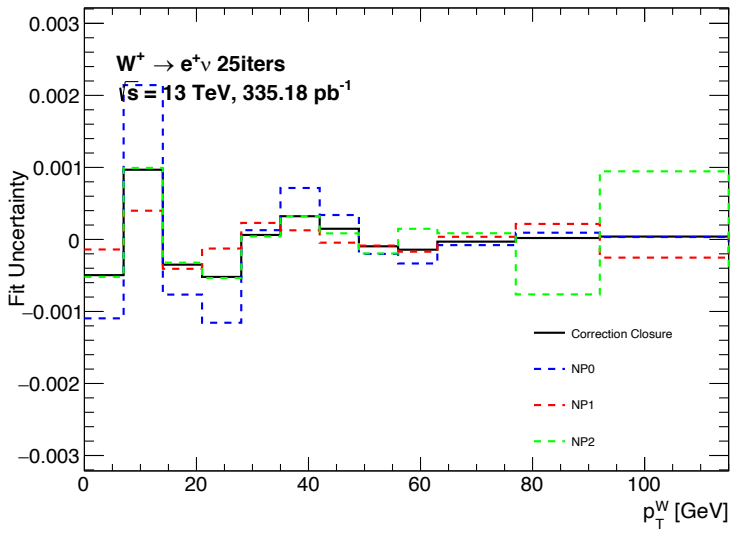

(a) $\sqrt{s} = 13$ TeV

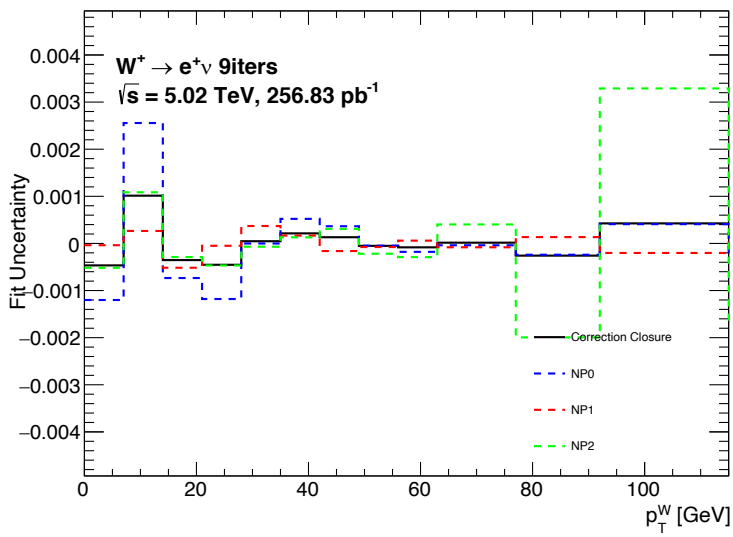

(b) $\sqrt{s} = 5$ TeV

Figure 8.9: Fit uncertainty in the $W^+ \to e^+\nu$ channel for $\sqrt{s} = 13$ TeV (top) and $\sqrt{s} = 5$ TeV (bottom). Each curve comes from unfolding the reweighted reconstructed-level p_{T} spectrum as pseudo-data and taking the relative difference with respect to the original non-reweighted truth-level p_{T}^{W} spectrum. The bias correction closure is shown in black, and each of the three nuisance parameters (NPs) are shown with coloured, dashed lines. Each reweighting factor is applied at truth-level and is based on the weighting function Eq. (8.8).

8.2.2 Parameterization Uncertainty

The parameterization uncertainty, Step 9 of Figure 8.2, is determined by following the same reweighting procedure as outlined in Section 8.1, but using alternative weighting functions w_T. For each channel and $\sqrt{s}$, each alternative weighting function (Equations (8.3) - (8.7)) is tested as a fit to the truth-level p_{T}^{W} and a potential alternative reweighting factor is produced. The reweighting procedure follows for each of these alternative reweighting factors, and the data-to-MC agreement is found. Figure 8.10 shows this data/MC ratio when the MC reweighting is performed using fits based on each possible weighting function.

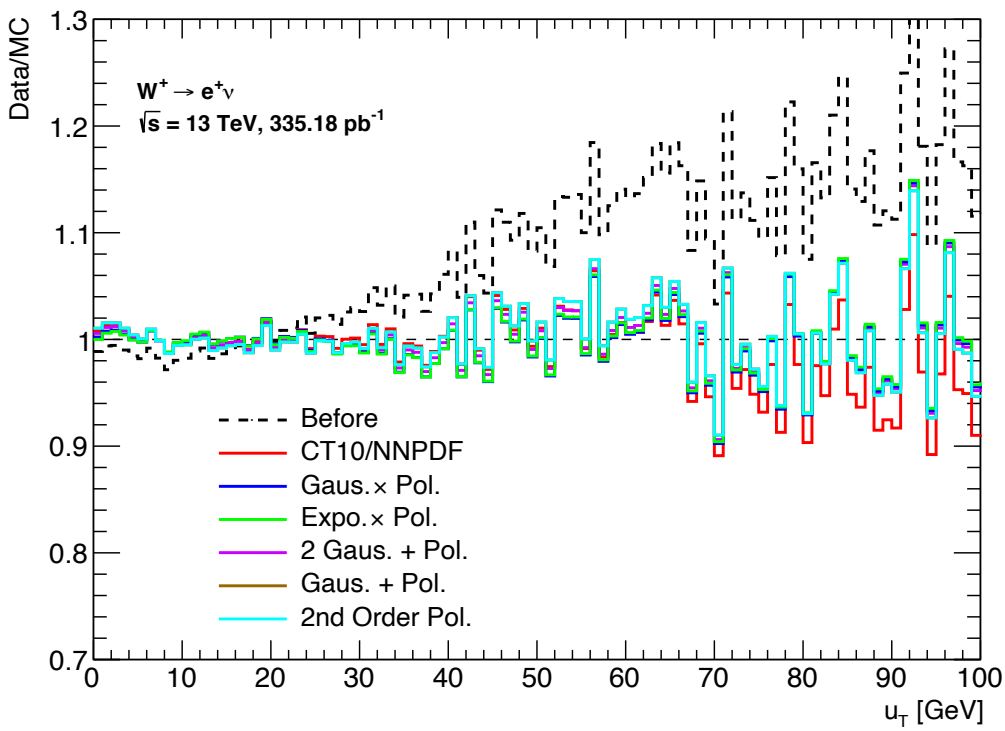

Figure 8.10: Data-to-MC ratio before (dashed black line) and after reweighting in the $W^+ \to e^+\nu$ channel at $\sqrt{s} = 13$ TeV. The ratio after reweighting is compared for each weighting function (Equations (8.3) - (8.8)).

The data-to-MC agreement after reweighting is tested by comparing the χ^2 (Equation (8.1)) for each alternative function to the nominal function. Alternative functions are discarded if the agreement is poor ($\Delta\chi^2 > 2$), or if the corresponding reweighting factor is a discontinuous function (i.e. it has unphysical jumps in individual bins).

The comparison threshold value of 2 was chosen after testing many functions, fit ranges, and thresholds, because this allowed for fits different from the nominal to be considered, while still ensuring that fits were good in the low and high-p_{T} ranges. The [0,50] GeV range was chosen to directly compare fit functions: the χ^2 was calculated using this range as a single bin, and $\Delta\chi^2 = \chi^2_{\mathrm{alt}} - \chi^2_{\mathrm{nom}}$, where "nom" refers to the nominal fit function and "alt" refers to an alternative fit function. Table 8.1 shows a sample of these tests in the $W^+ \to e^+\nu$ channel at $\sqrt{s} = 13$ TeV with the χ^2 and $\Delta\chi^2$ results, along with noting if the resulting fit function was "smooth" i.e. no discontinuous jumps, and also if the function was kept given the $\Delta\chi^2 < 2$ and smooth fit criteria. Overall, these tests found two acceptable alternative weighting functions

Function	χ^2	$\Delta\chi^2$	**Smooth Fit?**	**Keep?**
Nominal	39.5	0	Yes	Yes
2nd-Order Pol.	52.0	12.5	Yes	No
Gaus.×Pol.	37.7	-1.8	Yes	Yes
Expo.×Pol.	36.7	-2.8	Yes	Yes
2 Gaus.+Pol.	38.5	-1	No	No
Gaus.+Pol.	42.3	2.8	Yes	No

Table 8.1: Sample data/MC χ^2 fit results for the nominal and alternative fit functions for the $W^+ \to e^+\nu$ channel at $\sqrt{s} = 13$ TeV. $\Delta\chi^2$ is the difference between the alternative fit function χ^2 and the nominal fit function χ^2. If $\Delta\chi^2 < 2$ and the fit is smooth, then the function is kept and used to determine the parameterization uncertainty.

to use for the reweighting process for each $\sqrt{s}$, that are then used to estimate the parameterization uncertainty: Equations (8.4) (*Gaus.* × *Pol.*) and (8.5) (*Expo.* × *Pol.*) at $\sqrt{s} = 13$ TeV, and Equations (8.3) (*2nd-order Pol.*) and (8.7) (*Gaus.* + *Pol.*) at $\sqrt{s} = 5$ TeV. The reweighting factors obtained when using these alternative functions are shown in Figure 8.11 for the $W^+ \to l^+\nu$ channel at $\sqrt{s} = 13$ TeV (top) and $\sqrt{s} = 5$ TeV (bottom); the lower panel shows the ratio of each alternative function reweighting factor compared to the nominal reweighting factor. Remember that each reweighting factor is an average of the χ^2-minimized fit function for each respective $W \to e\nu$ and $W \to \mu\nu$ channel, so the same reweighting factor is applied

to each respective electron and muon channel.

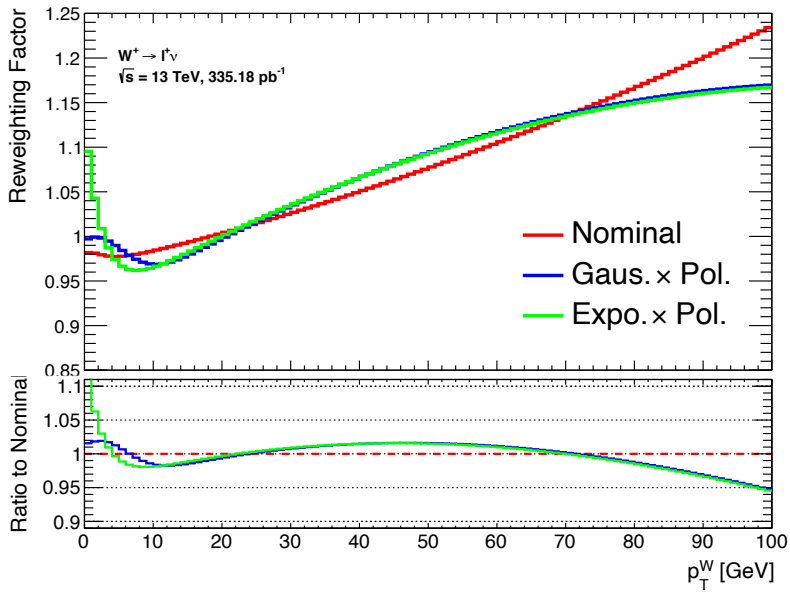

(a) $\sqrt{s} = 13$ TeV

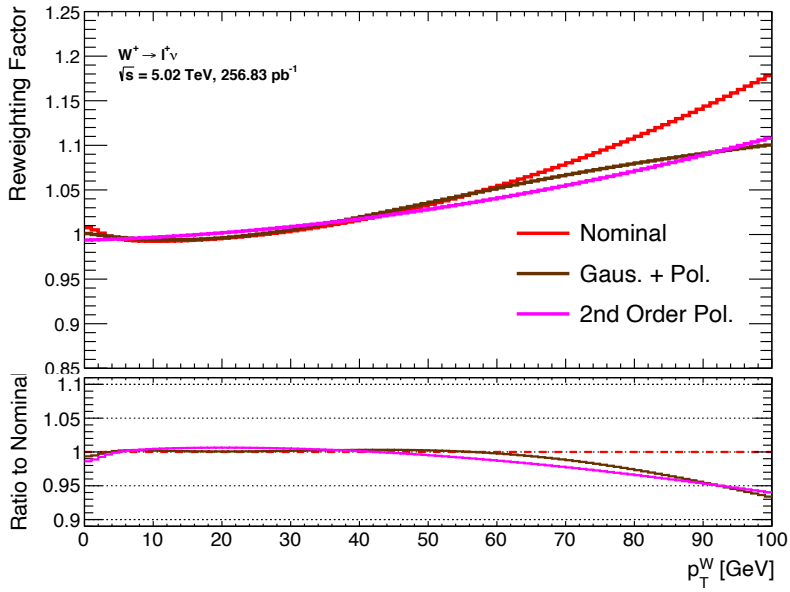

(b) $\sqrt{s} = 5$ TeV

Figure 8.11: Reweighting factors for the $W^+ \to l^+\nu$ channel at $\sqrt{s} = 13$ TeV (top) and $\sqrt{s} = 5$ TeV (bottom). The nominal reweighting factor (red), based on the weighting function in Eq. (8.8), is compared to the two alternative reweighting factors for each $\sqrt{s}$. The ratio panel shows the ratio of each of these two alternative reweighting factors to the nominal reweighting factor.

After each reweighting, the data are unfolded with the corresponding reweighted migration matrix. The relative difference between this unfolded result and the data unfolded with the original non-reweighted migration matrix is found. These relative differences are plotted in Figure 8.12 for the $W^+ \to e^+\nu$ channel at $\sqrt{s} = 13$ TeV (top) and $\sqrt{s} = 5$ TeV (bottom). The largest difference between these curves (the largest difference between relative differences) is the parameterization uncertainty. At $\sqrt{s} = 13$ TeV in the $W^+ \to l^+\nu$ channels, this is the difference between the *Nominal* fit and the *Expo.*$\times$*Pol.* fit (red and green curves). At $\sqrt{s} = 5$ TeV, this is the difference between the *Nominal* fit and the *Pol.* fit (red and blue curves). This source of unfolding bias uncertainty can be significant, as is seen in the $W^+ \to e^+\nu$ channel at $\sqrt{s} = 13$ TeV where the contribution is at the 1% level.

8.2.3 Alternative MC Uncertainty

The alternative MC uncertainty, Step 10 of Figure 8.2, is determined by once again following the same reweighting procedure outlined in Section 8.2, but beginning with an alternative MC as opposed to the nominal MC used for the p_{T}^{W} cross-section measurement. Four different alternative MCs are considered: two DYTurbo predictions using different PDF sets (DYTurbo with NNPDF3.0, denoted as *DYTurboNNPDF30*, and DYTurbo with CT10NLO, denoted as *DYTurboCT10*) – the same predictions that were used to form the $r_{\mathrm{NNPDF/CT10}}$ ratio function, Pythia 8 AZ (denoted as *Pythia*) – the same prediction that was used for the ATLAS m_W measurement [54], and Herwig 7.0 [93] (denoted as *Herwig7*), another commonly-used event generator. For each of these MCs, a similar process to the determination of the parameterization uncertainty alternative fit functions is employed: each of the six possible weighting functions (Equations (8.3) - (8.8)) is used to reweight each alternative MC, thereby obtaining a set of six alternative MC reweighting functions for each alternative MC, as well as data-to-MC ratios before and after reweighting for each combination. As usual, this is done for each channel at both $\sqrt{s} = 13$ TeV and $\sqrt{s} = 5$ TeV. Figure 8.13 shows the data-to-MC ratio before and after reweighting for two sample alternative MCs (DYTurboCT10 and DYTurboNNPDF30) in the $W^+ \to e^+\nu$ channel at $\sqrt{s} = 13$ TeV. The x-axis (reco-level data so labeled u_{T}) is scaled to the [0,30] GeV range in order to zoom in on the higher-statistics region of the distributions.

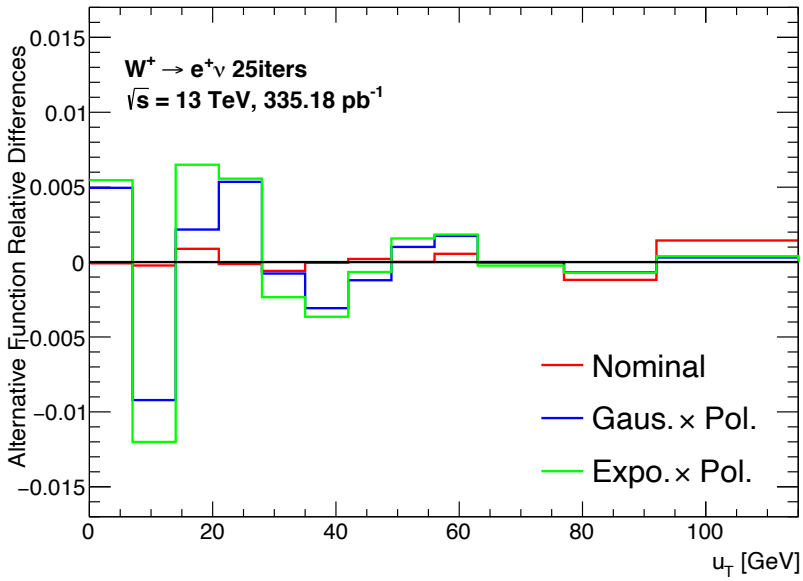

(a) $\sqrt{s} = 13$ TeV

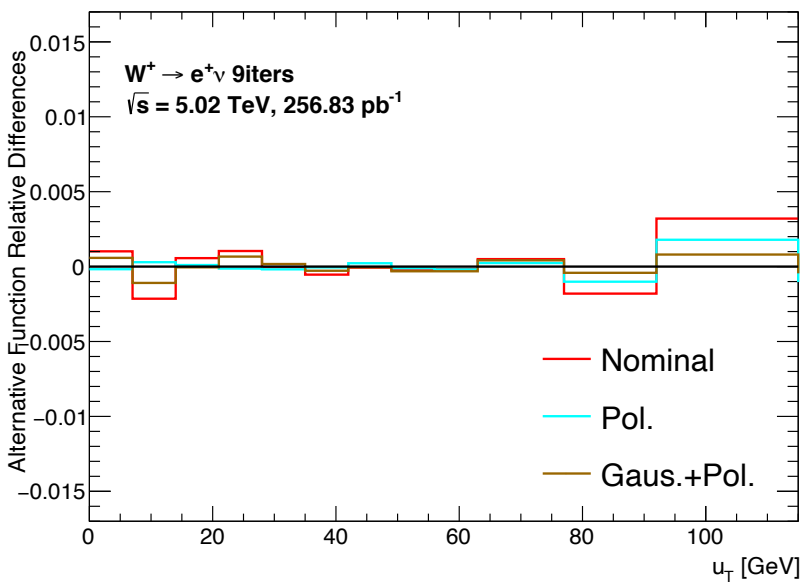

(b) $\sqrt{s} = 5$ TeV

Figure 8.12: Unfolded relative differences for the $W^+ \to e^+\nu$ channel at $\sqrt{s} = 13$ TeV (top) and $\sqrt{s} = 5$ TeV (bottom). The data are first unfolded with a reweighted migration matrix, where the reweighting is based on the *Nominal* fit function and each of the two alternative fit functions for each $\sqrt{s}$, and then the relative difference is the difference between this unfolded data, and the data unfolded with the non-reweighted migration matrix.

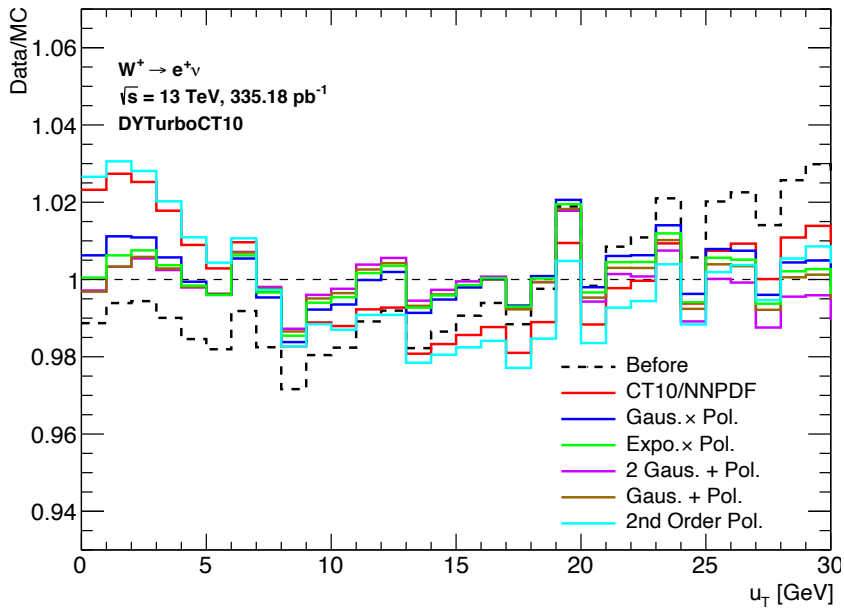

(a) DYTurbo CT10 Alternate MC

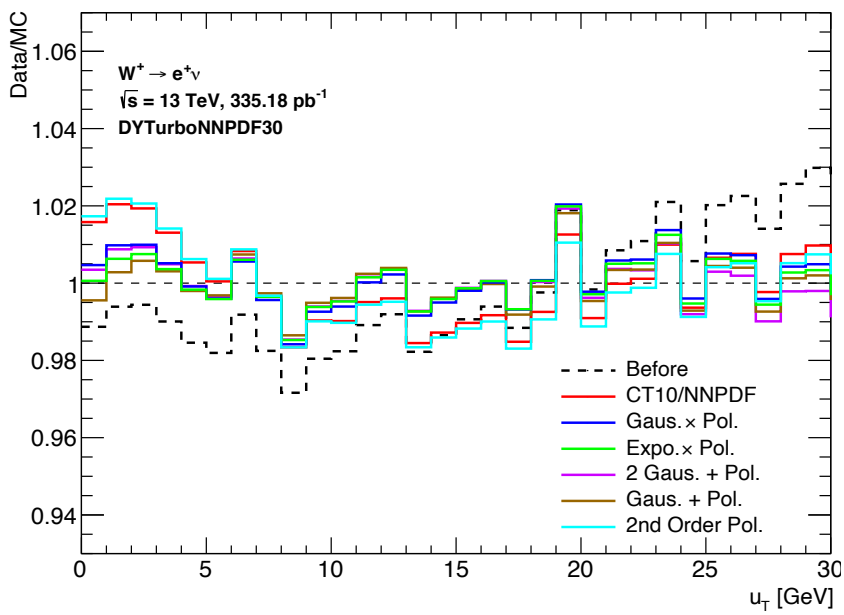

(b) DYTurboNNPDF 3.0 Alternate MC

Figure 8.13: Data-to-MC ratio before (dashed black line) and after reweighting in the $W^+ \to e^+\nu$ channel at $\sqrt{s} = 13$ TeV for two sample alternative MCs: DYTurboCT10 (top) and DYTurboNNPDF30 (bottom). The ratio after reweighting is compared for each weighting function (Equations (8.3) - (8.8)).

For each alternative MC, the weighting function that gives the best fit is selected to reweight that MC. This selection is again based on the χ^2 minimization of the data-to-MC agreement after reweighting (Eq. (8.1)), but instead of comparing to the fit based on the nominal weighting function (*NNPDF/CT10*) using the difference between χ^2s, simply the function with the best fit is chosen to be used for the reweighting. However it still must be possible to find a reasonable fit, and the reweighting factor still must be smooth without any unphysical jumps. If the reweighting factor is discontinuous, or if the fit parameters are found to have uncertainties that are larger than the nominal values and are consistent with zero, this means that no good fit can be found and so the next best-fitting function is chosen. If no weighting functions for a given alternative MC satisfy these conditions, that alternative MC is removed for the respective channel. Table 8.2 shows the χ^2 and smooth function results for the $W^+ \to e^+\nu$ channel at $\sqrt{s} = 13$ TeV for the DYTurboNNPDF30 alternative MC. Based on the best χ^2 and smooth fit function criteria, the *Gaus.*$\times$*Pol.* function (row in bold) was chosen as the fit function for this alternative MC. After this minimization

Function	χ^2	**Smooth Fit?**
Nominal	52.4	Yes
2nd-Order Pol.	67.9	Yes
Gaus.*$\times$*Pol.	**40.4**	**Yes**
Expo.$\times$*Pol.*	37.5	No
2 Gaus.+*Pol.*	39.4	No
Gaus.+*Pol.*	36	No

Table 8.2: Sample data/MC χ^2 fit results for the DYTurboNNPDF30 alternative MC for the $W^+ \to e^+\nu$ channel at $\sqrt{s} = 13$ TeV. The fit function with the smallest χ^2 value that provides a smooth fit function is chosen – in this case, that is the bolded *Gaus.*$\times$*Pol.* fit.

and selection process was completed for each channel, remembering that reweighting functions are the same for the electron and muon channels, the following alternative MCs were considered for the final step of the alternative MC uncertainty: all four alternative MCs in the $W^+ \to l^+\nu$ channel at $\sqrt{s} = 13$ TeV; all but DYTurboN-

NPDF30 in the $W^- \to l^-\bar{\nu}$ at $\sqrt{s} = 13$ TeV; all but DYTurboCT10 in the $W^+ \to l^+\nu$ channel at $\sqrt{s} = 5$ TeV; all but Herwig7 in the $W^- \to l^-\bar{\nu}$ channel at $\sqrt{s} = 5$ TeV. Therefore for each channel, at least three alternative MCs were considered for this uncertainty. Figure 8.14 shows the final reweighting factors for each alternative MC in the $W^+ \to l^+\nu$ channel at $\sqrt{s} = 13$ TeV and $\sqrt{s} = 5$ TeV. These reweighting factors are applied to the migration matrix (for each respective MC), and then that migration matrix is used to unfold the data.

Once each alternative MC has been reweighted, the alternative MC uncertainty can finally be determined. The data are unfolded using the migration matrix based on the alternative, reweighted MC. The relative difference between this unfolded data and the data unfolded with the nominal reweighted migration matrix (i.e. the migration matrix that is used to unfold the data to obtain the central value of the measurement) is plotted for each alternative MC. The alternative MC that contributes the largest relative difference is selected; its relative difference is treated as the delimiting uncertainty. This alternative MC uncertainty and the parameterization uncertainty are similar stress-tests of the unfolding procedure, although using different methods: in both cases, one ends up with a reweighted p_{T}^{W} spectrum that best matches the reconstructed-level distribution of the data before performing the unfolding. These two types of uncertainties essentially vary the starting point of this reweighted prediction. Figure 8.15 shows the unfolded relative differences that determine the alternative MC uncertainty for the $W^+ \to e^+\nu$ channel. The alternative MC that contributes to the final total unfolding bias uncertainty is chosen as the one that has the largest unfolded difference in the low-p_{T} bins. After examining these unfolded relative differences in each channel and center-of-mass energy, the DYTurboCT10 alternative MC (light blue curve in Fig. 8.15a) was selected as the contributing uncertainty for all $\sqrt{s} = 13$ TeV channels, and the DYTurboNNPDF30 alternative MC (dark blue curve in Fig. 8.15b) was selected as the contributing uncertainty for all $\sqrt{s} = 5$ TeV channels.

The final p_{T}^{W} unfolded cross-section measurement (not part of this thesis) will have combined cross-sections between the $W^+ \to l^+\nu$ channels as well as the $W \to e\nu$ and $W \to \mu\nu$ channels, separately. Selecting a single contributing alternative MC for each $\sqrt{s}$ conveniently allows for this source of uncertainty to be correlated between

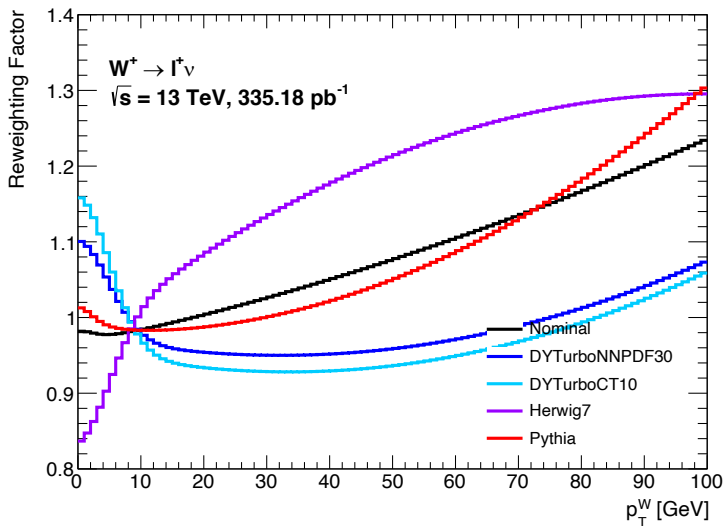

(a) $\sqrt{s} = 13$ TeV

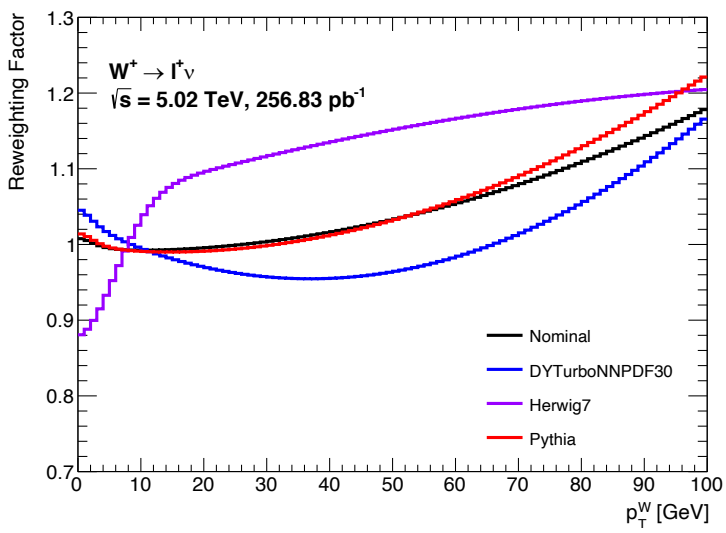

(b) $\sqrt{s} = 5$ TeV

Figure 8.14: Alternative MC reweighting factors for the $W^+ \to l^+\nu$ channel at $\sqrt{s} =$ 13 TeV (top) and $\sqrt{s} = 5$ TeV (bottom) for each alternative MC that is considered.

channels, reducing its contribution during the combination process.

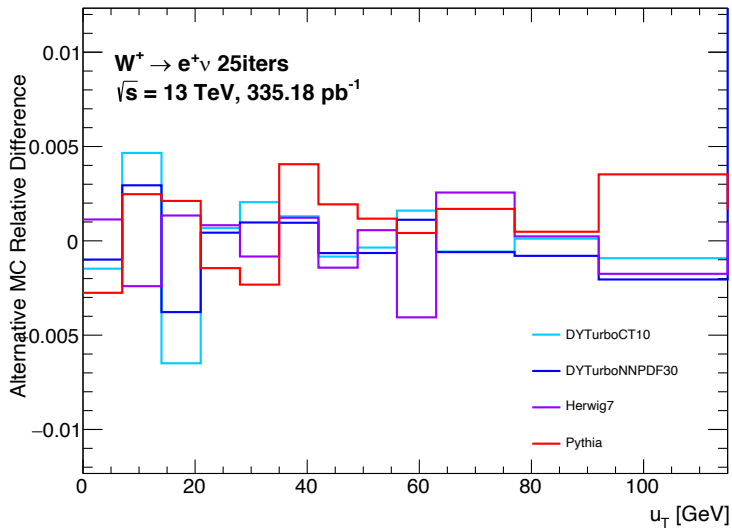

(a) $\sqrt{s} = 13$ TeV

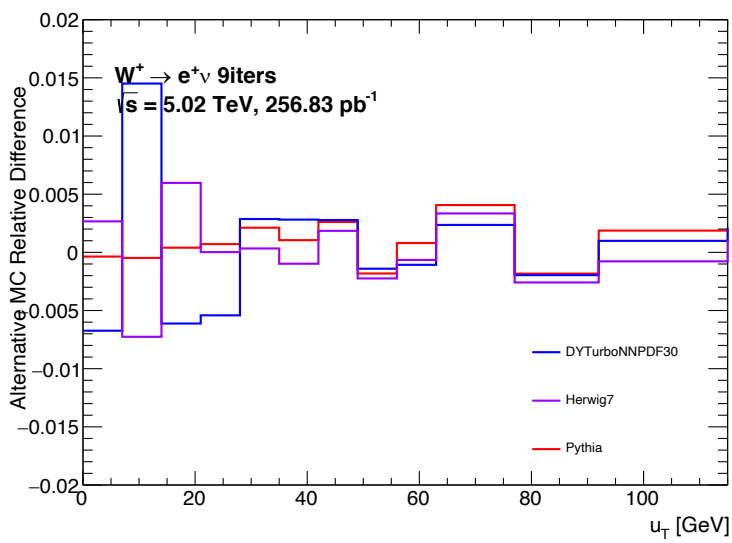

(b) $\sqrt{s} = 5$ TeV

Figure 8.15: Unfolded data relative differences between the alternative MC reweighting and the nominal reweighting for the $W^+ \to e^+\nu$ channel at $\sqrt{s} = 13$ TeV (top) and $\sqrt{s} = 5$ TeV (bottom). The data are unfolded with the alternative MC reweighted migration matrix and the nominal reweighted migration matrix and then the difference is taken. Each plot shows the alternative MCs that were considered.

8.2.4 Total Unfolding Bias Uncertainty

To summarize, the three sources of uncertainty that contribute to the unfolding bias uncertainty come from the statistical uncertainty of the nominal fit function that corrects the MC (**fit uncertainty**), the uncertainty based on the choice of parameterization function (**parameterization uncertainty**), and the uncertainty based on the choice of the initial truth-level MC prediction (**alternative MC uncertainty**). The fit uncertainty has three contributing sources coming from the three nuisance parameters, while the other two uncertainties each have one contributing source. These uncertainties are summed in quadrature to finally obtain the total unfolding bias uncertainty for each channel of the p_{T}^{W} cross-section measurement. As a reminder, all plots that require/show unfolded data, such as the data/MC ratio plots or the total unfolding bias uncertainty, are shown as a function of u_{T}, the measurement observable. Plots that do not include any unfolded data and only require MC information are shown as a function of truth-level p_{T}^{W}, like is the case for the reweighting factor plots (e.g. Fig. 8.11a). Figure 8.16 shows the total unfolding bias uncertainty as a function of u_{T} for the $W^{+} \to e^{+}\nu$ channel at both $\sqrt{s} = 13$ TeV and $\sqrt{s} = 5$ TeV, along with each of the contributing sources. Equivalent figures for the other channels are shown in Appendix E beginning with Figure E.5a. The total uncertainty is shown as a percent uncertainty relative to the differential cross-section measurement as a function of the unfolded data, u_{T}, similar to the p_{T}^{Z} total uncertainty plots in Section 7.2.5.

In each channel, the fit uncertainty has a nearly negligible contribution to the total uncertainty. At $\sqrt{s} = 5$ TeV, the parameterization uncertainty also has a small contribution to the total uncertainty, however its contribution is significant at $\sqrt{s} = 13$ TeV. The most consistently-dominant uncertainty across all channels and centre-of-mass energies is the alternative MC uncertainty, once again showing that the initial p_{T} distribution is not well-predicted since large variations are seen between different MCs.

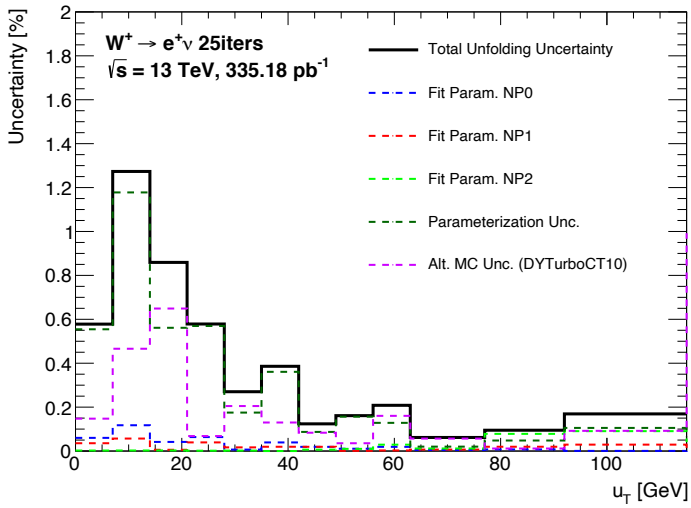

(a) $\sqrt{s} = 13$ TeV

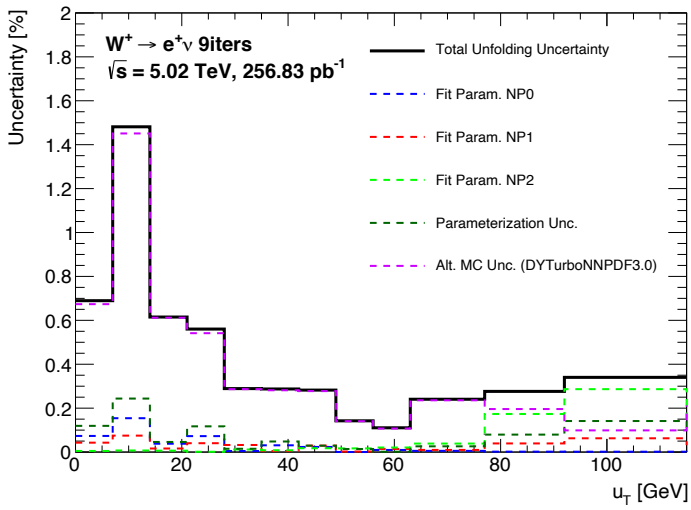

(b) $\sqrt{s} = 5$ TeV

Figure 8.16: All contributions to the unfolding bias uncertainty, shown as percent uncertainty as a function of unfolded u_{T} for the $W^+ \to e^+\nu$ channel at $\sqrt{s} = 13$ TeV (top) and $\sqrt{s} = 5$ TeV (bottom). The three fit parameter uncertainties, NP0 (blue curve), NP1 (red curve), and NP2 (light green curve), are the contributing sources from the fit uncertainty. The parameterization uncertainty (dark green curve) is the uncertainty from the choice of fit function, and the alternative MC uncertainty (purple curve) is the uncertainty based on the choice of initial MC prediction. The alternative MC that defines this uncertainty is shown in brackets in the legend. The total uncertainty (black curve) is the sum in quadrature of these five curves.

8.3 Conclusion

It may seem extensive and superfluous to spend the better part of two years understanding and finalizing a single analysis uncertainty, but for precision measurements, aspects like this are critical. Once the analysis team determined that the nominal MC had to be corrected to improve its agreement to the data, it became necessary to develop a rigorous method to identify and estimate all sources of uncertainties created by this nominal correction. The method was iterated and improved, especially once it became clear that the unfolding bias uncertainty would be the largest source of non-statistical uncertainty for the measurement. Once the nominal MC was corrected using a reweighting function, each aspect of the reweighting was critically examined, focusing on the uncertainties of the nominal fit function, the uncertainties coming from the choice of fit function, and the uncertainties coming from the original MC prediction that required correcting. Each of these sources sum up to the total unfolding bias uncertainty that enters into the final measurement.

In each individual channel and centre-of-mass energy, the total unfolding bias uncertainty is approximately an average of a factor of three times larger than the statistical uncertainty in the second bin of the measurement, comparable to the statistical uncertainty in the first and third bins of the measurement, and at least three times smaller than the statistical uncertainty in each higher-p_{T} bin. However, due to the optimized unfolding bias procedure, the unfolding bias uncertainty is now strongly correlated between lepton channels and charges for each $\sqrt{s}$, and so in the final result when these channels are combined, the unfolding bias uncertainty will be significantly reduced, which should lead to the statistical uncertainty being comparable or dominant in every bin. Quantifying these correlations is part of the final stage of the analysis which is currently underway. Both the correlations and the final combinations are not part of this thesis.

The need for such an intense unfolding bias uncertainty estimation process highlights some of the difficulties that go hand-in-hand with high-precision measurements, where every individual source of uncertainty must be scrutinized. This also highlights the need for an improved p_{T}^{W} cross-section measurement itself, so that better predictions can be generated, allowing for a more straightforward unfolding bias uncertainty determination method for the next high-precision Drell-Yan cross-section

measurement – this is the goal of this nearly-finalized analysis. Aside from the channel combinations, the final differential cross-section measurement for each individual channel has been completed. The result is not part of this thesis, but the differential cross-section distributions as a function of u_{T} look similar to the p_{T}^{Z} differential cross-section results, for example that of Figure 7.16. However, the precision of the unfolding bias uncertainty itself can be compared to that of the previous ATLAS p_{T}^{W} differential cross-section measurement [94]. Figure 8.17 shows the total percent uncertainty as a function of p_{T} for this previous ATLAS measurement, shown as a combination of all $W^{\pm} \to l^{\pm}\nu$ decay channels at a centre-of-mass energy $\sqrt{s} = 7$ TeV that this 2010 data was recorded at. For our purposes, the most important part of the plot is the purple "ResponseMatrix" curve, as this is the unfolding bias uncertainty. This uncertainty is of order 2 – 3 %, and the histogram has bin widths that are approximately double the size of our current measurement. Therefore, it can already be seen that the unfolding bias uncertainty has been greatly improved, since at its maximum (in a single 7 GeV-width bin) the unfolding bias uncertainty in our current measurement is approximately 1.5% in each channel *before* any combinations, and significantly smaller in each other bin. While the combination is not completed yet as has been mentioned, this will further reduce the unfolding bias uncertainty, leading to a large improvement compared to the previous ATLAS measurement.

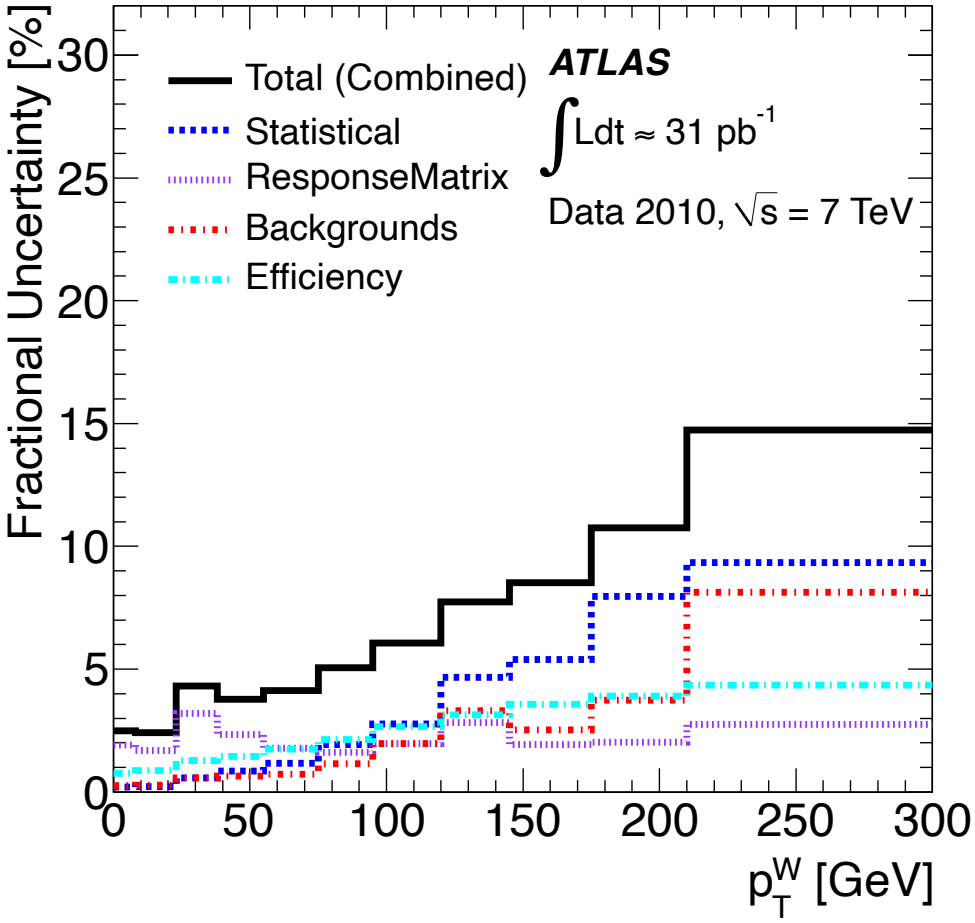

Figure 8.17: Uncertainty contributions to the previous ATLAS p_{T}^{W} differential cross-section measurement, made at $\sqrt{s} = 7$ TeV [94]. These uncertainties, shown as percent uncertainty relative to the cross section, are based on the combination of all $W^{\pm} \to l^{\pm}\nu$ channels. The uncertainties are divided between efficiency (light blue), background (red), statistical (dark blue), and response matrix (i.e. unfolding bias uncertainty) (purple). The summed uncertainty is shown in black [71].

Chapter 9

There and Back Again

The Standard Model of particle physics describes the properties of (and interactions between) fundamental particles – the smallest constituents that make up the Universe – making accurate predictions down to mind-boggling distance scales on the order of 10^{-18} metres. While the Standard Model can be represented by a simple graphic like that of Figure 2.1, making numerical predictions is complicated, and in fact in some cases currently impossible without some help, like for the masses of the W and Z bosons: the Standard Model can only predict relations between these particle properties. Therefore, the Standard Model requires critical assistance from experiment, not only to test its many predictions, but to provide the numerical values for some of these properties that it is unable to predict on its own.

The ATLAS Experiment is one of such experiments that tests the Standard Model, and is in fact the largest general-purpose particle physics experiment in the world. ATLAS records data from the proton-proton collisions generated by the Large Hadron Collider at CERN in order to make measurements to test Standard Model predictions, add to the missing pieces of the Standard Model, and even search for physics beyond the Standard Model. As we have seen in this thesis, a considerable chain of work is necessary in order to be able to use these data recorded by ATLAS to make meaningful measurements. The detector, itself requiring a series of different sub-components to measure different types and properties of particles, must be well-understood so that measurements can be fairly compared to theoretical predictions.

Understanding the detector means quantifying the efficiency at which it identifies

and measures the properties of particles like electrons – what I contributed to for my ATLAS authorship Qualification Task by redesigning and implementing W boson tag-and-probe – and also developing methods to ensure that effects of the detector itself are removed from the data – this is the process of unfolding, a major aspect of this thesis and my contribution to the $W^{\pm} \to l^{\pm}\nu$ differential cross-section measurement as a function of p_{T}. These are just two of the processes that must be performed at various ATLAS Collaboration levels: unfolding on an individual analysis level, and efficiency measurements on a performance-group level, which then shares its recommendations for use throughout the collaboration. This simple act of collaborative work only scratches the surface of the intense teamwork necessary for the success of a massive collaboration like ATLAS. The teamwork starts with the design, maintenance, and upgrades of the detector components themselves, the taking of the data within the ATLAS Control Room, the processing of these data, the calibration of the data and scaling of corresponding Monte Carlo simulations, and finally the analysis teams who make the final measurements for publication.

My analysis, the precision measurement of the differential cross section of W and Z bosons in Drell-Yan processes with respect to p_{T} using low-pileup data at centre-of-mass energy 13 and 5 TeV, is pushing the Standard Model to its limits, given that current predictions do not model these W and Z boson distributions well, especially at low-p_{T}. I spent my first 1.5 years of analysis work on the p_{T}^{Z} differential cross-section measurement, showing that all of the sources of systematic uncertainty for this measurement can be reduced to order 1%, measuring the differential cross-section itself, and proving that the hadronic recoil observable can accurately measure the Z boson's transverse momentum by comparing it to the usual dilepton transverse momentum. For my next 1.5 years, I switched focus to the p_{T}^{W} differential cross-section measurement, developing the novel procedure to estimate the unfolding bias uncertainty that goes hand-in-hand with unfolding the data, made extra-difficult due to the relatively unclean hadronic recoil signal. This process proved nearly excruciating to finalize, but in the end I was able to understand this uncertainty and quantify it such that it remains the dominant experimental uncertainty in only a single bin and only at the 1.5% level, but it is quantified so that the final analysis result will reduce its contribution even further due to tractable correlations that were previously

unattainable.

We have finally (nearly) reached the end of this thesis, but just like in "*A Hobbit's Tale*" [95], there remain a few pages in this story for a metaphorical Frodo and Sam to tell. Once our analysis result is published, it will be directly used as an input to the next ATLAS W boson mass measurement, for which a working group has already been established. Thanks to our analysis team's (and my) contributions, ATLAS will be able to reduce the uncertainty on the m_W measurement. This measurement will take a few years to complete. Therefore at the same time, Run 3 of data-taking has just begun, and since we expect to show that our measurement is statistics-dominated, we hope to convince ATLAS (and the LHC) to allow for another two weeks of low-pileup data-taking, which would further reduce the uncertainty on the p_{T}^{W} and p_{T}^{Z} measurements leading to a strengthened m_W measurement if the timescales align.

My key aforementioned contributions include my W tag-and-probe studies, and my work on the p_{T}^{Z} and p_{T}^{W} differential cross-section measurement. I wrote WTP into the ATLAS computing framework and validated the WTP trigger such that it can now be used effectively for Run 3. For the p_{T}^{Z} measurement, I designed and performed all unfolding, determined the multi-jet uncertainties, and extracted the final cross-section results. For the p_{T}^{W} measurement, I created the novel method to estimate the unfolding bias uncertainty and measured this uncertainty at the 1%-level.

Run 3 has just begun, and the excitement and renewed enthusiasm that comes along with this LHC restart will hopefully lead to updated, increased-precision results made possible by our Run-2 high-precision measurement. For now, we can view the beautiful ATLAS event display of one of the first $Z \to e^+e^-$ candidate events of Run 3, shown in Figure 9.1.

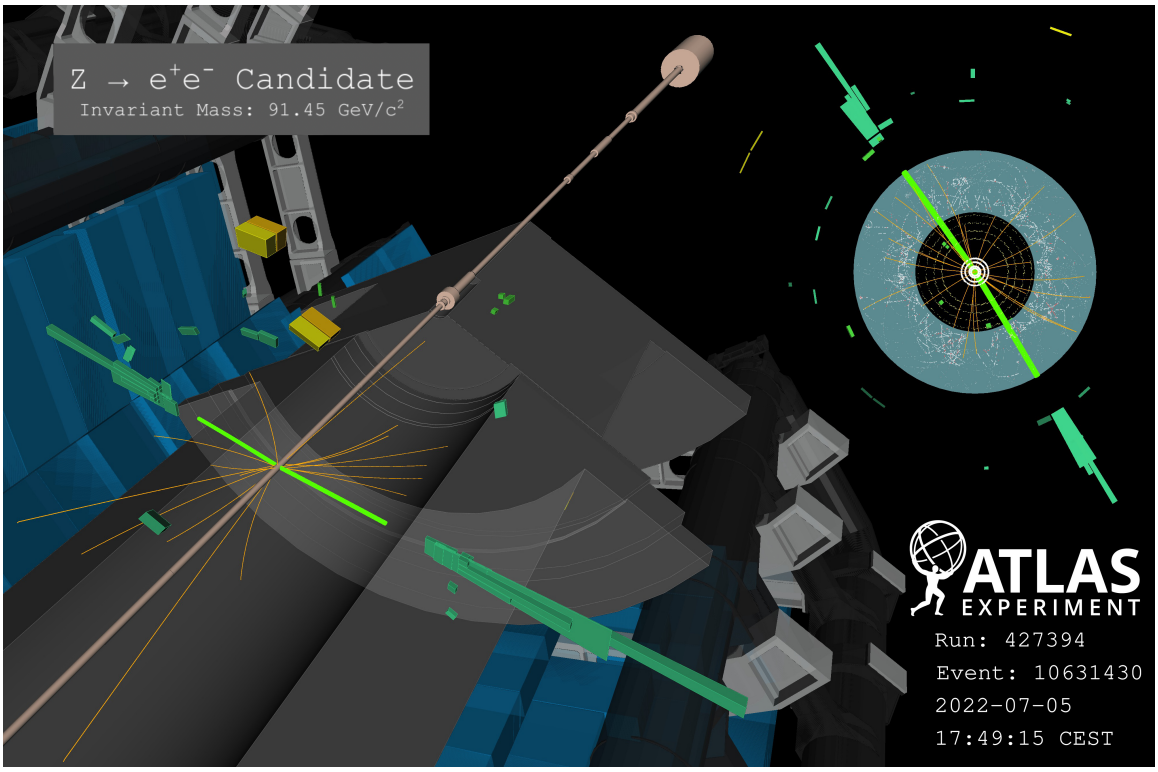

Figure 9.1: ATLAS event display of one of the first recorded candidate $Z \to e^+e^-$ events of Run 3 at $\sqrt{s} = 13.6$ TeV, recorded on July 5, 2022 [96].

Appendix A

Glossary of Terms

This appendix provides a list of acronyms and variables that are commonly used in this thesis. Each acronym/variable is also defined in the main text when it first appears. The list is ordered by when each term first appears in the thesis. Acronyms that only appear once are not listed.

ATLAS – A Large Toroidal LHC ApparatuS
LHC – Large Hadron Collider
p_{T} – Transverse Momentum
SM – Standard Model of Particle Physics
QFT – Quantum Field Theory
QED – Quantum Electrodynamics
QCD – Quantum Chromodynamics
PDF – Parton Distribution Function
EW – Electroweak
BSM – Beyond Standard Model
σ – Cross Section
$\mathcal{L}$ – Integrated Luminosity
IP – Interaction Point
p-p – Proton-Proton
η – Pseudorapidity
ID – Inner Detector

SCT – Silicon Microstrip Tracker

TRT – Transition Radiation Tracker

ECAL – Electromagnetic Calorimeter

HCAL – Hadronic Calorimeter

LAr – Liquid Argon

MS – Muon Spectrometer

L1 trigger – Level One Trigger

HLT – High Level Trigger

CM – Centre-of-Mass

$\sqrt{s}$ – Centre-of-Mass Energy

$\langle\mu\rangle$ – Average Pileup

QT – Qualification Task

MC – Monte Carlo

NLO – Next-to-Leading Order

SF – Scale Factor

TP – Tag-and-Probe

WTP – W boson Tag-and-Probe

ZTP – Z boson Tag-and-Probe

E_{T} – Transverse Energy

WP – Working Point

LH – Likelihood

EM – Electromagnetic

$E_{\mathrm{T}}^{\mathrm{miss}}$ – Missing Energy (MET)

u_{T} – Hadronic Recoil

m_{T} – Transverse Mass

m_W – W Boson Mass

SR – Signal Region

CR – Control Region

LL – Leading Log

Reco-level – Reconstructed Level

MJ – Multi-Jet

N_{iter} – Number of Unfolding Iterations

NP – Nuisance Parameter

ACR – ATLAS Control Room

Appendix B

Theory Background Material

B.1 Units

Due to the minuscule nature of the particles we study, in most cases it is not convenient to use the standard International System of Units (commonly known as SI) when defining quantities. Instead, atomic physicists introduced the unit called an *electron volt*, or eV for short. One electron volt is precisely defined as the energy acquired by an electron that has been accelerated from rest through a potential difference of one volt. Therefore, 1 eV is quite a small number (1 eV $= 1.602 \times 10^{-19}$ J).

Einstein's famous equation

$$E = mc^2, \tag{B.1}$$

stating that energy (E) is equivalent to mass (m) multiplied by the speed of light squared (c^2), also allows us to use electron volts for other useful quantities. The speed of light is constant: $c = 3.0 \times 10^8$ m/s. Therefore, Einstein's equation (B.1) is a statement that energy and mass are equivalent, hence why it is also known as the mass-energy equivalence equation. In particle physics, we use this equation to define our units of mass and momentum. The common units for mass are [eV/c^2], which comes directly from rearranging (B.1). Momentum, another common quantity, has the SI unit [kg $\cdot$ m/s]: mass multiplied by velocity. Therefore, in our units based on the constant speed of light c, momentum has units of [mass] $\times$ [velocity] = [eV/c^2] $\times$ c = [eV/c]. Particle physicists set $c = 1$ for convenience (and also the Planck constant, $\hbar$). This system is called *natural units*. Using natural units can lead to

some confusion when differing between energy or mass or momentum out of context.

B.2 Fields in Particle Physics

Quantum mechanics describes what happens at tiny scales, while special relativity describes what happens at very high energies. Naturally, high-energy particle physics meets both of these conditions, however this does not explain the need for fields. Conceptually, we can understand why particles must be described by evolving fields instead of individual point-masses by looking at two equations. The first equation, $E = mc^2$ (Eq. (B.1)), which states that energy and mass are equivalent, says that if you have enough energy, you can create mass (and vice-versa). The second important equation is Heisenberg's uncertainty principle which can be written in two ways:

$$\Delta x \Delta p \geq \frac{\hbar}{2}, \tag{B.2}$$

or

$$\Delta E \Delta t \geq \frac{\hbar}{2}, \tag{B.3}$$

where x is position, p is momentum, E is energy, t is time, and $\hbar$ is a fundamental constant (the reduced Planck's constant) with the value $\hbar = h/2\pi = 1.0545718 \times 10^{-34}\ \mathrm{m}^2 \cdot \mathrm{kg/s}$ ($\hbar = 1$ in natural units). The uncertainty principle states that we can only simultaneously know the position and momentum of a particle so precisely. Equivalently, it states that any energy fluctuation can occur as long as it happens within a minimum time frame given by Equation (B.3). Combining Equations (B.1) and (B.3) gives us

$$\Delta m = \left(\frac{\hbar}{2c^2}\right)\frac{1}{\Delta t}. \tag{B.4}$$

The bracketed term is just a constant, so this equation shows that given a short-enough time period, a particle with a given mass can appear and then disappear! Masses must correspond to physical particles, and quantum mechanics does not allow particles to appear and then disappear. Special relativity does not allow for energy to become multiple-particle states, which happens when particle-antiparticle pairs are created and then annihilate, for example. Therefore, we need a relativistic theory of quantum fields. Energy is stored in fields; fields have defined functions of position

and time. A massive particle is a large fluctuation, or singularity in a given field.

B.3 The Lagrangian Formalism

The Euler-Lagrange equations are a system of second-order differential equations whose solutions minimize (or more correctly, provide stationary points for) the *action*, S. In classical Newtonian mechanics, the Principle of Least Action states that the trajectory of a particle or system of particles (their *path*) is the function that minimizes the action S. We call this minimizing function the Lagrangian, L. In classical mechanics, this Lagrangian is simply total potential energy (V) subtracted from total kinetic energy (T):

$$L = T - V = \frac{1}{2}m\dot{x}^2 - V(x), \tag{B.5}$$

where m is mass, x is position, and $\dot{x} \equiv \frac{dx}{dt}$ is velocity, i.e. the first time derivative of position. Now let us assume that we are considering a single particle and its path. In order to find the path that the particle takes from position x_1 at time t_1 to position x_2 at time t_2, we must minimize the action:

$$S = \int_{t_1}^{t_2} L(t, x, \dot{x})dt. \tag{B.6}$$

In QFT, instead of examining individual positions (x) and velocities ($\dot{x}$) of particles, we are interested in functions of one or more fields, $\phi(x)$, and their derivatives, $\partial_\mu(x)$. Note that these are fields in *spacetime*, so they are fields of the spacetime four-vector x with three spatial dimensions and one time dimension, such that $x = (t, x, y, z)$ in Cartesian coordinates or $x = (x_0, x_1, x_2, x_3)$ more generally. We also define the partial derivative as

$$\partial_\mu = \left(\frac{\partial}{\partial x_0}, \frac{\partial}{\partial x_1}, \frac{\partial}{\partial x_2}, \frac{\partial}{\partial x_3}\right). \tag{B.7}$$

Using this field notation, we rewrite Equation (B.6) as

$$S = \int L dt = \int \mathcal{L}(\phi, \partial_\mu \phi) d^4x, \tag{B.8}$$

where $\mathcal{L}$ is the Lagrangian density. In QFT, we usually just refer to the Lagrangian density as the Lagrangian.

Now the principle of least action states that when a system of fields evolves from one configuration to another in time $[t_1, t_2]$, it does so along the path that extremizes S from Equation (B.8). The extremum condition is $\delta S = 0$. To solve, we first Taylor expand (B.8),

$$\delta S = \int d^4x \left\{ \frac{\partial \mathcal{L}}{\partial \phi} \delta\phi + \frac{\partial \mathcal{L}}{\partial(\partial_\mu \phi)} \delta(\partial_\mu \phi) \right\}, \tag{B.9}$$

and then integrate by parts to get

$$\delta S = \int d^4x \left\{ \frac{\partial \mathcal{L}}{\partial \phi} \delta\phi - \partial_\mu \left(\frac{\partial \mathcal{L}}{\partial(\partial_\mu \phi)} \right) \delta\phi + \partial_\mu \left(\frac{\partial \mathcal{L}}{\partial(\partial_\mu \phi)} \delta\phi \right) \right\}. \tag{B.10}$$

The third term in this equation vanishes due to boundary conditions. We can then factor out the $\delta\phi$ from the first and second terms, meaning that the remaining terms inside the brackets must be equal to 0 because we require this entire equation to equal 0 for arbitrary $\delta\phi$. This leaves us with the Euler-Lagrange equation for the evolution of a field:

$$0 = \partial_\mu \left(\frac{\partial \mathcal{L}}{\partial(\partial_\mu \phi)} \right) - \frac{\partial \mathcal{L}}{\partial \phi}. \tag{B.11}$$

One of these equations exists for each field in the given Lagrangian.

The Lagrangian formalism encapsulates the dynamics of a set of fields, and one can derive the equation of motion for a field by solving its Euler-Lagrange Equation (B.11). In general, a Lagrangian is still just the potential energy of a system subtracted from its kinetic energy, and one can write down the Lagrangian for a system or field if all the possible interactions are known. For a free, uninteracting scalar field, the Lagrangian is

$$\mathcal{L}_{\text{free}} = \frac{1}{2} \partial_\mu \phi \partial^\mu \phi - \frac{1}{2} m^2 \phi^2. \tag{B.12}$$

The full Lagrangian of the SM can be broken down into subsets of theories corresponding to the different types of interactions within the SM. These are briefly described in Chapter 2.

B.4 Feynman Diagrams

Feynman diagrams are useful tools for visualizing particle interactions, and also for setting up equations to calculate quantities about these interactions. Figure B.1 shows a sample Feynman diagram.

First of all, when reading a Feynman diagram, we generally assume that time flows horizontally from left to right. The lines in the diagram represent particles that are moving (we normally assign a momentum variable to each line such as p or q). Different types of lines can represent different types of particles. The arrows on the lines do not represent direction of motion; instead, they show the direction of the flow of charge, or alternatively, if a line represents a particle or an antiparticle. An arrow pointing in the same direction as time (i.e. to the right) represents a particle, and an arrow pointing in the opposite direction represents an antiparticle. When two (or more) lines connect in a vertex, this signifies an interaction between these particles. Therefore, Figure B.1 shows two particles moving towards each other and annihilating into a different particle, which then travels for a bit of time before decaying into a particle-antiparticle pair again. The angle between lines does not matter, so for example this diagram could be representing a direct, head-on collision.

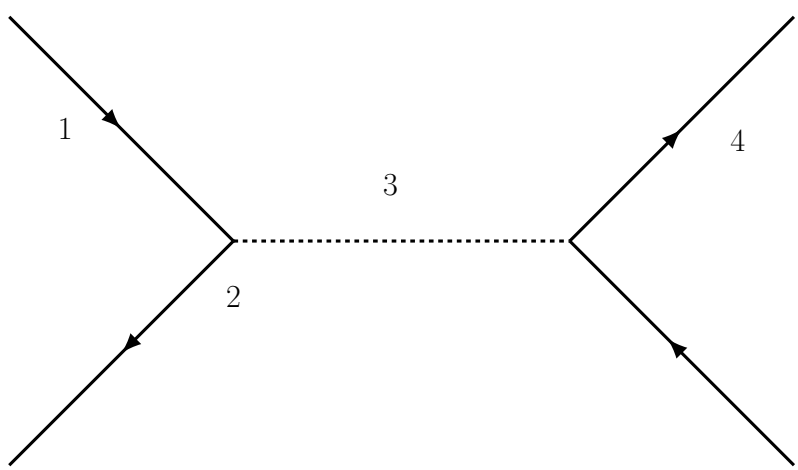

Figure B.1: A sample Feynman diagram. Feynman diagrams allow one to easily represent particle interactions and write down the equations associated with the interaction. Time usually flows from left to right. This diagram represents: (1) a particle and its antiparticle pair (2) annihilating into (3) a propagator, which then decays into (4) the particle-antiparticle pair again.

In general, Feynman diagrams have four important components that tell us about the interaction and the particles involved. These four components, also labeled in Figure B.1, are the following:

1. Incoming particles. There must be at least one, but theoretically there is no maximum. This is the initial state of the process that we are interested in.

2. Propagators. These are particles that only exist as intermediate states in the process. A process need not have any propagators, or it could have many.

3. Vertices. These are where any number of particle lines meet, representing an interaction. The number of vertices also tells us about the *order* of the diagram (or process as a whole). We would say that this is a *Leading Order* (LO) diagram. If we were to draw another line connected to the diagram (which would mean that at least one more particle must be involved), we would necessarily have one or two additional vertices, depending on if the particle is external or internal (propagators are internal). We would call this a *Next-to Leading Order* (NLO) diagram. This pattern continues with NNLO, NNNLO, etc. An example is shown in Figure B.2. Technically, a diagram can have no vertices, but that would mean no interactions, simply showing some number of particles moving without interacting with anything, which is not very interesting.

4. Outgoing particles. There must be at least one, but theoretically there is no maximum. This is the final state of the process that we are interested in, and is what can be measured by experiments.

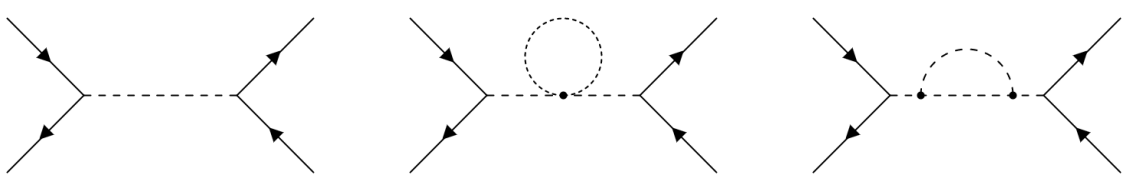

(a) LO (b) NLO (c) NNLO

Figure B.2: Sample Feynman diagrams exemplifying a Leading Order (LO), Next-to Leading Order (NLO), and Next-to-Next-to Leading Order (NNLO) process.

Once we know the Lagrangian for a given theory and can draw Feynman diagrams for processes within that theory, we can both understand and visualize all of the

allowed particle interactions within the theory and perform calculations to make theoretical predictions for experiments to test.

B.5 de Broglie Wavelength

The argument from Section 3.2 on probing subatomic systems can be summarized using the de Broglie wavelength of a particle:

$$\lambda = \frac{h}{p}, \tag{B.13}$$

where λ is the wavelength of the particle, coming from the quantum-mechanical fact that all matter exhibits wave-like behaviour, p is the particle's momentum, and h is the Planck constant. In order to resolve a structure, we must have $\lambda \leq d$, where d is the length scale of the structure of interest. Inserting the de Broglie wavelength (B.13), we see that we require $p \geq \frac{h}{d}$. Although this is not a detailed argument, the logic holds. For example, if we want to examine the internal structure of the proton with $d \sim 10^{-15}$ m, we need a particle with momentum that is at least

$$\begin{aligned}
p &\sim \frac{h}{d} \\
p &\sim \frac{6.626 \times 10^{-34}\ \mathrm{m}^2\ \mathrm{kg/s}}{10^{-15}\ \mathrm{m}} \\
p &\sim 6.626 \times 10^{-19}\ \mathrm{kg \cdot m/s} \\
p &\sim 1\ \mathrm{GeV},
\end{aligned}$$

where in the last step we have converted from SI units to electron volts. Following this pattern, if we hope to resolve effects of the even smaller-scale electroweak interactions, we need particles with even higher momenta (and therefore energy). Accelerators are the only way to consistently reach energies of these scales.

Appendix C

Additional W Tag-And-Probe Results

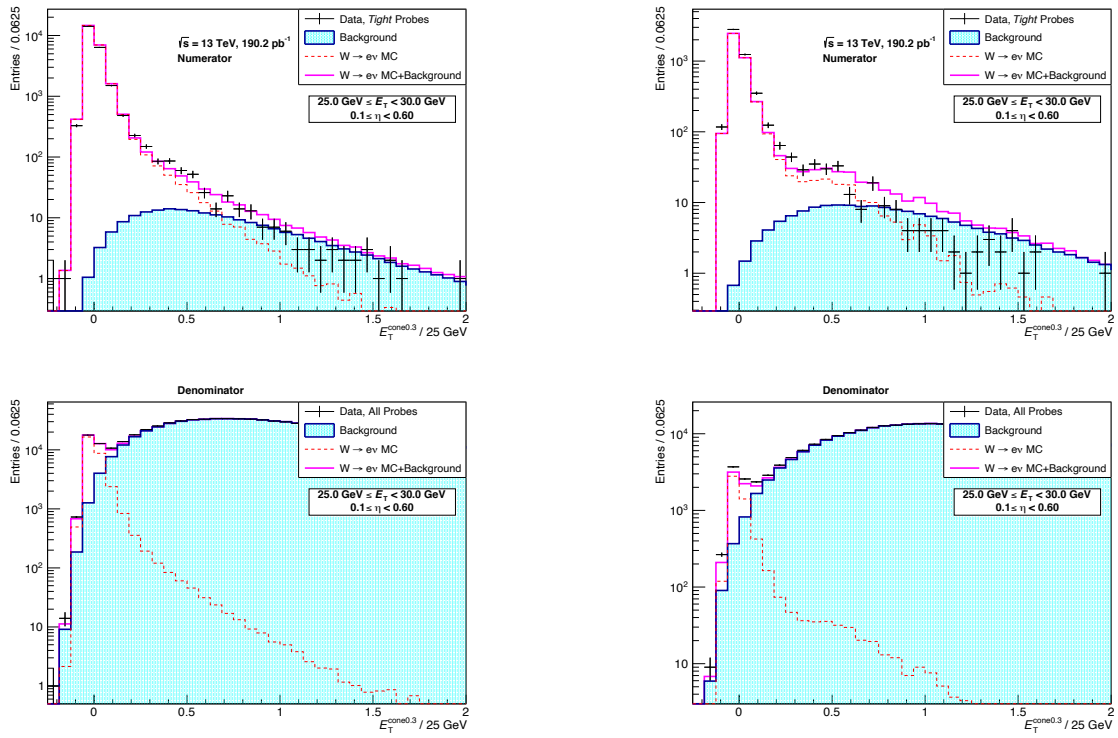

(a) WTP Trigger (b) $E_{\mathrm{T}}^{\mathrm{miss}}$ Trigger

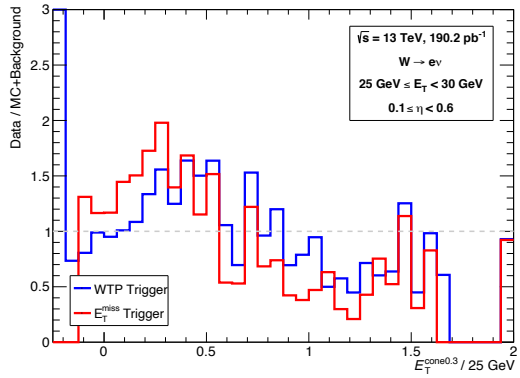

(c) Data/(MC+Background) Ratio

Figure C.1: Control plot comparison between event selection with the WTP trigger and the $E_{\mathrm{T}}^{\mathrm{miss}}$ triggers for WTP in the $E_{\mathrm{T}} = [25, 30]$ GeV and $\eta = [0.1, 0.6]$ bin.

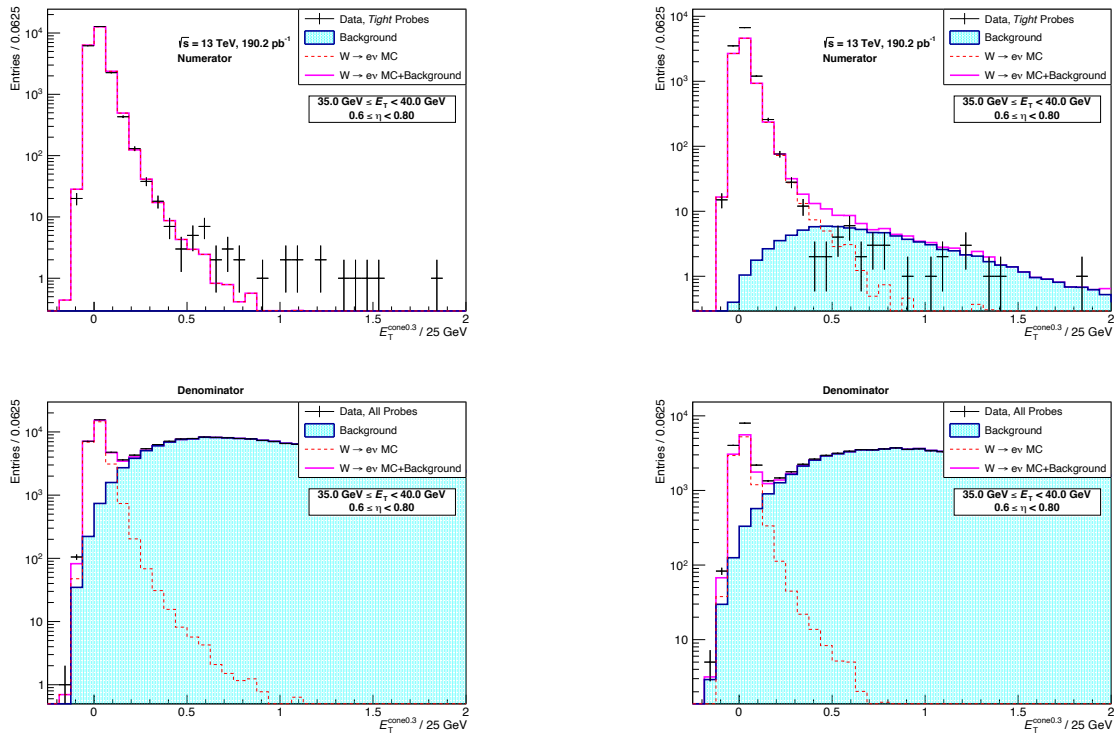

(a) WTP Trigger

(b) $E_{\mathrm{T}}^{\mathrm{miss}}$ Trigger

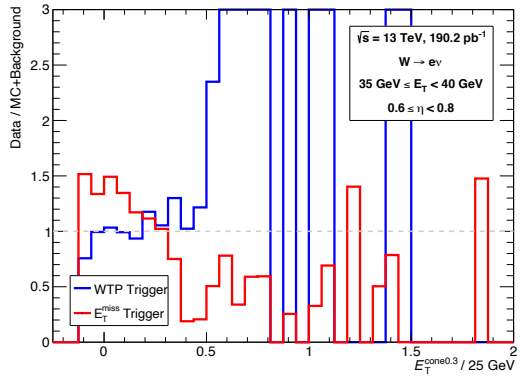

(c) Data/(MC+Background) Ratio

Figure C.2: Control plot comparison between event selection with the WTP trigger and the $E_{\mathrm{T}}^{\mathrm{miss}}$ triggers for WTP in the $E_{\mathrm{T}} = [35, 40]$ GeV and $\eta = [0.6, 0.8]$ bin.

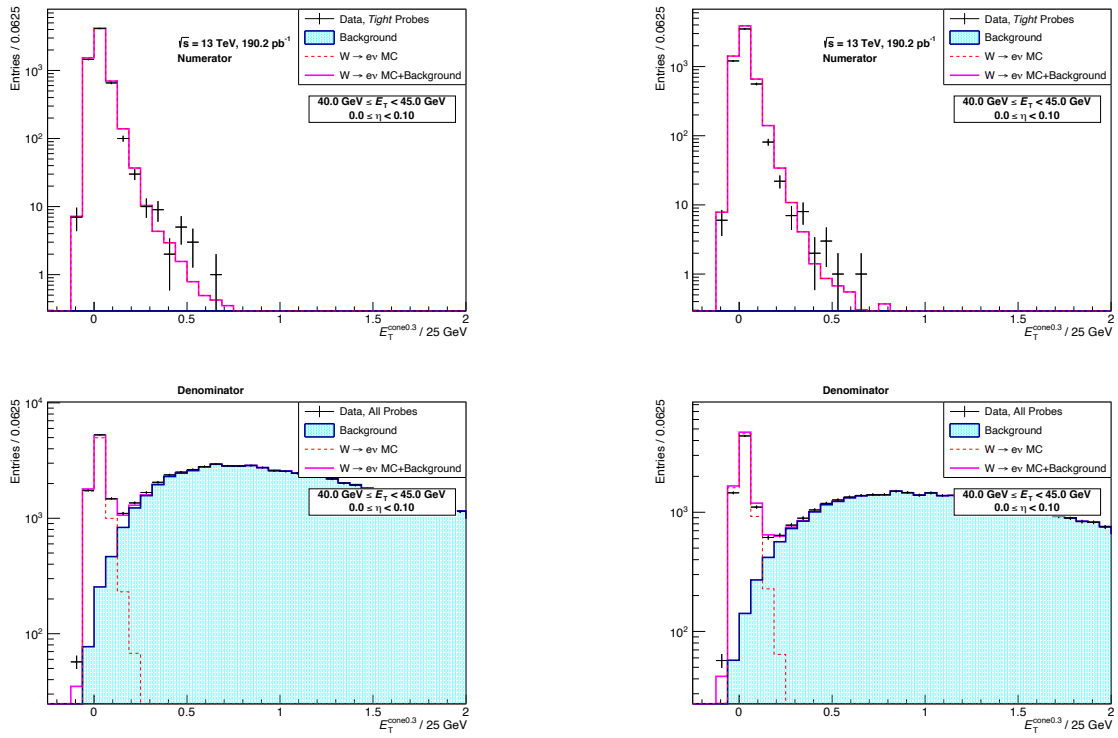

(a) WTP Trigger

(b) $E_{\mathrm{T}}^{\mathrm{miss}}$ Trigger

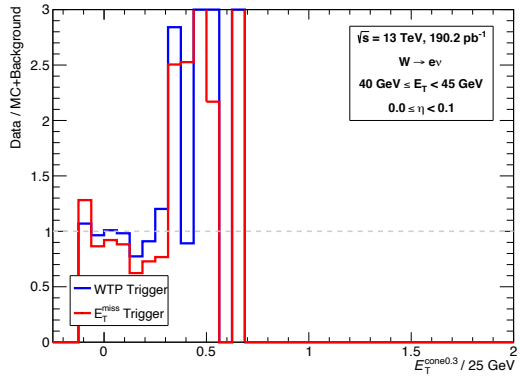

(c) Data/(MC+Background) Ratio

Figure C.3: Control plot comparison between event selection with the WTP trigger and the $E_{\mathrm{T}}^{\mathrm{miss}}$ triggers for WTP in the $E_{\mathrm{T}} = [40, 45]$ GeV and $\eta = [0.0, 0.1]$ bin.

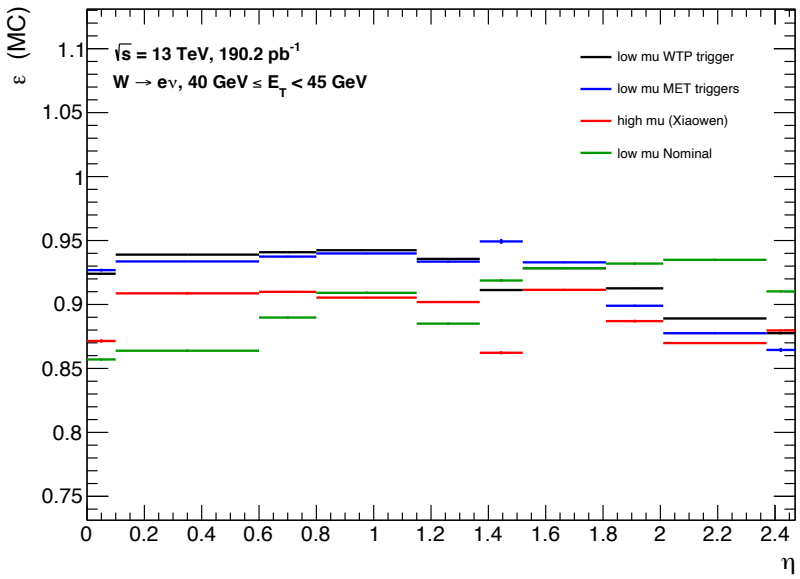

(a) *Medium* Probes

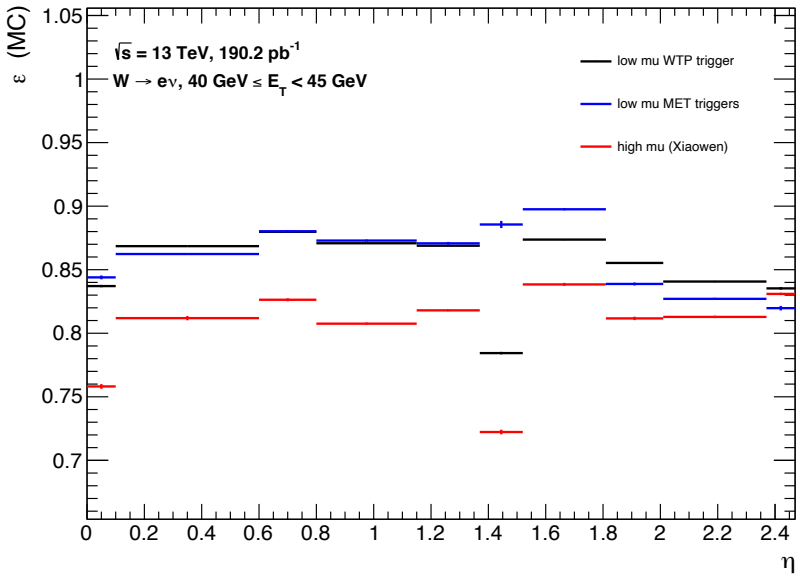

(b) *Tight* Probes

Figure C.4: MC efficiency as a function of η for *Medium* (top) and *Tight* probes (bottom) for a high-statistics E_{T} bin ($E_{\mathrm{T}} = [40, 45]$ GeV). For *Medium* probes, four different efficiencies are compared: low-μ WTP results using the WTP trigger (black), low-μ WTP results using the $E_{\mathrm{T}}^{\mathrm{miss}}$ triggers (blue, 'MET' = $E_{\mathrm{T}}^{\mathrm{miss}}$), high-$\mu$ ZTP results (red), and the current nominal low-μ efficiencies that have been extrapolated from high-μ results (green). The nominal low-μ efficiencies are not available for *Tight* probes.

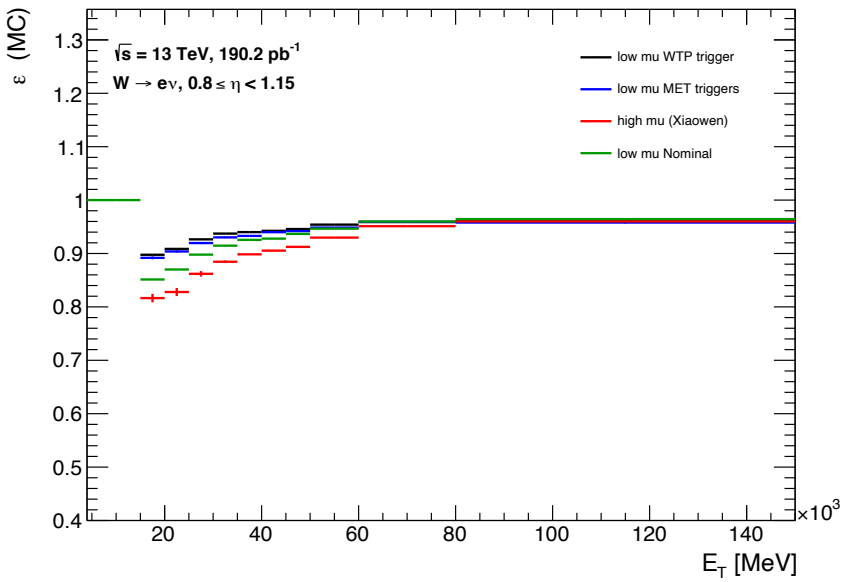

(a) *Medium* Probes

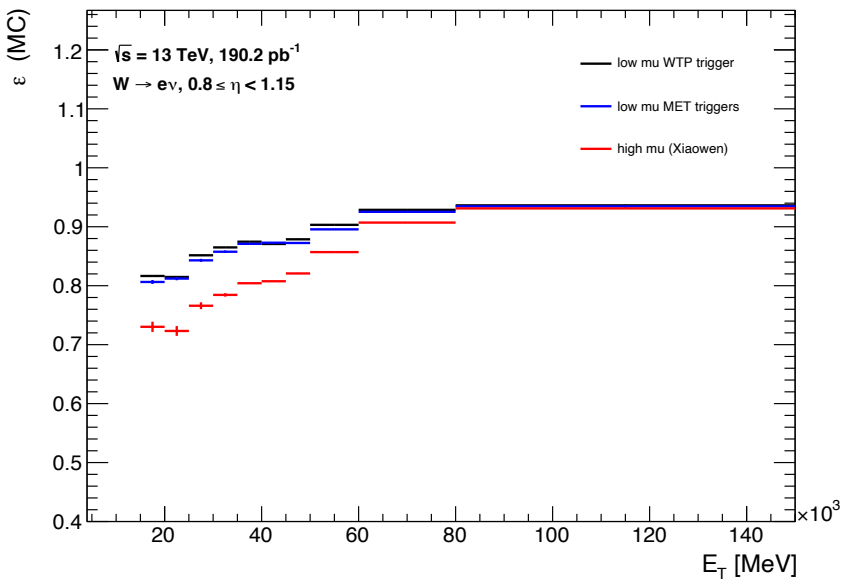

(b) *Tight* Probes

Figure C.5: MC efficiency as a function of E_{T} for *Medium* (top) and *Tight* probes (bottom) for a high-statistics η bin ($\eta = [0.8, 1.15]$). For *Medium* probes, four different efficiencies are compared: low-μ WTP results using the WTP trigger (black), low-μ WTP results using the $E_{\mathrm{T}}^{\mathrm{miss}}$ triggers (blue, 'MET' = $E_{\mathrm{T}}^{\mathrm{miss}}$), high-$\mu$ ZTP results (red), and the current nominal low-μ efficiencies that have been extrapolated from high-μ results (green). The nominal low-μ efficiencies are not available for *Tight* probes.

Appendix D

Complete p_{T}^{Z} Results

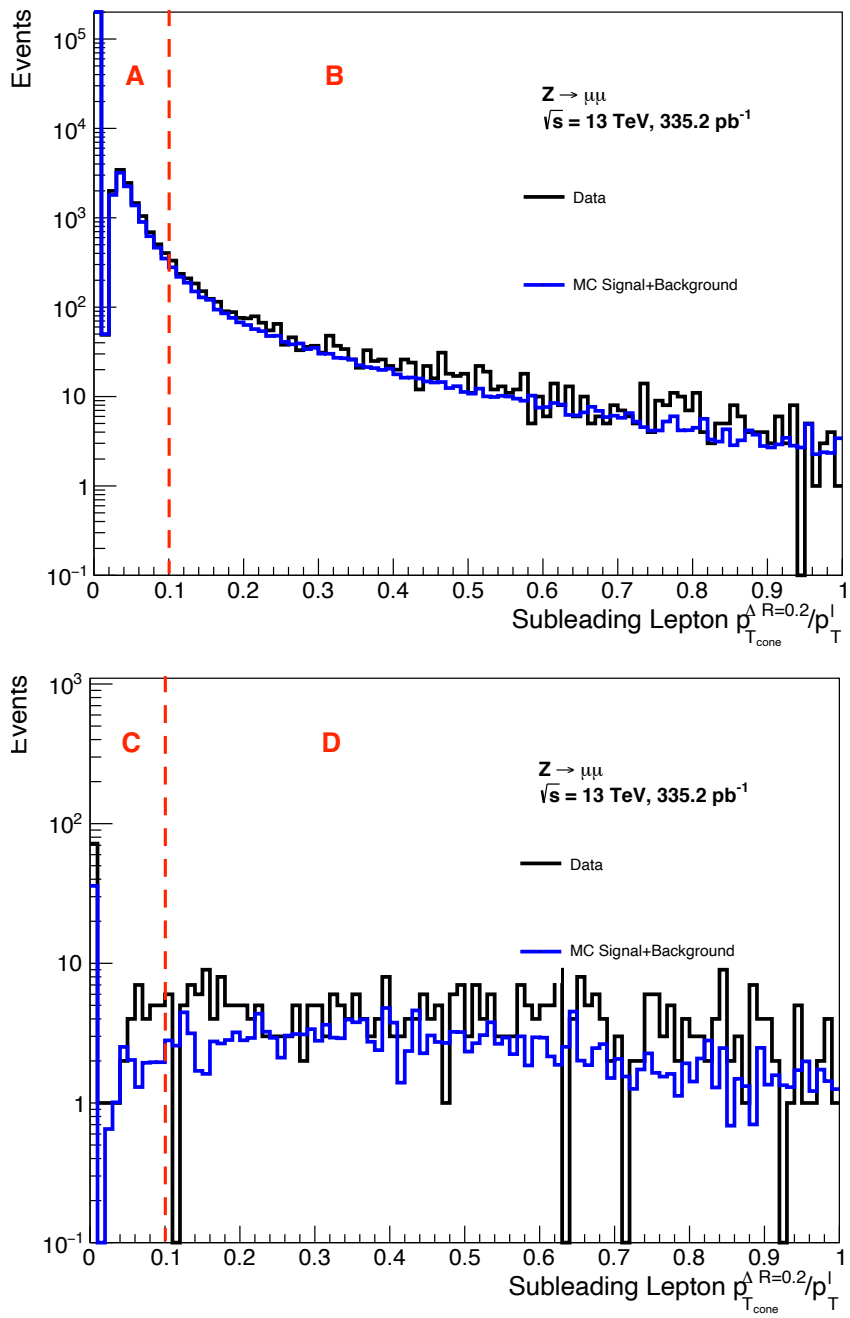

Figure D.1: $\sqrt{s} = 13$ TeV $Z \to \mu^+\mu^-$ sub-leading lepton isolation event distribution for the four regions of the ABCD method as part of the MJ estimation. Data (black) and the addition of the signal and background MCs (blue) are shown. Events on the left side of the red line are considered to be isolated, and events on the right of the red line are anti-isolated.

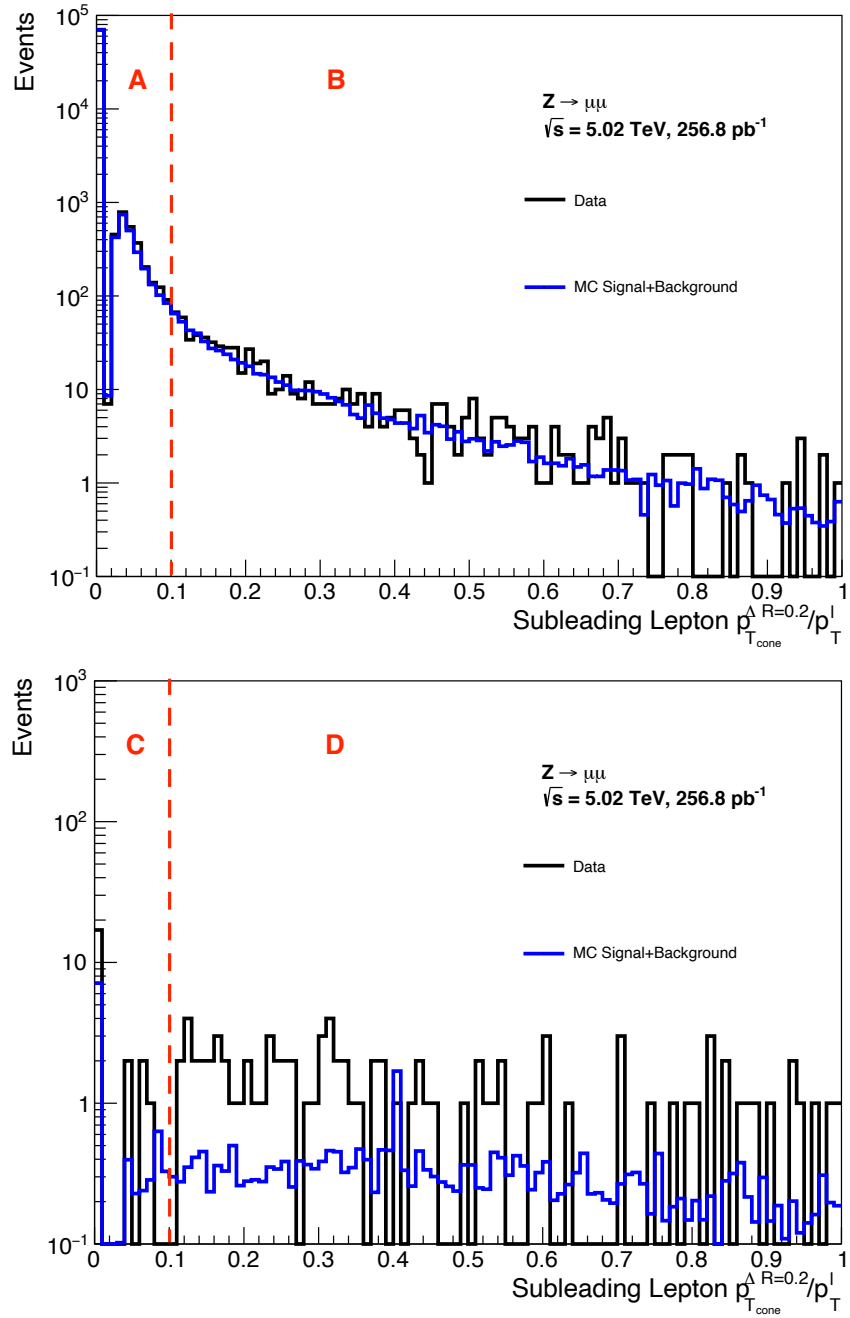

Figure D.2: $\sqrt{s} = 5$ TeV $Z \to \mu^+\mu^-$ sub-leading lepton isolation event distribution for the four regions of the ABCD method as part of the MJ estimation. Data (black) and the addition of the signal and background MCs (blue) are shown. Events on the left side of the red line are considered to be isolated, and events on the right of the red line are anti-isolated.

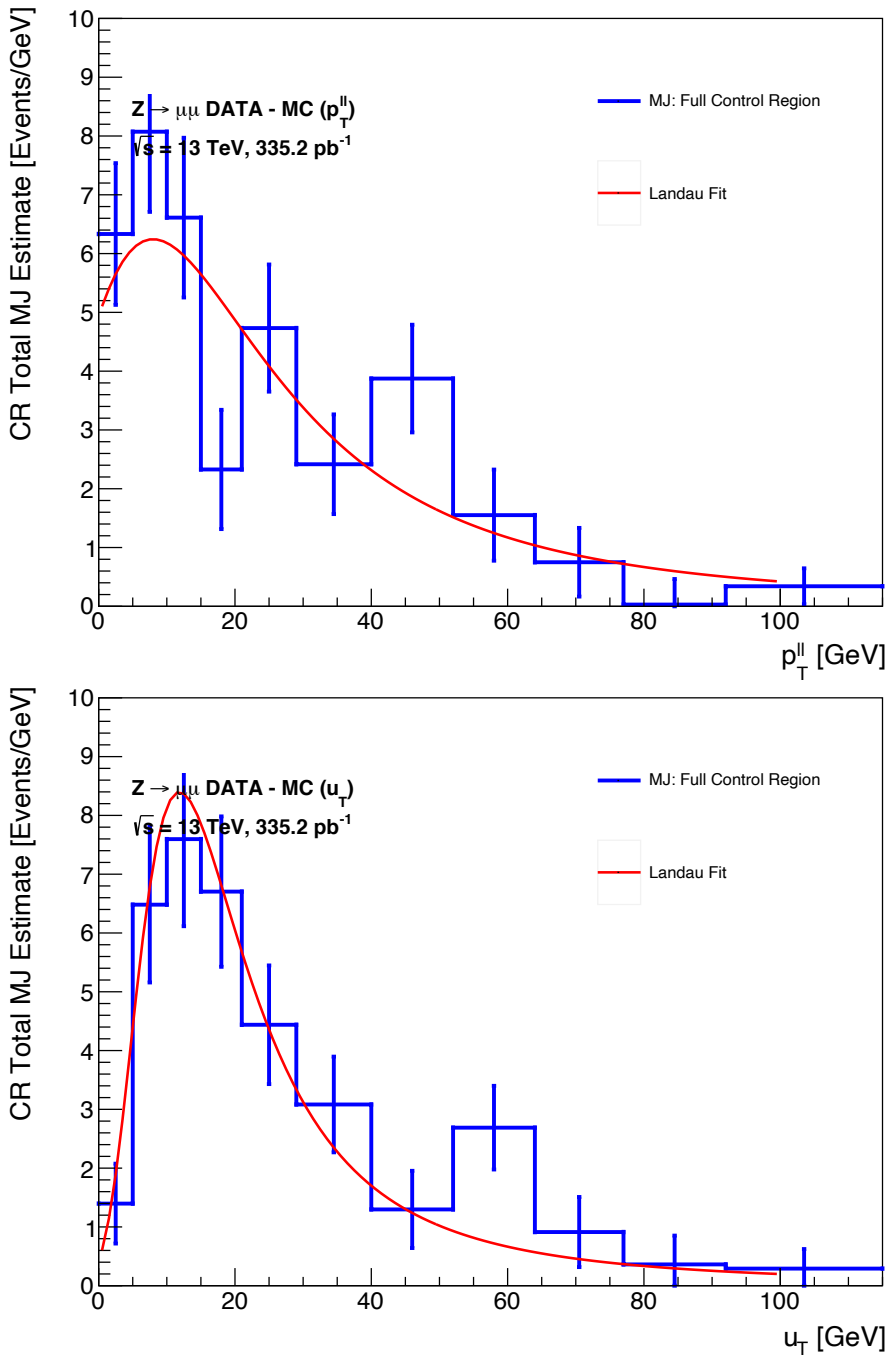

Figure D.3: Landau fit (red) to the shape of the MJ control region (black) as a function of the p_{T}^{ll} (top) and u_{T} (bottom) observables for the $Z \to \mu^+\mu^-$ channel at $\sqrt{s} = 13$ TeV.

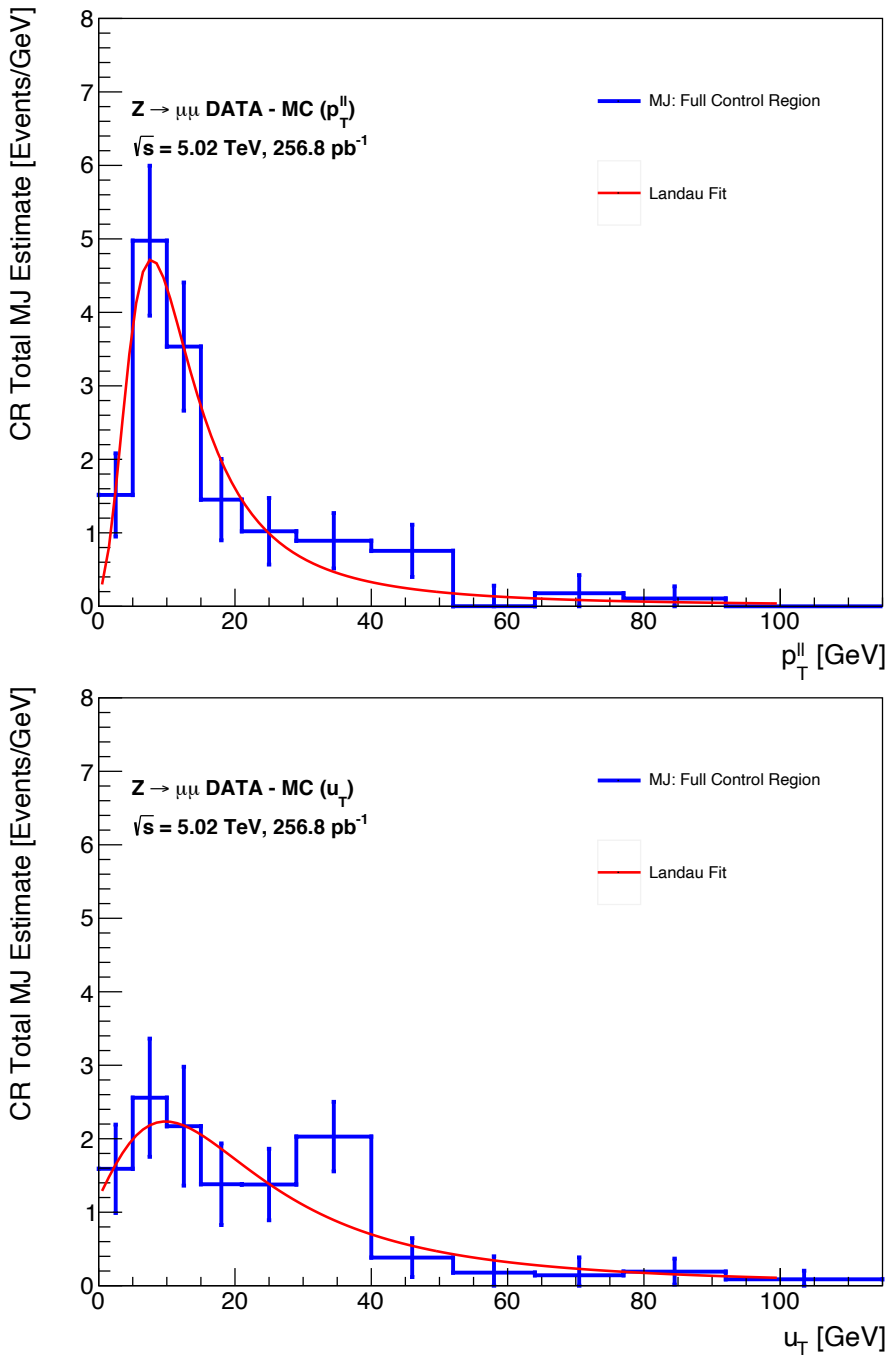

Figure D.4: Landau fit (red) to the shape of the MJ control region (black) as a function of the p_{T}^{ll} (top) and u_{T} (bottom) observables for the $Z \to \mu^+\mu^-$ channel at $\sqrt{s} = 5$ TeV.

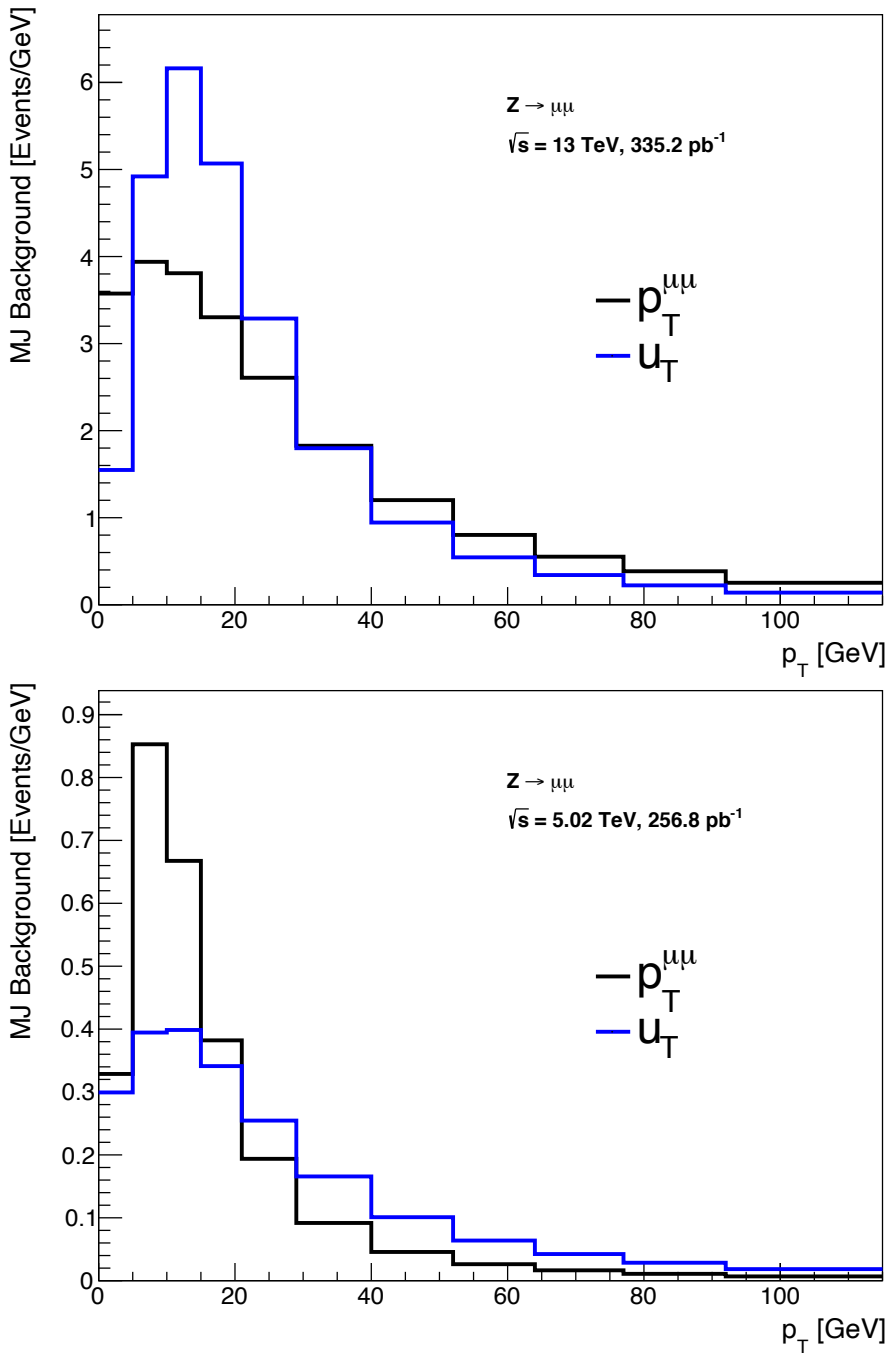

Figure D.5: MJ distributions for the p_{T}^{ll} and u_{T} observables at $\sqrt{s} = 13$ TeV (top) and 5 (bottom) TeV in the $Z \to \mu^+\mu^-$ channel determined using the ABCD method.

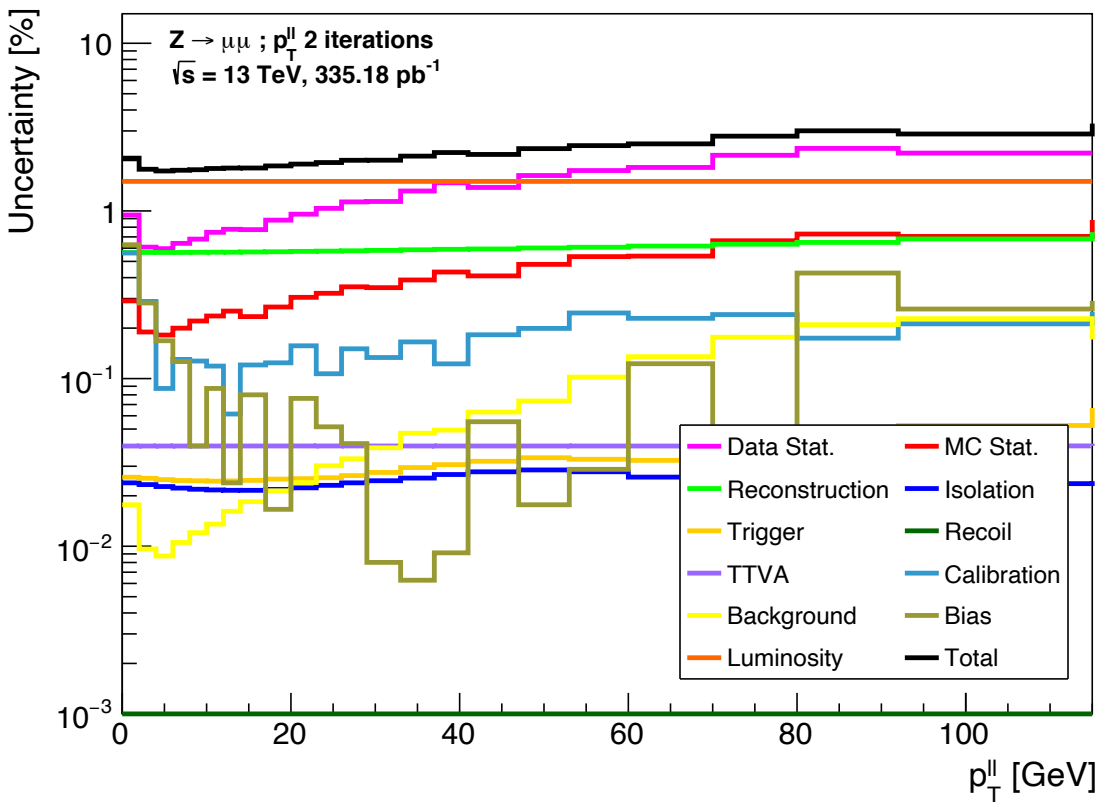

Figure D.6: Total percent uncertainty as a function of p_{T} for all the sources of uncertainty that contribute to the final p_{T}^{Z} measurement in the $Z \to \mu^{+}\mu^{-}$ channel at $\sqrt{s} = 13$ TeV for the p_{T}^{ll} observable. Each contributing source is unfolded with 2 unfolding iterations (aside from luminosity which is not affected by unfolding). The total uncertainty (black) is the sum in quadrature of each individual source.

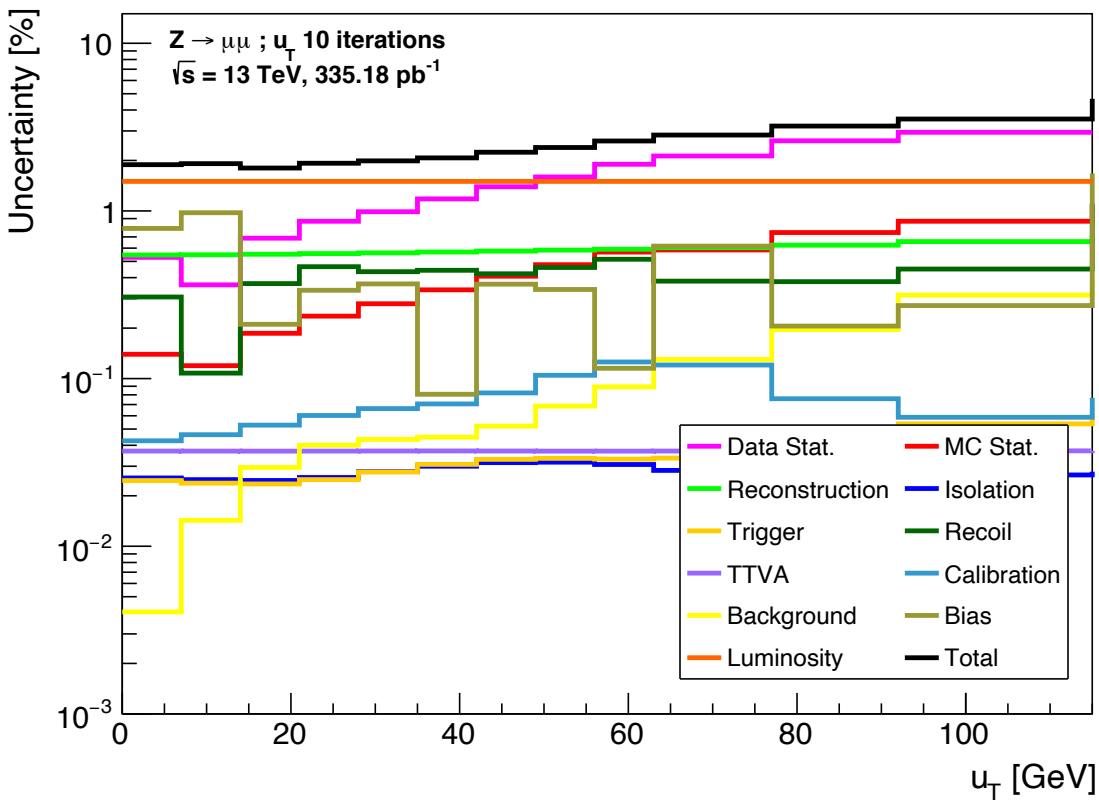

Figure D.7: Total percent uncertainty as a function of u_{T} for all the sources of uncertainty that contribute to the final p_{T}^{Z} measurement in the $Z \to \mu^{+}\mu^{-}$ channel at $\sqrt{s} = 13$ TeV for the u_{T} observable. Each contributing source is unfolded with 10 unfolding iterations (aside from luminosity which is not affected by unfolding). The total uncertainty (black) is the sum in quadrature of each individual source.

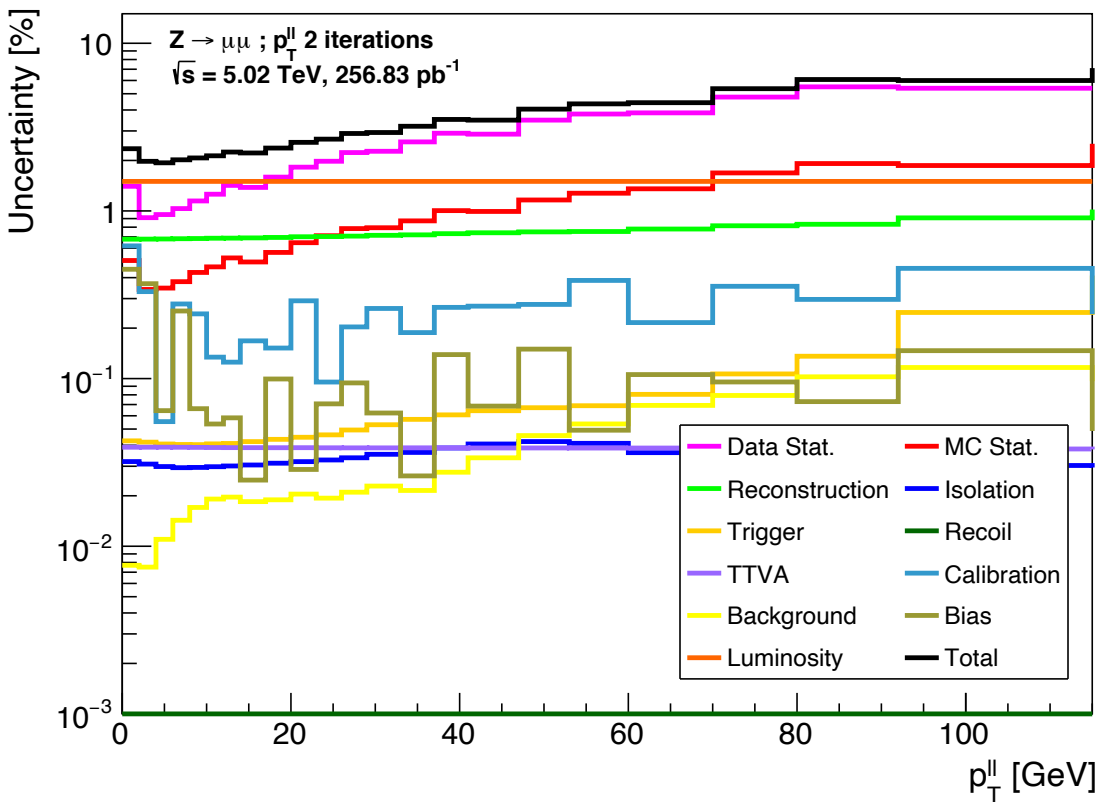

Figure D.8: Total percent uncertainty as a function of p_{T} for all the sources of uncertainty that contribute to the final p_{T}^{Z} measurement in the $Z \to \mu^+\mu^-$ channel at $\sqrt{s} = 5$ TeV for the p_{T}^{ll} observable. Each contributing source is unfolded with 2 unfolding iterations (aside from luminosity which is not affected by unfolding). The total uncertainty (black) is the sum in quadrature of each individual source.

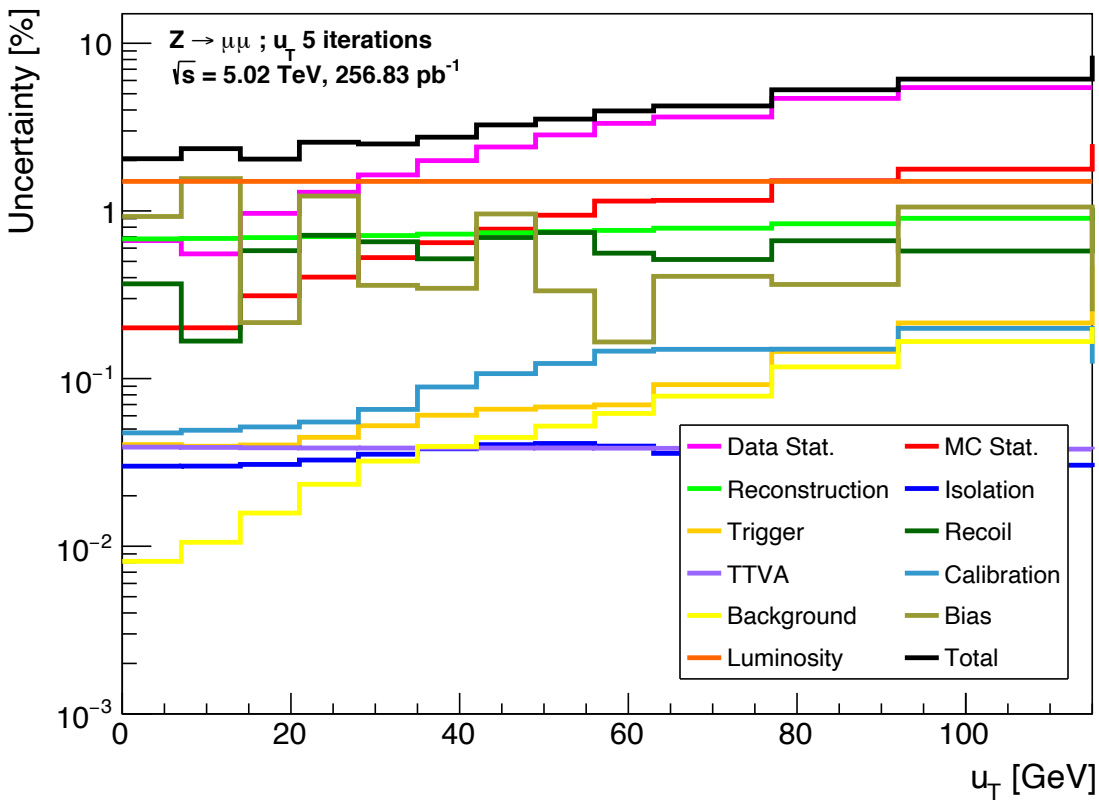

Figure D.9: Total percent uncertainty as a function of u_{T} for all the sources of uncertainty that contribute to the final p_{T}^{Z} measurement in the $Z \to \mu^{+}\mu^{-}$ channel at $\sqrt{s} = 5$ TeV for the u_{T} observable. Each contributing source is unfolded with 5 unfolding iterations (aside from luminosity which is not affected by unfolding). The total uncertainty (black) is the sum in quadrature of each individual source.

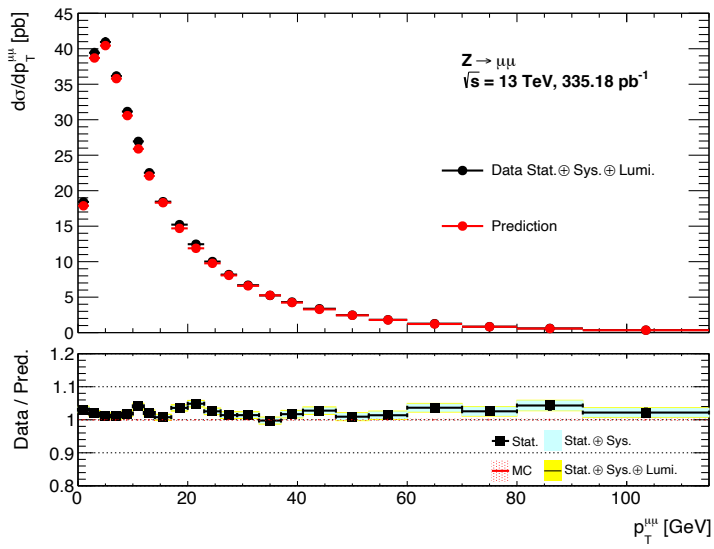

(a) p_{T}^{ll}

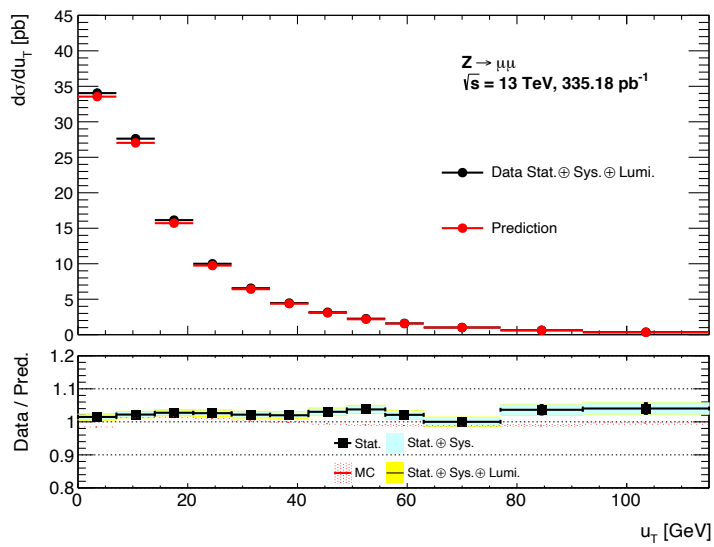

(b) u_{T}

Figure D.10: Differential cross section as a function of p_{T} in the $Z \to \mu^+\mu^-$ channel at $\sqrt{s} = 13$ TeV. The p_{T}^{Z} differential cross section is measured using both the p_{T}^{ll} observable (top) and the u_{T} observable (bottom). The data are shown with its total uncertainty and plotted alongside the nominal MC prediction. The lower ratio panel shows the data-to-prediction ratio. The uncertainty on the data points are shown as increasingly large bands, incorporating the statistical (black vertical bars), systematic (blue band), and luminosity (yellow band) uncertainties. The MC statistical uncertainty (red dotted band) is also shown along the x-axis but it is negligible on this plot.

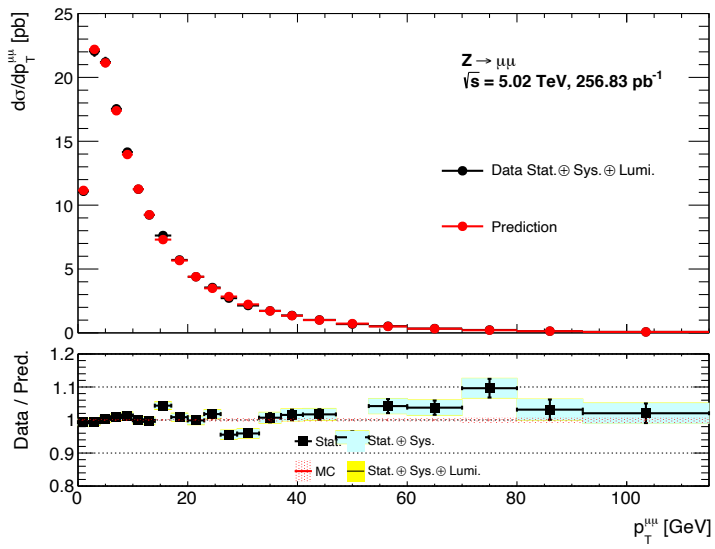

(a) p_{T}^{ll}

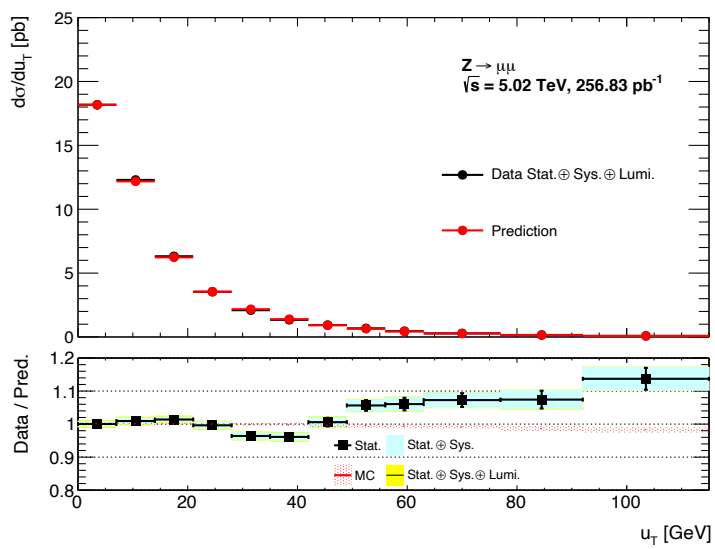

(b) u_{T}

Figure D.11: Differential cross section as a function of p_{T} in the $Z \to \mu^+\mu^-$ channel at $\sqrt{s} = 5$ TeV. The p_{T}^{Z} differential cross section is measured using both the p_{T}^{ll} observable (top) and the u_{T} observable (bottom). The data are shown with its total uncertainty and plotted alongside the nominal MC prediction. The lower ratio panel shows the data-to-prediction ratio. The uncertainty on the data points are shown as increasingly large bands, incorporating the statistical (black vertical bars), systematic (blue band), and luminosity (yellow band) uncertainties. The MC statistical uncertainty (red dotted band) is also shown along the x-axis.

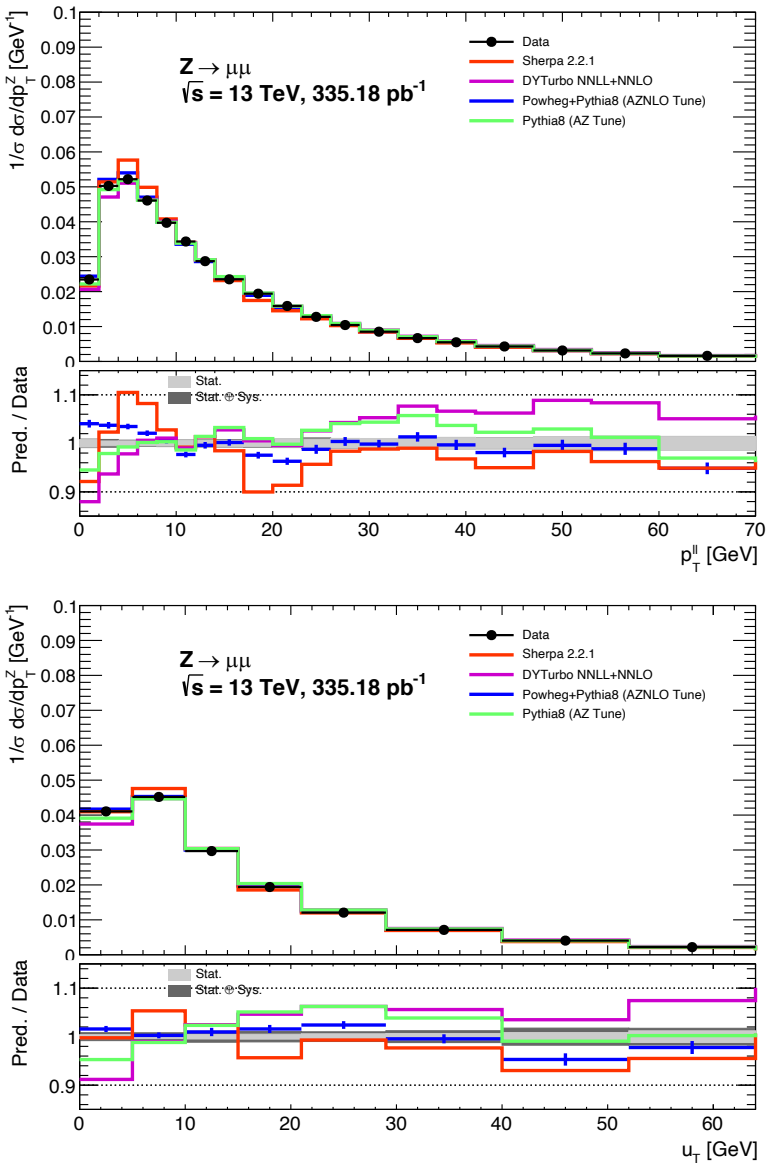

Figure D.12: $Z \to \mu^+\mu^-$ normalized differential cross section as a function of p_{T} for the p_{T}^{ll} (top) and u_{T} (bottom) observables at $\sqrt{s} = 13$ TeV. The differential cross section is normalized to the total cross section. In each plot, the data are compared to four different predictions: the nominal Powheg+Pythia8 MC shown with its statistical error bars (blue curve), Sherpa (red curve), DYTurbo (purple curve), Pythia8 AZ (green curve). The ratio plot in the lower panel shows each prediction divided by the data. The data, with its central value of 1 along the lower panel x-axis, are shown with its statistical uncertainty band (light grey) and the statistical plus systematics uncertainty band (dark grey).

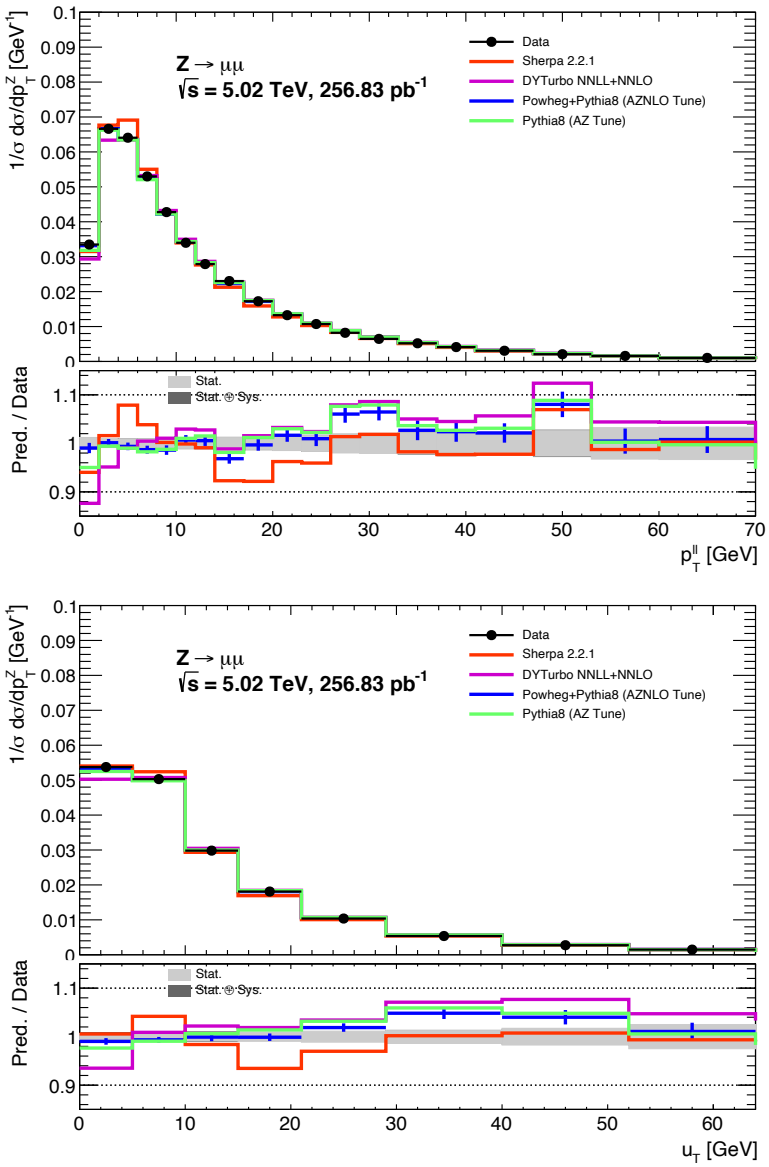

Figure D.13: $Z \to \mu^+\mu^-$ normalized differential cross section as a function of p_{T} for the p_{T}^{ll} (top) and u_{T} (bottom) observables at $\sqrt{s} = 5$ TeV. The differential cross section is normalized to the total cross section. In each plot, the data are compared to four different predictions: the nominal Powheg+Pythia8 MC shown with its statistical error bars (blue curve), Sherpa (red curve), DYTurbo (purple curve), Pythia8 AZ (green curve). The ratio plot in the lower panel shows each prediction divided by the data. The data, with its central value of 1 along the lower panel x-axis, are shown with its statistical uncertainty band (light grey) and the statistical plus systematics uncertainty band (dark grey).

Appendix E

Additional p_{T}^{W} Unfolding Bias Uncertainty Channels

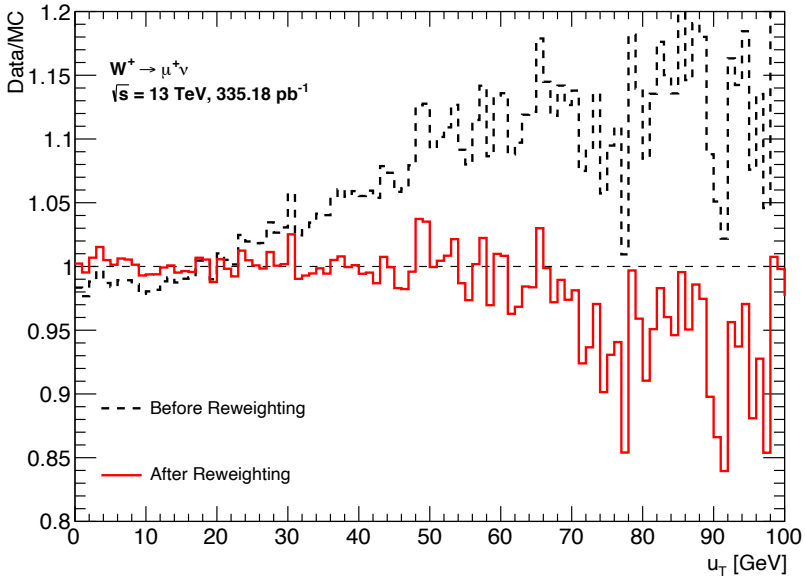

(a) $W^+ \to \mu^+\nu$

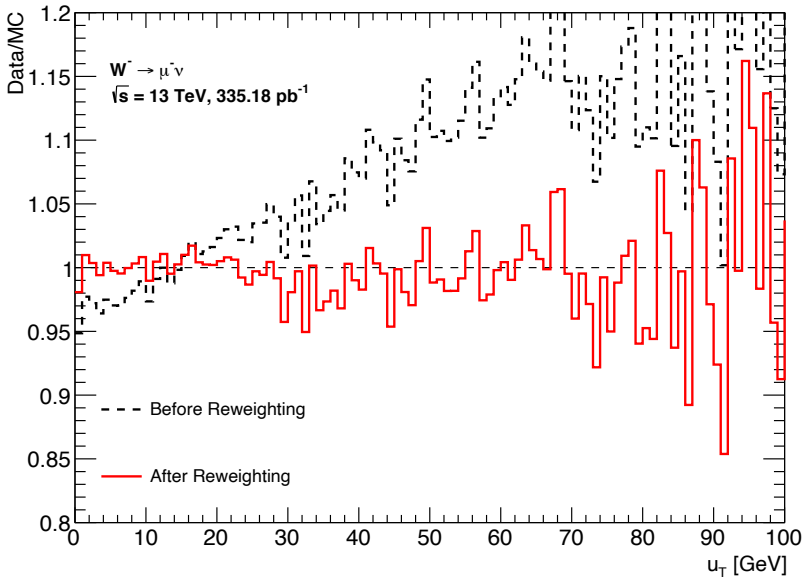

(b) $W^- \to \mu^-\bar{\nu}$

Figure E.1: Data-to-MC ratio at reconstructed-level in the $W^+ \to \mu^+\nu$ (top) and $W^- \to \mu^-\bar{\nu}$ (bottom) channels at $\sqrt{s} = 13$ TeV before and after the nominal MC has been reweighted.

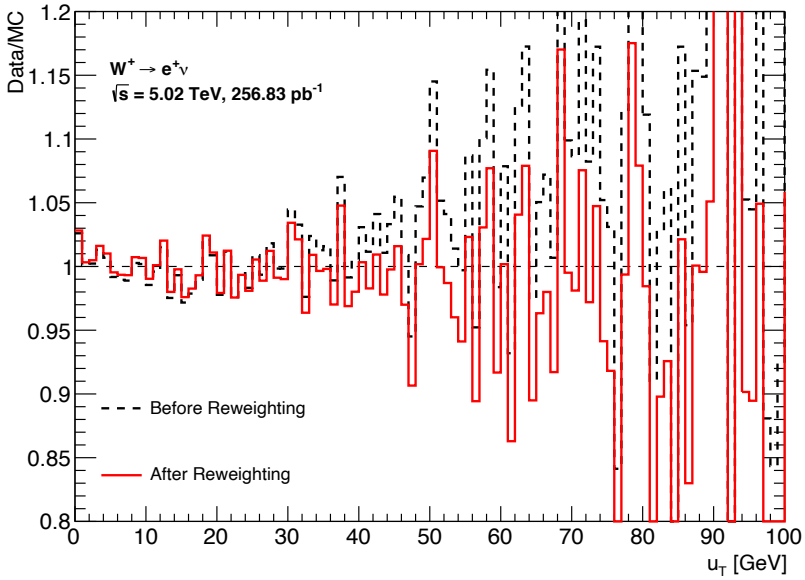

(a) $W^+ \to e^+\nu$

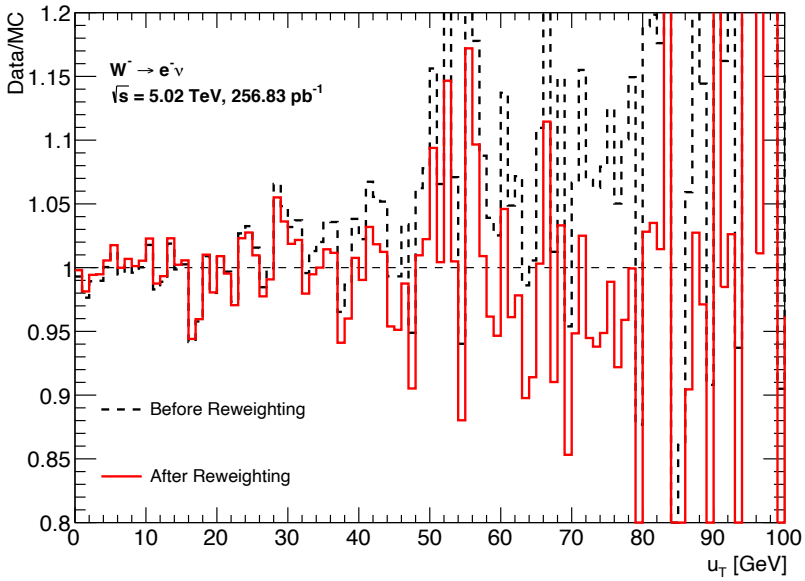

(b) $W^- \to e^-\bar{\nu}$

Figure E.2: Data-to-MC ratio at reconstructed-level in the $W^+ \to e^+\nu$ (top) and $W^- \to e^-\bar{\nu}$ (bottom) channels at $\sqrt{s} = 5$ TeV before and after the nominal MC has been reweighted.

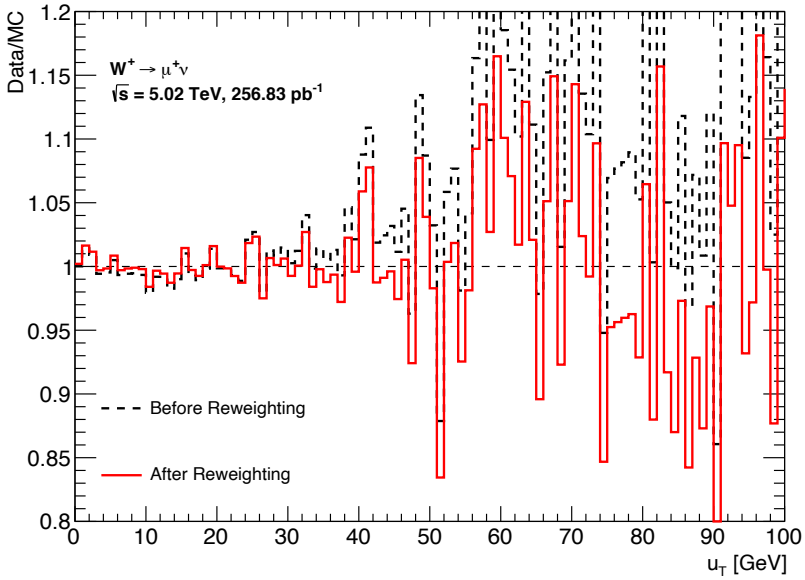

(a) $W^+ \to \mu^+\nu$

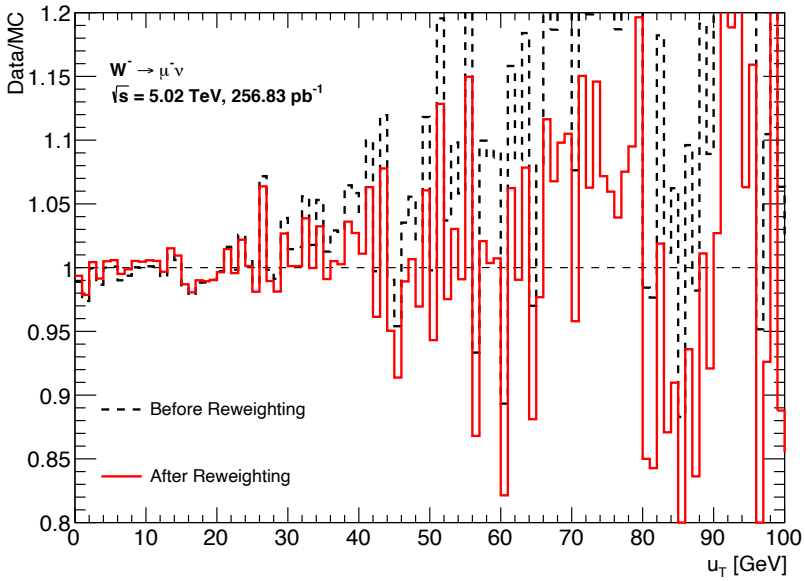

(b) $W^- \to \mu^-\bar{\nu}$

Figure E.3: Data-to-MC ratio at reconstructed-level in the $W^+ \to \mu^+\nu$ (top) and $W^- \to \mu^-\bar{\nu}$ (bottom) channels at $\sqrt{s} = 5$ TeV before and after the nominal MC has been reweighted.

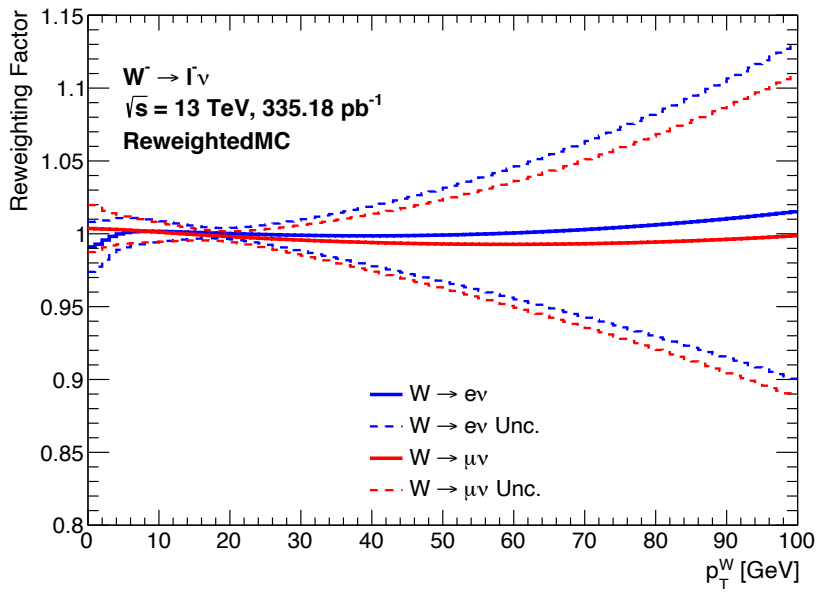

(a) $\sqrt{s} = 13$ TeV

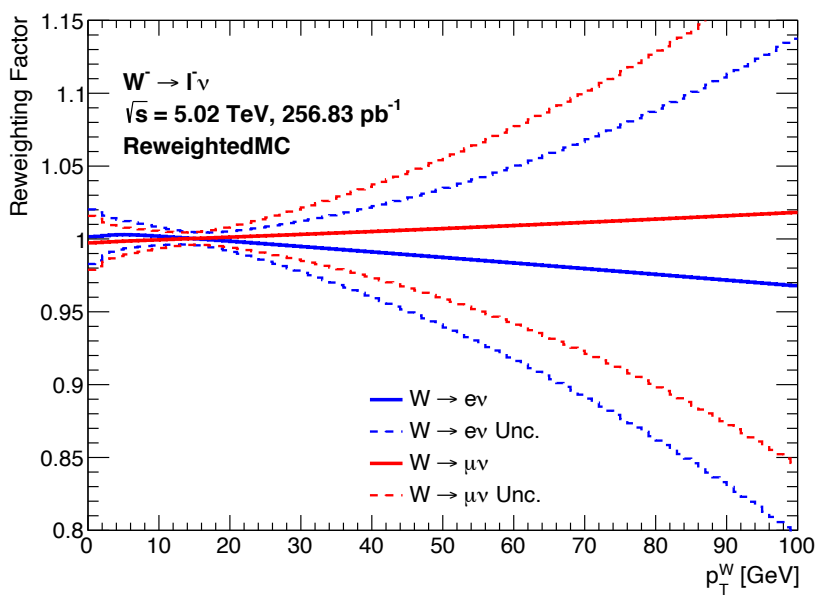

(b) $\sqrt{s} = 5$ TeV

Figure E.4: Bias correction closure reweighting factors for the $W^- \to l^-\bar{\nu}$ channels at $\sqrt{s} = 13$ TeV (top) and $\sqrt{s} = 5$ TeV (bottom). The $W \to e\nu$ channels and their corresponding uncertainty bands are shown in blue, with the $W \to \mu\nu$ channels in red.

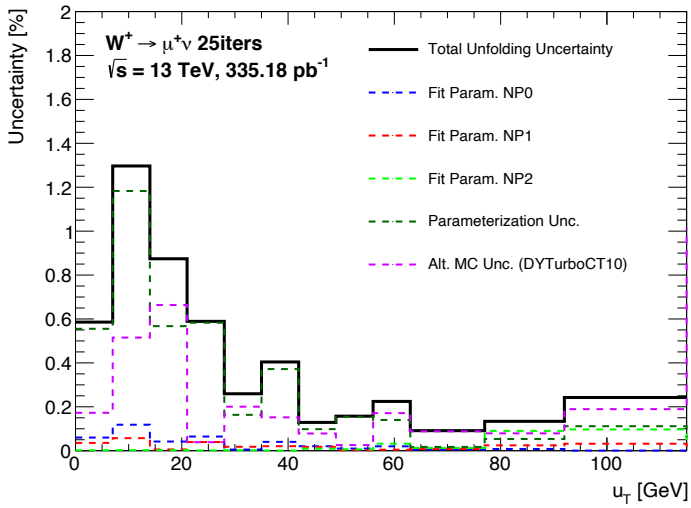

(a) $\sqrt{s} = 13$ TeV

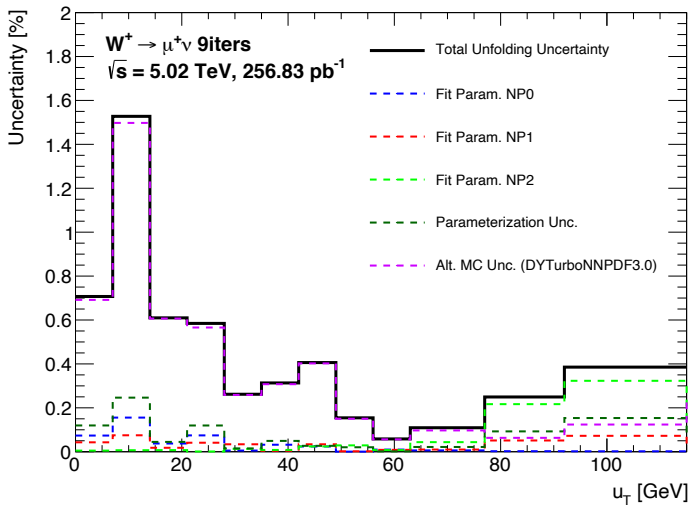

(b) $\sqrt{s} = 5$ TeV

Figure E.5: Contributions to the unfolding bias uncertainty, shown as percent uncertainty as a function of unfolded u_{T} for the $W^+ \to \mu^+\nu$ channel at $\sqrt{s} = 13$ TeV (top) and $\sqrt{s} = 5$ TeV (bottom). The three fit parameter uncertainties, NP0 (blue curve), NP1 (red curve), and NP2 (light green curve), are the contributing sources from the fit uncertainty. The parameterization uncertainty (dark green curve) is the uncertainty from the choice of fit function, and the alternative MC uncertainty (purple curve) is the uncertainty based on the choice of initial MC prediction. The alternative MC that defines this uncertainty is shown in brackets in the legend. The total uncertainty (black curve) is the sum in quadrature of these five curves.

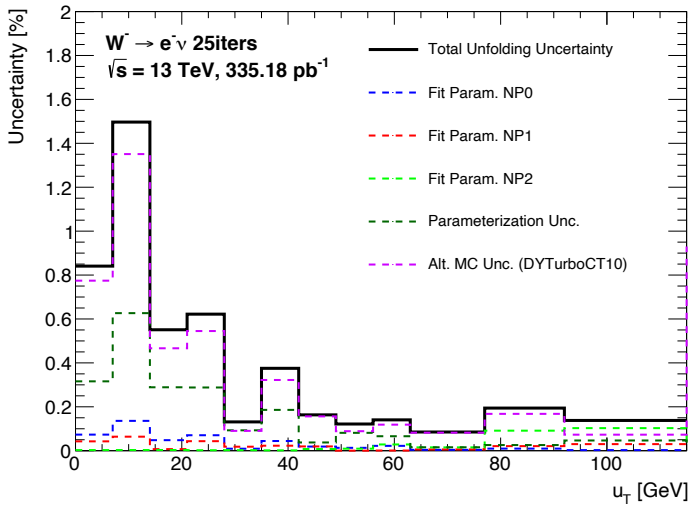

(a) $\sqrt{s} = 13$ TeV

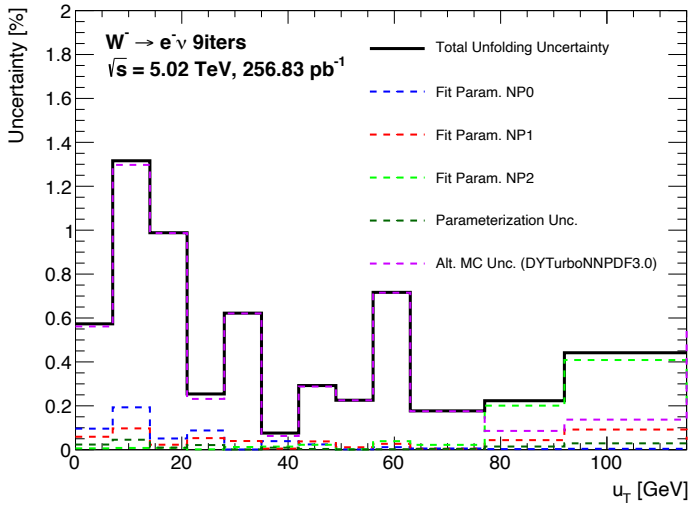

(b) $\sqrt{s} = 5$ TeV

Figure E.6: Contributions to the unfolding bias uncertainty, shown as percent uncertainty as a function of unfolded u_{T} for the $W^- \to e^-\bar{\nu}$ channel at $\sqrt{s} = 13$ TeV (top) and $\sqrt{s} = 5$ TeV (bottom). The three fit parameter uncertainties, NP0 (blue curve), NP1 (red curve), and NP2 (light green curve), are the contributing sources from the fit uncertainty. The parameterization uncertainty (dark green curve) is the uncertainty from the choice of fit function, and the alternative MC uncertainty (purple curve) is the uncertainty based on the choice of initial MC prediction. The alternative MC that defines this uncertainty is shown in brackets in the legend. The total uncertainty (black curve) is the sum in quadrature of these five curves.

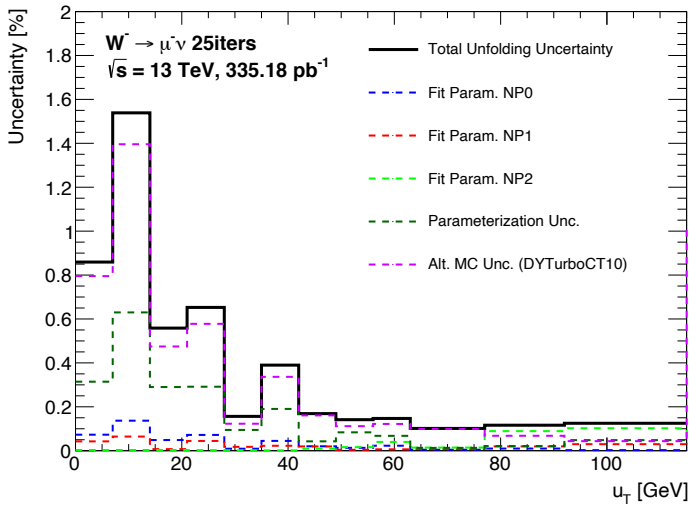

(a) $\sqrt{s} = 13$ TeV

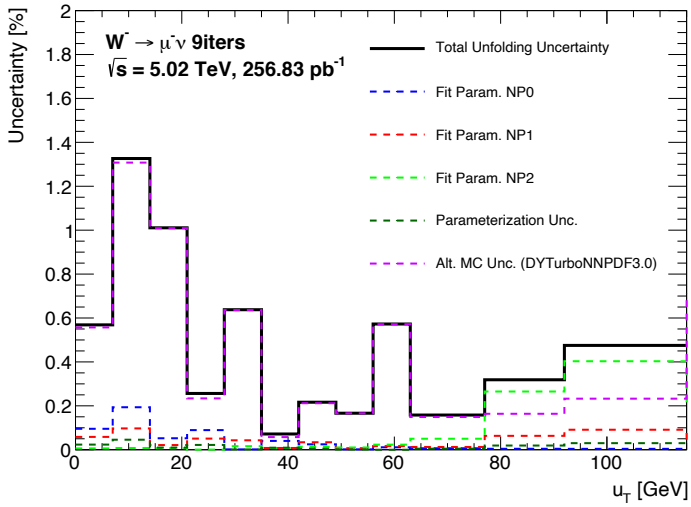

(b) $\sqrt{s} = 5$ TeV

Figure E.7: Contributions to the unfolding bias uncertainty, shown as percent uncertainty as a function of unfolded u_{T} for the $W^- \to \mu^- \bar{\nu}$ channel at $\sqrt{s} = 13$ TeV (top) and $\sqrt{s} = 5$ TeV (bottom). The three fit parameter uncertainties, NP0 (blue curve), NP1 (red curve), and NP2 (light green curve), are the contributing sources from the fit uncertainty. The parameterization uncertainty (dark green curve) is the uncertainty from the choice of fit function, and the alternative MC uncertainty (purple curve) is the uncertainty based on the choice of initial MC prediction. The alternative MC that defines this uncertainty is shown in brackets in the legend. The total uncertainty (black curve) is the sum in quadrature of these five curves.

Appendix F

ATLAS Control Room Operations

As a member of the large experimental particle physics collaboration that is ATLAS, I, along with the other physicists in the collaboration, use the data that ATLAS records to make measurements. There are many advantages to being part of a huge team like this, such as the fact that collaborators from all over the world have equal access to the data without ever having to leave their home institutions or countries. One potential downside, however, is that a collaborator, for example a PhD student, can spend their entire PhD career working with these data remotely from their university without ever actively participating in the data-taking and entering the ATLAS Control Room (ACR) at CERN, let alone coming to CERN for a visit in the first place. The ACR is the main room from which ATLAS detectors are turned on and monitored, and is where data-taking takes place. Being in the ACR and participating in data-taking is, in my opinion, a coveted experience that can really help to fill holes in one's understanding of the experiment. I can read about the actual operations of ATLAS, but taking shifts in the ACR is a whole different experience.

Each major detector and central control room activity has its own area in the ACR to enact and monitor their operations. These areas are known as "desks", because they do each have physical desks and computers. At the time of this thesis writing, I have been trained to take shifts on desks in the ACR. I will be taking these shifts later in the summer. In this chapter, I will touch on my experiences during training that helped grow my connection to the experiment, as I can now relate some aspects of my previous work to direct decisions that are taken in the ACR. This brief chapter will

overview daily operations in the ACR, and discuss how the desks that I am trained for – Run Control and Trigger – connect back to points that were mentioned in previous sections of my thesis.

F.1 ACR Overview

The ACR is the data-taking centre of the ATLAS Experiment. Located 100 metres above the ATLAS detector itself, the ACR is where the protons from the LHC are monitored as they are delivered to ATLAS for p-p collisions. The ACR is still active even when there are no p-p collisions for activities like detector commissioning where cosmic rays are recorded as data, where random triggers are fired to test the detector response, and where the detector subsystems undergo their regular calibration runs. Of course, the ACR is most active when p-p collisions are underway, and general excitement is at its highest during the start of a new run. One of these exciting times happens to be right now, as we start Run 3 in July, 2022. ATLAS has been in shutdown mode since the last collisions late in 2018, just after the start of my PhD. Therefore this summer is my first opportunity to participate in the data-taking.

The ACR is divided into six main desk areas, with each assigned to a specific task. There are three desks associated with the operations of detector subsystems (Inner Detector, Calorimeters & Forward Detectors and Muon Spectrometer) and three desks for centralized activities (Run Control, Trigger and Data Quality). Each of these desks require 24/7 operation by a specifically-trained shifter. In addition, there are two more managerial roles: the Shift Leader, who oversees all ACR operations, and the SLIMOS (Shift Leader in Matters of Safety), both roles requiring 24/7 operation as well. Therefore at minimum, there are eight people in the ACR at any given time, typically from March to December of every running year. This number is usually higher, for example, more specialized detector experts must be available in the ACR when tasks like commissioning are underway, and multiple operators are needed during high-intensity tasks like the start of a new LHC run. Additionally, there are often shadow shifters training to become desk experts.

Figure F.1 shows a diagram of the eight core ACR roles discussed above and their layout within the control room: Trigger, RC (Run Control), Safety (SLIMOS), ID

(Inner Detector), Muon (Muon Spectrometer), DQ (Data Quality), SL (Shift Leader), and Calo/FWD (Calorimeter and Forward Detectors). The numbers at each desk are the local desk phone numbers.

I have trained as a Run Control and Trigger desk shifter. Both of these desks are positioned near the front of the control room in order to be able to see important relevant information that is projected onto the screens on the front wall of the control room. For the Trigger desk, this includes live trigger rates, and for Run Control, this includes the user interface displaying error messages and detector components that are active/inactive that is shared via Zoom with experts who may need to connect to help with specific issues that arise. Figure F.2 shows a photo of the ACR during one of my shadow shifts at the Run Control desk, taken by one of the cameras that live-monitors the ACR.

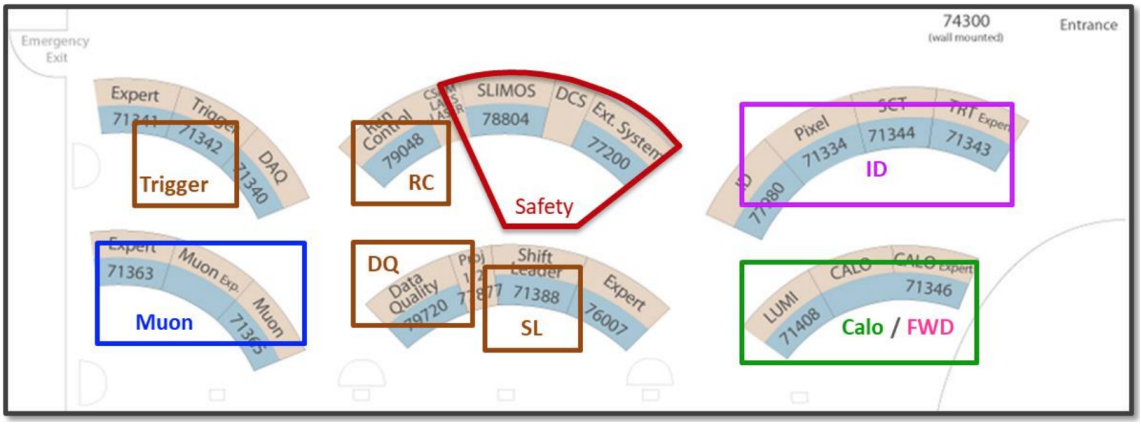

Figure F.1: Schematic of the ATLAS Control Room main desks. The numbers on each desk correspond to the phone numbers of each desk phone [97].

The following sections discuss the duties and some interesting aspects of the Run Control (Sec. F.2) and Trigger (Sec. F.3) desks.

F.2 Run Control Desk

The Run Control shifter is the main operator of a run. But what is a 'run' in this sense? When protons are colliding in the ATLAS detector, ATLAS does not automatically record data. Someone must physically press a `START` button so that data is recorded. This person is the Run Control shifter! When the `START` button

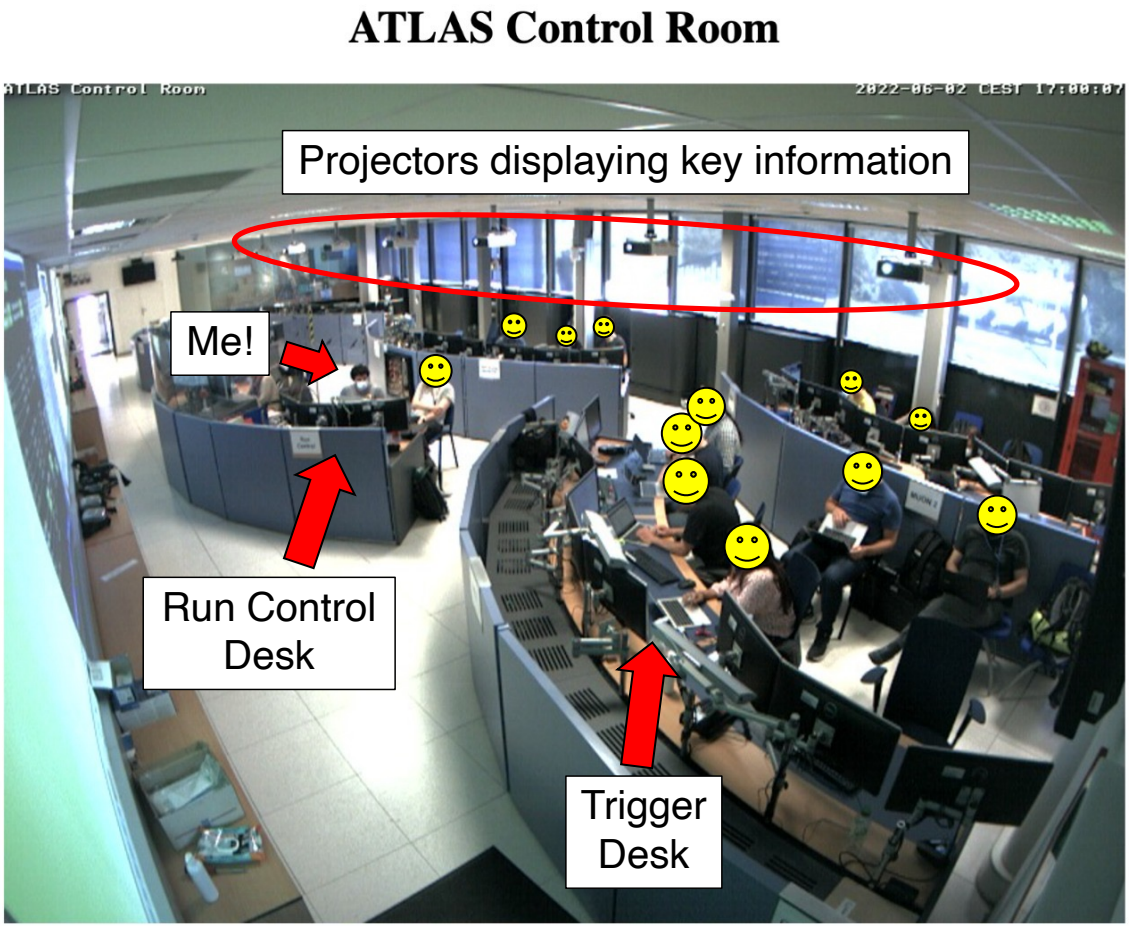

Figure F.2: Photo of the ATLAS Control Room during my shadow shift at the Run Control desk. The Run Control and Trigger desks are labeled. Important information is projected to the wall-height screens at the from of the room. Faces of other shifters are covered for privacy.

is pressed, a new run – assigned a six-digit number – begins. This run lasts until the `STOP` button is pressed, also by the Run Control shifter. It sounds obvious, but this was a profound realization for me. In Section 4.1, I mentioned how the low-μ dataset was taken across eight days of running. I had cross-listed this information by looking at the run numbers assigned to the dataset – run numbers just like the ones that appear on the Run Control graphical user interface when a new run is started. In fact, all runs can be traced by run number through the history of ATLAS

data-taking, to understand the precise conditions of each run, and even to check the log book (filled out by the Run Control shifter each shift) that notes everything important that happened during a given eight-hour shift. One shift may constitute multiple runs during a calibration-focused shift or one where the beam or detector conditions change sufficiently to warrant the start of a new run, or a shift might only have a single run that was neither started nor stopped during a long data-taking sequence.

Of course it is not quite as simple as pressing start and stop. Before starting a run, all the correct detector components needed for a run must be enabled and the correct trigger keys (the L1 and HLT trigger settings that define the target and maximum trigger rates) must be loaded. There are also initialization and configuration steps before the actual starting of the run. If an error occurs during these steps, for example a detector component might not be loading properly, it is up to the Run Control shifter to identify the error and contact the relevant expert if there is no known quick solution. Similarly, to stop a run, these steps must be taken in reverse, so that first the run is stopped (meaning data are no longer being recorded), then the detector components are unconfigured, and finally the system is shutdown. In addition to starting and stopping, the "hold trigger" button can be pressed (`HOLD TRG`), which will temporarily stop the triggers from firing so that no data is recorded. This option is selected when there is a small issue that requires a simple, quick fix, like if a small detector component is not working properly so it must be removed from the run, but it will not significantly affect data-taking given the nature of the run. Figure F.3 shows the Run Control desk commands for starting and stopping a run, along with holding and resuming the trigger.

In addition to operating runs, the Run Control shifter must actively monitor an ongoing run and react to error messages to minimize dead time where data are not recorded. For example, if a detector component fails, the system will automatically hold the trigger and prevent data from being recorded. This is what is meant by dead time. When something like this happens, the Run Control shifter must quickly identify the source of the error, and communicate with the other shifters in the room to solve the problem if a quick solution is not found. Consistent communication is vital. One aspect of a Run Control shift is that almost everyone in the ACR comes to

Figure F.3: Run Control desk commands for starting and stopping a run.

talk to you to help identify specific minor detector components (known as partitions) that must be enabled/disabled, and to generally work together to solve problems. All issues are reported in the logbook and frequent discussions are had with the Shift Leader. It is important to note that the *decision* to start/stop a run does not come from the Run Control shifter: these decisions are made by the Shift Leader, who the Run Control shifter reports to. The Run Control desk also works closely with the Trigger desk shifter, as we will see in the next section.

F.3 Trigger Desk

ATLAS shifters who want to train to take shifts at the Run Control desk must also train as a Trigger desk shifter (and vice-versa). This is because these two desks work closely together to configure runs and to identify potential issues during a run. The first responsibility of the Trigger shifter is to provide the trigger configuration to the

Run Control shifter to configure the run. This is a set of four numbers that as an example might look like: SMK = 3084; BGK = 1397; L1 = 1323; HLT = 1255. SMK, the Super Master Key, defines the type of run: physics, cosmic, or heavy ion. The SMK specified here is from an early Run-3 physics run. The BGK (Bunch Group Key) defines a set of up to 16 (proton) bunch group options, specifying things like whether or not there are bunches of protons colliding and if there will be empty bunch crossings. The next two keys, L1 and HLT, define the pre-scaled trigger conditions for each of the L1 trigger and HLT. The combination of L1 and HLT keys listed here specify that both the L1 trigger and the HLT can have rates of up to 100 kHz. While the Run Control shifter is the person who loads in the trigger keys, the Trigger shifter is the one who identifies the trigger setup based on the plan of the run and provides the Run Control shifter with the trigger keys. As the example showed, trigger keys define the base setup of a run for the trigger system: the expected and maximum trigger rates for both the L1 trigger and HLT. These trigger rates are the sum of each individual trigger that is included in a run. One example of an individual trigger is the WTP trigger that was defined in Section 4.3.2.

Once trigger keys are loaded for a run and a run is ongoing, the Trigger shifter must monitor the trigger rates of both the L1 trigger and HLT to ensure that the rates are as expected. The Trigger shifter has access to an extensive monitoring system where each individual trigger rate can be observed as a function of time. This monitoring setup is completely customizable. Due to this setup, the Trigger shifter is the first person to notice any potential problems with the data-taking rate. Short spikes in the trigger rate (lasting for $\leq$ 1 second) are somewhat common and are recorded in the logbook and identified, but generally do not cause issues. However, if the overall trigger rate is larger than expected for more than a few seconds and is persisting, the Trigger shifter must identify which specific trigger(s) is causing the issue, track it to a detector system if possible, and alert the detector desk expert and the on-call trigger expert (there is always someone available by phone in case expert advice is needed).

During one of my shadow shifts during an ongoing calibration run, where nothing exciting was expected to happen, the trigger rate was spiking to 50 kHz when the maximum rate was expected to be 1 kHz based on the pre-defined trigger keys. The

issue persisted, so my Trigger desk shifter and I had to identify the specific triggers that were causing the spike. We tracked the issued to a trigger associated with the calorimeter and alerted the Calorimeter desk shifter. They had noticed the issue as well, but did not know what was happening. The Trigger desk also has access to individual trigger rates in each small component of the detector; after isolating the issue to the calorimeter, we pulled up the calorimeter cell map and found that one single cell had a trigger rate that was off the chart, meaning that there was an issue with its electronics. We alerted the Calorimeter desk shifter who called the expert. Sure enough, this individual cell had an electronics issue and had to be quickly removed from the calorimeter data-taking in order to be repaired offline. The entire data rate of the run had increased to unmanageable levels simply due to a single calorimeter cell (see for example Section 4.2.2 on topo-clusters and calorimeter cells), and as Trigger shifters we were able to identify the issue and notify the relevant experts in order to have the problem solved, allowing the run continue.

While this example happened during a run where no protons were colliding, the experience showed the importance of constantly monitoring trigger rates and the need for an active Trigger desk shifter and frequent communication within the ACR. During data-taking runs, issues like this can (and do) still occur, and it is not the end of the world. If a small detector component like an individual calorimeter cell has to be removed from a run, the run can still continue and the removed detector component is noted in a log. It is possible that this missing cell can be compensated for by information from neighbouring cells. If the missing component affects a large region of the detector, for example something like $2.0 < |\eta| < 2.1$, then datasets using this specific run may need to remove events from this region associated with that run.

All runs are measured in units called Luminosity Blocks (LB), which are periods of time in which the LHC and ATLAS conditions are considered constant and for which the average luminosity is calculated. LBs are usually 60 seconds long. Therefore ATLAS also has the power to remove individual LBs, merely 60s of data-taking, should something go wrong but then be quickly solved. This again highlights the need for a Trigger desk shifter's awareness and reaction time, because the exclusion granularity can be as fine as single LBs. Things like this are tracked with the "Good Run List" (first mentioned in Section 3.4.8). Events can be recorded, but after event

selection they may not be part of a good run in a selected region, so they must be removed. For example, "Good Run List" cuts are part of the Region A cuts in Figure 4.8 and Table 4.1. Sometimes due to more extreme issues, entire subsets of the data must be removed, which contributes to the difference between total integrated luminosity as delivered by the LHC, recorded by ATLAS, and considered good for physics, like what is shown for Run 2 in Figure 3.15.

F.4 Conclusion

In my brief ACR experiences, I have already started to feel much closer to the data that I have been using, as I begin to understand the "real" aspects of data-taking. The responsibility and vigilance that is necessary for each successful run is exciting, and it makes working with the data all that more meaningful. I am happy to know that I will have my fingerprints on ATLAS Run-3 data in another way – directly helping to ensure that high-quality data are successfully recorded.

Appendix G

Analysis Timeline, Contributions and Scholarships

In addition to research, I made a variety of other contributions to ATLAS, Carleton University, particle physics, and broader science communities during my time as a PhD student from September, 2018 to August, 2022. These contributions, along with scholarships that I was awarded, are briefly summarized in this CV-style appendix. The appendix begins with a graphic showing the timeline of my contributions to the Drell-Yan p_{T}^{W} and p_{T}^{Z} differential cross-section analysis (Figure G.1).

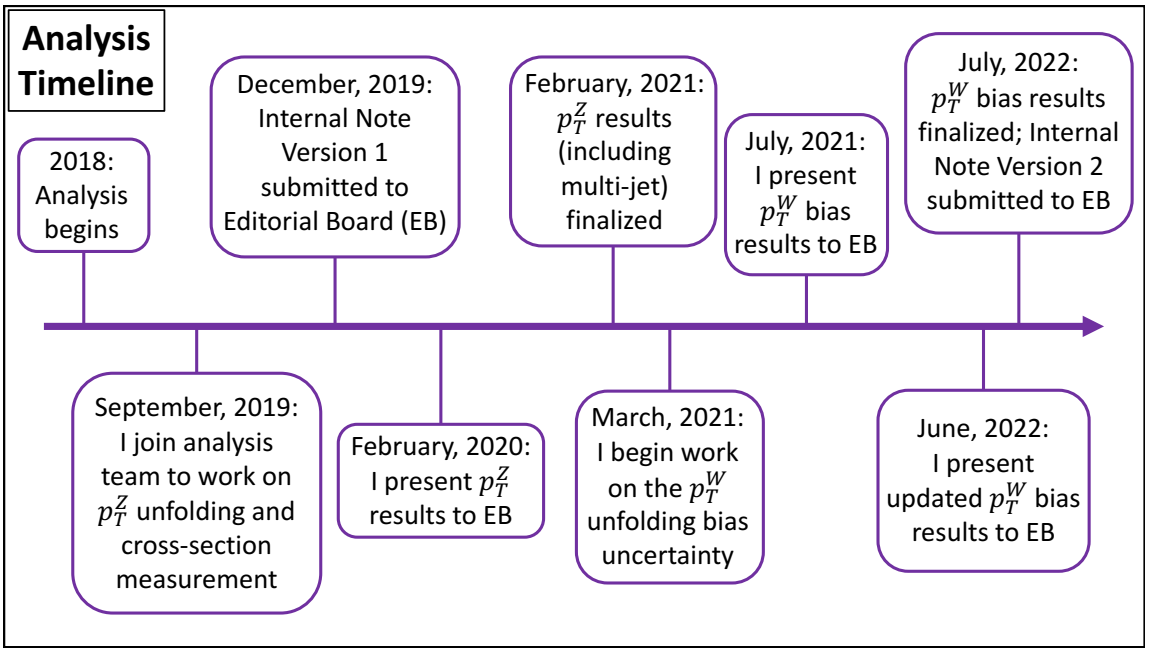

Figure G.1: Timeline of my analysis contributions to the Drell-Yan differential cross-section measurement with respect to p_{T}^{W} and p_{T}^{Z}.

Scholarships

- NSERC CGS-D Scholarship (2019 – 2022)
- Maureen Anne and Guljee Ismaily Scholarship (2021 – 2022)
- Gary S. Duck Graduate Bursary in Science (2020 – 2021)
- Physics Departmental Scholarship (2018 – 2022)
- Dean of Graduate Studies Entrance Scholarship (2018 – 2019)

ATLAS Research Notes and Presentations

- Wrote Internal Note on W tag-and-probe studies
- Contributed to Internal Note on p_{T}^{W} & p_{T}^{Z} multi-jet measurement
- Contributed to Internal Note on p_{T}^{W} & p_{T}^{Z} differential cross-section measurement at $\sqrt{s} = 13$ TeV and 5 TeV
- Presented W tag-and-probe results to Electron identification subgroup four times, Electron-Photon Combined Performance group once
- Presented p_{T}^{Z} & p_{T}^{W} analysis results to W/Z precision group more than 30 times
- Gave three presentations to Editorial Board: two for p_{T}^{W} analysis and one for p_{T}^{Z} analysis

Conference/Workshop/Invited Presentations

- *Electroweak Teamwork: Studying W and Z bosons to make precision Standard Model measurements with the ATLAS detector,* Ottawa-Carleton Institute for Physics Graduate Symposium (Virtual, 2021)
- *Precision measurement of the Z-boson transverse momentum with the ATLAS detector,* Canadian Association of Physicists Congress (Virtual, 2021)
- *Precision measurement of the Z-boson transverse momentum with the ATLAS detector,* Winter Nuclear & Particle Physics Conference (Virtual, 2021)

- **[Invited.]** *From SNOLAB to CERN: A Journey Through Space and Time,* Institute for Earth & Space Exploration (Western University, Virtual, 2021)
- *Measurement of the p_T spectrum of W & Z bosons with low-pileup data,* Poster Presentation, ATLAS Standard Model Workshop (Virtual, 2020)
- *Measurement of the p_T spectrum of W & Z bosons with low-pileup data,* Poster Presentation, ATLAS Week Collaboration Meeting (Geneva, Switzerland, 2020)

Conference/Workshop Attendance (non-presenting)

- ComSciConCAN (limited acceptance Canadian science communication conference) (Virtual, 2021)
- ICHEP Conference (Virtual, 2020, 2021)
- LHCP Conference (Virtual, 2020)
- US-Canada ATLAS Computing Bootcamp (Virtual, 2020)
- ATLAS Standard Model Workshop (Belgrade, Serbia, 2019)

Teaching Assistant Positions

- Taught six first-year introductory physics courses for physicists, engineers, life scientists
- Taught upper-year Thermal Physics, Advanced Lab Development, Science for Everyday Life

Committees

- ATLAS Early Career Scientist Board; July, 2020 – Aug., 2022
  - Nominated by ATLAS Collaboration Board to join team of seven early career scientists (ECS) who represent the ATLAS ECS cohort of ~ 1500 members by meeting with ATLAS Management, running Town Halls, other events for ECS collaboration members
  - Organized, presented at, and ran seven *"Induction Days"* to welcome new members to the Collaboration

  - Organized and moderated two *"A Year in ATLAS"* events, the follow-up event to Induction Day covering more advanced ATLAS topics for newly-qualified authors
  - Planned and moderated the first-ever LHC Early Career Scientist Fora Mental Health Workshop
  - Revamped ATLAS Advice Corner – expert assistance program for ECS
  - Wrote Internal Note on results of collaboration-wide survey to understand the collaboration's thoughts on topics like ATLAS meetings and the effect of the COVID-19 pandemic
  - Presented ECSB Update to ATLAS Collaboration during ATLAS Week meeting (February, 2022)

- Carleton U. Phys. Dept. EDI Committee; Sept., 2021 – Aug., 2022
  - Co-wrote department Code of Conduct and Equity, Diversity & Inclusion (EDI) Statement
  - Presented EDI recommendations for physics teaching to faculty

Outreach

- Conference Organization
  - *ComSciConCAN Nonprofit*: Treasurer, Workshop & Panel Organizer for 2022 national outreach conference
  - *Science Writers & Communicators of Canada*: Designed and ran poster session for 2021 virtual conference

- Presentations & Activities
  - *Skype A Scientist*: Design and deliver interactive physics talks, Q & A sessions for elementary and high school classrooms around the world ($\sim$ 10 talks given) (2020 – 2022)
  - *Pint of Science Canada*: Delivered virtual public lecture for 200 attendees (2020)

  - *Let's Talk Science*: Carleton University Team Leader (2018 – 2019)

- Podcast Guest Appearances
  - Learn Real Good: Precisely Pinpointing Bosons with Ben Davis-Purcell
  - PhD Balance Grad Chat: Finding your Voice within a Large Collaboration
  - BrainBuzzPod: Particle Physics with Ben Davis-Purcell
  - AlmaMAC: ATLAS, LHC, and Particle Physics with Ben Davis-Purcell
  - Random Walk: Pint of Science and Particle Smashing at the LHC with Ben Davis-Purcell

- Laboratory Tour Guide
  - *ATLAS Experiment*: Underground Experiment Tour Guide
  - *CERN*: CERN Open Days Tour Guide (Sept. 2019) – 75,000 people from around the world visited CERN over the course of a weekend to see the experiments and participate in particle physics activities led by volunteer experts

My time as a PhD student as a member of the ATLAS Collaboration was an incredible experience that I will cherish forever. I am glad that I was able to share this experience with others, and make contributions that should prove useful for future collaboration members and the field of particle physics as a whole. I hope that students and members who come after me enjoy their time as well, and can push through the hardships to share smiles like that which is on my face in this Figure G.2 photo, where I am seen outside the ATLAS Control Room in front of the mural of the ATLAS detector getting ready to give an underground tour of the ATLAS Experiment.

Figure G.2: Me outside of the ATLAS Control Room, standing in front of the ATLAS mural painted on the side of the building, as I prepare to give underground tours of the ATLAS Experiment to visitors from around the world during the CERN Open Days in September, 2019.

References

[1] D. Griffiths. *Introduction to Elementary Particles*. Wiley-VCH, second edition, 2008.

[2] M. Peskin and D. Schroeder. *An Introduction to Quantum Field Theory*. CRC Press, 1995.

[3] C. Burgess and G. Moore. *The Standard Model: A Primer*. Cambridge University Press, 2007.

[4] M. D. Schwartz. *Quantum Field Theory and The Standard Model*. Cambridge University Press, 2014.

[5] A. Zee. *Quantum Field Theory in a Nutshell*. Princeton University Press, second edition, 2010.

[6] S. Gasiorowicz and P. Langacker. *Elementary Particles in Physics*. University of Pennsylvania, 2005.

[7] P. A. Zyla et al. (Particle Data Group). The Review of Particle Physics. *Prog. Theor. Exp. Phys.*, 2020(8):083C01, 2020.

[8] DESY. The most precise picture of the proton. https://www.desy.de/e409/e116959/e119238/media/2891/Proton_Quark-Gluon-Gewimmel_blau.jpg, 2015.

[9] Sherpa Team. Monte Carlo Event Generators. https://sherpa-team.gitlab.io/monte-carlo.html, 2019.

[10] S. L. Glashow. Partial-symmetries of weak interactions. *Nuclear Physics*, 22(4):579–588, 1961.

[11] S. Weinberg. A model of leptons. *Phys. Rev. Lett.*, 19:1264–1266, 1967.

[12] A. Salam. Weak and Electromagnetic Interactions. *Conf. Proc. C*, 680519:367–377, 1968.

[13] S. D. Drell and T.-M. Yan. Massive Lepton-Pair Production in Hadron-Hadron Collisions at High Energies. *Phys. Rev. Lett.*, 25:316–320, 1970.

[14] The CDF Collaboration. Observation of Top Quark Production in $\overline{p}p$ Collisions with the Collider Detector at Fermilab. *Phys. Rev. Lett.*, 74:2626–2631, 1995.

[15] The D0 Collaboration. Observation of the Top Quark. *Phys. Rev. Lett.*, 74:2632–2637, 1995.

[16] The UA1 Collaboration. Experimental observation of isolated large transverse energy electrons with associated missing energy at $s = 540$ GeV. *Physics Letters B*, 122(1):103–116, 1983.

[17] The UA2 Collaboration. Observation of single isolated electrons of high transverse momentum in events with missing transverse energy at the CERN pp collider. *Physics Letters B*, 122(5):476–485, 1983.

[18] The UA1 Collaboration. Experimental observation of lepton pairs of invariant mass around 95 GeV/c^2 at the CERN SPS collider. *Physics Letters B*, 126(5):398–410, 1983.

[19] The UA2 Collaboration. Evidence for $Z^0 \to e^+e^-$ at the CERN pp collider. *Physics Letters B*, 129(1):130–140, 1983.

[20] The ATLAS Collaboration. Observation of a new particle in the search for the Standard Model Higgs boson with the ATLAS detector at the LHC. *Physics Letters B*, 716(1):1–29, 2012.

[21] The CMS Collaboration. Observation of a new boson at a mass of 125 GeV with the CMS experiment at the LHC. *Physics Letters B*, 716(1):30–61, 2012.

[22] CERN. Our Member States. https://home.cern/about/who-we-are/our-governance/member-states, 2022.

[23] E. Mobs. The CERN accelerator complex - 2019. Complexe des accélérateurs du CERN - 2019. 2019. General Photo.

[24] CERN. The birth of the Web. https://home.cern/science/computing/birth-web, 2022.

[25] E. Henley and A. Garcia. *Subatomic Physics*. World Scientific Publishing Co. Pte. Ltd., third edition, 2007.

[26] W. Leo. *Techniques for Nuclear and Particle Physics Experiments*. Springer-Verlag, 1987.

[27] The ALICE Collaboration. The ALICE experiment at the CERN LHC. *Journal of Instrumentation*, 3(08):S08002–S08002, 2008.

[28] The ATLAS Collaboration. The ATLAS Experiment at the CERN Large Hadron Collider. *Journal of Instrumentation*, 3(08):S08003–S08003, 2008.

[29] The CMS Collaboration. The CMS experiment at the CERN LHC. *Journal of Instrumentation*, 3(08):S08004–S08004, 2008.

[30] The LHCb Collaboration. The LHCb Detector at the LHC. *Journal of Instrumentation*, 3(08):S08005–S08005, 2008.

[31] CERN. LHC the guide. https://home.cern/resources/brochure/cern/lhc-guide, 2017.

[32] CERN. Longer term LHC schedule. https://lhc-commissioning.web.cern.ch/schedule/LHC-long-term.htm, 2022.

[33] The ATLAS Collaboration. ATLAS Collaboration Maps. https://cds.cern.ch/record/2654110, 2022. General Photo.

[34] JabberWok - Wikipedia-en. A graphic showing the relationship between angle and pseudorapidity. https://en.wikipedia.org/wiki/Pseudorapidity#/media/File:Pseudorapidity2.png, 2007.

[35] B. Abbott et al. Production and integration of the ATLAS Insertable B-Layer. *Journal of Instrumentation*, 13(05):T05008–T05008, 2018.

[36] The ATLAS Collaboration. Experiment Briefing: Keeping the ATLAS Inner Detector in perfect alignment. https://cds.cern.ch/record/2723878, 2020. General Photo.

[37] J. Goodson. ATLAS Magnet System. http://www.jetgoodson.com/images/thesisImages/magnetSystems.png, 2016.

[38] M. Brice. Installing the ATLAS calorimeter. Vue centrale du détecteur ATLAS avec ses huit toroides entourant le calorimètre avant son déplacement au centre du détecteur. https://cds.cern.ch/record/910381, 2005.

[39] J. Pequenao and P. Schaffner. How ATLAS detects particles: diagram of particle paths in the detector. https://cds.cern.ch/record/1505342, 2013.

[40] The ATLAS Collaboration. Operation of the ATLAS trigger system in Run 2. *Journal of Instrumentation*, 15(10):P10004–P10004, 2020.

[41] ROOT Team. ROOT Data Analysis Framework. https://root.cern/, 2021.

[42] J. Elmsheuser et al. Evolution of the ATLAS analysis model for Run-3 and prospects for HL-LHC. *Eur. Phys. J Web Conf.*, 245:06014, 2020.

[43] The ATLAS Collaboration. Luminosity Public Results Run 2. https://twiki.cern.ch/twiki/bin/view/AtlasPublic/LuminosityPublicResultsRun2, 2019.

[44] The ATLAS Collaboration. Simulated $Z \to \mu\mu$ Event Display $\langle\mu\rangle = 2$. https://atlas.web.cern.ch/Atlas/GROUPS/PHYSOFFICE/event_display/twiki_original/ATLAS_highMultiplicityZmumu_VP1EventDisplays_mu2.png.

[45] The ATLAS Collaboration. Simulated $Z \to \mu\mu$ Event Display $\langle\mu\rangle = 50$. https://atlas.web.cern.ch/Atlas/GROUPS/PHYSOFFICE/event_display/twiki_original/ATLAS_highMultiplicityZmumu_VP1EventDisplays_mu50.png.

[46] The ATLAS Collaboration. Electron reconstruction and identification in the ATLAS experiment using the 2015 and 2016 LHC proton-proton collision data at $\sqrt{s} = 13$ TeV. *Eur. Phys. J. C*, 79(639), 2019.

[47] The ATLAS Collaboration. Electron and photon performance measurements with the ATLAS detector using the 2015–2017 LHC proton-proton collision data. *Journal of Instrumentation*, 14(12):P12006–P12006, 2019.

[48] The ATLAS Collaboration. Electron efficiency measurements with the ATLAS detector using 2012 LHC proton-proton collision data. *Eur. Phys. J. C*, 77(195), 2017.

[49] The ATLAS Collaboration. Performance of the ATLAS track reconstruction algorithms in dense environments in LHC Run 2. *Eur. Phys. J. C*, 77(673), 2017.

[50] The ATLAS Collaboration. Performance of electron and photon triggers in ATLAS during LHC Run 2. *Eur. Phys. J. C*, 80(47), 2020.

[51] The ATLAS Collaboration. Electron reconstruction and identification efficiency measurements with the ATLAS detector using the 2011 LHC proton–proton collision data. *Eur. Phys. J. C*, 74(2941), 2014.

[52] The ATLAS Collaboration. Performance of the missing transverse momentum triggers for the ATLAS detector during Run-2 data taking. *J. High Energ. Phys.*, 2020(80), 2020.

[53] M. Corradi. Measurement of the W mass. https://cds.cern.ch/record/2634304, 2018.

[54] The ATLAS Collaboration. Measurement of the W-boson mass in pp collisions at $\sqrt{s} = 7$ TeV with the ATLAS detector. *Eur. Phys. J. C*, 78(110), 2018.

[55] M. Awramik et al. Precise prediction for the W-boson mass in the standard model. *Phys. Rev. D*, 69:053006, Mar 2004.

[56] The Gfitter Group., M. Baak, J. Cúth, et al. The global electroweak fit at NNLO and prospects for the LHC and ILC. *Eur. Phys. J. C*, 74(3046), 2014.

[57] Electroweak precision observables and Higgs-boson signal strengths in the Standard Model and beyond: present and future. *J. High Energ. Phys.*, 2016(135), 2016.

[58] The ALEPH Collaboration. Measurement of the W boson mass and width in e^+e^- collisions at LEP. *Eur. Phys. J. C*, 47(309-335), 2006.

[59] The DELPHI Collaboration. Measurement of the mass and width of the W boson in e^+e^- collisions at $\sqrt{s} = 161 - 209$ GeV. *Eur. Phys. J. C*, 55(1), 2008.

[60] The L3 Collaboration. Measurement of the mass and the width of the W boson at LEP. *Eur. Phys. J. C*, 45(569-587), 2006.

[61] The OPAL Collaboration. Measurement of the mass and width of the W boson. *Eur. Phys. J. C*, 45(307-335), 2006.

[62] The CDF Collaboration. Precise Measurement of the W-Boson Mass with the CDF II Detector. *Phys. Rev. Lett.*, 108:151803, 2012.

[63] The D0 Collaboration. Measurement of the W Boson Mass with the D0 Detector. *Phys. Rev. Lett.*, 108:151804, 2012.

[64] The CDF Collaboration and The D0 Collaboration. Combination of CDF and D0 W-Boson mass measurements. *Phys. Rev. D*, 88:052018, 2013.

[65] The CDF Collaboration. High-precision measurement of the W boson mass with the CDF II detector. *Science*, 376(6589):170–176, 2022.

[66] The ATLAS Collaboration. Measurement of the transverse momentum distribution of Drell-Yan lepton pairs in proton-proton collisions at $\sqrt{s} = 13$ TeV with the ATLAS detector. *Eur. Phys. J. C*, 80(616), 2020.

[67] S. Catani et al. Vector Boson Production at Hadron Colliders: A Fully Exclusive QCD Calculation at Next-to-Next-to-Leading Order. *Phys. Rev. Lett.*, 103:082001, 2009.

[68] S. Catani et al. Vector boson production at hadron colliders: transverse-momentum resummation and leptonic decay. *J. High Energ. Phys.*, 2015(1-47), 2015.

[69] T. Sjöstrand and S. Mrenna and P. Skands. A brief introduction to PYTHIA 8.1. *Computer Physics Communications*, 178(11):852–867, 2008.

[70] The ATLAS Collaboration. Measurement of the Z/γ^* boson transverse momentum distribution in pp collisions at $\sqrt{s} = 7$ TeV with the ATLAS detector. *J. High Energ. Phys.*, 2014(145), 2014.

[71] The ATLAS Collaboration. Prospects for the measurement of the W-boson transverse momentum with a low pileup data sample at $\sqrt{s} = 13$ TeV with the ATLAS detector. https://cds.cern.ch/record/2298152, 2017. ATL-PHYS-PUB-2017-021.

[72] The ATLAS Collaboration. Measurement of $W^{\pm}$-boson and Z-boson production cross-sections in pp collisions at $\sqrt{s} = 2.76$ TeV with the ATLAS detector. *Eur. Phys. J. C*, 79(901), 2019.

[73] G. Cowan. A survey of unfolding methods for particle physics. *Conf. Proc. C*, 0203181:248–257, 2002.

[74] L. Lyons. Unfolding: Introduction. *Proceedings of the PHYSTAT 2011 Workshop on Statistical Issues Related to Discovery Claims in Search Experiments and Unfolding*, pages 225–228, 2011.

[75] G. Choudalakis. Unfolding in ATLAS. *Proceedings of the PHYSTAT 2011 Workshop on Statistical Issues Related to Discovery Claims in Search Experiments and Unfolding*, pages 297–308, 2011.

[76] G. D'Agostini. Improved iterative Bayesian unfolding. *arXiv:1010.0632*, 2010.

[77] T. Adye. Unfolding algorithms and tests using RooUnfold. *Proceedings of the PHYSTAT 2011 Workshop on Statistical Issues Related to Discovery Claims in Search Experiments and Unfolding*, pages 313–318, 2011.

[78] P. Nason. A New Method for Combining NLO QCD with Shower Monte Carlo Algorithms. *J. High Energ. Phys.*, 2004(11):040–040, 2004.

[79] S. Frixione, P. Nason, and C. Oleari. Matching NLO QCD computations with parton shower simulations: the POWHEG method. *J. High Energ. Phys.*, 2007(11):070–070, 2007.

[80] S. Alioli et al. NLO vector-boson production matched with shower in POWHEG. *J. High Energ. Phys.*, 2008(07):060–060, 2008.

[81] S. Alioli et al. A general framework for implementing NLO calculations in shower Monte Carlo programs: the POWHEG BOX. *J. High Energ. Phys.*, 2010(43), 2010.

[82] M. Guzzi et al. CT10 parton distributions and other developments in the global QCD analysis. *arXiv:1101.0561*, 2011.

[83] W. Buttinger. Background Estimation with the ABCD Method. https://twiki.cern.ch/twiki/pub/Main/ABCDMethod/ABCDGuide_draft18Oct18.pdf, 2018.

[84] S. Choi and H. Oh. Improved extrapolation methods of data-driven background estimations in high energy physics. *Eur. Phys. J. C*, 81(643), 2021.

[85] B. Efron. Bootstrap Methods: Another Look at the Jackknife. *The Annals of Statistics*, 7(1):1 – 26, 1979.

[86] The ATLAS Collaboration. Evaluating statistical uncertainties and correlations using the bootstrap method, 2021. ATL-PHYS-PUB-2021-011.

[87] The ATLAS Collaboration. Muon reconstruction performance of the ATLAS detector in proton–proton collision data at $\sqrt{s} = 13$ TeV. *Eur. Phys. J. C*, 76(292), 2016.

[88] G. Avoni et al. The new LUCID-2 detector for luminosity measurement and monitoring in ATLAS. *Journal of Instrumentation*, 13(07):P07017, 2018.

[89] The ATLAS Collaboration. Luminosity determination in pp collisions at $\sqrt{s} = 13$ TeV using the ATLAS detector at the LHC, 2019. ATLAS-CONF-2019-021.

[90] S. Höche et al. NLO matrix elements and truncated showers. *J. High Energ. Phys.*, 2011(123), 2011.

[91] S. Camarda et al. DYTurbo: fast predictions for Drell-Yan processes. *Eur. Phys. J. C*, 80(251), 2020.

[92] The NNPDF Collaboration. Parton distributions for the LHC run II. *J. High Energ. Phys.*, 2015(40), 2015.

[93] J. Bellm et al. Herwig 7.0/Herwig++ 3.0 release note. *Eur. Phys. J. C*, 76(196), 2016.

[94] The ATLAS Collaboration. Measurement of the transverse momentum distribution of W bosons in pp collisions at $\sqrt{s} = 7$ TeV with the ATLAS detector. *Phys. Rev. D*, 85:012005, 2012.

[95] J. R. R. Tolkien. *The return of the king: being the third part of The Lord of the rings*. G. Allen & Unwin, 1955.

[96] The ATLAS Collaboration. 13.6 TeV collisions July 5, 2022. https://twiki.cern.ch/twiki/pub/AtlasPublic/EventDisplayRun3Collisions/event_display_Zee_Run_427394_Event10631430_5Jul2022.png, 2022.

[97] S. Zimmerman and A. Polini. ATLAS Run Coordination: Run-2 Shift Operations. https://edms.cern.ch/ui/file/1348082/1/Run2_OperationsModel_Draft_version_08.pdf, 2014.